

**Springer Theses**

Recognizing Outstanding Ph.D. Research

Zhandong Wang

**Experimental  
and Kinetic Modeling  
Study of Cyclohexane  
and Its Mono-alkylated  
Derivatives Combustion**

 Springer

# **Springer Theses**

Recognizing Outstanding Ph.D. Research

## **Aims and Scope**

The series “Springer Theses” brings together a selection of the very best Ph.D. theses from around the world and across the physical sciences. Nominated and endorsed by two recognized specialists, each published volume has been selected for its scientific excellence and the high impact of its contents for the pertinent field of research. For greater accessibility to non-specialists, the published versions include an extended introduction, as well as a foreword by the student’s supervisor explaining the special relevance of the work for the field. As a whole, the series will provide a valuable resource both for newcomers to the research fields described, and for other scientists seeking detailed background information on special questions. Finally, it provides an accredited documentation of the valuable contributions made by today’s younger generation of scientists.

### **Theses are accepted into the series by invited nomination only and must fulfill all of the following criteria**

- They must be written in good English.
- The topic should fall within the confines of Chemistry, Physics, Earth Sciences, Engineering and related interdisciplinary fields such as Materials, Nanoscience, Chemical Engineering, Complex Systems and Biophysics.
- The work reported in the thesis must represent a significant scientific advance.
- If the thesis includes previously published material, permission to reproduce this must be gained from the respective copyright holder.
- They must have been examined and passed during the 12 months prior to nomination.
- Each thesis should include a foreword by the supervisor outlining the significance of its content.
- The theses should have a clearly defined structure including an introduction accessible to scientists not expert in that particular field.

More information about this series at <http://www.springer.com/series/8790>

Zhandong Wang

# Experimental and Kinetic Modeling Study of Cyclohexane and Its Mono-alkylated Derivatives Combustion

Doctoral Thesis accepted by  
the University of Science and Technology of China,  
Hefei, China

 Springer

*Author*  
Dr. Zhandong Wang  
University of Science and Technology  
of China  
Hefei  
People's Republic of China

*Supervisor*  
Prof. Fei Qi  
University of Science and Technology  
of China  
Hefei  
People's Republic of China

ISSN 2190-5053                      ISSN 2190-5061 (electronic)  
Springer Theses  
ISBN 978-981-10-5692-5              ISBN 978-981-10-5693-2 (eBook)  
<https://doi.org/10.1007/978-981-10-5693-2>

Library of Congress Control Number: 2017963973

© Springer Nature Singapore Pte Ltd. 2018

This work is subject to copyright. All rights are reserved by the Publisher, whether the whole or part of the material is concerned, specifically the rights of translation, reprinting, reuse of illustrations, recitation, broadcasting, reproduction on microfilms or in any other physical way, and transmission or information storage and retrieval, electronic adaptation, computer software, or by similar or dissimilar methodology now known or hereafter developed.

The use of general descriptive names, registered names, trademarks, service marks, etc. in this publication does not imply, even in the absence of a specific statement, that such names are exempt from the relevant protective laws and regulations and therefore free for general use.

The publisher, the authors and the editors are safe to assume that the advice and information in this book are believed to be true and accurate at the date of publication. Neither the publisher nor the authors or the editors give a warranty, express or implied, with respect to the material contained herein or for any errors or omissions that may have been made. The publisher remains neutral with regard to jurisdictional claims in published maps and institutional affiliations.

Printed on acid-free paper

This Springer imprint is published by the registered company Springer Nature Singapore Pte Ltd. part of Springer Nature  
The registered company address is: 152 Beach Road, #21-01/04 Gateway East, Singapore 189721, Singapore

# Supervisor's Foreword

The combustion of fossil fuels provides most of the energy used worldwide, and it promotes the growth of society and the economy. However, large amounts of emitted pollutants are harmful to human health and to the sustainability of human civilization. The design of high-efficiency low-emission engines and the development of detailed kinetic models of fossil fuels are crucial to alleviating the energy shortage and reducing pollution. Cycloalkanes are an important component of fossil fuels and their surrogates. In China, for example, No. 3 Kerosene has large mass fraction of cycloalkanes, and the recent discovery of oil sands may contain larger fractions of cycloalkanes. The combustion of cyclohexane and its derivatives produces large amounts of dienes (carcinogenic 1,3-butadiene) and cyclic intermediates, and it has a relatively high sooting tendency.

The object of this Ph.D. thesis is to clarify the combustion chemistry of cyclohexane and its two mono-alkylated derivatives (methylcyclohexane and ethylcyclohexane), which are commonly chosen as surrogate components for transport fuels. The pyrolysis and laminar premixed flames of these three model compounds were studied using state-of-the-art synchrotron radiation photoionization mass spectrometry. Their initial reaction pathways during combustion were calculated with high-level quantum chemistry methods, and the rate constants were evaluated. A detailed kinetic model was developed and validated against experimental data covering a wide range of combustion conditions, including pyrolysis at various pressures, flame structure at low pressures, as well as species concentrations from jet-stirred reactor oxidation at intermediate and high temperatures, ignition delay times, and laminar flame speeds. This model contributes to understanding the combustion chemistry of these cycloalkanes (initial decomposition pathways,

distribution of intermediates, and formation of air pollutants), developing combustion models for substituted cycloalkanes with long alkyl side chains and/or multiple side chains, and it has application to engine and fuel design, and emission control.

Hefei, People's Republic of China  
September 2017

Prof. Fei Qi

**Parts of this thesis have been published in the following journals:**

- Z. Wang, Z. Cheng, W. Yuan, J. Cai, L. Zhang, F. Zhang, F. Qi, J. Wang, *Combust. Flame* 159 (2012) 2243–2253.
- F. Zhang, Z.D. Wang, Z.H. Wang, L.D. Zhang, Y.Y. Li, F. Qi, *Energy Fuels* 27 (2013) 1679–1687.
- Z. Wang, L. Ye, W. Yuan, L. Zhang, Y. Wang, Z. Cheng, F. Zhang, F. Qi, *Combust. Flame* 161 (2014) 84–100.
- Z. Wang, H. Bian, Y. Wang, L. Zhang, Y. Li, F. Zhang, F. Qi, *Proc. Combust. Inst.* 35 (2015) 367–375.
- Z. Wang, L. Zhao, Y. Wang, H. Bian, L. Zhang, F. Zhang, Y. Li, S.M. Sarathy, F. Qi, *Combust. Flame* 162 (2015) 2873–2892.



# Acknowledgements

This Ph.D. thesis was based on research at the National Synchrotron Radiation Laboratory, University of Science and Technology of China, from 2008 to 2014, under the supervision of Prof. Fei Qi. As my mentor in my Ph.D. studies and throughout my academic career, Prof. Qi's impressive knowledge, his enthusiasm for scientific exploration, and his constant search for excellence have influenced me significantly. I would also like to thank Prof. Frédérique Battin-Leclerc, Prof. Katharina Kohse-höinghaus, Prof. Olivier Herbinet, Prof. Lidong Zhang, Prof. Yuyang Li, and Prof. Feng Zhang for their guidance, and Prof. Mani Sarathy for the support of this work.

Finally, I wish to thank the members of the combustion and flame team for their help and companionship. Many thanks to my family for their continuous support.

September 2017

Zhandong Wang

# Contents

<b>1</b>	<b>Introduction</b>	1
1.1	Background	1
1.2	Diagnostics of Laboratory Combustion System	2
1.2.1	<i>In Situ</i> Optical Spectroscopy	3
1.2.2	Product Analysis After Gas-Sampling	3
1.3	Fossil Fuel Surrogates	7
1.3.1	Surrogates for Gasoline	8
1.3.2	Surrogates for Jet Fuel	8
1.3.3	Surrogates for Diesel	9
1.4	Research on Cycloalkane Fuels	11
1.5	Thesis Content	15
	References	16
<b>2</b>	<b>Experimental Method and Kinetic Modeling</b>	23
2.1	Experimental Method	23
2.1.1	Synchrotron Radiation Beamline	23
2.1.2	Flow Reactor Pyrolysis Apparatus	24
2.1.3	Low-Pressure Laminar Premixed Flame	30
2.2	Kinetic Modeling	32
2.2.1	Thermodynamic Data	33
2.2.2	Chemical Kinetic Data	34
2.2.3	Transport Data	35
	References	36
<b>3</b>	<b>Experimental and Modeling Study of Cyclohexane Combustion</b>	39
3.1	Background	39
3.2	Kinetic Model	42
3.2.1	Unimolecular Decomposition and Isomerization of Cyclohexane	42
3.2.2	Dissociation of 1-Hexene	52

3.2.3	H-atom Abstraction of Cyclohexane . . . . .	53
3.2.4	Decomposition and Isomerization of Cyclohexyl Radical . . . . .	53
3.2.5	Decomposition and Isomerization of 5-Hexen-1-yl Radical . . . . .	55
3.2.6	Decomposition and Dehydrogenation of Cyclohexene . . . . .	57
3.3	Flow Reactor Pyrolysis of Cyclohexane . . . . .	60
3.3.1	Consumption of Cyclohexane . . . . .	61
3.3.2	Formation and Consumption of Cyclopentadiene and Benzene . . . . .	68
3.4	Laminar Premixed Flame of Cyclohexane . . . . .	70
3.5	JSR Oxidation of Cyclohexane . . . . .	75
3.6	Ignition Delay Time and Laminar Flame Speed of Cyclohexane . . . . .	80
3.7	Summary and Conclusions . . . . .	81
	References . . . . .	83
<b>4</b>	<b>Experimental and Modeling Study of Methylcyclohexane Combustion . . . . .</b>	<b>89</b>
4.1	Background . . . . .	89
4.2	Decomposition and Isomerization of Methylcyclohexane . . . . .	91
4.2.1	Theoretical Method . . . . .	93
4.2.2	Results and Discussion . . . . .	94
4.3	H-atom Abstraction of Methylcyclohexane . . . . .	100
4.4	Unimolecular Reactions of Methylcyclohexane Radicals . . . . .	103
4.5	Estimation of Thermodynamic Data . . . . .	105
4.6	Kinetic Model for Methylcyclohexane Combustion . . . . .	109
4.7	Flow Reactor Pyrolysis . . . . .	110
4.7.1	Consumption of Methylcyclohexane . . . . .	110
4.7.2	Isomerization of Cyclohexyl Radical and Methylcyclohexane Radicals . . . . .	120
4.7.3	Dissociation of Cyclohexyl and Methylcyclohexane Radicals . . . . .	125
4.7.4	Reaction Pathway Analysis for Toluene and Benzene . . . . .	129
4.8	Low-Pressure Premixed Flame of Methylcyclohexane . . . . .	131
4.9	Ignition Delay Time and Laminar Flame Speed . . . . .	136
4.10	Summary and Conclusions . . . . .	139
	References . . . . .	140

<b>5 Experimental and Modeling Study of Ethylcyclohexane</b>	
<b>Combustion</b> . . . . .	145
5.1 Background . . . . .	145
5.2 Preliminary Investigation of Ethylcyclohexane	
Decomposition . . . . .	146
5.2.1 Dissociation and Isomerization of Ethylcyclohexane . . . . .	146
5.2.2 Ring-Opening Isomerization of Ethylcyclohexane	
Radicals . . . . .	149
5.2.3 Dissociation of Ethylcyclohexane Radicals . . . . .	153
5.3 Kinetic Model of Ethylcyclohexane . . . . .	156
5.4 Pyrolysis of Ethylcyclohexane . . . . .	161
5.5 Premixed Flame of Ethylcyclohexane . . . . .	171
5.6 JSR Oxidation of Ethylcyclohexane . . . . .	175
5.7 Laminar Flame Speed of Ethylcyclohexane . . . . .	179
5.8 Summary and Conclusions . . . . .	180
References . . . . .	181
<b>6 Combustion Kinetics of Cyclohexane and C1–C2 Mono-alkyl</b>	
<b>Cyclohexanes</b> . . . . .	183
6.1 Flow Reactor Pyrolysis . . . . .	183
6.1.1 Species Pool . . . . .	184
6.1.2 Mole Fraction Distribution . . . . .	188
6.2 Low-Pressure Premixed Flame . . . . .	193
6.3 Laminar Flame Speed . . . . .	197
References . . . . .	199
<b>7 Conclusions and Perspective</b> . . . . .	201
<b>Appendix A</b> . . . . .	205
<b>Appendix B</b> . . . . .	210
<b>Appendix C</b> . . . . .	214

# Chapter 1

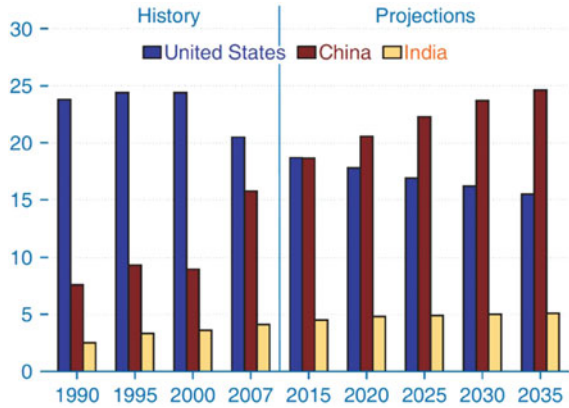
## Introduction

### 1.1 Background

Energy—its safety and availability—determines the future of human society. Although there continues to be significant development in renewable energies, more than 85% of current energy still originates with combustion of fossil fuels, guaranteeing a prosperous global economy and quality of life. In China, coal combustion plays a significant role in energy supply and accounts for 70% of the resource consumed [1]. Internal combustion engines, powered by gasoline and diesel fuels, represent 60% of the oil consumed [2]. Global demand for energy is increasing, especially in emerging markets. Figure 1.1 shows the proportion of world energy consumption in the U.S., China and India from 1990 to 2035. In 2015, China exceeded the U.S. to become the world's largest energy consuming country [3]. In 2010, China became the world's second largest economy and the world's second largest importer and consumer of oil. However, general energy utilization efficiency in China is only around 33%, about 10% lower than developed countries [4], causing energy consumption per GDP in China to be three times higher than the U.S. and five times higher than in Japan. Thus, it is imperative that fossil fuel combustion efficiency is increased, especially in emerging markets.

Fossil fuel combustion is also the dominant source of air pollutants, including greenhouse gas CO<sub>2</sub>, unburnt hydrocarbons, NO<sub>x</sub>, SO<sub>x</sub>, and soot. These emissions cause serious environmental issues, such as global warming, photochemical smog and acid rains. Recent studies show that the atmospheric temperature of Antarctica is positively related to the concentration of CO<sub>2</sub> and CH<sub>4</sub> [5], originating mainly from the combustion process [6]. As noted above, the combustion of internal combustion engines consumed ~60% of oil in China, contributing to more than 25% of CO<sub>2</sub> emissions and more than 60% of urban air pollutants [4]. Cleaner, more efficient combustion—especially in internal combustion engines—is crucial to reducing the energy shortage, migrating air pollutant emissions, and maintaining global economic growth. To this end, a comprehensive understanding of the

**Fig. 1.1** Proportion of energy consumption in U.S., China, and India from 1990–2035 [3]. *Source* U.S. Energy Information Administration



combustion process of fossil fuels is necessary to improve traditional combustion engines and develop new combustion techniques such as homogeneous charge compression ignition engines (HCCI) [7, 8]. A key component of computational fluid dynamics (CFD) simulation is the reduced combustion mechanism of fossil fuels.

The prevalent method for developing a well-defined reduced model uses a detailed kinetic model of the candidate fuels. The model is then validated comprehensively with laboratory-based experimental data under a wide range of combustion conditions, such as pressure, temperature, and equivalence ratios. These experimental data—with well-defined physical models—include ignition delay times, laminar flame speeds and species speciation, etc. However, hundreds to thousands of hydrocarbon components make development of detailed kinetic models for gasoline, jet fuel and diesel very challenging. Instead, surrogates for fossil fuels with similar physical and chemical properties have been employed to mimic the combustion process of real fuels. In the following sections, combustion diagnostics for laboratory combustion systems, progress in surrogate fuels research, and the contents of this thesis are highlighted.

## 1.2 Diagnostics of Laboratory Combustion System

Laboratory-based combustion systems include shock tube (ST), rapid compression machine (RCM), flow reactor (FR), jet-stirred reactor (JSR), burner-stabilized laminar premixed flame, spherical laminar premixed flame, co-flow diffusion flame, and counterflow diffusion flame, etc. The combustion diagnostics related to these

systems mainly consist of in situ analysis by optical spectroscopy and gas-sampling, combined with different analytical methods [e.g., optical spectroscopy, gas chromatography (GC), and mass spectrometer (MS)].

### ***1.2.1 In Situ Optical Spectroscopy***

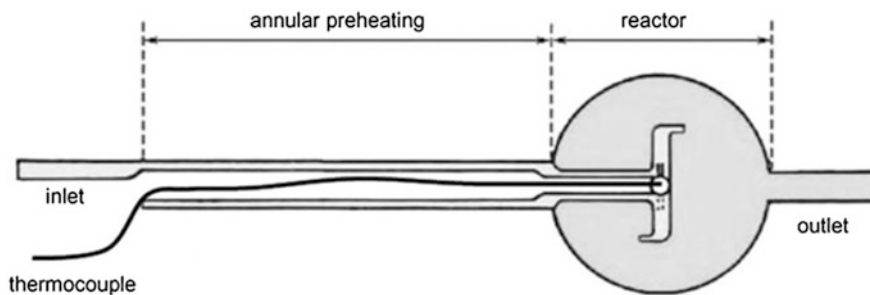
In situ optical spectroscopy is a non-intrusive diagnostic with no perturbation in the combustion process [9–13]. It has been widely adopted for solutions to fundamental and applied combustion problems. In combustion chemistry studies, in situ optical spectroscopy is often used to investigate fuel ignition properties in ST oxidation; the time-dependent emission signals of OH\* and CH\* [14] are measured to derive ignition delay times. Recently, infrared laser absorption, ultraviolet laser absorption and CO<sub>2</sub> laser absorption [15, 16] were adopted by Prof. Ronald Hanson's group to measure the time histories of species such as OH, CH<sub>3</sub>, CO, CO<sub>2</sub>, H<sub>2</sub>O and C<sub>2</sub>H<sub>4</sub> during ST pyrolysis and/or oxidation. The time-dependent decay of OH radical by OH radical absorption spectroscopy was also monitored to measure H-abstraction rate constants of OH radical. Although in situ optical spectroscopy has been widely used in combustion studies, it can only detect molecules using simple structures, and it hinders the detection of complex combustion products [9, 11].

### ***1.2.2 Product Analysis After Gas-Sampling***

For a thorough analysis of combustion products, gas-sampling from the combustion process, such as flame, JSR/FR/ST pyrolysis and oxidation, and RCM oxidation have been applied. A quartz probe, or nozzle, was inserted into the combustion system to sample the products, which were then separated and analyzed using various analytical methods. Although the probe or nozzle disturbed the combustion field and/or flame intermediates/temperature distribution, gas-sampling combined with GC analysis and/or mass spectrometer is powerful enough to probe the comprehensive species' pool of intermediates. Furthermore, the perturbation effect can be reduced significantly with well-defined nozzle geometry [17, 18]. Thus, gas-sampling has been widely employed in combustion-related experiments [19, 20].

The advantages of GC analysis include low detection limit and high separation efficiency, especially for separating isomers [21, 22]. On one hand, identifying reaction products is achieved by comparing retention time with that of known compounds; in complex reaction systems, the GC-MS is very useful in identifying the structure of the products [23]. On the other hand, a flame ionization detector (FID) and thermal conductivity detector (TCD) can be installed at the outlet of the GC column to quantify the reaction products.

Several research groups have used gas-sampling (e.g., quartz probe) combined with GC/GC-MS to analyze combustion products. This method has been used to



**Fig. 1.2** Schematic of JSR used in Battin-Leclerc's group [32]. Reprinted from Ref. [32], with kind permission from Springer Science+Business Media

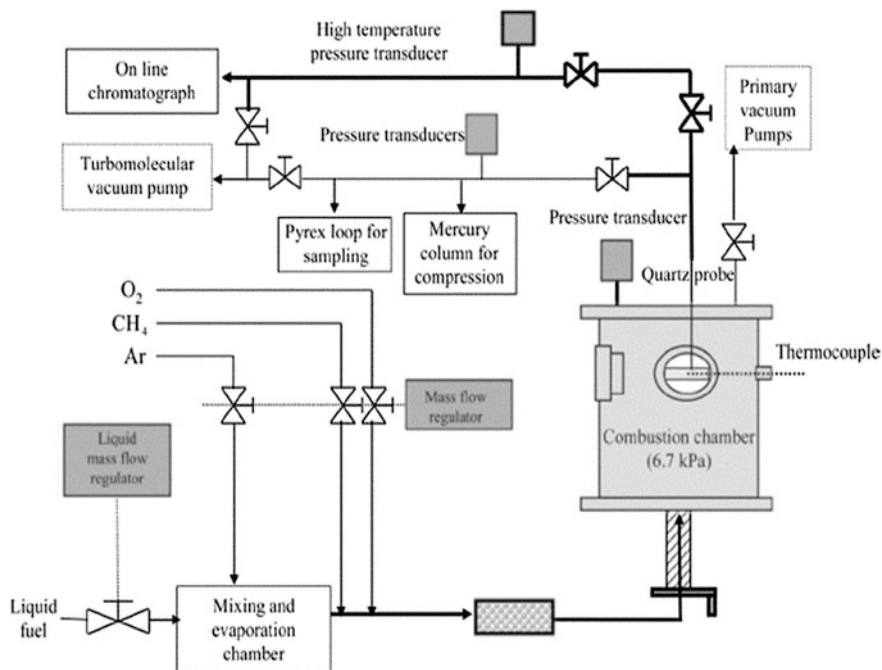
study the JSR oxidation of various kind of fuels by groups working with Philippe Dagaut and Frédérique Battin-Leclerc [24–26]. JSR is an idea reactor for studying low- and high-temperature oxidation of fuels [20, 25–29]; the fused silica reactor prevents wall catalytic reactions [30]. Figure 1.2 shows the scheme of the JSR from Prof. Battin-Leclerc's group. The gas mixture of fuel/O<sub>2</sub>/dilution flows into the reactor through the preheating zone. The four nozzles at the centre of the reactor achieve high-speed stirring, which ensures the homogeneity of species and temperature during reaction. The mixture from the outlet of the reactor was then sampled and analyzed [28, 31].

The Princeton group [33–39] also used gas-sampling combined with GC/GC-MS to investigate reaction products from atmospheric and high-pressure fuel pyrolysis and oxidation in a turbulent flow reactor. Other applications of gas-sampling combined with GC/GC-MS include mainly pyrolysis and oxidation in ST and RCM, laminar premixed flame and counterflow diffusion flame [40–58]. Figure 1.3 shows the scheme of the low-pressure laminar premixed flame apparatus combined with gas-sampling and GC analysis [52].

To form the molecular beam (MB) for mass spectrometry (MS) analysis, a quartz nozzle is commonly used for gas-sampling. The sampled products are then ionized with a different ionization source, such as electron impact ionization (EI), chemical ionization (CI), and laser photoionization (Laser-PI). EI-MBMS and Laser-PI-MBMS have been applied in many flame studies to find the intermediate speciation. However, these two ionization methods have their own drawbacks. For example, the EI source produces many fragments, which interfere with the analysis of reaction intermediates; the low energy resolution of the EI source makes it untenable to separate isomers. The wavelength of the Laser-PI is often fixed, or the tunability in the UV range is limited, preventing the identification of isomers; it is also difficult to detect species with very high ionization energy.

At the beginning of the 21st century, the synchrotron radiation photoionization (SR-PI) mass spectrometer was combined with molecular beam sampling to investigate low-pressure premixed flames [59, 60]. The tunable synchrotron radiation was used in a single photon ionization technique. Fragments could be reduced

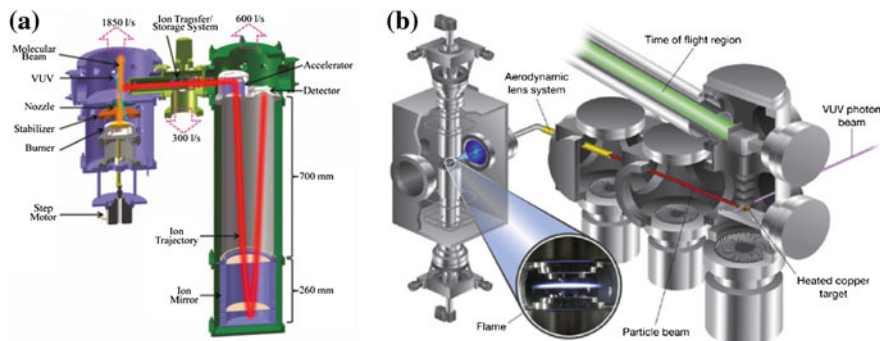




**Fig. 1.3** Low-pressure laminar premixed flame apparatus combined with gas-sampling and GC analysis [52]. Reprinted from Ref. [52], Copyright 2008, with permission from Elsevier

from carefully selected photon energies [20], and isomers of the reaction products could be separated from the scan of the photon energies. Since then, SR-PI-MBMS have been successfully used to study the flame structure of low-pressure premixed flame of hydrocarbons, oxygenated, and nitrogenous compounds [20]. Later, this diagnostic was adopted to sample and analyze the products in flow reactor pyrolysis [61–70], JSR oxidation [21, 29, 31, 71, 72], and co-flow diffusion flame [73–75]. Recently, Prof. Fei Qi and co-workers developed new apparatus for the laminar premixed flame, which can be used to study flame structure from several Torr to 760 Torr. The new designed mass spectrometer has a higher mass resolution ( $\sim 3500$  at  $m/z$  40), a lower detection limit ( $<1$  ppm), and a wider dynamic range (better than five orders of magnitude) [76]. The ethylene flame at 30, 150, and 760 Torr was studied; radical intermediates were detected not only at low-pressure flame, but also at atmospheric-pressure flame.

Professor Nils Hansen and co-workers applied the SR-PI-MBMS to probe counterflow diffusion flames of acetylene at low pressure [77] and acetylene, ethylene and propane at quasi-atmospheric pressure [78]. In the quasi-atmospheric flames, flame species from  $m/z$  15–900 were detected using an aerosol mass spectrometer. Figure 1.4 shows the laminar premixed flame and counterflow diffusion flame apparatus combined with SR-PI-MBMS.



**Fig. 1.4** Laminar premixed flame [76] and counterflow diffusion flame [78] apparatus combined with SR-PI-MBMS. Reprinted with permission from Ref. [76]. Copyright 2013, American Institute of Physics; Reprinted from Ref. [78], Copyright 2013, with permission from Elsevier

In addition to GC and MS analysis, optical spectroscopy was also used to detect smaller intermediates after the gas-sampling. For example, Prof. Dagaut's group combined Fourier transform infrared (FTIR) spectroscopy with JSR to measure oxidation products such as CO, CO<sub>2</sub>, H<sub>2</sub>O, NO, NO<sub>2</sub>, and CH<sub>2</sub>O [79]. Recent work by Profs. Battin-Leclerc and Fittschen combined cavity ring-down spectroscopy (CRDS) with JSR and detected CH<sub>2</sub>O, H<sub>2</sub>O, C<sub>2</sub>H<sub>4</sub>, and H<sub>2</sub>O<sub>2</sub> [80, 81] during *n*-butane low-temperature oxidation. They also combined the fluorescence assay using gas expansion (FAGE) with JSR, and measured the temperature-dependent speciation of OH and HO<sub>2</sub> radicals during *n*-butane low-temperature oxidation [82]. HO<sub>2</sub> radical was also detected by Prof. Yiguang Ju's group, at the outlet of flow reactor oxidation of dimethyl ether; the mid-infrared Faraday rotation spectroscopy and dual modulation Faraday rotation spectroscopy [83, 84] was applied in this study.

In summary, the macroscopic and microscopic combustion properties of fuels can be obtained from these laboratory combustion systems and the combined diagnostics. The macroscopic combustion properties include laminar flame speeds, auto-ignition temperature, extinction strain rates, and ignition delay time, etc.; microscopic combustion properties include detailed species mole fraction profiles in FR/JSR/ST pyrolysis and oxidation, laminar premixed flames, counterflow diffusion flames, and co-flow diffusion flames, etc. These experimental data feature combustion processes from low to high pressure, low to high temperature, and fuel-lean combustion to fuel-rich combustion, significantly contributing to understanding of combustion physics, chemistry and their application in industry. They are also the basis for development and examination of comprehensive combustion kinetic models.

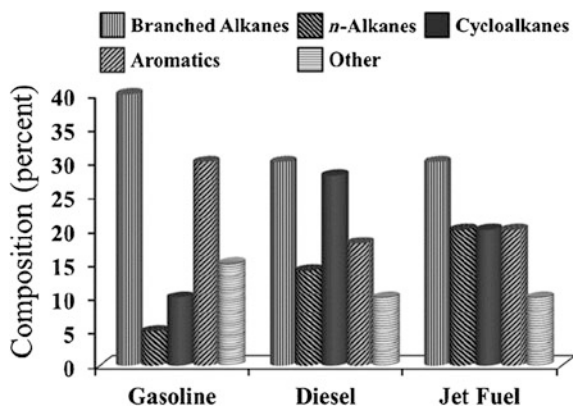
### 1.3 Fossil Fuel Surrogates

To establish comprehensive combustion models of fossil fuels, the combustion properties of fossil fuel components must be clarified and corresponding combustion models developed. One challenge is the hundreds to thousands of components of the fossil fuels themselves; these components may differ among markets, refining processes, and storage periods. Surrogate fuel strategies are proposed for a molecular-level understanding of fossil fuel combustion.

Surrogate fuels are a mixture of several simple compounds that mimic the physical and chemical properties of fossil fuels. Physical properties include vaporization, viscosity, density, surface tension, and diffusion coefficient, etc. The chemical properties include flame speeds, ignition properties, molecular weight, C/H ratio, adiabatic flame temperature, and pollutant formation, etc. Surrogate fuels reduce the chemical and/or physical complexity of the fossil fuel; their experimental and combustion models provide valuable insight into the combustion process of fossil fuels [85].

Gasoline, jet and diesel fuels are obtained through the fractional distillation of petroleum; their average molecular weight, density, and boiling point increases accordingly. For example, gasoline consists mainly of hydrocarbons with four to 12 carbon numbers, with a density of 0.71–0.77 g/mL and boiling point of 303–463 K. Jet fuel consists mainly of hydrocarbons with eight to 16 carbon numbers, a density of 0.78–0.81 g/mL and boiling point of 433–553 K. Diesel is mostly hydrocarbons with ten to 24 carbon numbers, and a density of 0.81–0.86 g/mL and boiling point of 463–633 K [88–93]. One approach to formulating surrogate fuels is to choose compounds that represent the hydrocarbon class of fossil fuels, composed mainly of normal alkanes, branched alkanes, cycloalkanes, aromatics, and a variety of additive [86], as shown in Fig. 1.5.

**Fig. 1.5** Components of gasoline, jet fuel, and diesel [86]. Reproduced from Ref. [87] by permission of John Wiley & Sons Ltd.



### 1.3.1 *Surrogates for Gasoline*

The major components of alkanes in gasoline contain five to seven carbon numbers; and the fraction of iso-alkanes is higher than *n*-alkanes. Generally, *n*-butane, *n*-pentane, iso-pentane, methyl pentanes (iso-hexanes), and iso-octane are the prevalent alkanes [91]. *n*-heptane and iso-octane are the components of primary reference fuel (PRF) and they have been extensively studied [94–96]. Indeed, the concentration of *n*-heptane in gasoline is very low; iso-octane also exhibits relatively low concentration in regular gasoline but can have a higher fraction in premium gasoline. The most abundant cycloalkanes in gasoline such as methylcyclopentane, methylcyclohexane, and cyclohexane, have six to seven carbon numbers. Similar to alkanes, the major components of olefins in gasoline are isomers with five to seven carbon numbers. Branched olefins are much more prevalent than linear olefins, e.g., methylbutenes and methylpentenes. The most abundant aromatic in gasoline is toluene, along with aromatics with eight or more carbon numbers (e.g., surrogate benzene with two to three methyl groups).

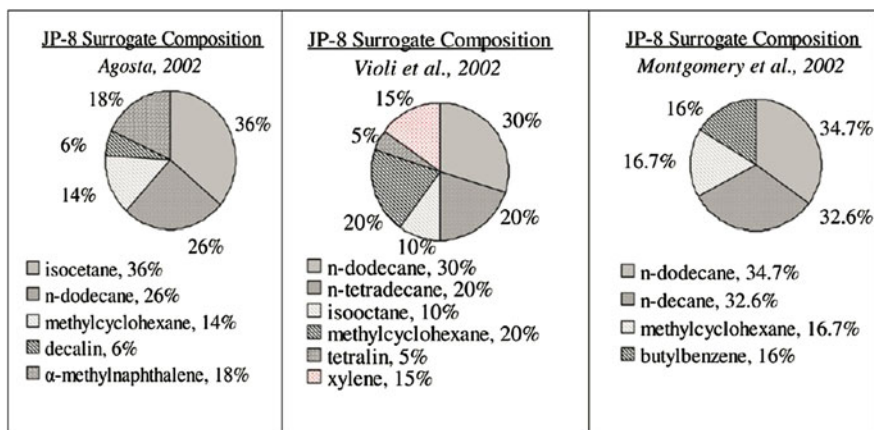
For gasoline surrogates, the commonly accepted three component surrogates are *n*-heptane, iso-octane, and toluene. Other components with reported kinetic models, like 1-pentene, diisobutylene, cyclohexane, and methylcyclohexane, could also be presumed to build the multicomponent gasoline surrogates [91].

### 1.3.2 *Surrogates for Jet Fuel*

Jet fuel is a type of aviation fuel designed for aircrafts powered by gas-turbine engines for commercial and military purposes. The most commonly used commercial aviation fuels are jet A and jet A-1, which are produced from a standardized international specification. The China commercial jet fuel—China NO. 3 Kerosene—is similar to jet A-1. For military jet fuels in the U.S., descriptions are taken from the work of Edwards and Maurice [85]:

JP-4 is an aviation gasoline/kerosene mixture used by the U.S. Air Force (USAF) until the 1980s, when it was replaced by JP-8. JP-8 is a “kerosene” fuel used by the USAF for jet aircraft. JP-8 is very similar to Jet A and A-1. JP-8 is essentially Jet A-1, with three additives: a lubricity improver/corrosion inhibitor, an antistatic additive, and a fuel system icing inhibitor. JP-5 is a high flash point kerosene used for aircraft flying from U.S. Navy ships. JP-7 is a specialty kerosene fuel used for the SR-71. RP-1 is the standard U.S. kerosene rocket propellant. The Jet A/A-1/JP-8 specifications are fairly broad, and a wide variety of hydrocarbon mixtures can meet the specification requirements.

According to the boiling point range, the carbon number of jet fuels is mainly in the range of ten to 14. As shown in Fig. 1.5, normal alkanes constitute ~20% of jet fuel. *n*-decane, *n*-dodecane, and *n*-tetradecane are often selected as surrogate candidates. Branched alkanes constitute ~35–40% of jet fuel. Although iso-octane and iso-cetane are not in the C<sub>10</sub> to C<sub>14</sub> range, they have been selected as surrogate

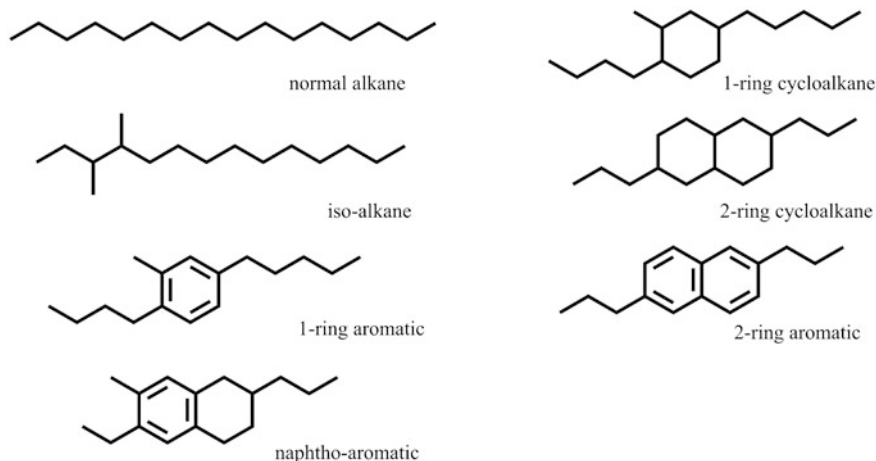


**Fig. 1.6** Surrogate palette for JP-8 [97]. Reprinted from Ref. [97], Copyright 2004, with permission from Elsevier

components of jet fuels because of their moderate cost and the relatively good development of their kinetic models (especially for iso-octane). Recent GC-MS analysis reveals that the branched alkanes in jet fuel are better represented by slightly branched molecules, with one to two branches. Thus, one-branched alkanes such as methyl-decane are better candidates for jet fuel surrogate. Jet fuel has  $\sim 20\%$  of cycloalkanes, which are mainly mono-cycloalkanes (e.g., *n*-butyl-cyclohexane) and di-cycloalkanes (e.g., decalin). Most of the aromatic components in jet fuel are alkyl benzenes, such as *n*-propylbenzene, *n*-butylbenzene, and 1,3,5-trimethylbenzene [92]. Figure 1.6 shows the jet fuel surrogate palettes for JP-8 [97], which were proposed based on modest cost, experimental and computational tractability and reproducibility [98].

### 1.3.3 Surrogates for Diesel

The carbon number range of diesel is from  $C_{10}$  to  $C_{24}$ . Possible structures of typical components of diesel are very complex and a significant number of isomers exist. Figure 1.7 shows an example of the major classes of molecules in diesel, with specific  $C_{16}$  isomers including *n*-alkane, branched alkane, one-ring cycloalkane and two-ring cycloalkane with multiple alkyl side-chains, one-ring and two-ring aromatics with multiple alkyl side-chains, and tetralin with a multiple alkyl side chain [90]. Similar to jet fuel, the branched alkane in diesel contains one or two methyl substitutions. The majority of cycloalkane in diesel is one-ring cycloalkane with multiple alkyl side chains. The aromatic fraction of commercial diesel in the U.S. is  $\sim 20\text{--}40\%$  [99], and the most abundant component is one-ring aromatics with alkyl side chains.



**Fig. 1.7** Structures of major classes of molecules in diesel fuels with  $C_{16}$  isomers as examples [90]

Experimental and modeling studies for molecules in diesel fuel are scarce. Significant compositional variability among commercial diesel fuels exist; and the high boiling point of the diesel fuel component makes it difficult to carry out experimental studies. The complexity of the diesel fuel component also increases the cost of formulating the surrogate palette, since not all pure compounds can be commercially obtained [90]. Farrell et al. [90] proposed to formulate the surrogates in diesel fuel surrogate development with *n*-decane, iso-octane, toluene, and methylcyclohexane; their long-term goal was to build the diesel surrogates with *n*-hexadecane, heptamethylnonane, *n*-decylbenzene, and 1-methylnaphthalene.

In summary, the motivation for surrogate fuels is to mimic combustion behaviors of fossil fuels; so, formulation of the surrogate depends on the intended application, i.e., a target-oriented surrogate. Three types of targets were distinguished by Farrell et al. [90]: property targets, development targets, and application targets.

“Property targets refers to fundamental physical and chemical fuel properties; development targets refer to kinetic and fluid dynamic processes that are important for validating surrogate mixture behavior, and that are typically evaluated in devices with better controlled conditions than those in real engines; application targets refer to results obtained from engine experiments”.

To this end, a comprehensive understanding of the chemical fuel properties of surrogate components, such as fuel decomposition, ignition, and pollutant formation is one prerequisite.

## 1.4 Research on Cycloalkane Fuels

As shown in Fig. 1.5, cycloalkanes are important components of transport fuels, accounting for  $\sim 10\%$  in gasoline,  $\sim 20\%$  in jet fuel, and  $\sim 30\%$  in diesel [86]. Diesel derived from oil sands [100], and coal-derived synthetic fuels [101], have even higher fractions of cycloalkanes. Combustion of diesel fuel with higher concentrations of cycloalkanes will produce different ignition properties and pollutant emissions (e.g., soot). Enhanced energy and volumetric density, and lowered freeze point make cycloalkanes a fuel component to enable aircraft to reach higher altitude operability [97]. For example, China NO. 3 Kerosene contains  $\sim 40\%$  of cycloalkanes (Table 1.1) [102]. Considering the importance of cycloalkanes in transport fuels and their surrogates, detailed experimental and modeling studies of these fuels are necessary.

In a study of cycloalkanes, cyclohexane and alkyl-cyclohexanes (e.g., methylcyclohexane, ethylcyclohexane, *n*-propylcyclohexane, and *n*-butylcyclohexane) are often selected as model compounds. Cyclohexane is the basis for the cycloalkane kinetic model while methylcyclohexane and ethylcyclohexane are the model compounds that clarify the combustion mechanism of cycloalkanes with long side-chains. Table 1.2 presents the literature review of experimental studies of cyclohexane and C<sub>1</sub> to C<sub>4</sub> alkyl-cyclohexanes.

Here, the gap between experimental and kinetic modeling studies of cyclohexane and its alkyl-cyclohexane derivatives are discussed.

- (a) Initial decomposition mechanism of cycloalkanes. Tsang and Brown et al. proposed that the initial decomposition product of cyclohexane is 1-hexene [40, 123] via ring-opening isomerization. However, 1-hexene was not detected during the atmospheric-pressure pyrolysis of cyclohexane carried out by Aribike et al. [124]. Similarly, 1-hexene was also not detected during the JSR oxidation of cyclohexane at 10 atm [125]. Due to the absence of 1-hexene from their experiment, EI Bakali et al., Aribike et al., and Voisin et al., proposed other initial dissociation channels of cyclohexane [103, 124, 125]. Recently, Kiefer et al. studied the pyrolysis of cyclohexane in a shock tube and calculated the reaction pathways for cyclohexane dissociation [126]. Their theoretical calculation confirmed that the initial decomposition of cyclohexane produces 1-hexene. A simplified model built from the quantum chemistry calculation captured the experimental observation. However, their experiment could not detect 1-hexene.

In addition to cyclohexane, some studies were performed to investigate the initial decomposition of methylcyclohexane. Brown and King proposed three channels for methylcyclohexane decomposition. They stated that ring opening isomerization via dissociation of the C–C bond adjacent to the methyl side-chain is easy to continue. Compared to the ring-opening channel, C–C bond dissociation to remove the methyl side-chain is difficult to continue and can be neglected [127].

Recently, Skeen et al. [116] investigated the low-pressure laminar premixed flame of methylcyclohexane. They employed high-level quantum chemistry

**Table 1.1** Component of China NO. 3 Kerosene (mass fraction) [102]

Saturated hydrocarbons		Aromatic hydrocarbons			Total					
Alkanes	Naphthenes	Alkyl benzenes	Indane& tetralin	Naphthalene	Naphthalene derivatives	Total				
	Monoyclic						Bicylic	Tricyclic		
52.2	33.8	6.0	0.1	92.1	5.1	1.3	0.6	0.9	7.9	100



**Table 1.2** Literature review of experimental studies on cyclohexane and C1–C4 alkylcyclohexane

Fuel	Experiment	Data	T(K)	P (atm)	References
Cyclohexane	JSR oxidation	Speciation	750–1200	1–10	[103]
	RCM oxidation	IDT speciation	600–900	7–14	[104]
	Premixed flame	Speciation	<sup>a</sup>	0.04	[105]
	ST oxidation	IDT	1280–1840	7.3–9.5	[106]
	ST oxidation	IDT	847–1379	11–61	[107]
	Engine oxidation	Speciation	750–860	10–25	[108]
	Premixed flame	Speciation	<sup>a</sup>	1	[109]
	Premixed flame	LFS	353 <sup>b</sup>	1–10	[110]
	FR pyrolysis	Speciation	950–1520	0.04	[69]
	RCM oxidation	IDT	680–910	12.5, 20, 40	[111]
Methylcyclohexane	ST oxidation	IDT	1250–2100	1–4	[112]
	RCM oxidation	IDT	680–980	10–20	[113]
	RCM oxidation	IDT	680–905	15.1, 25.5	[114]
	ST oxidation	IDT	881–1319	10.8–69.5	[115]
	Engine oxidation	Speciation	750–860	10–25	[108]
	Premixed flame	Speciation	<sup>a</sup>	0.04	[116]
	Premixed flame	LFS	353 <sup>b</sup>	1–10	[110]
Ethylcyclohexane	ST oxidation	IDT	881–1319	10.8–69.5	[115]
	Premixed flame	LFS	353 <sup>b</sup>	1–10	[110]
	JSR oxidation	Speciation	500–1100	1.05	[117]
<i>n</i> -propylcyclohexane	JSR oxidation	Speciation	950–1250	1	[118]
	Premixed flame	Speciation	<sup>a</sup>	0.066	[53]
	RCM oxidation	IDT speciation	620–930	4.5–13.4	[119]
	Premixed flame	LFS	353 <sup>b</sup>	1	[120]
<i>n</i> -butylcyclohexane	FR oxidation	Speciation	600–820	8	[121]
	Premixed flame	LFS	353 <sup>b</sup>	1	[120]
	ST oxidation	IDT	1280–1480	1.5–3	[122]

Note <sup>a</sup>flame temperature profile; <sup>b</sup>unburnt gas temperature; *JSR* jet-stirred reactor; *RCM* rapid compression machine; *ST* shock tube; *FR* flow reactor; *IDT* ignition delay time; *LFS* laminar flame speed

calculations to study the initial decomposition of methylcyclohexane. The potential energy surface shows that methylcyclohexane has three ring-opening channels forming six heptene isomers and one dissociation channel to remove the methyl side chain. They deduced that the methyl side chain has only a negligible effect on the ring-opening process and estimated that the three

ring-opening pathways have a comparable rate constant. The methyl side chain decomposition has the lowest energy barrier and is the most prevalent pathway; however, considering the number of degenerate ring-opening pathways, they deduced that the overall rate constants of isomerization pathways are likely to be similar to the methyl loss channel. The conclusions from Skeen et al. [116] differ significantly from those of Brown and King [127]. Furthermore, the competition of ring-opening isomerization and methyl-loss channel (e.g., their temperature- and pressure- dependent branching ratios), has a significant effect on the formation of aromatics. For cyclohexanes with longer side-chains, the initial decomposition pathways are even more complex, and detailed experimental and theoretical study are required.

- (b) Aromatic formation pathways during cycloalkane combustion. The first aromatic ring (e.g., benzene and benzyl radical) is regarded as the rate controlling step to form polycyclic aromatic hydrocarbons (PAHs) and soot. Several reaction pathways have been proposed to produce benzene, such as a combination of resonance stabilized radicals, e.g.,  $C_3 + C_3$ ,  $C_4 + C_2$ , and  $C_5H_5 + CH_3$ , the isomerization of fulvene, and stepwise dehydrogenation of cyclohexane. Although previous studies addressed benzene formation pathways in cycloalkane combustion [100, 104, 105, 109, 116, 125, 128–131], the reaction mechanism was not fully clarified. Studies of cyclohexane flame have shown that flame configuration, zone, and stoichiometry [105, 109, 130, 131] affect benzene formation pathways. In methylcyclohexane flames, Skeen et al. [116] suggested that benzene originates with the stepwise dehydrogenation of the cyclohexyl radical, which is produced from the decomposition of methylcyclohexane. Toluene is produced mainly from the stepwise dehydrogenation of methylcyclohexane. These previous studies seldom addressed aromatic formation pathways during cycloalkane pyrolysis. Furthermore, the effect of the side chain (e.g., cyclohexane vs. alkyl-cyclohexanes) and the length of side chain (e.g., methylcyclohexane vs. ethylcyclohexane) on aromatic formation is unclear.
- (c) Scarcity of experimental and kinetic modeling studies of cycloalkane combustion. Table 1.2 shows that previous literature focused on the combustion of cyclohexane; studies on alkyl-cyclohexanes are scant, especially for alkyl-cyclohexanes with longer side-chains. Furthermore, previous studies have mainly addressed the macroscopic combustion properties of cycloalkanes, e.g., ignition delay times and laminar flame speeds (Table 1.2). Experimental data for detailed species speciation were seldom reported—especially in a pyrolysis process without the participation of oxidation reactions. The pyrolysis environment is suitable to study unimolecular decomposition pathways of the reactant and the reaction mechanism for aromatics. Moreover, compared to

alkanes and aromatics, the combustion kinetic models for alkyl-cyclohexanes are not well developed, and well validated kinetic models are required to predict the combustion properties of cycloalkanes.

## 1.5 Thesis Content

The importance of cycloalkanes in fossil fuels and their surrogates, and the research gap mentioned above, are the motivation for the present study. This thesis examines the reaction mechanism of cyclohexane, methylcyclohexane, and ethylcyclohexane combustion from state-of-the-art experiments, high-level quantum chemistry calculations and detailed kinetic modeling. (1) Synchrotron radiation photoionization mass spectrometry was employed to examine the flow reactor pyrolysis of the three cycloalkanes from low to atmospheric pressure; pyrolysis intermediates were identified and quantified, including radicals and various isomers. In a pyrolysis study of ethylcyclohexane, GC/GC-MS was employed to analyze the intermediates, and especially to separate the isomers and detect low-concentration intermediates. The synchrotron radiation photoionization mass spectrometry was also used to study low-pressure laminar premixed flames of methylcyclohexane and ethylcyclohexane. Spatial distribution of the flame intermediates was obtained. (2) Important reaction pathways during methylcyclohexane and ethylcyclohexane combustion were calculated, and the corresponding rate constants were evaluated. (3) Based on a review of the literature and calculated reaction pathways, a detailed combustion model for cyclohexane, methylcyclohexane, and ethylcyclohexane was developed in a hierarchical manner. The kinetic model was validated from the pyrolysis and flame data in this work, as well as data from the literature—including species speciation in laminar premixed flame and JSR oxidation, ignition delay times, and laminar flame speeds.

Thesis organization:

Chapter 2: Experimental method and kinetic modeling

Chapter 3: Experimental and modeling study of cyclohexane combustion

Chapter 4: Experimental and modeling study of methylcyclohexane combustion

Chapter 5: Experimental and modeling study of ethylcyclohexane combustion

Chapter 6: Combustion kinetics of cyclohexane and C1–C2 mono-alkyl cyclohexanes

Chapter 7: Conclusions and perspective.

## References

1. Ding, Y. Yu, H., Wan, Z., & Wang, P. (2011). *China statistical yearbook-2011*. China Statistics Press.
2. Yao, M., Zheng, Z., & Liu, H. (2009). Progress and recent trends in homogeneous charge compression ignition (HCCI) engines. *Progress in Energy and Combustion Science*, 35(5), 398–437.
3. International energy outlook (2010). U.S. Energy information administration: Washington, DC 20585.
4. Development strategy on engineering thermal physics and energy utilization (2011–2020). Science Press.
5. Petit, J. R., Jouzel, J., Raynaud, D., Barkov, N. I., Barnola, J. M., Basile, I., et al. (1999). Climate and atmospheric history of the past 420,000 years from the Vostok ice core. *Antarctica Nature*, 399(6735), 429–436.
6. Basic research needs for clean and efficient combustion of 21st century transportation fuels. [http://www.sc.doe.gov/bes/reports/files/CTF\\_rpt.pdf](http://www.sc.doe.gov/bes/reports/files/CTF_rpt.pdf).
7. Stanglmaier, R. H. & Roberts, C. E. (1999). Homogeneous charge compression ignition (HCCI): Benefits, compromises, and future engine applications. *Society of Automotive Engineers*, SAE-1999-01-3682.
8. Elkelawy, M., Zhang, Y., Hagar, A. E., & Yu, Y. (2008). Challenging and future of homogeneous charge compression ignition engines: An advanced and novel concepts review. *Journal of Power and Energy Systems*, 2, 1108–1119.
9. Kohse-Höinghaus, K., & Jeffries, J. B. (2002). Applied combustion diagnostics, In K. C. Smyth & D. R. Crosley (Eds.), New York: Taylor & Francis.
10. Melton, L. A. (1984). Soot diagnostics based on laser heating. *Applied Optics*, 23(13), 2201–2208.
11. McIlroy, A. (1998). Direct measurement of  $^1\text{CH}_2$  in flames by cavity ringdown laser absorption spectroscopy. *Chemical Physics Letters*, 296(1–2), 151–158.
12. Akhter, M. S., Chughtai, A. R., & Smith, D. M. (1985). The structure of hexane soot I: Spectroscopic studies. *Applied Spectroscopy*, 39(1), 143–153.
13. Oltmann, H., Reimann, J., & Will, S. (2010). Wide-angle light scattering (WALS) for soot aggregate characterization. *Combustion and Flame*, 157(3), 516–522.
14. Vasu, S. S., Davidson, D. F., Hong, Z., & Hanson, R. K. (2009). Shock tube study of methylcyclohexane ignition over a wide range of pressure and temperature. *Energy & Fuels*, 23(1), 175–185.
15. Davidson, D. F., Hong, Z., Pilla, G. L., Farooq, A., Cook, R. D., & Hanson, R. K. (2010). Multi-species time-history measurements during n-heptane oxidation behind reflected shock waves. *Combustion and Flame*, 157(10), 1899–1905.
16. Lam, K.-Y., Ren, W., Hong, Z., Davidson, D. F., & Hanson, R. K. (2012). Shock tube measurements of 3-pentanone pyrolysis and oxidation. *Combustion and Flame*, 159(11), 3251–3263.
17. Biordi, J. C., Lazzara, C. P., & Papp, J. F. (1974). Molecular-beam mass-spectrometry applied to determining kinetics of reactions in flames. 1. empirical characterization of flame perturbation by molecular-beam sampling probes. *Combustion and Flame*, 23(1), 73–82.
18. Biordi, J. C. (1977). Molecular beam mass spectrometry for studying the fundamental chemistry of flames. *Progress in Energy and Combustion Science*, 3(3), 151–173.
19. Hansen, N., Cool, T. A., Westmoreland, P. R., & Kohse-Höinghaus, K. (2009). Recent contributions of flame-sampling molecular-beam mass spectrometry to a fundamental understanding of combustion chemistry. *Progress in Energy and Combustion Science*, 35(2), 168–191.
20. Qi, F. (2013). Combustion chemistry probed by synchrotron VUV photoionization mass spectrometry. *Proceedings of the Combustion Institute*, 34, 33–63.

21. Cord, M., Husson, B., Lizardo Huerta, J. C., Herbinet, O., Glaude, P.-A., Fournet, R., et al. (2012). Study of the low temperature oxidation of propane. *The Journal of Physical Chemistry A*, 116(50), 12214–12228.
22. Serinyel, Z., Herbinet, O., Frottier, O., Dirrenberger, P., Warth, V., Glaude, P. A., et al. (2013). An experimental and modeling study of the low- and high-temperature oxidation of cyclohexane. *Combustion and Flame*, 160, 2319–2332.
23. NIST/EPA/NIH Mass spectral library (NIST 08). NIST.
24. Dagaut, P. (2002). On the kinetics of hydrocarbons oxidation from natural gas to kerosene and diesel fuel. *Physical Chemistry Chemical Physics*, 4(11), 2079–2094.
25. Dagaut, P., & Cathonnet, M. (2006). The ignition, oxidation, and combustion of kerosene: A review of experimental and kinetic modeling. *Progress in Energy and Combustion Science*, 32(1), 48–92.
26. Battin-Leclerc, F. (2008). Detailed chemical kinetic models for the low-temperature combustion of hydrocarbons with application to gasoline and diesel fuel surrogates. *Progress in Energy and Combustion Science*, 34(4), 440–498.
27. Matras, D., & Villermaux, J. (1973). Un réacteur continu parfaitement agité par jets gazeux pour l'étude cinétique de réactions chimiques rapides. *Chemical Engineering Science*, 28(1), 129–137.
28. Battin-Leclerc, F., Blurock, E., Bounaceur, R., Fournet, R., Glaude, P. A., Herbinet, O., et al. (2011). Towards cleaner combustion engines through groundbreaking detailed chemical kinetic models. *Chemical Society Reviews*, 40(9), 4762–4782.
29. Battin-Leclerc, F., Herbinet, O., Glaude, P. A., Fournet, R., Zhou, Z., Deng, L., et al. (2010). Experimental confirmation of the low-temperature oxidation scheme of alkanes. *Angewandte Chemie International Edition*, 49(18), 3169–3172.
30. Porter, R., Glaude, P.-A., Buda, F., & Battin-Leclerc, F. (2008). A tentative modeling study of the effect of wall reactions on oxidation phenomena. *Energy & Fuels*, 22(6), 3736–3743.
31. Herbinet, O., Battin-Leclerc, F., Bax, S., Le Gall, H., Glaude, P. A., Fournet, R., et al. (2011). Detailed product analysis during the low temperature oxidation of n-butane. *Physical Chemistry Chemical Physics*, 13(1), 296–308.
32. Herbinet, O., & Dayma, G. (2013). Jet-Stirred reactors. In F. Battin-Leclerc, J. M. Simmie & E. Blurock (Eds.), *Cleaner combustion: Developing detailed chemical kinetic models* (pp. 183–210). Springer London: London.
33. Zeppleri, S., Brezinsky, K., & Glassman, I. (1997). Pyrolysis studies of methylcyclohexane and oxidation studies of methylcyclohexane and methylcyclohexane/toluene blends. *Combustion and Flame*, 108(3), 266–286.
34. Curran, H. J., Pitz, W. J., Westbrook, C. K., Callahan, G. V., & Dryer, F. L. (1998). Oxidation of automotive primary reference fuels at elevated pressures. *Symposium (International) on Combustion*, 27(1), 379–387.
35. Mueller, M. A., Kim, T. J., Yetter, R. A., & Dryer, F. L. (1999). Flow reactor studies and kinetic modeling of the H<sub>2</sub>/O<sub>2</sub> reaction. *International Journal of Chemical Kinetics*, 31(2), 113–125.
36. Curran, H. J., Fischer, S. L., & Dryer, F. L. (2000). The reaction kinetics of dimethyl ether. II: Low-temperature oxidation in flow reactors. *International Journal of Chemical Kinetics*, 32(12), 741–759.
37. Li, J., Zhao, Z., Kazakov, A., & Dryer, F. L. (2004). An updated comprehensive kinetic model of hydrogen combustion. *International Journal of Chemical Kinetics*, 36(10), 566–575.
38. Li, J., Zhao, Z., Kazakov, A., Chaos, M., Dryer, F. L., & Scire, J. J. (2007). A comprehensive kinetic mechanism for CO, CH<sub>2</sub>O, and CH<sub>3</sub>OH combustion. *International Journal of Chemical Kinetics*, 39(3), 109–136.
39. Zhao, Z., Chaos, M., Kazakov, A., & Dryer, F. L. (2008). Thermal decomposition reaction and a comprehensive kinetic model of dimethyl ether. *International Journal of Chemical Kinetics*, 40, 1–18.

40. Tsang, W. (1978). Thermal stability of cyclohexane and 1-hexene. *International Journal of Chemical Kinetics*, 10, 1119–1138.
41. Tsang, W., Walker, J. A., & Manion, J. A. (1998). Single-pulse shock-tube study on the decomposition of 1-pentyl radicals. *Symposium (International) on Combustion*, 27(1), 135–142.
42. Tsang, W. (2005). Mechanism and rate constants for the decomposition of 1-pentenyl radicals. *The Journal of Physical Chemistry A*, 110(27), 8501–8509.
43. Tsang, W., Walker, J. A., & Manion, J. A. (2007). The decomposition of normal hexyl radicals. *Proceedings of the Combustion Institute*, 31(1), 141–148.
44. McGivern, W. S., Awan, I. A., Tsang, W., & Manion, J. A. (2008). Isomerization and decomposition reactions in the pyrolysis of branched hydrocarbons: 4-methyl-1-pentyl radical. *The Journal of Physical Chemistry A*, 112(30), 6908–6917.
45. Tsang, W., McGivern, W. S., & Manion, J. A. (2009). Multichannel decomposition and isomerization of octyl radicals. *Proceedings of the Combustion Institute*, 32(1), 131–138.
46. Manion, J. A., & Awan, I. A. (2013). The decomposition of 2-pentyl and 3-pentyl radicals. *Proceedings of the Combustion Institute*, 34(1), 537–545.
47. Gudiya, S., & Brezinsky, K. (2012). High pressure study of *n*-propylbenzene oxidation. *Combustion and Flame*, 159, 940–958.
48. Gudiya, S., & Brezinsky, K. (2013). The high pressure study of *n*-propylbenzene pyrolysis. *Proceedings of the Combustion Institute*, 34(1), 1767–1774.
49. Malewicki, T., & Brezinsky, K. (2013). Experimental and modeling study on the pyrolysis and oxidation of *n*-decane and *n*-dodecane. *Proceedings of the Combustion Institute*, 34(1), 361–368.
50. Malewicki, T., Comandini, A., & Brezinsky, K. (2013). Experimental and modeling study on the pyrolysis and oxidation of iso-octane. *Proceedings of the Combustion Institute*, 34(1), 353–360.
51. Malewicki, T., Gudiya, S., & Brezinsky, K. (2013). Experimental and modeling study on the oxidation of Jet A and the *n*-dodecane/iso-octane/*n*-propylbenzene/1,3,5-trimethylbenzene surrogate fuel. *Combustion and Flame*, 160(1), 17–30.
52. Pousse, E., Glaude, P. A., Fournet, R., & Battin-Leclerc, F. (2009). A lean methane premixed laminar flame doped with components of diesel fuel: I. *n*-Butylbenzene. *Combustion and Flame*, 156(5), 954–974.
53. Pousse, E., Porter, R., Warth, V., Glaude, P. A., Fournet, R., & Battin-Leclerc, F. (2010). Lean methane premixed laminar flames doped by components of diesel fuel II: *n*-Propylcyclohexane. *Combustion and Flame*, 157(1), 75–90.
54. Pousse, E., Tian, Z. Y., Glaude, P. A., Fournet, R., & Battin-Leclerc, F. (2010). A lean methane premixed laminar flame doped with components of diesel fuel part III: Indane and comparison between *n*-butylbenzene, *n*-propylcyclohexane and indane. *Combustion and Flame*, 157(7), 1236–1260.
55. Sarathy, S. M., Yeung, C., Westbrook, C. K., Pitz, W. J., Mehl, M., & Thomson, M. J. (2011). An experimental and kinetic modeling study of *n*-octane and 2-methylheptane in an opposed-flow diffusion flame. *Combustion and Flame*, 158(7), 1277–1287.
56. Dayma, G., Sarathy, S. M., Togbé, C., Yeung, C., Thomson, M. J., & Dagaut, P. (2011). Experimental and kinetic modeling of methyl octanoate oxidation in an opposed-flow diffusion flame and a jet-stirred reactor. *Proceedings of the Combustion Institute*, 33(1), 1037–1043.
57. Yeung, C., & Thomson, M. J. (2013). Experimental and kinetic modeling study of 1-hexanol combustion in an opposed-flow diffusion flame. *Proceedings of the Combustion Institute*, 34(1), 795–802.
58. Mani Sarathy, S., Niemann, U., Yeung, C., Gehmlich, R., Westbrook, C. K., Plomer, M., et al. (2013). A counterflow diffusion flame study of branched octane isomers. *Proceedings of the Combustion Institute*, 34(1), 1015–1023.

59. Cool, T. A., Nakajima, K., Mostefaoui, T. A., Qi, F., McIlroy, A., Westmoreland, P. R., et al. (2003). Selective detection of isomers with photoionization mass spectrometry for studies of hydrocarbon flame chemistry. *Journal of Chemical Physics*, *119*(16), 8356–8365.
60. Cool, T. A., McIlroy, A., Qi, F., Westmoreland, P. R., Poisson, L., Peterka, D. S., et al. (2005). Photoionization mass spectrometer for studies of flame chemistry with a synchrotron light source. *Review of Scientific Instruments*, *76*(9), 094102.
61. Zhang, T., Wang, J., Yuan, T., Hong, X., Zhang, L., & Qi, F. (2008). Pyrolysis of Methyl tert-Butyl Ether (MTBE). 1. experimental study with molecular-beam mass spectrometry and tunable synchrotron VUV photoionization. *Journal of Physical Chemistry A*, *112*(42), 10487–10494.
62. Zhang, T., Zhang, L., Hong, X., Zhang, K., Qi, F., Law, C. K., et al. (2009). An experimental and theoretical study of toluene pyrolysis with tunable synchrotron VUV photoionization and molecular-beam mass spectrometry. *Combustion and Flame*, *156*(11), 2071–2083.
63. Zhang, Y., Cai, J., Zhao, L. O., Yang, J., Jin, H., Cheng, Z., Li, Y., Zhang, L., & Qi, F. (2012). An experimental and kinetic modeling study of three butene isomers pyrolysis at low pressure. *Combustion and Flame*, *159*, 905–917.
64. Cai, J., Zhang, L., Zhang, F., Wang, Z., Cheng, Z., & Qi, F. (2012). Experimental and kinetic modeling study of n-butanol pyrolysis and combustion. *Energy & Fuels*, *26*, 5550–5568.
65. Cai, J., Zhang, L., Yang, J., Li, Y., & Qi, F. (2012). Experimental and kinetic modeling study of tert-butanol combustion at low pressure. *Energy*, *43*, 94–102.
66. Cai, J., Yuan, W., Ye, L., Cheng, Z., Wang, Y., Zhang, L., et al. (2013). Experimental and kinetic modeling study of 2-butanol pyrolysis and combustion. *Combustion and Flame*, *160*(10), 1939–1957.
67. Li, Y., Zhang, L., Wang, Z., Ye, L., Cai, J., Cheng, Z., et al. (2013). Experimental and kinetic modeling study of tetralin pyrolysis at low pressure. *Proceedings of the Combustion Institute*, *34*(1), 1739–1748.
68. Lucassen, A., Wang, Z., Zhang, L., Zhang, F., Yuan, W., Wang, Y., et al. (2013). An experimental and theoretical study of pyrrolidine pyrolysis at low pressure. *Proceedings of the Combustion Institute*, *34*(1), 641–648.
69. Wang, Z., Cheng, Z., Yuan, W., Cai, J., Zhang, L., Zhang, F., et al. (2012). An experimental and kinetic modeling study of cyclohexane pyrolysis at low pressure. *Combustion and Flame*, *159*(7), 2243–2253.
70. Wang, Z., Ye, L., Yuan, W., Zhang, L., Wang, Y., Cheng, Z., et al. (2014). Experimental and kinetic modeling study on methylcyclohexane pyrolysis and combustion. *Combustion and Flame*, *161*, 84–100.
71. Herbinet, O., Husson, B., Serinyel, Z., Cord, M., Warth, V., Fournet, R., et al. (2012). Experimental and modeling investigation of the low-temperature oxidation of n-heptane. *Combustion and Flame*, *159*(12), 3455–3471.
72. Battin-Leclerc, F., Rodriguez, A., Husson, B., Herbinet, O., Glaude, P. A., Wang, Z., et al. (2014). Products from the oxidation of linear isomers of hexene. *The Journal of Physical Chemistry A*, *118*(4), 673–683.
73. Cuoci, A., Frassoldati, A., Faravelli, T., Jin, H., Wang, Y., Zhang, K., et al. (2013). Experimental and detailed kinetic modeling study of PAH formation in laminar co-flow methane diffusion flames. *Proceedings of the Combustion Institute*, *34*(1), 1811–1818.
74. Jin, H., Wang, Y., Zhang, K., Guo, H., & Qi, F. (2013). An experimental study on the formation of polycyclic aromatic hydrocarbons in laminar coflow non-premixed methane/air flames doped with four isomeric butanols. *Proceedings of the Combustion Institute*, *34*(1), 779–786.
75. Jin, H., Cuoci, A., Frassoldati, A., Faravelli, T., Wang, Y., Li, Y., et al. (2014). Experimental and kinetic modeling study of PAH formation in methane coflow diffusion flames doped with n-butanol. *Combustion and Flame*, *161*(3), 657–670.

76. Zhou, Z., Wang, Y., Tang, X., Wu, W., & Qi, F. (2013). A new apparatus for study of pressure-dependent laminar premixed flames with vacuum ultraviolet photoionization mass spectrometry. *Review of Scientific Instruments*, 84(1), 014101.
77. Skeen, S. A., Yang, B., Michelsen, H. A., Miller, J. A., Violi, A., & Hansen, N. (2013). Studies of laminar opposed-flow diffusion flames of acetylene at low-pressures with photoionization mass spectrometry. *Proceedings of the Combustion Institute*, 34(1), 1067–1075.
78. Skeen, S. A., Michelsen, H. A., Wilson, K. R., Popolan, D. M., Violi, A., & Hansen, N. (2013). Near-threshold photoionization mass spectra of combustion-generated high-molecular-weight soot precursors. *Journal of Aerosol Science*, 58, 86–102.
79. Dubreuil, A., Foucher, F., Mounaïm-Rousselle, C., Dayma, G., & Dagaut, P. (2007). HCCI combustion: Effect of NO in EGR. *Proceedings of the Combustion Institute*, 31(2), 2879–2886.
80. Bahrini, C., Morajkar, P., Schoemaeker, C., Frottier, O., Herbinet, O., Glaude, P. A., et al. (2013). Experimental and modeling study of the oxidation of n-butane in a jet stirred reactor using cw-CRDS measurements. *Physical Chemistry Chemical Physics*, 15(45), 19686–19698.
81. Bahrini, C., Herbinet, O., Glaude, P.-A., Schoemaeker, C., Fittschen, C., & Battin-Leclerc, F. (2012). Quantification of hydrogen peroxide during the low-temperature oxidation of alkanes. *Journal of the American Chemical Society*, 134(29), 11944–11947.
82. Blocquet, M., Schoemaeker, C., Amedro, D., Herbinet, O., Battin-Leclerc, F., & Fittschen, C. (2013). Quantification of OH and HO<sub>2</sub> radicals during the low-temperature oxidation of hydrocarbons by Fluorescence Assay by Gas Expansion technique. *Proceedings of the National Academy of Sciences*, 110, 20014–20017.
83. Brumfield, B., Sun, W., Ju, Y., & Wysocki, G. (2013). Direct In situ quantification of HO<sub>2</sub> from a flow reactor. *The Journal of Physical Chemistry Letters*, 4(6), 872–876.
84. Brumfield, B., Sun, W., Wang, Y., Ju, Y., & Wysocki, G. (2014). Dual modulation Faraday rotation spectroscopy of HO<sub>2</sub> in a flow reactor. *Optics Letters*, 39(7), 1783–1786.
85. Edwards, T., & Maurice, L. Q. (2001). Surrogate mixtures to represent complex aviation and rocket fuels. *Journal of Propulsion and Power*, 17(2), 461–466.
86. Westbrook, C. K., & Smith, P. J. (2006). *Basic research needs for clean and efficient combustion of 21st century transportation fuels*. Livermore: Office of Science, U.S. Department of Energy.
87. Davis, A. C., Tangprasertchai, N., & Francisco, J. S. (2012). Hydrogen Migrations in Alkylcycloalkyl Radicals: Implications for Chain-Branching Reactions in Fuels. *Chemistry—A European Journal*, 18(36), 11296–11305.
88. Hadaller, O. J., & Johnson, J. M. (2006). World fuel sampling program. CRC Aviation Fuel, Lubricant & Equipment research committee of the coordinating research council, Inc.
89. Edwards, T., Shafer, L., Striebich, R., & Gomach, J. (2006). Chemical class composition of commercial jet fuels and other specialty kerosene fuels. In *14th AIAA/AHI space planes and hypersonic systems and technologies conference*. American Institute of Aeronautics and Astronautics.
90. Farrell, J. T., Cernansky, N. P., Dryer, F. L., Law, C. K., Friend, D. G., Hergart, C. A., et al. (2007). Development of an experimental database and kinetic models for surrogate diesel fuels. *Society of Automotive Engineers*, SAE Paper 2007-01-0201.
91. Pitz, W. J., Cernansky, N. P., Dryer, F. L., Egolfopoulos, F. N., Farrell, J. T., Friend, D.G., et al. (2007). Development of an experimental database and chemical kinetic models for surrogate gasoline fuels. *Society of Automotive Engineers*, SAE Paper 2007-01-0175.
92. Colket, M., Edwards, T., Williams, S., Cernansky, N., Miller, D.L., Egolfopoulos, F., et al. (2007). Development of an experimental database and kinetic models for surrogate jet fuels. in *45th AIAA Aerospace Sciences Meeting and Exhibit Proceedings*. Reno, NV.
93. Pitz, W. J., & Mueller, C. J. (2011). Recent progress in the development of diesel surrogate fuels. *Progress in Energy and Combustion Science*, 37(3), 330–350.



94. Curran, H. J., Gaffuri, P., Pitz, W. J., & Westbrook, C. K. (1998). A comprehensive modeling study of n-heptane oxidation. *Combustion and Flame*, 114(1–2), 149–177.
95. Sheen, D. A., & Wang, H. (2011). Combustion kinetic modeling using multispecies time histories in shock-tube oxidation of heptane. *Combustion and Flame*, 158(4), 645–656.
96. Curran, H. J., Gaffuri, P., Pitz, W. J., & Westbrook, C. K. (2002). A comprehensive modeling study of iso-octane oxidation. *Combustion and Flame*, 129(3), 253–280.
97. Agosta, A., Cernansky, N. P., Miller, D. L., Faravelli, T., & Ranzi, E. (2004). Reference components of jet fuels: Kinetic modeling and experimental results. *Experimental Thermal and Fluid Science*, 28(7), 701–708.
98. Violi, A., Yan, S., Eddings, E. G., Sarofim, A. F., Granata, S., Faravelli, T., et al. (2002). Experimental formulation and kinetic model for JP-8 surrogate mixtures. *Combustion Science and Technology*, 174(11–2), 399–417.
99. Grumman, N. (2003). Diesel fuel oils. *Report NGMS-232 PPS*, January 2004.
100. Silke, E. J., Pitz, W. J., Westbrook, C. K., & Ribaucour, M. (2007). Detailed chemical kinetic modeling of cyclohexane oxidation. *Journal of Physical Chemistry A*, 111(19), 3761–3775.
101. Shafer, L., Striebich, R., Gomach, J., & Edwards, T. (2006, November) Chemical class composition of commercial jet fuels and other specialty kerosene fuels. *AIAA Paper 2006–7972*.
102. Fan, X., Yu, G. (2006). Analysis of thermophysical properties of Daqing RP-3 aviation kerosene. *Journal of Propulsion Technology*, 27(2): 187–192.
103. El Bakali, A., Braun-Unkhoff, M., Dagaut, P., Frank, P., & Cathonnet, M. (2000). Detailed kinetic reaction mechanism for cyclohexane oxidation at pressure up to ten atmospheres. *Proceedings of the Combustion Institute*, 28, 1631–1638.
104. Lemaire, O., Ribaucour, M., Carlier, M., & Minetti, R. (2001). The production of benzene in the low-temperature oxidation of cyclohexane, cyclohexene, and cyclohexa-1,3-diene. *Combustion and Flame*, 127(1–2), 1971–1980.
105. Law, M. E., Westmoreland, P. R., Cool, T. A., Wang, J., Hansen, N., Taatjes, C. A., et al. (2007). Benzene precursors and formation routes in a stoichiometric cyclohexane flame. *Proceedings of the Combustion Institute*, 31, 565–573.
106. Sirjean, B., Buda, F., Hakka, H., Glaude, P. A., Fournet, R., Warth, V., et al. (2007). The autoignition of cyclopentane and cyclohexane in a shock tube. *Proceedings of the Combustion Institute*, 31, 277–284.
107. Daley, S. M., Berkowitz, A. M., & Oehlschlaeger, M. A. (2008). A shock tube study of cyclopentane and cyclohexane ignition at elevated pressures. *International Journal of Chemical Kinetics*, 40(10), 624–634.
108. Yang, Y., & Boehman, A. L. (2009). Experimental study of cyclohexane and methylcyclohexane oxidation at low to intermediate temperature in a motored engine. *Proceedings of the Combustion Institute*, 32, 419–426.
109. Ciajolo, A., Tregrossi, A., Mallardo, M., Faravelli, T., & Ranzi, E. (2009). Experimental and kinetic modeling study of sooting atmospheric-pressure cyclohexane flame. *Proceedings of the Combustion Institute*, 32, 585–591.
110. Wu, F., Kelley, A. P., & Law, C. K. (2012). Laminar flame speeds of cyclohexane and mono-alkylated cyclohexanes at elevated pressures. *Combustion and Flame*, 159(4), 1417–1425.
111. Vranckx, S., Lee, C., Chakravarty, H. K., & Fernandes, R. X. (2013). A rapid compression machine study of the low temperature combustion of cyclohexane at elevated pressures. *Proceedings of the Combustion Institute*, 34(1), 377–384.
112. Orme, J. P., Curran, H. J., & Simmie, J. M. (2006). Experimental and modeling study of methyl cyclohexane pyrolysis and oxidation. *Journal of Physical Chemistry A*, 110(1), 114–131.
113. Pitz, W. J., Naik, C. V., Mhaoldúin, T. N., Westbrook, C. K., Curran, H. J., Orme, J. P., et al. (2007). Modeling and experimental investigation of methylcyclohexane ignition in a rapid compression machine. *Proceedings of the Combustion Institute*, 31, 267–275.

114. Mittal, G., & Sung, C. J. (2009). Autoignition of methylcyclohexane at elevated pressures. *Combustion and Flame*, 156(9), 1852–1855.
115. Vanderover, J., & Oehlschlaeger, M. A. (2009). Ignition time measurements for methylcyclohexane- and ethylcyclohexane-air mixtures at elevated pressures. *International Journal of Chemical Kinetics*, 41(2), 82–91.
116. Skeen, S. A., Yang, B., Jasper, A. W., Pitz, W. J., & Hansen, N. (2011). Chemical structures of low-pressure premixed methylcyclohexane flames as benchmarks for the development of a predictive combustion chemistry model. *Energy & Fuels*, 25, 5611–5625.
117. Husson, B., Herbinet, O., Glaude, P. A., Ahmed, S. S., & Battin-Leclerc, F. (2012). Detailed product analysis during low- and intermediate-temperature oxidation of ethylcyclohexane. *Journal of Physical Chemistry A*, 116(21), 5100–5111.
118. Ristori, A., Dagaut, P., El Bakali, A., & Cathonnet, M. (2001). The oxidation of n-propylcyclohexane: Experimental results and kinetic modeling. *Combustion Science and Technology*, 165, 197–228.
119. Crochet, M., Minetti, R., Ribaucour, M., & Vanhove, G. (2010). A detailed experimental study of n-propylcyclohexane autoignition in lean conditions. *Combustion and Flame*, 157(11), 2078–2085.
120. Ji, C., Dames, E., Sirjean, B., Wang, H., & Egolfopoulos, F. N. (2011). An experimental and modeling study of the propagation of cyclohexane and mono-alkylated cyclohexane flames. *Proceedings of the Combustion Institute*, 33, 971–978.
121. Natelson, R. H., Kurman, M. S., Cernansky, N. P., & Miller, D. L. (2011). Low temperature oxidation of n-butylcyclohexane. *Combustion and Flame*, 158(12), 2325–2337.
122. Hong, Z., Lam, K.-Y., Davidson, D. F., & Hanson, R. K. (2011). A comparative study of the oxidation characteristics of cyclohexane, methylcyclohexane, and n-butylcyclohexane at high temperatures. *Combustion and Flame*, 158(8), 1456–1468.
123. Brown, T. C., King, K. D., & Nguyent, T. T. (1986). Kinetics of primary processes in the pyrolysis of cyclopentanes and cyclohexanes. *Journal of Physical Chemistry*, 90, 419–424.
124. Aribike, D. S., Susu, A. A., & Ogunye, A. F. (1981). Mechanistic and mathematical modeling of the thermal decomposition of cyclohexane. *Thermochimica Acta*, 51(2–3), 113–127.
125. Voisin, D., Marchal, A., Reuillon, M., Boettner, J. C., & Cathonnet, M. (1998). Experimental and kinetic modeling study of cyclohexane oxidation in a JSR at high pressure. *Combustion Science and Technology*, 138(1–6), 137–158.
126. Kiefer, J. H., Gupte, K. S., Harding, L. B., & Klippenstein, S. J. (2009). Shock tube and theory investigation of cyclohexane and 1-hexene decomposition. *Journal of Physical Chemistry A*, 113(48), 13570–13583.
127. Brown, T. C., & King, K. D. (1989). Very low-pressure pyrolysis (VLPP) of methyl- and ethynyl-cyclopentanes and cyclohexanes. *International Journal of Chemical Kinetics*, 21(4), 251–266.
128. Billaud, F., Chaverot, P., Berthelin, M., & Freund, E. (1988). Thermal decomposition of cyclohexane at approximately 810 °C. *Industrial and Engineering Chemistry Research*, 27, 759–764.
129. Bennett, P. J., Gregory, D., & Jackson, R. A. (1996). Mechanistic studies on the combustion of isotopically labelled cyclohexanes within a single cylinder internal combustion engine. *Combustion Science and Technology*, 115(1–3), 83–103.
130. McEnally, C. S., & Pfefferle, L. D. (2004). Experimental study of fuel decomposition and hydrocarbon growth processes for cyclohexane and related compounds in nonpremixed flames. *Combustion and Flame*, 136(1–2), 155–167.
131. Li, W., Law, M. E., Westmoreland, P. R., Kasper, T., Hansen, N., & Kohse-Höinghaus, K. (2011). Multiple benzene-formation paths in a fuel-rich cyclohexane flame. *Combustion and Flame*, 158(11), 2077–2089.

# Chapter 2

## Experimental Method and Kinetic Modeling

### 2.1 Experimental Method

This thesis investigates flow reactor pyrolysis and laminar premixed flame of cyclohexane, methylcyclohexane and ethylcyclohexane. The experiment was performed at the National Synchrotron Radiation Laboratory (NSRL), at the University of Science and Technology of China. The combustion diagnostic employed in this work is the synchrotron radiation photoionization molecular beam mass spectrometry (SR-PI-MBMS) [1]. The properties of synchrotron radiation (e.g., continuous tunability and high resolution of photon energy), enable the separation of isomers and mitigate the interference of fragmentations. The MBMS freezes the reactions after sampling and detects reactive radicals and peroxides. The combination of synchrotron radiation and MBMS provides a thorough analysis of the species pool of intermediates in pyrolysis and flames.

In some cases, the results of SR-PI-MBMS analysis are difficult to separate and to quantify isomers, for example when the isomers have very close ionization energies and/or when a specific mass-to-charge ( $m/z$ ) has several isomers. In this work, another flow reactor pyrolysis apparatus was developed, which utilized a probe for sampling and GC/GC-MS for analysis. Pyrolysis of ethylcyclohexane was investigated using this apparatus and the products were analyzed by the GC/GC-MS. The synchrotron radiation beamline, flow reactor pyrolysis apparatus, and the laminar premixed flame apparatus are briefly discussed in the following sections.

#### 2.1.1 Synchrotron Radiation Beamline

NSRL is the first dedicated synchrotron radiation facility in China. Laboratory construction was started in 1984 and completed in 1991. From 1999 to 2004 a Phase II Project was performed to upgrade the machines. The storage ring is

operated with an energy of 800 MeV. The U10 and U14 beamlines were designed to study topics related to combustion and energy.

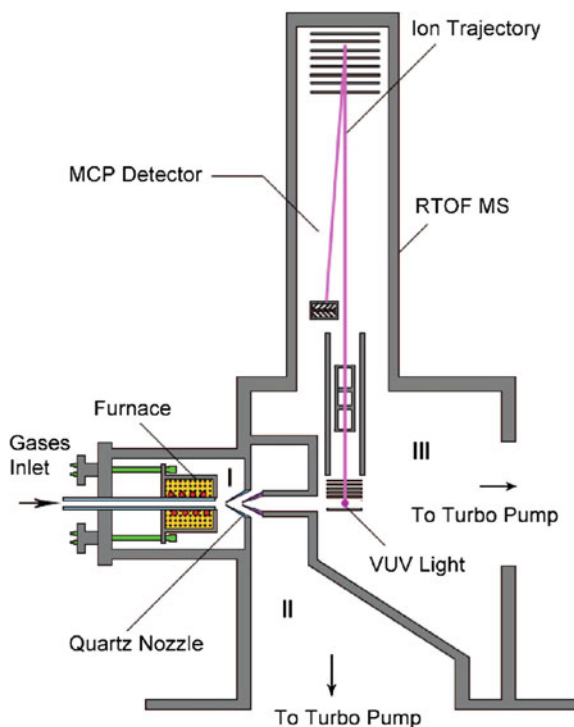
Synchrotron radiation of a U10 beamline results from the bending magnet. The beamline has a 1 m Seya-Namioka monochromator, equipped with two gratings (2400 and 1200 lines/mm) and capable of energy resolution of  $\sim 500$ . LIF and  $\text{MgF}_2$  windows eliminate high order harmonic radiation. The photon energy range of the U10 beamline is 6.2–11.8 eV. Synchrotron radiation of the U14C beamline results from the undulator with a photon flux of  $\sim 1 \times 10^{13}$  photons/s. This beamline is also equipped with a 1 m Seya-Namioka monochromator with energy resolution of  $\sim 1000$ . A gas filter was employed to eliminate high order radiation [2]. The photon energy range for this beamline is 7.8–21.6 eV. In this work, experiments using U10 beamline detected pyrolysis and flame intermediates while experiments using U14 beamline detected species with high ionization energies, such as  $\text{H}_2$ ,  $\text{CH}_4$ ,  $\text{H}_2\text{O}$ ,  $\text{CO}$ ,  $\text{CO}_2$ , and Ar.

### ***2.1.2 Flow Reactor Pyrolysis Apparatus***

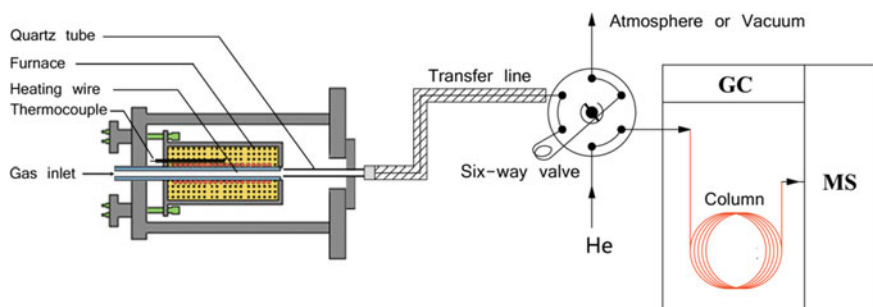
Two flow reactor pyrolysis apparatus were used in this work, as shown in Figs. 2.1 and 2.2. For the two models, the configuration of the pyrolysis chamber is the same, they include the flow reactor, heating wire, and an oven; the difference is in the gas-sampling and analytical methods. The first flow reactor in Fig. 2.1 is combined with SR-PI-MBMS and the second flow reactor in Fig. 2.2 is combined with GC/GC-MS. The configuration of the flow reactor, temperature distribution along the centerline of the reactor, injection system, sampling system, experimental mode, and data evaluation procedure are discussed in the sections that follow.

#### **2.1.2.1 Configuration of the Flow Reactor**

The flow reactor, made of alumina, has an inner diameter of 6.8 mm and outside diameter of 10 mm.  $\alpha$ -alumina was used to mitigate catalytic effects on the surface of the reactor material [5]. The alumina tube must be changed after a period of experimentation, due to soot deposition on the surface of the reactor material. To facilitate the change of the flow reactor and to avoid the damage to the heating wires, another tube—made of boron nitride (BN) with inner diameter of 10.5 mm and length of 150 mm—was inserted between the heating wire and flow reactor. The BN material has high stability and thermal conductivity. The heating wire is molybdenum with a diameter of 1 mm. The temperature of the heating wire was controlled using a temperature controller. To reduce heat loss, the flow reactor, BN tube, and heating wire were fixed inside the insulation materials. The alumina flow reactor, BN tube, heating wire, and the insulation materials are presented in Fig. 2.3.



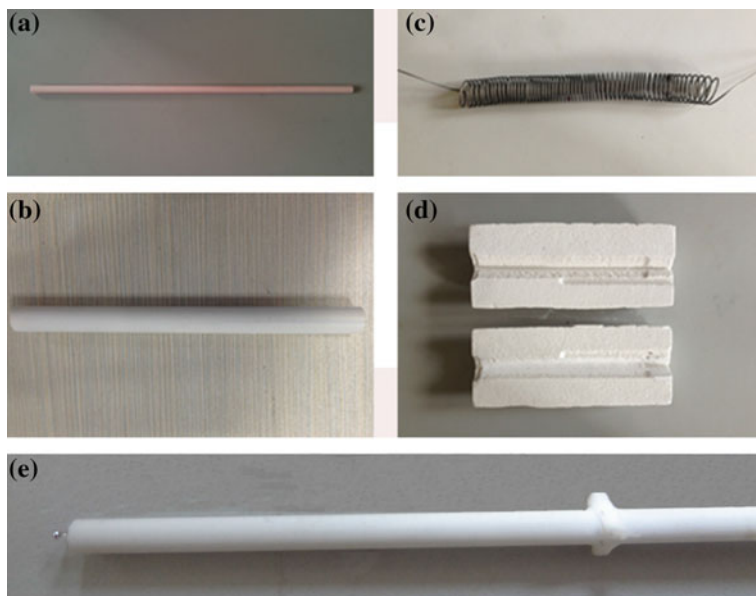
**Fig. 2.1** Schematic of the flow reactor pyrolysis combined with SR-PI-MBMS. Reprinted with permission from Ref. [3]. Copyright 2008 by American Chemical Society



**Fig. 2.2** Schematic of flow reactor pyrolysis combined with GC/GC-MS. Reprinted from Ref. [4]. Copyright 2015, with permission from Elsevier

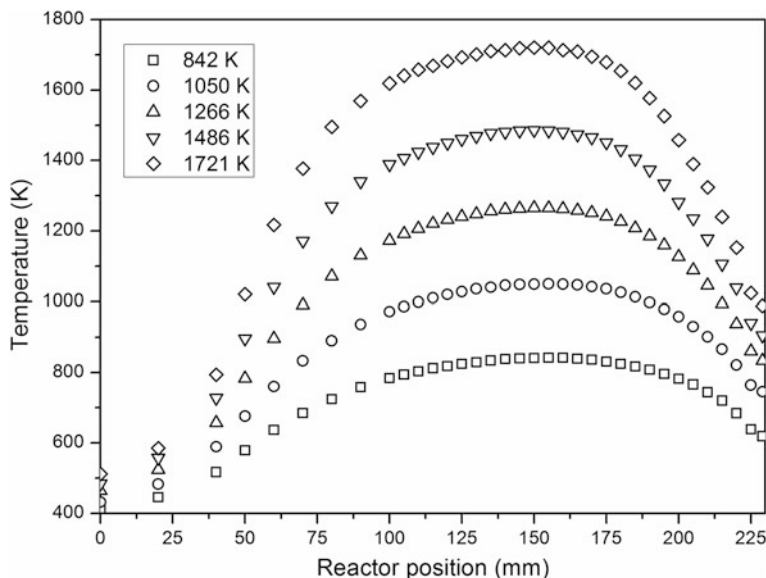
### 2.1.2.2 Temperature Distribution Along the Centerline of the Reactor

Temperature is an important parameter in determining chemical reactions and it is the key to kinetic model simulation. Temperature distribution along the centerline



**Fig. 2.3** Alumina flow reactor (a), BN tube (b), heating wire (c), insulation materials (d), S-type thermocouple and ceramic protection tube (e)

of the flow reactor was measured using a type S thermocouple (platinum-10% rhodium/platinum). This type of thermocouple can be used with a high degree of accuracy and stability in high temperature applications under inert or oxidative atmosphere. For example, the maximum continuous operating temperature of a type S thermocouple is up to 1573 K, and up to 1873 K for short term use. The type S thermocouple used in this work has a diameter of 0.2 mm and a length of 750 mm. To protect the thermocouple, and for the convenience of temperature measurement, the thermocouple was fixed in a two-hole ceramic protection tube with a diameter of 3 mm. The special design of the ceramic tube (Fig. 2.3e), insures that the junction of the thermocouple is in the center of the flow reactor. In temperature measurements, argon was made to flow into the reactor with the same total flow rate as in fuel pyrolysis experiments (i.e., 1000 standard cubic centimeters per minute (sccm)). This precaution avoided carbon deposition on the thermocouple during fuel pyrolysis. The preliminary experiment shows that under low fuel mole fraction conditions (e.g., 2% in this work), the endothermic effect of fuel pyrolysis was not significant. Figure 2.4 presents the temperature distribution along the centerline of the flow reactor under different oven temperature and argon flow rates of 1000 sccm. 0 mm is the inlet of the reactor, while 229 mm corresponds to the sampling position. The heating zone is from 70 to 220 mm. The maximum temperature ( $T_{\max}$ ) of each temperature profile was used as the experimental temperature. The uncertainty of  $T_{\max}$  was estimated to be within  $\pm 30$  K, while the temperatures at other positions had lower uncertainty levels.



**Fig. 2.4** Temperature profiles along reactor centerline. 0 mm is reactor inlet; 229 mm corresponds to sampling position. Argon flow rate is 1000 sccm. Temperatures named by maximum temperature along flow reactor. Reprinted from Ref. [6]. Copyright 2014, with permission from Elsevier

### 2.1.2.3 Injection System

The flow rate of cycloalkanes was controlled by a high performance liquid chromatography (HPLC) pump (FL2000, Fuli) with a range of 0.001–10.000 ml/min; the flow rate of dilution gas argon was controlled using calibrated mass flow controllers (MKS) with a range of 1000 sccm. Fuel was injected into a handcrafted vaporizer and mixed with argon before flowing into the flow reactor. The vaporizer was filled with a stainless steel ball with a diameter of 3 mm. The metal ball first increased thermal conductivity and uniformity of the vaporizer; then it increased the specific surface area for the fuel droplet vaporization. For complete vaporization of the fuel, the temperature of the vaporizer was usually set at 30 to 50 K higher than the boiling point of the fuel.

### 2.1.2.4 Sampling System

The flow reactor pyrolysis, combined with SR-PI-MBMS apparatus, includes three parts: the pyrolysis chamber, a differentially pumped chamber with molecular beam sampling, and a photoionization chamber with a homemade time-of-flight mass spectrometer (Fig. 2.1). The pressure of the pyrolysis chamber was measured using a capacitance manometer (MKS) and adjusted with a downstream butterfly valve

(MKS). The molecular beam sampling system consisted of a quartz nozzle and a nickel skimmer. In the experiment, the pressure of the pyrolysis chamber was 30–760 Torr, while the pressure of the differential pump chamber was on the level of  $10^{-4}$  Torr. The pressure difference of  $10^5$ – $10^6$  between the pyrolysis chamber and the differential pump chamber resulted in a molecular beam after sampling. The centerline of the molecular beam was sampled with the nickel nozzle and ionized using the synchrotron radiation. The photon ions were then separated by the homemade time-of-flight mass spectrometer. To achieve the vacuum environment of photoionization mass spectrometer ( $\sim 10^{-5}$  Torr or lower), a quartz nozzle with a tip hole of a different diameter was required. In this work, the quartz nozzle with  $\sim 500$ , 200, and 50  $\mu\text{m}$  tip hole was used for 30, 150, and 760 Torr experiments, respectively [7–11].

The flow reactor combined with GC/GC-MS apparatus also consisted of three parts: the pyrolysis chamber, the probe sampling system, and the GC-GC/MS (Fig. 2.2). The pyrolysis chamber was the same used in the SR-PI-MBMS experiment. A mechanical pump was connected to the pyrolysis chamber and operated for the 30 and 150 Torr pyrolysis experiments. A quartz tube with an inner diameter of 3 mm was used for gas product sampling. The products were then transferred to the six-way valve of the GC system through a heated transfer line (a stainless steel tube with inner diameter of 6 mm). Temperature of the transfer line was set at 473 K to avoid condensation during transfer. The products were separated by the GC column after the injection from the six-way valve, and detected by FID, TCD, and/or MS. The volume of the loop was 2.5 mL for the 30 and 150 Torr experiments and was 100  $\mu\text{L}$  during the 760 Torr experiment. High injection volume during the 30 and 150 Torr experiments compensated for the signal reduction at low pressure.

### 2.1.2.5 Experimental Mode and Data Evaluation

Two experimental modes were used in the SR-PI-MBMS experiment, the energy and the temperature scan. The energy scan was carried out at a fixed temperature to achieve the photoionization efficiency (PIE) spectra of the pyrolysis intermediates. The PIE spectra helped to identify the structure of the species. The temperature scan was performed at a fixed photon energy to find the temperature-dependent signal profiles of the pyrolysis intermediates. The signal profile was then converted into a mole fraction profile using the data evaluation procedure. In the pyrolysis experiment, several photon energies were usually selected in order to avoid fragmentation and find the near-threshold ionization of the intermediates.

In a species  $i$ , its signal  $S_i(T, E)$  is proportional to its mole fraction  $X_i$ , the photoionization cross section  $\sigma_i(E)$  at the specific photon energy  $E$ , mass discrimination factor  $D_i$ , photon flux  $\Phi_p(E)$  at the specific photon energy  $E$ , and expansion factor  $\lambda(T)$ , as shown in E1.



$$S_i(T, E) \propto X_i(T) \times \sigma_i(E) \times D_i \times \Phi_p(E) \times \lambda(T) \quad (\text{E1})$$

The mole fraction of species  $i$  can be obtained from the standard species  $s$  with known mole fraction through E2.

$$X_i(T) = \frac{S_i(T, E) \sigma_s(E) D_s \lambda(T_0)}{S_s(T_0, E) \sigma_i(E) D_i \lambda(T)} X_s(T_0) \quad (\text{E2})$$

In the experiment, the mole fractions of  $\text{H}_2$  and  $\text{CH}_4$  were calculated from argon at 16.65 eV. The relative ratio of  $\sigma_i(E)D_i/\sigma_{Ar}(E)D_{Ar}$  between  $\text{H}_2$  ( $\text{CH}_4$ ) and argon was obtained from the cold gas experiment at 16.65 eV. The mole fraction of fuel was calculated using its signals at the temperature where no reaction occurred ( $S_{\text{fuel}}(T_0)$ ); the  $S_{\text{fuel}}(T_0)$  corresponded to its initial mole fraction. The mole fraction of pyrolysis intermediate can be obtained using fuel as the standard, or other intermediates such as 1,3-butadiene and 1,3-pentadiene, when a fuel signal is not available. The expansion factor  $\lambda(T)$  represents thermal expansion due to temperature increase, and mole number expansion from fuel decomposition. During pyrolysis, the mole fractions of all the species are calculated after correction for the expansion effect. Errors of quantification result mainly from the uncertainty of the photoionization cross sections. The mole fraction uncertainty of species from direct calibration, such as  $\text{H}_2$  and  $\text{CH}_4$ , is estimated to be  $\pm 10\%$ ; the uncertainty for species with known photoionization cross sections was estimated to be  $\pm 25\%$ ; and the uncertainty for species with unknown photoionization cross sections was estimated to be a factor of two.

In flow reactor pyrolysis with GC-GC/MS analysis, identification of the intermediate was carried out by comparing retention time with the standard compound, or by comparing its fragments in the GC-MS analysis with the NIST mass spectral library [12]. Quantification of pyrolysis intermediates was performed using the flame ionization detector (FID). In these experiments, the Plot-Q and HP-1 columns were selected to separate C1–C5 intermediates and intermediates with more than five carbon numbers, respectively. The Plot-Q column (i.e., HP Plot-Q) was purchased from Agilent technologies, with an inner diameter of 320  $\mu\text{m}$  and a length of 30 m. The GS-Tek HP-1 column (i.e., GsBP-1 ms), had an inner diameter of 250  $\mu\text{m}$  and a length of 30 m. The mole fraction of the intermediate was calculated from the corresponding response factor, obtained directly for species with available standard samples, such as  $\text{CH}_4$ ,  $\text{C}_2\text{H}_2$ ,  $\text{C}_2\text{H}_4$ ,  $\text{C}_2\text{H}_6$ , and  $\text{C}_3\text{H}_8$ ; the response factor for other intermediate was obtained indirectly from the estimation of effective carbon number. The mole fraction uncertainty of species from direct calibration was  $\pm 10\%$  while that from indirect calibration was  $\pm 20\%$ .

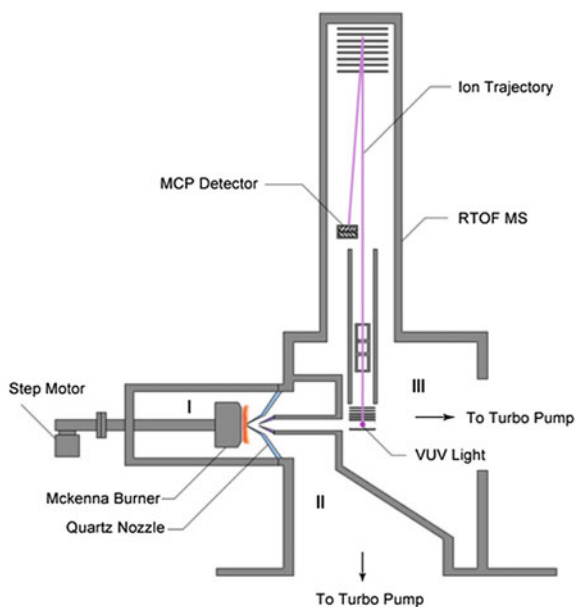
## 2.1.3 Low-Pressure Laminar Premixed Flame

### 2.1.3.1 Experimental Setup

The low-pressure laminar premixed flame instrument in Fig. 2.5 consists of a low-pressure flame chamber, a differential pump flame-sampling chamber, and the ionization chamber with a handmade reflectron time-of-flight mass spectrometer. The flame was stabilized on a McKenna burner with a 60 mm diameter and sampled using a quartz cone with  $\sim 500 \mu\text{m}$  orifice. The MBMS system and the reflectron time-of-flight mass spectrometer are similar to those in the flow reactor pyrolysis experiment. The pressure of the flame chamber was regulated at 30 Torr. The flame species at a different flame zone was sampled by moving the McKenna burner with a step-motor. The flow rate of fuel in liquid phase was controlled by a syringe pump (ISCO, 1000D, USA, 0.001–408 mL/min) and vaporized in a handmade vaporizer. The flow rate of  $\text{O}_2$  and argon was regulated using a calibrated mass flow controller (MKS) [7, 10, 11, 13, 14].

Flame temperature is important information for combustion kinetic simulation, which is often measured by optical spectroscopy or thermocouple. In this work, the flame temperature was measured with a type B thermocouple (Pt-6%Rh/Pt-30%Rh) with a diameter of 0.10 mm. To inhibit the catalytic effect, the thermocouple was coated with  $\text{Y}_2\text{O}_3\text{-BeO}$  anti-catalytic ceramic [15, 16]. Preparation of the thermocouple and the anti-catalytic ceramic can be found in Ref. [17]. Radiation heat loss during the thermocouple temperature measurement was corrected by E3:

**Fig. 2.5** Low-pressure laminar premixed flame instrument with SR-PI-MBMS. Reprinted from Ref. [1]. Copyright 2013, with permission from Elsevier



$$T_g - T_c = \frac{\varepsilon\sigma d(T_c^4 - T_w^4)}{2\lambda} \quad (\text{E3})$$

$T_g$  is the temperature of the flame;  $T_c$  is the temperature measured by thermocouple,  $T_w$  is wall temperature of the combustion chamber,  $d$  is diameter of the thermocouple,  $\varepsilon$  is emissivity of the thermocouple,  $\sigma$  is the Boltzmann constant,  $\lambda$  is thermal conductivity of the flame. The  $\varepsilon/\lambda$  value was obtained by measuring the flame temperature of standard flames in the literature [18]. In addition to the radiation heat loss correction, the cooling effect of the sampling nozzle was also corrected [18]. The uncertainty of thermocouple temperature measurement was  $\pm 100$  K [13].

### 2.1.3.2 Experimental Mode and Data Evaluation

Like the pyrolysis experiment, the flame intermediates were identified first, from the photoionization efficiency spectra, by scanning the photon energy at a fixed flame position. Normally, the flame position corresponding to the maximum signal intensity of the intermediates is selected. The signal intensity of the flame intermediates along the axial position of the burner were measured next. Several photon energies were chosen to achieve near-threshold ionization. The signal intensity was then evaluated to obtain species speciation along the flame. A brief description of the data evaluation procedure follows. Details can be found in the work of Li et al. and Cai et al. [11, 13]

In laminar premixed flame, the relationship between the signal of species  $i$ ,  $S_i(T, E)$ , and its mole fraction  $X_i$  is shown in E4.  $\sigma_i(E)$  is the photoionization cross section of species  $i$  at the specific photon energy  $E$ .  $D_i$  is the mass discrimination factor of species  $i$ ;  $\Phi_p(E)$  is the photon flux at the specific photon energy  $E$ , and  $F(T, T_0)$  is the instrumental factor—the function of sampling—which is the same for all the flame species.

$$S_i(T, E) \propto X_i(T) \times \sigma_i(E) \times D_i \times \Phi_p(E) \times F(T, T_0) \quad (\text{E4})$$

The first step in the data evaluation is to obtain the instrumental factor  $F(T, T_0)$ . According to Cool et al. [19], the argon mole fraction at the initial (e.g., 0.7 mm in this work) and final positions (e.g., 30.7 mm in this work) of the flame is required. At the initial and final position, the major species are fuel,  $O_2$ ,  $H_2$ ,  $H_2O$ ,  $CO$ ,  $CO_2$ , and Ar. The mole fraction summation of these species is equal to one at the final position and is close to one at the initial position. The mole fraction ratio of the aforementioned six major species with argon at 16.65 eV is shown in E5, which can be applied to the initial and final position.

$$X_i(T) = X_{Ar}(T) \frac{S_i(T, E)}{S_{Ar}(T, E)} \frac{\sigma_{Ar}(E)D_{Ar}}{\sigma_i(E)D_i} \quad (E5)$$

The mole fraction of the seven species can then be obtained at the initial and final position after normalization. Once the mole fraction of argon at the initial and final position is obtained, the  $F(T, T_0)$  can be calculated accordingly. To reduce the uncertainty in E5, the relative ratio of  $\sigma_i(E)D_i/\sigma_{Ar}(E)D_{Ar}$  among the six major species and argon is obtained from the cold gas experiment. The mole fraction of the seven species at different flame positions can be calculated from E6, in which  $X_i(T_0, E)$  and  $S_i(T_0, E)$  are the mole fraction and signal intensity of these species at the initial position.

$$X_i(T) = X_i(T_0) \frac{S_i(T, E)}{S_i(T_0, E)} F(T, T_0) \quad (E6)$$

The mole fraction of the flame intermediates can be obtained from fuel or other intermediates with known mole fraction. The uncertainty of mole fraction is estimated to be  $\pm 10\%$  for major flame species,  $\pm 25\%$  for species with known photoionization cross sections, and a factor of two for those with unknown photoionization cross sections.

## 2.2 Kinetic Modeling

The object-oriented software tool, CHEMKIN, was developed to solve complex problems involving chemical kinetics, thermodynamics, and/or transport processes. CHEMKIN was originally developed at the Sandia National Laboratories and has been used worldwide in combustion and chemical processing, etc. In the past thirty years, the software had been updated with several versions: CHEMKIN 1 (1980), CHEMKIN 2 (1989), CHEMKIN 3 (1996), CHEMKIN 4 (2004), and CHEMKIN-PRO (2009). The simulation in this work was performed by CHEMKIN-PRO software [20], which includes a large number of application programs, a set of core utilities (e.g., gas-phase kinetics, surface kinetics, and transport), an application user interface to establish and solve problems and a graphical post-processor to quickly visualize results.

The combustion kinetic simulation in this work involves mainly gas-phase kinetics and transport (e.g., thermodynamic data, kinetic mechanism, and transport data), which are the three components of a combustion kinetic model. The following sections briefly introduce these three components.

### 2.2.1 Thermodynamic Data

The thermodynamic database includes the species name, its elemental composition, phase, temperature range, and 14 polynomial coefficients. The first seven coefficients are used to calculate the thermodynamic properties at high temperature (normally higher than 1000 K), such as specific heat capacity  $C_p/R$ , enthalpy  $H^0/RT$ , and entropy  $S^0/R$ , as shown in E7–E9. The last seven parameters are used to calculate thermodynamic properties at low temperature (normally lower than 1000 K). Other thermodynamic data, such as Gibbs free energy and internal energy, can be derived from  $C_p$ ,  $H^0$ , and  $S^0$ .

$$\frac{C_p}{R} = a_1 + a_2T + a_3T^2 + a_4T^3 + a_5T^4 \quad (\text{E7})$$

$$\frac{H^0}{RT} = a_1 + \frac{a_2}{2}T + \frac{a_3}{3}T^2 + \frac{a_4}{4}T^3 + \frac{a_5}{5}T^4 + \frac{a_6}{T} \quad (\text{E8})$$

$$\frac{S^0}{R} = a_1 \ln T + a_2T + \frac{a_3}{2}T^2 + \frac{a_4}{2}T^2 + \frac{a_5}{2}T^2 + a_7 \quad (\text{E9})$$

To obtain the thermodynamic properties of a species, the additivity method of Benson's group was frequently employed [21–23] to estimate the thermodynamic data (i.e.,  $\Delta_f H^0(298 \text{ K})$ ,  $S^0(298 \text{ K})$ , and  $C_p$ ). The FITDAT program in CHEMKIN-PRO software can also be used to gather thermodynamic data. The inputs are molecular vibrational frequencies, standard enthalpy of formation  $\Delta_f H^0(298 \text{ K})$ , and standard molar entropy  $S^0(298 \text{ K})$ . The molecular vibrational frequencies and standard molar entropy can be calculated from the quantum chemistry calculation. Methods used to estimate the standard enthalpy of formation of a species are discussed briefly here.

The standard enthalpy of formation  $\Delta_f H^0(298 \text{ K})$  of a species can be calculated from quantum chemistry calculations with a variety of schemes, such as the atomization energy method and the isodesmic reaction method. In the atomization energy method, the enthalpy of atomization of a compound is calculated; this is the amount of enthalpy change when the compound bonds are broken and individual atoms are produced [24]. For example, atomization of one mol  $C_m H_n$  forms  $m$  mole of carbon atoms and  $n$  mole of hydrogen atoms. The total energy of  $C_m H_n$ , carbon atom, and H atom (e.g.,  $H_{\text{calcd}}$ ) in R1 can be calculated using quantum chemistry calculations, e.g. Gaussian 09 program [25].



The  $\Delta_f H_{\text{exp}}^0(298 \text{ K})$  of carbon atom and H atom can be found in the NIST database [26]. Thus the  $\Delta_f H^0(298 \text{ K})$  of  $C_m H_n$  can be calculated from E10.

$$\Delta_f H(C_m H_n; 298 \text{ K}) = m\Delta_f H_{\text{exp}}(\text{C}; 298 \text{ K}) + n\Delta_f H_{\text{exp}}(\text{H}; 298 \text{ K}) - [mH_{\text{calcd}}(\text{C}; 298 \text{ K}) + nH_{\text{calcd}}(\text{H}; 298 \text{ K}) - H_{\text{calcd}}(C_m H_n; 298 \text{ K})] \quad (\text{E10})$$

In the isodesmic reaction method, an isodesmic reaction (i.e., type of chemical bonds broken in the reactant are the same as the type of bonds formed in the reaction product) is created [24, 27]. Compared to the atomization method, isodesmic reactions result in maximum cancelation of errors [24].

One isodesmic reaction to calculate the  $\Delta_f H^0(298 \text{ K})$  of propane is shown in R2 and E11.



$$\Delta_f H(\text{C}_3\text{H}_8; 298 \text{ K}) = 2\Delta_f H_{\text{exp}}(\text{C}_2\text{H}_6; 298 \text{ K}) - \Delta_f H_{\text{exp}}(\text{CH}_4; 298 \text{ K}) - [2H_{\text{calcd}}(\text{C}_2\text{H}_6; 298 \text{ K}) - H_{\text{calcd}}(\text{CH}_4; 298 \text{ K}) - H_{\text{calcd}}(\text{C}_3\text{H}_8; 298 \text{ K})] \quad (\text{E11})$$

The total energy of  $\text{C}_3\text{H}_8$ ,  $\text{CH}_4$ , and  $\text{C}_2\text{H}_6$  (e.g.,  $H_{\text{calcd}}$ ) in R2 can be calculated from quantum chemistry calculation. The  $\Delta_f H^0_{\text{exp}}(298 \text{ K})$  of  $\text{CH}_4$  and  $\text{C}_2\text{H}_6$  can be found in the NIST database [26].

## 2.2.2 Chemical Kinetic Data

The reaction mechanism in the CHEMKIN format consists of element, species name, chemical reaction, and its rate constant. For reaction R3, the reaction rate is expressed in E12.



$$q = k_f [\text{A}]^a [\text{B}]^b \quad (\text{E12})$$

$k_f$  is the forward rate constant. The modified Arrhenius equation of  $K_f$  is shown in E13:

$$k_f = AT^n \exp(-E/RT) \quad (\text{E13})$$

The three parameters A, n, E must be given in the reaction mechanism file. The rate constant of some reactions, e.g., unimolecular/recombination reactions, is also influenced by pressure. Troe parameters, Chebyshev expansions, and Plog format were frequently adopted to describe the fall-off rate constant of the reactions. The rate constant of a reaction could be estimated by analogy to similar reactions, measured from experiments, and computed from quantum chemistry. Analogy is a

simple way to obtain the rate constant of unknown reactions, but this estimation often has a high degree of uncertainty. The rate constant measured from well-defined experimentation has greater accuracy and is widely used in combustion and atmospheric chemistry. However, data are often obtained within a narrow range of temperature and pressure. The overall rate constant is often measured, while the branching ratio is not clarified. The cost to develop new diagnostics and instruments is high, and some reactions cannot be studied experimentally. Instead, quantum chemistry calculation has been used to obtain the rate constant under a wide range of experimental conditions. The calculation with high-level theory effectively reduces errors in activation energy and rate constant. Another routine method for reducing uncertainty is to compare the calculation with experimental measurements, which helps refine key parameters in rate constant calculations, such as thermodynamic data and collisional energy transfer parameter  $\langle \Delta E \rangle_{\text{down}}$ . The prevalence of rate constant calculations is accompanied by the development of several computer codes, e.g., Chemrate [28], Mesmer [29], and Variflex [30].

### 2.2.3 Transport Data

In a multicomponent gaseous mixture, the evaluation of diffusion coefficients, viscosities, thermal conductivities, and thermal diffusion coefficients is needed to characterize the molecular transport of species, momentum and energy. The transport data in the database consists of seven components: species name, geometry of the molecule (0 for a single atom, 1 for linear molecule, and 2 for nonlinear molecule), Lennard-Jones potential well depth  $\epsilon/kB$  in Kelvins, the Lennard-Jones collision diameter  $\delta$  in angstroms, the dipole moment  $\mu$  in Debye, the polarizability  $\alpha$  in cubic angstroms, and the rotational relaxation collision number  $Z_{\text{rot}}$  at 298 K [31].

The three core utilities in CHEMKIN are gas-phase kinetics, surface kinetics, and transport. Gas-phase kinetics subroutine libraries calculate gas phase properties and reaction rates; surface kinetics determine the chemical reactions occurring at a gas-surface interface, and the transport subroutine libraries determine the multicomponent transport properties of gas phase mixtures. These subroutines are the basis of the application program. Once the problem is solved, the results can be visualized using the graphical post-processor. Rate of production (ROP) and sensitivity analyses can also aid in understanding the combustion process and improving kinetic models.

## References

1. Qi, F. (2013). Combustion chemistry probed by synchrotron VUV photoionization mass spectrometry. *Proceedings of the Combustion Institute*, 34, 33–63.
2. Zhang, T., Zhu, A., Hong, X., Pan, Y., Shan, X., Sheng, L., Zhang, Y., Qi, F. (2007). A gas filter system of U14C beamline at National Synchrotron Radiation Laboratory. *Journal of University of Science and Technology of China*, 37, 582–585.
3. Zhang, T., Wang, J., Yuan, T., Hong, X., Zhang, L., & Qi, F. (2008). Pyrolysis of Methyl tert-Butyl Ether (MTBE). 1. Experimental study with molecular-beam mass spectrometry and tunable synchrotron VUV photoionization. *Journal of Physical Chemistry A*, 112(42), 10487–10494.
4. Wang, Z., Bian, H., Wang, Y., Zhang, L., Li, Y., Zhang, F., et al. (2015). Investigation on primary decomposition of ethylcyclohexane at atmospheric pressure. *Proceedings of the Combustion Institute*, 35(1), 367–375.
5. Cheng, Z., Xing, L., Zeng, M., Dong, W., Zhang, F., Qi, F., et al. (2014). Experimental and kinetic modeling study of 2,5-dimethylfuran pyrolysis at various pressures. *Combustion and Flame*, 161, 2496–2511.
6. Wang, Z., Ye, L., Yuan, W., Zhang, L., Wang, Y., Cheng, Z., et al. (2014). Experimental and kinetic modeling study on methylcyclohexane pyrolysis and combustion. *Combustion and Flame*, 161, 84–100.
7. Yuan, T. (2010). *Studies on pyrolysis and premixed flames of n-heptane and iso-octane*. Ph.D. Thesis, University of Science and Technology of China.
8. Zhang, Y. (2011). *Experimental and kinetic modeling studies on pyrolysis of C4 alkenes and alkanes*. Ph.D. Thesis, University of Science and Technology of China.
9. Xie, M. (2012). *Experimental and kinetic modeling studies on pyrolysis of C3–C5 chain fat acid methyl esters*. Ph.D. Thesis, University of Science and Technology of China.
10. Yang, J. (2012). *Experimental and modeling study of low-pressure combustion of benzene and benzene/C<sub>2</sub>H<sub>6</sub>O mixtures*. Ph.D. Thesis, University of Science and Technology of China.
11. Cai, J. (2013). *Experimental and kinetic modeling studies of butanol combustion*. Ph.D. Thesis, University of Science and Technology of China.
12. NIST/EPA/NIH Mass Spectral Library (NIST 08). NIST.
13. Li, Y. (2010). *Experimental and kinetic modeling study of premixed aromatic hydrocarbon flames at low pressure*. Ph.D. Thesis, University of Science and Technology of China.
14. Qi, F., Yang, R., Yang, B., Huang, C., Wei, L., Wang, J., et al. (2006). Isomeric identification of polycyclic aromatic hydrocarbons formed in combustion with tunable vacuum ultraviolet photoionization. *Review of Scientific Instruments*, 77(8), 084101.
15. Kint, J. H. (1970). A noncatalytic coating for platinum-rhodium thermocouples. *Combustion and Flame*, 14(2), 279–281.
16. Shandross, R. A., Longwell, J. P., & Howard, J. B. (1991). Noncatalytic thermocouple coating for low-pressure flames. *Combustion and Flame*, 85(1–2), 282–284.
17. Wei, L. (2006). *Studies on VUV Photoionization and Combustion of Some C3 Oxygen-Contained Compounds*. Ph.D. Thesis, University of Science and Technology of China.
18. Hartlieb, A. T., Atakan, B., & Kohse-Höinghaus, K. (2000). Effects of a sampling quartz nozzle on the flame structure of a fuel-rich low-pressure propene flame. *Combustion and Flame*, 121(4), 610–624.
19. Cool, T. A., Nakajima, K., Taatjes, C. A., McIlroy, A., Westmoreland, P. R., Law, M. E., et al. (2005). Studies of a fuel-rich propane flame with photoionization mass spectrometry. *Proceedings of the Combustion Institute*, 30(1), 1681–1688.
20. Reaction Design. (2009). CHEMKIN-PRO 15092. San Diego: Reaction Design.
21. Benson, S. W., & Buss, J. H. (1958). Additivity rules for the estimation of molecular properties: Thermodynamic properties. *The Journal of Chemical Physics*, 29(3), 546–572.
22. Benson, S. W. (1976). *Thermochemical kinetics*. New Jersey: Wiley.



23. Cohen, N. (1996). Revised group additivity values for enthalpies of formation (at 298 K) of carbon-hydrogen and carbon-hydrogen-oxygen compounds. *Journal of Physical and Chemical Reference Data*, 25(8), 1411–1481.
24. Van Speybroeck, V., Gani, R., & Meier, R. J. (2010). The calculation of thermodynamic properties of molecules. *Chemical Society Reviews*, 39(5), 1764–1779.
25. Frisch, M. J., Trucks, G. W., Schlegel, H. B., & Scuseria, G. E. (2009). *Gaussian 09, Revision B.01*. Wallingford, CT: Gaussian Inc.
26. Linstrom, P. J., & Mallard, W. G. (2005). NIST chemistry webbook. National Institute of Standard and Technology, Number 69, Gaithersburg, MD. <http://webbook.nist.gov/>.
27. Wheeler, S. E., Houk, K. N., Schleyer, P. V. R., & Allen, W. D. (2009). A hierarchy of homodesmotic reactions for thermochemistry. *Journal of the American Chemical Society*, 131(7), 2547–2560.
28. Mokrushin, V., Bedanov, V., Tsang, W., Zachariah, M., & Knyazev, V. (2009). *ChemRate, Version 1.5.8*. Gaithersburg, MD: National Institute of Standard and Technology.
29. Robertson, S. H., Glowacki, D. R., Liang, C.-H., Morley, C., Shannon, R., Blitz, M., et al. (2008–2013). MESMER (Master Equation Solver for Multi-Energy Well Reactions), an object oriented C ++ program implementing master equation methods for gas phase reactions with arbitrary multiple wells. <http://sourceforge.net/projects/mesmer>.
30. Klippenstein, S. J., Wagner, A. F., Dunbar, R. C., Wardlaw, D. M., & Robertson, S. H. (1999). *Variflex. 1999, Version 1.0*. Lemont: Argonne National Laboratory.
31. Kee, R. J., Rupley, F. M., Miller, J. A., Coltrin, M. E., Grcar, J. F., Meeks, E. et al. (2000). CHEMKIN Collection, Release 3.6. Reaction Design Inc., San Diego, CA.

# Chapter 3

## Experimental and Modeling Study of Cyclohexane Combustion

### 3.1 Background

Cyclohexane (C<sub>6</sub>H<sub>12</sub>) has the following properties: molar mass 84.160 g/mol, boiling point 354 K, freezing point 280 K, density 0.799 g/mL, standard enthalpy of formation  $123.1 \pm 0.79$  kJ/mol [1], standard molar entropy 298.19 J/mol/K [2], and ionization potential  $9.88 \pm 0.03$  eV. Cyclohexane has several conformers: chair, half-chair, twist-boat, and boat; its most stable conformation is the chair conformer. The chair and twist-boat conformers are separated from the entire conformation. The half-boat conformation is the transition state (TS) between chair and twist-boat, while the boat conformation is the TS between the two twist-boats. The standard enthalpy of twist-boat, boat, and half-boat conformers is 22.4, 27.0, and 44.0 kJ/mol [3], relative to the chair conformer. Thus, the chair conformer is the most abundant conformation. However, the distribution of the conformation changes with temperature, for example, a tiny amount of cyclohexane is in twist-boat (<0.1%) at room temperature, while the contribution of the twist boat increases to 30% when the temperature is 1073 K.

The combustion of cyclohexane has been studied extensively because it is an important surrogate component and its reaction mechanism is the basis for understanding the combustion properties of alkyl-cyclohexanes. The literature of cyclohexane combustion covers experimental study of its pyrolysis, oxidation, and flame, reaction pathway and rate constant calculation and kinetic modeling.

Wing Tsang studied the pyrolysis of cyclohexane from single-pulse shock tube experiments in 1978; the pressure was 2–7 atm and the temperature range 1073–1123 K. Reaction products were analyzed by GC-FID and reaction temperature was calibrated by the dissociation of cyclohexene [4]. The results showed that the only decomposition channel of cyclohexane forms 1-hexene. Two probable reaction pathways were proposed: The first reaction channel proceeds via a one-step reaction, which directly produces 1-hexene. The second channel proceeds via a

two-step reaction, i.e., ring-opening of cyclohexane forms a diradical intermediates, which then undergoes an intramolecular 1,5-H shift to form 1-hexene.

Later, Aribike et al. [5] investigated the decomposition of cyclohexane in an annular reactor at atmospheric pressure, and a temperature range of 1000–1300 K, with  $N_2$  as the dilution gas. Their experiment did not detect 1-hexene and they proposed another dissociation channel for cyclohexane. In 1986, Brown et al. [6] studied the pyrolysis of cyclohexane in 900–1200 K using a very low pressure pyrolysis (VLPP) technique. Their results supported the two-step reaction pathways of cyclohexane to 1-hexene by Tsang [4]. Recently, Kiefer et al. investigated cyclohexane decomposition in a shock tube using the laser Schlieren technique. The experiment was carried out in a temperature range of 1300–2000 K, pressure of 25–200 Torr, and 2, 4, 10, and 20% cyclohexane in Kr [7]. They also calculated the dissociation channels of cyclohexane, which confirmed that 1-hexene is the initial decomposition product of cyclohexane, via a two-step reaction with a diradical as an intermediate.

Several studies have investigated the oxidation of cyclohexane in ideal reactors and engines. Viosin et al. [8], El-Bakali et al. [9], and Serinyel et al. [10] measured the low and intermediate temperature (500–1100 K) oxidation intermediates of cyclohexane oxidation in jet-stirred reactors (JSR) under 1, 2, and 10 atm and equivalence ratios from 0.5 to 2.0. Sirjean et al. [11], Daley et al. [12], and Hong et al. [13] investigated the ignition delay times of cyclohexane in shock tubes (ST) in the temperature range of 850–1500 K, under pressure of 1.5–50 atm, and various equivalence ratios from fuel-lean to fuel-rich conditions. Lemaire et al. [14], and Vranckx et al. [15] measured the ignition delay times of cyclohexane in a rapid compression machine (RCM) from 7 to 40 bar. The intermediates from cyclohexane RCM oxidation were measured by Lemaire et al. using GC and mass spectrometer [14]. In addition, Yang and Boehman [16] studied the low and intermediate temperature oxidation of cyclohexane in a motor engine and observed the negative temperature coefficient zone.

The flame study of cyclohexane investigated benzene formation pathways. Apart from the combination of resonance stabilized radicals, the stepwise dehydrogenation of cyclohexane is a novel route to forming benzene [8, 14, 17–19]. Ciajolo et al. [20] studied sooting cyclohexane premixed flame. Their results showed that in the preheated and reaction zone, benzene is produced from the rapid dehydrogenation of cyclohexane; in the post flame zone, the recombination/addition of smaller radicals, especially the self-combination of propargyl radicals contribute to benzene production.

Law et al. [21] and Li et al. [22] investigated the low pressure laminar premixed flame of cyclohexane and found that benzene derives mainly from the step-wise dehydrogenation of cyclohexane in the stoichiometric flame. In the fuel rich flame, both the step-wise dehydrogenation of cyclohexane and the combination of smaller radicals contribute to benzene formation. In a non-premixed flame of cyclohexane, McEnally and Pfefferle [23] showed that the combination of smaller radicals is the dominant route for benzene, while the contribution from dehydrogenation of

cyclohexane is insignificant. These studies proved that the benzene formation mechanism is affected by flame configuration, C/O ratios, and the flame zone. In addition to these studies, laminar flame speed of cyclohexane was measured by Davis et al. [24], Ji et al. [25], Wu et al. [26], and Serinyel et al. [10] in the pressure range of 1–20 atm.

Based on experimental and theoretical studies, the kinetic models of cyclohexane combustion were developed by Dagaut et al. [8, 9], Ranzi et al. [27], Westbrook et al. [17], Wang et al. [28], and Battin-Leclerc et al. [10, 11, 29, 30]. Dagaut et al. developed the high temperature oxidation model of cyclohexane which was validated by the species speciation measured from JSR oxidation of cyclohexane at 1, 2, and 10 atm [8, 9] and the laminar flame speed of cyclohexane by Davis et al. [24]. In addition to the JSR species speciation [8, 9] and the laminar flame speed [24], the kinetic model developed by Ranzi et al. was also validated by the ignition delay time and species speciation from cyclohexane RCM oxidation [14]. Westbrook et al. proposed the rate rule for the low temperature oxidation reactions of cyclohexane; the kinetic model was validated from the ignition delay time and species speciation from cyclohexane RCM oxidation [14], in addition to the species speciation measured from JSR oxidation [8, 9]. Wang et al. developed the JetSurF model, which includes the sub-mechanism of cyclohexane and the C<sub>1</sub>–C<sub>4</sub> alkyl-cyclohexanes. Sirjean et al. [11], Daley et al. [12], and Hong et al. [13] examined this model using the shock tube ignition delay times of cyclohexane. The laminar flame speed by Davis et al. [23], Ji et al. [25] and Wu et al. [26], and the JSR species speciation by EI-Bakali et al. [9] were also used to validate the model. Battin-Leclerc et al. developed a low and high temperature oxidation model of cyclohexane using the automatic reaction mechanism generator, EXGAS. The model was validated by the species speciation from JSR oxidation and ignition delay time in shock tube and RCM [11, 29]; it was recently improved by the new JSR oxidation data of cyclohexane from 500 to 1100 K, measured by the same group [10].

Studies in the literature focus on the oxidation of cyclohexane; there is a scarcity of data reporting detailed species speciation—especially under pyrolysis conditions. The pyrolysis process is suitable for investigating initial decomposition of fuel molecules and the aromatics formation mechanism. Moreover, fuel pyrolysis reactions are an important component of combustion models. In this chapter, the pyrolysis of cyclohexane at 30 and 760 Torr is investigated by the synchrotron radiation photoionization molecular beam mass spectrometry (SR-PI-MBMS). Temperature-dependent mole fraction profiles of more than 30 species were obtained. The pyrolysis mechanism of cyclohexane was developed and examined by the data reported in this work. Since the goal of this thesis is to develop the combustion model of cyclohexane and its alkyl-cyclohexanes, the high-temperature oxidation mechanism of cyclohexane is included, as well as the validation of the model by the data in the literature. The following section is organized as follows: kinetic model, flow reactor pyrolysis, JSR oxidation, laminar premixed flame, ignition delay time, laminar flame speed and conclusions.

## 3.2 Kinetic Model

In the kinetic model of cyclohexane, the following reaction classes are considered. The detailed sub-mechanism of high temperature pyrolysis and oxidation of cyclohexane is presented in Table 3.1.

- (a) Unimolecular decomposition and isomerization of cyclohexane
- (b) Dissociation of 1-hexene
- (c) H-atom abstraction of cyclohexane
- (d) Decomposition and isomerization of cyclohexyl radical
- (e) Decomposition and isomerization of 5-hexen-1-yl radical
- (f) Decomposition and dehydrogenation of cyclohexene

### 3.2.1 *Unimolecular Decomposition and Isomerization of Cyclohexane*

Kiefer et al. [7] calculated the dissociation channels of cyclohexane and 1-hexene, as shown in Fig. 3.1. The lowest energy barrier of cyclohexane is isomerization to 1-hexene; this pathway proceeds via a two-step reaction. The value of 88.7 kcal/mol in Fig. 3.1 corresponds to the highest energy barrier of the two-step reaction. Compared to this channel, the energy barrier of the H-elimination channel is around nine kcal/mol higher; the energy barriers of other three channels (e.g., to loss H<sub>2</sub>, to form two cyclopropane, and to form three ethylene molecules) are very high. Therefore, only the isomerization of cyclohexane to 1-hexene and the direct H-elimination of cyclohexane are considered in the model. The rate constant of direct H-elimination of cyclohexane is estimated from the H-elimination of propane [31], as R9 in Table 3.1.

As mentioned above, two possible isomerization channels exist for cyclohexane: a one-step channel with one transition state (TS2 in Fig. 3.2), and a two-step channel with two transition states (TS1 and TS3 in Fig. 3.2). Although the energy barrier of the one-step reaction is lower than that of the two-step reaction, the entropy change of the two-step reaction is greater, leading to much higher rate constants in the two-step reaction than in the one-step reaction. Kiefer et al. estimated that the rate constant of the one-step reaction contributes less than 10% of the total rate constant of cyclohexane isomerization. This observation is in accordance with the findings of Tsang and Brown et al. [4, 6].

Kiefer et al. [7] calculated the high pressure limit rate constant of cyclohexane to 1-hexene. Rate constants at 25, 50, and 200 Torr were obtained from simplified RRKM calculations and experimental results. The high pressure limit rate constants by Kiefer et al. were close to those of Sirjean et al. [32] and Brown et al. [6], but they were three to four times higher than those of Tsang [4], as shown in Fig. 3.3.

**Table 3.1** Important reactions and corresponding rate constants for the sub-mechanism of cyclohexane

No.	Reactions	A	n	E	Pressure (Torr)	References
<i>Reactions of cyclohexane</i>						
1	$cC_6H_{12} + H = cC_6H_{11} + H_2$	2.70E+10	1.4	8229		[7]
2	$cC_6H_{12} + CH_3 = cC_6H_{11} + CH_4$	9.06E+00	3.5	5480		a
3	$cC_6H_{12} + OH = cC_6H_{11} + H_2O$	5.85E+05	2.5	-1164		[33]
4	$cC_6H_{12} + O = cC_6H_{11} + OH$	2.58E+06	2.6	2565		[34]
5	$cC_6H_{12} + O_2 = cC_6H_{11} + HO_2$	2.40E+14	0.0	47,590		b
6	$cC_6H_{12} + HO_2 = cC_6H_{11} + H_2O_2$	1.12E+05	2.5	14,163		[35]
7	$cC_6H_{12} + HCO = cC_6H_{11} + CH_2O$	1.35E+12	0.0	9540		[8]
8	$cC_6H_{12} + CH_3O = cC_6H_{11} + CH_3OH$	4.32E+11	0.0	4473		[8]
9	$cC_6H_{11} + H (+M) = cC_6H_{12} (+M)$ Low pressure limit Troc: 0.649   213.1   213.1   13,369.7	4.80E+13 1.70E+58	0.0 -12.1	0 11,264		c
10	$cC_6H_{12} = C_6H_{12-1}$	1.33E+137 5.96E+139 1.82E+143 8.76E+17	-34.7 -35.3 -36.0 0.0	162,775 166,598 172,904 91,940	25 50 200 HPL	[7] [7] [7] [7]
<i>Reactions of cyclohexyl radical</i>						
11	$cC_6H_{11} = PXC_6H_{11}$	1.26E+22 3.57E+26 2.59E+32 2.07E+41 5.79E+44 3.87E+13	-3.9 -4.9 -6.3 -8.5 -9.2 0.2	22,627 26,638 32,020 40,814 46,530 31,782	30 150 760 7600 76,000 HPL	d d d d d d (continued)

Table 3.1 (continued)

No.	Reactions	A	n	E	Pressure (Torr)	References
12	$cC_6H_{11} = cC_6H_{10} + H$	8.38E+20	-3.6	23,771	30	d
		8.32E+25	-4.8	28,120	150	d
		5.73E+32	-6.5	34,206	760	d
		1.37E+43	-9.0	44,242	7600	d
		7.21E+47	-10.0	51,272	76,000	d
		3.78E+12	0.6	34,881	HPL	d
13	$cC_6H_{11} + H = cC_6H_{10} + H_2$	3.60E+12	0.0	0		e
14	$cC_6H_{11} + CH_3 = cC_6H_{10} + CH_4$	2.20E+13	-0.3	0		e
15	$cC_6H_{11} + OH = cC_6H_{10} + H_2O$	4.80E+13	0.0	0		e
16	$cC_6H_{11} + O_2 = cC_6H_{10} + HO_2$	1.30E+11	0.0	0		f
17	$cC_6H_{11} + O = cC_6H_{10} + OH$	9.64E+13	0.0	0		[8]
18	$cC_6H_{11} + HO_2 = cC_6H_{10} + H_2O_2$	2.00E+12	0.0	2000		[8]
19	$cC_6H_{11} + HCO = cC_6H_{10} + CH_2O$	4.00E+12	0.0	0		[8]
<i>Reactions of 1-hexene</i>						
20	$C_6H_{12-1} = aC_3H_5 + nC_3H_7$	1.07E+80	-19.3	95,177	25	[7]
		2.50E+68	-16.0	86,832	50	[7]
		1.48E+59	-13.3	82,596	100	[7]
		2.43E+61	-14.0	82,637	150	[7]
		3.75E+59	-13.4	82,179	200	[7]
		1.46E+16	0.0	69,120	HPL	[7]

(continued)

Table 3.1 (continued)

No.	Reactions	A	n	E	Pressure (Torr)	References
21	$C_6H_{12-1} = C_4H_7 + C_2H_5$	2.70E+80	-19.3	107,015	25	[7]
		6.27E+68	-16.0	98,670	50	[7]
		3.70E+59	-13.3	94,434	100	[7]
		6.08E+61	-14.0	94,475	150	[7]
		9.38E+59	-13.4	94,017	200	[7]
22	$C_6H_{12-1} = C_3H_6 + C_3H_6$	1.46E+16	0.0	81,020	HPL	[7]
		3.54E+05	1.7	53,752	30	est
23	$C_6H_{12-1} + H = SAXC_6H_{11} + H_2$	7.08E+06	1.7	53,752	HPL	[4]
		3.38E+05	2.4	207		[46, 47]
24	$C_6H_{12-1} + CH_3 = SAXC_6H_{11} + CH_4$	3.69E+00	3.3	4002		[46, 47]
25	$C_6H_{12-1} + O = SAXC_6H_{11} + OH$	6.60E+05	2.4	1210		[46, 47]
26	$C_6H_{12-1} + OH = SAXC_6H_{11} + H_2O$	2.76E+04	2.6	-1919		[46, 47]
27	$C_6H_{12-1} + H = SXC_6H_{11} + H_2$	1.30E+06	2.4	4471		[46, 47]
28	$C_6H_{12-1} + CH_3 = SXC_6H_{11} + CH_4$	1.51E+00	3.5	5481		[46, 47]
29	$C_6H_{12-1} + O = SXC_6H_{11} + OH$	5.51E+05	2.5	2830		[46, 47]
30	$C_6H_{12-1} + OH = SXC_6H_{11} + H_2O$	4.67E+07	1.6	-35		[46, 47]
31	$C_6H_{12-1} + HO_2 = SXC_6H_{11} + H_2O_2$	9.64E+03	2.6	13,910		[46, 47]
32	$C_6H_{12-1} + O_2 = SXC_6H_{11} + HO_2$	2.00E+13	0.0	49,640		[46, 47]
33	$C_6H_{12-1} + H = S2XC_6H_{11} + H_2$	1.30E+06	2.4	4471		[46, 47]
34	$C_6H_{12-1} + CH_3 = S2XC_6H_{11} + CH_4$	1.51E+00	3.5	5481		[46, 47]
35	$C_6H_{12-1} + O = S2XC_6H_{11} + OH$	5.51E+05	2.5	2830		[46, 47]
36	$C_6H_{12-1} + OH = S2XC_6H_{11} + H_2O$	4.67E+07	1.6	-35		[46, 47]
37	$C_6H_{12-1} + HO_2 = S2XC_6H_{11} + H_2O_2$	9.64E+03	2.6	13,910		[46, 47]

(continued)



Table 3.1 (continued)

No.	Reactions	A	n	E	Pressure (Torr)	References
38	$C_6H_{12}-1 + O_2 = S2XC_6H_{11} + HO_2$	2.00E+13	0.0	49,640		[46, 47]
39	$C_6H_{12}-1 + H = PXC_6H_{11} + H_2$	6.65E+05	2.5	6756		[46, 47]
40	$C_6H_{12}-1 + CH_3 = PXC_6H_{11} + CH_4$	4.52E-01	3.7	7154		[46, 47]
41	$C_6H_{12}-1 + O = PXC_6H_{11} + OH$	9.80E+05	2.4	4750		[46, 47]
42	$C_6H_{12}-1 + OH = PXC_6H_{11} + H_2O$	5.27E+09	1.0	1586		[46, 47]
43	$C_6H_{12}-1 + HO_2 = PXC_6H_{11} + H_2O_2$	2.38E+04	2.6	16,494		[46, 47]
44	$C_6H_{12}-1 + O_2 = PXC_6H_{11} + HO_2$	3.00E+13	0.0	52,290		[46, 47]
<i>Reactions of hexenyl radicals</i>						
45	$PXC_6H_{11} (+M) = C_4H_7 + C_2H_4 (+M)$ Low pressure limit Troce: -13.87 227 28 50,000.0	3.98E+12 3.30E-43	0.1 18.4	27,572 -603		[28]
46	$PXC_6H_{11} (+M) = SAXC_6H_{11} (+M)$ Low pressure limit Troce: -13.59 214 28 50,000.0	1.55E+02 1.50E-30	2.8 14.6	15,566 -602		[28]
47	$PXC_6H_{11} (+M) = PXCH_2C_3H_9 (+M)$ Low pressure limit Troce: -18.98 214 28 50,000.0	9.55E+08 2.30E-28	0.4 14.3	10,704 -603		[28]
48	$SAXC_6H_{11} (+M) = C_4H_6 + C_2H_5 (+M)$ Low pressure limit Troce: -18.50 246 28 50000.0	3.39E+11 4.00E-42	0.7 18.1	32,263 -603		[28]
49	$SXC_6H_{11} (+M) = C_3H_6 + aC_3H_5 (+M)$ Low pressure limit Troce: -13.17 268 28 50000.0	4.57E+12 2.50E-31	0.1 14.6	24,386 -579		[28]
50	$S2XC_6H_{11} (+M) = C_5H_8-14 + CH_3 (+M)$ Low pressure limit Troce: -7.03 314.0 28.0 50000.0	8.13E+10 4.00E-39	0.8 16.8	29,648 -600		[28]

(continued)

Table 3.1 (continued)

No.	Reactions	A	n	E	Pressure (Torr)	References
<i>Reactions of cyclohexene</i>						
51	$cC_6H_{10} = C_4H_6 + C_2H_4$	5.00E+78	-18.9	98,386	30	est
		2.60E+70	-16.4	95,510	150	est
		3.81E+25	-3.6	64,034	760	est
		8.31E+13	0.4	64,116	HPL	est
52	$cC_6H_{10} + H = SAXcC_6H_9 + H_2$	6.75E+05	2.4	207		[46, 47]
53	$cC_6H_{10} + CH_3 = SAXcC_6H_9 + CH_4$	7.38E+00	3.3	4002		[46, 47]
54	$cC_6H_{10} + O = SAXcC_6H_9 + OH$	1.32E+06	2.4	1210		[46, 47]
55	$cC_6H_{10} + OH = SAXcC_6H_9 + H_2O$	5.53E+04	2.6	-1919		[46, 47]
56	$SAXcC_6H_9 = cC_6H_8-13 + H$	1.62E+57	-13.0	66,036	30	[22]
		2.67E+12	0.7	49,792	HPL	[49]
57	$SAXcC_6H_9 = PXC_6H_9-13$	5.36E+50	-11.9	48,276	30	[22]
		1.30E+13	0.0	35,900	HPL	[48]
58	$SAXcC_6H_9 + H = cC_6H_8-13 + H_2$	1.80E+13	0.0	0		§
59	$SAXcC_6H_9 + OH = cC_6H_8-13 + H_2O$	6.00E+12	0.0	0		§
60	$SAXcC_6H_9 + O_2 = cC_6H_8-13 + HO_2$	1.60E+12	0.0	15,160		[48]
61	$cC_6H_8-13 + H = SAXcC_6H_7 + H_2$	6.75E+05	2.4	207		[46, 47]
62	$cC_6H_8-13 + CH_3 = SAXcC_6H_7 + CH_4$	7.38E+00	3.3	4002		[46, 47]
63	$cC_6H_8-13 + O = SAXcC_6H_7 + OH$	1.32E+06	2.4	1210		[46, 47]
64	$cC_6H_8-13 + OH = SAXcC_6H_7 + H_2O$	5.53E+04	2.6	-1919		[46, 47]
65	$SAXcC_6H_7 = A1 + H$	3.40E+10	0.8	30,230	30	est
		6.76E+11	0.8	30,230	HPL	[49]

(continued)

Table 3.1 (continued)

No.	Reactions	A	n	E	Pressure (Torr)	References
66	$\text{SAXcC}_6\text{H}_7 + \text{H} = \text{A1} + \text{H}_2$	1.80E+13	0.0	0		[8]
67	$\text{SAXcC}_6\text{H}_7 + \text{OH} = \text{A1} + \text{H}_2\text{O}$	6.00E+12	0.0	0		[8]
68	$\text{SAXcC}_6\text{H}_7 + \text{O}_2 = \text{A1} + \text{HO}_2$	1.60E+12	0.0	15,160		[48]
<i>Reactions of benzene and fulvene</i>						
69	$\text{C}_3\text{H}_3 + \text{C}_3\text{H}_3 = \text{A1}$	1.64E+66	-15.9	27,529	30	[54]
		3.16E+55	-12.6	22,264	760	[79]
		3.89E+50	-11.0	20,320	7600	[79]
70	$\text{C}_3\text{H}_3 + \text{C}_3\text{H}_3 = \text{fulvene}$	7.25E+65	-16.0	25,035	30	[54]
		1.38E+66	-15.7	28,260	760	[79]
		1.26E+56	-12.6	23,515	7600	[79]
71	$\text{aC}_3\text{H}_4 + \text{C}_3\text{H}_3 = \text{A1} + \text{H}$	2.20E+11	0.0	2000		[59]
72	$\text{pC}_3\text{H}_4 + \text{C}_3\text{H}_3 = \text{A1} + \text{H}$	2.20E+11	0.0	2000		[60]
73	$\text{nC}_4\text{H}_5 + \text{C}_2\text{H}_2 = \text{A1} + \text{H}$	2.94E+16	-1.1	9257		[61]
74	$\text{iC}_4\text{H}_5 + \text{C}_2\text{H}_2 = \text{A1} + \text{H}$	1.47E+23	-3.3	24,907		[61]
75	$\text{C}_4\text{H}_4 + \text{C}_2\text{H}_3 = \text{A1} + \text{H}$	1.90E+12	0.0	2510		[62]
76	$\text{nC}_4\text{H}_5 + \text{C}_2\text{H}_2 = \text{fulvene} + \text{H}$	1.52E+15	-0.8	8762		[61]
77	$\text{iC}_4\text{H}_5 + \text{C}_2\text{H}_2 = \text{fulvene} + \text{H}$	1.01E+34	-5.9	28,786		[61]
78	$\text{fulvene} = \text{A1}$	5.62E+81	-19.4	121,500	30	[79]
		1.45E+45	-8.9	96,999	760	[79]
		2.95E+31	-5.0	88,465	7600	[79]

(continued)

Table 3.1 (continued)

No.	Reactions	A	n	E	Pressure (Torr)	References
79	fulvene + H = A1 + H	3.00E+12	0.5	2000		[63]
80	$C_3H_3 + aC_3H_5 = \text{fulvene} + 2H$	3.26E+29	-5.4	3390		[54]
81	A1 = A1- + H	1.35E+108	-25.8	181,750	30	[79]
		6.31E+60	-12.4	148,070	760	[79]
		5.50E+38	-6.2	132,000	7600	[79]
82	fulvene = A1- + H	2.57E+97	-23.2	153,470	30	[79]
		2.24E+68	-14.7	142,570	760	[79]
		8.51E+24	-2.5	113,330	7600	[79]
83	A1 + H = A1- + H <sub>2</sub>	1.42E+08	1.8	13,056		[66]
84	A1 + OH = A1- + H <sub>2</sub> O	2.38E+04	2.7	734		[67]
85	A1- + CH <sub>4</sub> = A1 + CH <sub>3</sub>	3.89E-03	4.6	5256		[80]
86	A1 + O <sub>2</sub> = A1- + HO <sub>2</sub>	6.31E+13	0.0	60,014		[81]
87	A1 + O = A1- + OH	2.00E+13	0.0	14,700		[82]
88	A1 + O = A1O + H	2.20E+13	0.0	4530		[82]
89	A1 + OH = A1OH + H	1.30E+13	0.0	10,600		[83]
<i>Reactions of cyclopentadiene and cyclopentadienyl radical</i>						
90	$C_5H_5 + H (+M) = C_5H_6 (+M)$ Low pressure limit T <sub>roo</sub> : 0.068 400.7 4135.8 5501.9	1.00E+14	0.0	0		[28]
		4.40E+80	-18.3	12,994		
91	$C_5H_6 + H = C_5H_5 + H_2$	3.03E+08	1.7	5590		[72]
92	$C_5H_6 + OH = C_5H_5 + H_2O$	3.08E+06	2.0	0		[73]

(continued)

Table 3.1 (continued)

No.	Reactions	A	n	E	Pressure (Torr)	References
93	$C_3H_3 + C_2H_2 = C_5H_5$	6.17E+66	-15.7	47,729	100	[72]
		6.87E+55	-12.5	42,000	760	[72]
		1.13E+43	-8.8	34,983	7600	[72]

Note  $k = AT^n \exp(-E/RT)$ , Unit is  $cm^3$ , mol, s, cal

<sup>a</sup>Analogy to  $C_3H_8 + CH_3$  [31], rate constant multiplied by 6

<sup>b</sup>Analogy to  $C_3H_8 + O_2$  [31], rate constant multiplied by 6

<sup>c</sup>Analogy to the H-elimination of  $C_3H_8$  [31]

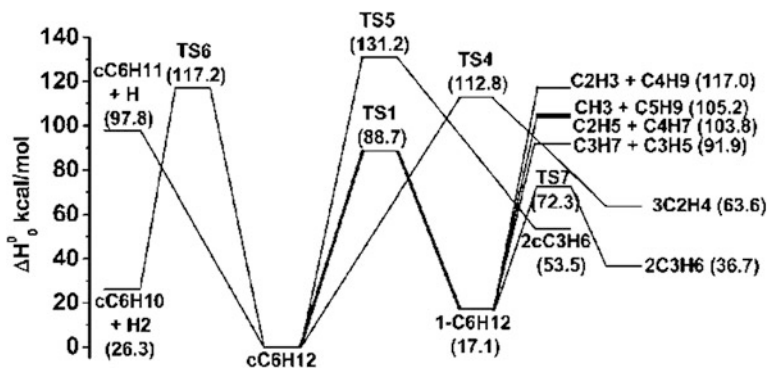
<sup>d</sup>Analogy to 4-methyl-cyclohexyl radical [39]

<sup>e</sup>Analogy to  $nC_3H_7$  [31], rate constant multiplied by 2

<sup>f</sup>Analogy to  $iC_3H_7$  [31]

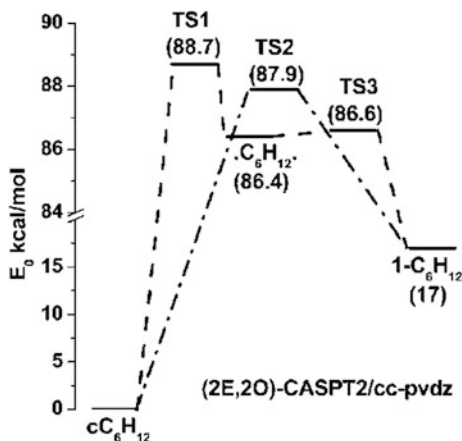
<sup>g</sup>Analogy to 1-buten-3-yl radical

HPL high pressure limit



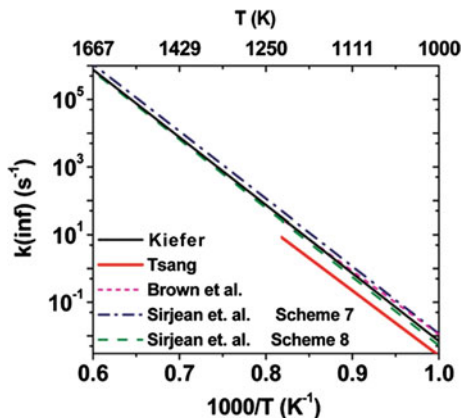
**Fig. 3.1** Energy diagram of possible dissociation channels of cyclohexane and 1-hexene. Energies of the transition state and products are relative to cyclohexane [7]. Reprinted with the permission from Ref. [7]. Copyright 2009 American Chemical Society

**Fig. 3.2** Potential energy surface of cyclohexane isomerization/dissociation. TS1 is the transition state from cyclohexane ring-opening isomerization to a diradical; TS2 is the transition state from cyclohexane to 1-hexene through one-step isomerization; TS3 is the transition state from the diradical to 1-hexene via 1,5-H shift [7]. Reprinted with permission from Ref. [7]. Copyright 2009 American Chemical Society



In this work, the high pressure limit and pressure dependent rate constants at 25, 50, and 200 Torr for cyclohexane to 1-hexene are adopted from Kiefer et al. [7], as R10 in Table 3.1.

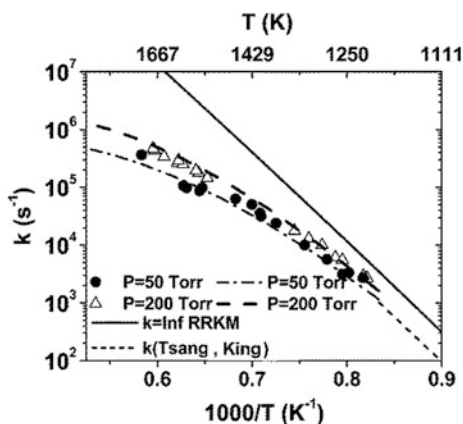
**Fig. 3.3** Comparison of high pressure limit rate constants of cyclohexane to 1-hexene in Kiefer et al. [7], Tsang et al. [4], Brown et al. [6], and Sirjean et al. [32]. Reprinted with permission from Ref. [7]. Copyright 2009 by American Chemical Society



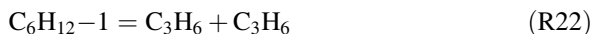
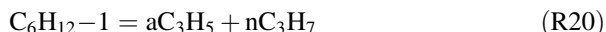
### 3.2.2 Dissociation of 1-Hexene

1-hexene is the dominant product resulting from the initial decomposition of cyclohexane. Kiefer et al. also calculated the probable reaction pathways of 1-hexene [7], as shown in Fig. 3.1. Of the C–C scission channels, the break of the allylic C–C bond (R20 in Table 3.1) has the lowest energy barrier. In addition to the dissociation channels, the 1,5-H shift of 1-hexene forms two propenes (R22 in Table 3.1). Although the energy barrier of R22 is the lowest, Tsang’s investigation [4] showed that the rate constant of R20 is 3–70 times higher than R22 in 1000–2000 K. This occurred because the 1,5-H shift via a six-membered ring transition state (TS) has a lower entropy change between TS and the reactant. Kiefer et al. calculated the rate constants of R20 at the high-pressure-limit, 25, 50, 100, 150, and 200 Torr [7]. The pressure dependent rate constants at 50 and 200 Torr agree with the experimental measurement, as shown in Fig. 3.4. Like the isomerization rate

**Fig. 3.4** Rate constant of 1-hexene dissociation via the break of allylic C–C bond at 50, 200 Torr, and high-pressure-limit [7]. Reprinted with permission from Ref. [7]. Copyright 2009 by American Chemical Society



constant of cyclohexane to 1-hexene, the calculated high pressure limit rate constant of **R20** is three times higher than those of Tsang [4].



Both **R20** and **R22** are included in the kinetic model. The rate constant of **R20** was adopted from the calculation of Kiefer et al. [7] at 25, 50, 100, 150, 200 Torr, and the high pressure limit. The high pressure limit rate constant of **R22** was taken from Tsang [4], and the pressure dependent rate constant at 30 Torr was estimated from this work.

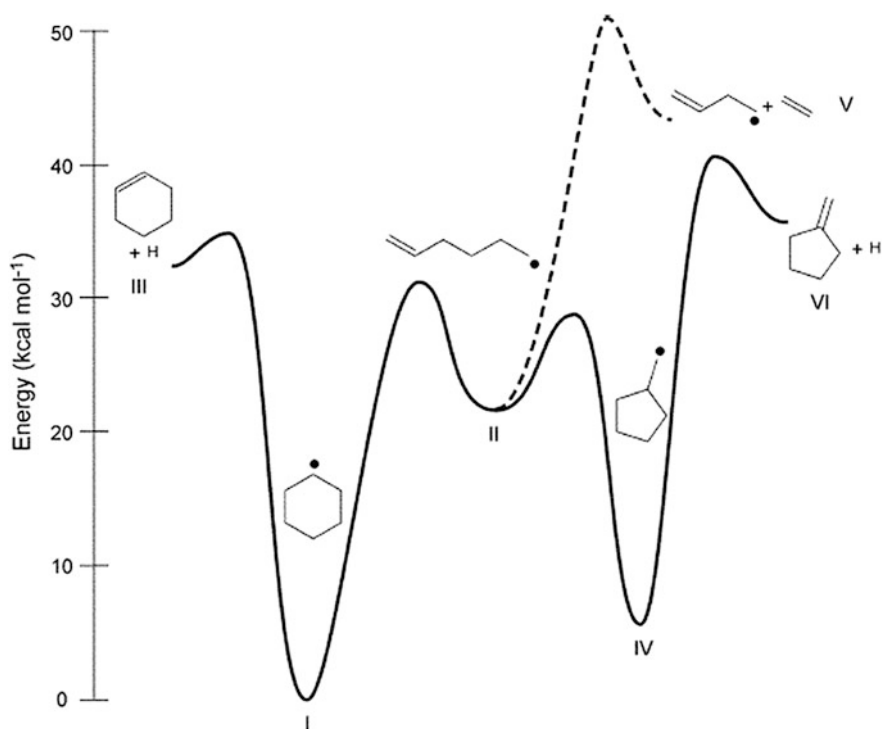
### 3.2.3 H-atom Abstraction of Cyclohexane

H-atom abstraction reactions by H, O, OH, HO<sub>2</sub>, and CH<sub>3</sub> are important pathways for the consumption of cyclohexane. The rate constant of H-atom abstraction of cyclohexane by the H atom was adopted from the calculation of Kiefer et al. [7]. In their work, B3LYP/6-311++G\*\* level of theory was used to calculate the geometries, vibration frequencies, and rotation constants. The energy of the transition state was calculated using G2-like method RQCISD(T)/6-311++G\*\* + RMP2(full)/6-311++G(3df,2pd) – RMP2/6-311++G\*\*. The rate constants for both boat and chair conformers were calculated by the transition state theory, with Eckart tunneling correction. An average rate constant was then obtained by considering the composition of the chair and boat conformers. Rate constants of H-atom abstraction by OH radical were from experimental measurement and quantum chemistry calculation of Sivaramakrishnan and Michael [33]. The rate constants of H-atom abstraction by O radical were taken from the quantum chemistry calculation of Cohen and Westberg [34]; and the rate constants of H-atom abstraction by HO<sub>2</sub> radical were from experimental measurement of Handford-Styring and Walker [35]. The rate constants of H-atom abstraction by CH<sub>3</sub> radical were estimated from that of propane, and were increased by six times, considering the different degeneracy of the secondary C–Hs between cyclohexane and propane [31].

### 3.2.4 Decomposition and Isomerization of Cyclohexyl Radical

The H-atom abstraction of cyclohexane forms a cyclohexyl radical, which undergoes ring-opening isomerization to form 5-hexen-1-yl radical and β–C–H scission to form cyclohexene. Knepp et al. [36] and Sirjean et al. [37] calculated these two

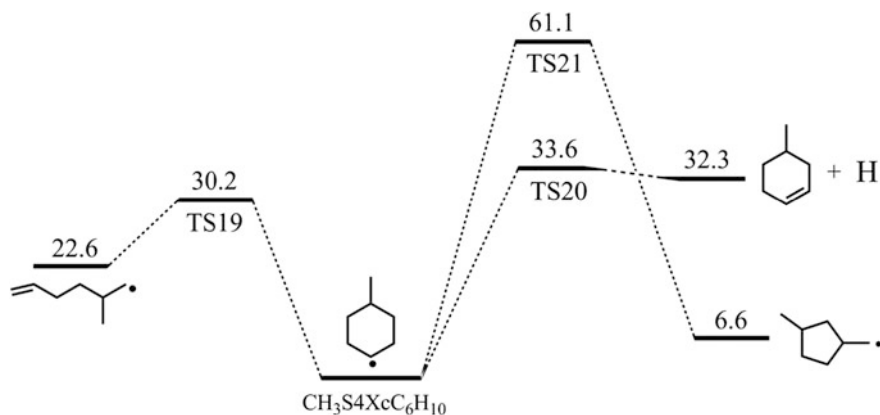




**Fig. 3.5** Potential energy surface of cyclohexyl radical decomposition and isomerization from Knepp et al. [36]. Reproduced from Ref. [36] with permission from the PCCP Owner Societies

pathways, Fig. 3.5 from calculations of Knepp et al. Compared to the  $\beta$ -C-H scission (35 kcal/mol) of cyclohexyl radical, the energy barrier of its ring-opening isomerization (31 kcal/mol) is  $\sim 4$  kcal/mol lower. Thus, the ring-opening isomerization pathway happens much more easily. Based on the potential energy surface, Knepp et al. calculated the high pressure limit rate constants of these two channels. Iwan et al. [38] also investigated the decomposition mechanism of cyclohexyl radical and 5-hexen-1-yl radical from single-pulse shock tube experiments; the rate constants at high pressure limit were also obtained.

The rate constants and branching ratios of these two channels are not only affected by temperature, but also by pressure. To simulate the 30, 150, and 760 Torr experiments in this work, their pressure dependent rate constants are needed. Here, pressure-dependent rate constants of 4-methyl-cyclohexyl radical dissociation and isomerization at 30, 150, 760, 7600, and 76,000 Torr [39] were used to estimate the rate constants of cyclohexyl radical. Figure 3.6 shows the calculated unimolecular decomposition pathways of 4-methyl-cyclohexyl radical at CBS-QB3 level of theory by Wang et al. [39]. The methyl group in 4-methyl-cyclohexyl radical is para to the radical site and has little effect on it. Thus, the decomposition and isomerization of 4-methyl-cyclohexyl radical is similar to those of the cyclohexyl radical;



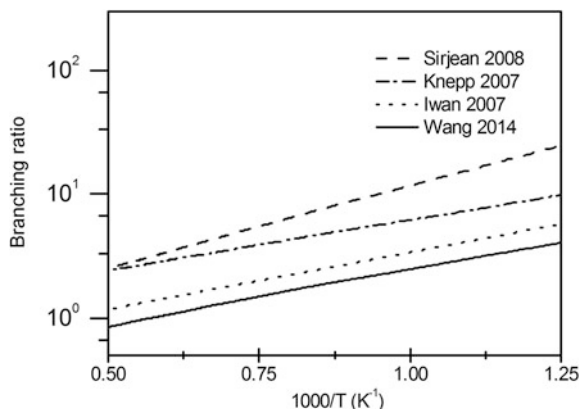
**Fig. 3.6** Potential energy surface of 4-methyl-cyclohexyl radical decomposition and isomerization from Wang et al. [39] (Unit: kcal/mol). Reprinted from Ref. [39], Copyright 2014, with permission from Elsevier

the rate constants from 4-methyl-cyclohexyl radical decomposition and isomerization could be used to estimate those of the cyclohexyl radical. The calculated energy barriers for the  $\beta$ -C-H scission and ring-opening isomerization of 4-methyl-cyclohexyl radical are 33.6 and 30.2 kcal/mol, respectively. Considering the uncertainty of the calculation method from Wang et al. [39] and Knepp et al. [36], the energy barriers for 4-methyl-cyclohexyl radical decomposition and isomerization are close to those of cyclohexyl radical. Here, we also compared the high pressure limit branching ratios of  $\beta$ -C-H scission and ring-opening isomerization of cyclohexyl radical by Knepp et al. [36], Sirjean et al. [37], and Iwan et al. [38], and a 4-methyl-cyclohexyl radical by Wang et al. [39], as shown in Fig. 3.7. The calculation by Sirjean et al. and Wang et al. is the upper and lower limit in the four dataset. However, the branching ratio calculated by Wang et al. is close to the experimental measurement by Iwan et al.

### 3.2.5 Decomposition and Isomerization of 5-Hexen-1-yl Radical

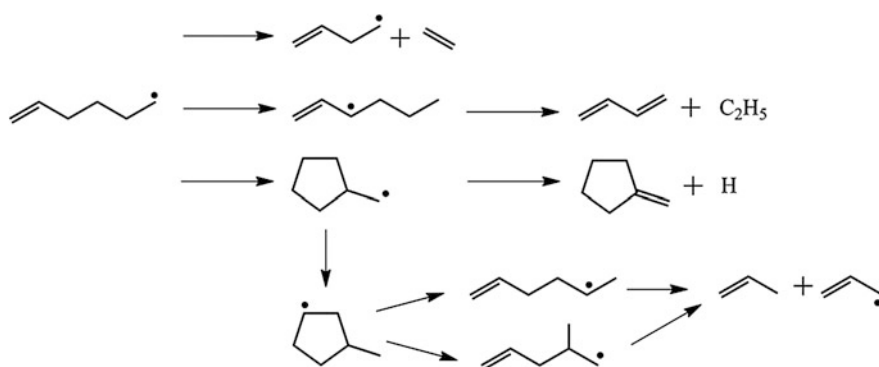
The ring-opening isomerization of cyclohexyl radical forms a 5-hexen-1-yl radical, whose decomposition then forms smaller intermediates. Compared to the large number of experimental and theoretical studies of alkyl radicals [40–43], reaction pathways of alkenyl radical and their rate constants have not been fully investigated. For alkenyl radicals, two types of reactions are commonly considered, intramolecular H-shift and  $\beta$ -scission. Gong et al. [44] calculated the reaction pathways of a 5-hexen-1-yl radical at CCSD(T)/cc-pVDZ level of theory. An important intramolecular H-shift pathway is a 1,4-H shift to abstract the allylic C-H. Another

**Fig. 3.7** Branching ratios of cyclohexyl radical decomposition and isomerization [36–38] at high pressure limit and those of 4-methyl-cyclohexyl radical at high pressure limit [39]. Reprinted from Ref. [39], Copyright 2014, with permission from Elsevier



pathway with a low energy barrier is the radical addition to the double bond leading to the cyclopentylmethyl radical.

In the shock tube pyrolysis experiment, Iwan et al. [38] studied the mechanism and rate constant for the decomposition of a 5-hexen-1-yl radical, which was produced from the decomposition of 1,8-nonadiene. The major products were ethylene and 1,3-butadiene; minor products were cyclohexene, propene, 1,3-pentadiene, and methylenecyclopentane. In their work, the pressure dependent rate constants for intramolecular H-shift and  $\beta$ -scission of 5-hexen-1-yl radical were estimated from rate rules in the literature and adjusted from the experimental branching ratios of the pyrolysis products. The reaction pathways for the 5-hexen-1-yl radical are presented in Fig. 3.8 and adopted in the kinetic model of this work. The rate constants for these pathways were adopted from Iwan et al. [38], with pressure dependence in Troe parameters.



**Fig. 3.8** Reaction mechanism for 5-hexen-1-yl radical decomposition and isomerization

### 3.2.6 Decomposition and Dehydrogenation of Cyclohexene

According to shock tube studies on decomposition of cyclohexene [45], the dissociation of cyclohexene leads to ethylene and 1,3-butadiene, i.e., retro-Diels-Alder reaction. The high pressure limit rate constant for this reaction was taken from the JetSurF 2.0 [28] model, while the pressure dependent rate constant at 30, 150, and 760 Torr were estimated in this work. The H-atom abstraction of the allylic C–H of cyclohexene by H atom, O atom, CH<sub>3</sub> radical, and OH radical forms 2-cyclohexen-1-yl radical; the rate constants for these reactions were estimated from the rate rules of H-atom abstraction reactions by Pitz et al. [46, 47]. On one hand, the ring-opening of 2-cyclohexen-1-yl radical by β–C–C scission leads to 3,5-hexadien-1-yl radical; its rate constants at 30 Torr were adopted from the quantum chemistry calculation using QRRK theory by Li et al. [22] while the high pressure limit rate constants were taken from the oxidation model of cyclohexene by Dayma et al. [48]; on the other hand, the β–C–H scission of 2-cyclohexen-1-yl radical forms 1,3-cyclohexadiene. The rate constants at 30 Torr were also adopted from the QRRK calculation by Li et al. [22], while the high pressure limit rate constants were taken from the quantum chemistry calculation of Sirjean et al. [49]. Similar to cyclohexene, the rate constants of H-atom abstraction reaction of 1,3-cyclohexadiene were estimated from the rate rules by Pitz et al. [46, 47]. Further β–C–H scission of 1,3-cyclohexadiene radical leads to benzene; the high pressure limit rate constants of this reaction were from the quantum chemistry calculation by Sirjean et al. [49] while those at 30 Torr were estimated in this work. In summary, the step-wise dehydrogenation of cyclohexene forms benzene, which is a more novel benzene formation route than that in *n*-alkane and branched alkanes.

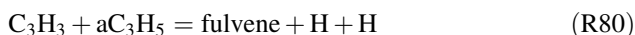
In addition to the sub-mechanism of cyclohexane, the reaction mechanism for aromatics pyrolysis and oxidation was also included in the model, to simulate the formation and consumption of benzene and other aromatics. The kinetic model for aromatics was developed from the pyrolysis of toluene, and further validated from the laminar premixed flame of toluene, ethylbenzene, and *n*-propylbenzene [50–53]. The first aromatic rings, such as benzene and benzyl radical, are considered to be the rate-limiting step to forming polycyclic aromatic hydrocarbons and soot. The reactions leading to benzene (A1) in the model include the C<sub>3</sub> + C<sub>3</sub>, C<sub>4</sub> + C<sub>2</sub>, and the isomerization of fulvene.





The rate constants for R69 and R70 were adopted from experimental and modeling studies of allene and propyne flame [54]. The original data were from the reaction mechanism and rate constant investigations of  $\text{C}_3\text{H}_3 + \text{C}_3\text{H}_3$  reactions by Miller and Klippenstein [55], and Georgievskii et al. [56]. Georgievskii et al., compared overall rate constants for the  $\text{C}_3\text{H}_3 + \text{C}_3\text{H}_3$  reactions with several experimental data in the literature, such as Scherer et al. [57] and Fernandes et al. [58]; good agreement between experiment and simulation was observed. The rate constants of  $\text{C}_3\text{H}_3 + \text{C}_3\text{H}_4$  (R71 and R72) were taken from the reaction mechanism of aromatics by D'Anna and Kent in their study of methane non-premixed flame [59], and the shock tube and theoretical study of allene pyrolysis by Wu and Kern [60]. The reactions of  $\text{C}_2\text{H}_2$  with  $\text{C}_4\text{H}_5$  are potential pathways for benzene and fulvene. Senosiain and Miller carefully investigated the reaction mechanism of  $\text{C}_2\text{H}_2$  with  $\text{C}_4\text{H}_5$ , and calculated their rate constants [61], which were adopted in this work for R73, R74, R76 and R77. The combination of  $\text{C}_4\text{H}_4$  with  $\text{C}_2\text{H}_3$  forms benzene and H atom (R75), whose rate constants were taken from the kinetic model by Lindstedt and Skevisused [62] in their simulation of laminar premixed acetylene flame. The isomerization of fulvene to benzene (R78) was studied by Miller and Klippenstein [55], and their calculated rate constants were adopted in this work. The H-atom assisted isomerization of fulvene to benzene (R79) was from Marinov et al. [63], who studied the fuel-rich laminar premixed flame of propane at atmospheric pressure.

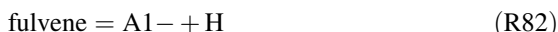
Another potential pathway for benzene in cyclohexane pyrolysis is the combination of  $\text{C}_3\text{H}_3 + a\text{C}_3\text{H}_5$  (R80). As discussed in Sects. 3.2.1 and 3.2.2, the isomerization of cyclohexane leads to 1-hexene, which largely dissociates into allyl radical ( $a\text{C}_3\text{H}_5$ ). The subsequent reactions of allyl radical form propargyl radical ( $\text{C}_3\text{H}_3$ ).



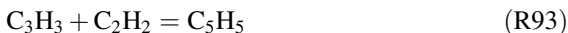
The overall rate constants of R80 originated from the work of Georgievskii et al. [56] and a subsequent, highly accurate analysis of the potential energy surface of

$aC_3H_5 + C_3H_3$  [64]. The rate constants of R80 were adopted from Hansen et al. [54] in the simulation of allene and propyne flame, which were at the high-limit [64, 65].

The unimolecular decomposition of benzene and fulvene forms phenyl radical (A1-, R81 and R82); rate constants for these reactions were taken from the investigations of Miller and Klippenstein [55]. The phenyl radical is also produced from the H-atom abstraction of benzene by H atom and/or OH radical (R83 and R84); the rate constants for these reactions were taken from experimental measurement or theoretical calculation in the literature [66, 67].



Cyclopentadiene ( $C_5H_6$ ) is also an important intermediate during cycloalkane combustion and its pyrolysis had been studied by Roy et al. [68], and by Bacskay and Mackie [69]. In this work, the sub-mechanism of this molecule is mainly adopted from USC Mech II [70], the work of Richter et al. [71], and Bacskay and Mackie [69]. Specifically, the unimolecular decomposition of cyclopentadiene (R90) forms a cyclopentadienyl radical ( $C_5H_5$ ) and its rate constants were taken from the JetSurF 2.0 model [28], with pressure dependence in Troe parameters. The rate constants of H-atom abstraction of cyclopentadiene by H atom (R91) and OH radical (R92) were adopted from the work of Moskaleva and Lin [72], and Zhong and Bozzelli [73]. The decomposition of cyclopentadienyl radical leads to  $C_3H_3$  and  $C_2H_2$ ; its reverse reaction (R93) was used in this work and the rate constants were from a quantum chemistry calculation by Moskaleva and Lin [72].



The core model, i.e.,  $H_2/CO-C_4$  mechanism is based on USC Mech II [70]. The sub-mechanism of 1-butene and 2-butene was updated from the work of Zhang et al. [74]. The sub-mechanism of 1,3-butadiene in USC Mech II is from Laskin et al. [75], which was validated by flow reactor pyrolysis and oxidation, shock tube pyrolysis, ignition delay times, and laminar flame speeds. The sub-mechanism of  $C_3H_5$  and  $C_3H_4$  is based on the work of USC Mech II [70], Kiefer et al. [7], and Miller et al. [76]. To simulate the experimental data obtained from various pressures, the pressure dependent rate constants for unimolecular decomposition

**Table 3.2** Nomenclature, molecular formula and structure of selected species in cyclohexane sub-mechanism

Formula	Nomenclature	Structure	Formula	Nomenclature	Structure
C <sub>3</sub> H <sub>3</sub>	C <sub>3</sub> H <sub>3</sub>	Propargyl	C <sub>3</sub> H <sub>4</sub>	aC <sub>3</sub> H <sub>4</sub>	Allene
C <sub>3</sub> H <sub>4</sub>	pC <sub>3</sub> H <sub>4</sub>	Propyne	C <sub>3</sub> H <sub>5</sub>	aC <sub>3</sub> H <sub>5</sub>	Allyl
C <sub>3</sub> H <sub>6</sub>	C <sub>3</sub> H <sub>6</sub>	Propene	C <sub>3</sub> H <sub>7</sub>	nC <sub>3</sub> H <sub>7</sub>	n-Propyl
C <sub>4</sub> H <sub>2</sub>	C <sub>4</sub> H <sub>2</sub>	Diacetylene	C <sub>4</sub> H <sub>4</sub>	C <sub>4</sub> H <sub>4</sub>	Vinylacetylene
C <sub>4</sub> H <sub>6</sub>	C <sub>4</sub> H <sub>6</sub>	1,3-butadiene	C <sub>4</sub> H <sub>7</sub>	C <sub>4</sub> H <sub>7</sub>	
C <sub>4</sub> H <sub>7</sub>	SAXC <sub>4</sub> H <sub>7</sub>		C <sub>4</sub> H <sub>8</sub>	C <sub>4</sub> H <sub>8</sub> -2	
C <sub>4</sub> H <sub>8</sub>	C <sub>4</sub> H <sub>8</sub> -1		C <sub>4</sub> H <sub>9</sub>	pC <sub>4</sub> H <sub>9</sub>	
C <sub>4</sub> H <sub>9</sub>	sC <sub>4</sub> H <sub>9</sub>		C <sub>5</sub> H <sub>7</sub>	lC <sub>5</sub> H <sub>7</sub>	
C <sub>6</sub> H <sub>9</sub>	PXC <sub>6</sub> H <sub>9</sub> -13		C <sub>6</sub> H <sub>11</sub>	PXC <sub>6</sub> H <sub>11</sub>	
C <sub>6</sub> H <sub>11</sub>	SXC <sub>6</sub> H <sub>11</sub>		C <sub>6</sub> H <sub>11</sub>	S2XC <sub>6</sub> H <sub>11</sub>	
C <sub>6</sub> H <sub>11</sub>	SAXC <sub>6</sub> H <sub>11</sub>		C <sub>6</sub> H <sub>11</sub>	PXCH <sub>2</sub> cC <sub>5</sub> H <sub>9</sub>	
C <sub>6</sub> H <sub>12</sub>	C <sub>6</sub> H <sub>12</sub> -1		C <sub>5</sub> H <sub>5</sub>	C <sub>5</sub> H <sub>5</sub>	
C <sub>5</sub> H <sub>6</sub>	C <sub>5</sub> H <sub>6</sub>		C <sub>6</sub> H <sub>6</sub>	A1	
C <sub>6</sub> H <sub>6</sub>	fulvene		C <sub>6</sub> H <sub>7</sub>	SAXcC <sub>6</sub> H <sub>7</sub>	
C <sub>6</sub> H <sub>8</sub>	cC <sub>6</sub> H <sub>8</sub> -13		C <sub>6</sub> H <sub>9</sub>	SAXcC <sub>6</sub> H <sub>9</sub>	
C <sub>6</sub> H <sub>10</sub>	cC <sub>6</sub> H <sub>10</sub>		C <sub>6</sub> H <sub>11</sub>	cC <sub>6</sub> H <sub>11</sub>	
C <sub>6</sub> H <sub>12</sub>	cC <sub>6</sub> H <sub>12</sub>				

reactions, e.g., the reactions for C<sub>3</sub>H<sub>5</sub> (aC<sub>3</sub>H<sub>5</sub>, CH<sub>3</sub>CCH<sub>2</sub>, and CH<sub>3</sub>CHCH) [77], C<sub>4</sub> species (C<sub>4</sub>H<sub>3</sub>, C<sub>4</sub>H<sub>4</sub>, C<sub>4</sub>H<sub>5</sub>, C<sub>4</sub>H<sub>6</sub>, and C<sub>4</sub>H<sub>7</sub>, etc.) [7, 78], and C<sub>5</sub>H<sub>5</sub> [72] were considered in Plog format. Table 3.1 shows the important reactions for the sub-mechanism of cyclohexane. The nomenclature, molecular formula and structure of the selected species are presented in Table 3.2.

### 3.3 Flow Reactor Pyrolysis of Cyclohexane

In this work, the flow reactor pyrolysis of cyclohexane at 30 and 760 Torr was investigated by SR-PI-MBMS. The initial composition of the gas mixture was 0.02 cyclohexane and 0.98 Argon. More than 30 pyrolysis products were detected, including radicals of CH<sub>3</sub>, C<sub>3</sub>H<sub>3</sub>, C<sub>3</sub>H<sub>5</sub>, and C<sub>5</sub>H<sub>5</sub>, and many isomers. The product distribution was similar under 30 and 760 Torr, except that radicals were not detected at 760 Torr; the short lifetime of radicals at higher pressure made their concentration lower than the detection limit of the mass spectrometer. The pressure of pyrolysis also affected the mole fraction of pyrolysis intermediates. For example, the mole fraction of 1-hexene in 760 Torr pyrolysis was 50% of that in 30 Torr pyrolysis; the mole fraction of allene, propyne, propene, 1-butene, and fulvene at 760 Torr was also lower than that at 30 Torr. The mole fraction of H<sub>2</sub>, CH<sub>4</sub>, C<sub>2</sub>H<sub>4</sub>,

$C_2H_2$ , and 1,3-butadiene was similar at both pressures, instead, more aromatics were produced in 760 Torr pyrolysis.

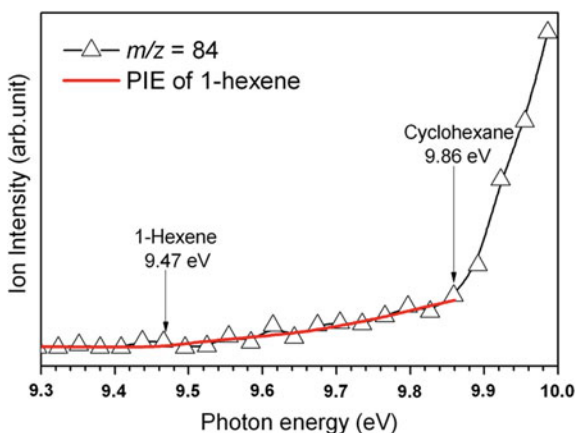
As noted in Sect. 3.1, several studies proposed that 1-hexene is the initial decomposition product of cyclohexane [4, 6]. In this work, the experiment identified 1-hexene from the photoionization efficiency spectra (PIE) of  $m/z$  84. Figure 3.9 shows two onsets for the PIE curve of  $m/z$  84. The onsets at 9.86 and 9.47 eV correspond to the ionization energies of cyclohexane and 1-hexene, respectively. The detection of 1-hexene is crucial to clarification of the initial decomposition of cyclohexane. The photon energy of 9.69 eV was selected in this work to ionize 1-hexene while ruling out interference from cyclohexane. However, this energy was only 0.2 eV higher than the ionization energy of 1-hexene, causing the signal to scatter due to the low photoionization cross sections.

The cyclohexane kinetic model was validated by the species speciation from 30 to 760 Torr pyrolysis. In the simulation, the plug flow reactor in the CHEMKIN-PRO software [95] was used; the measured temperature profiles and initial conditions of the pyrolysis experiment were used as input. The kinetics of cyclohexane pyrolysis at 30 and 760 Torr were discussed with the help of the model simulation.

### 3.3.1 Consumption of Cyclohexane

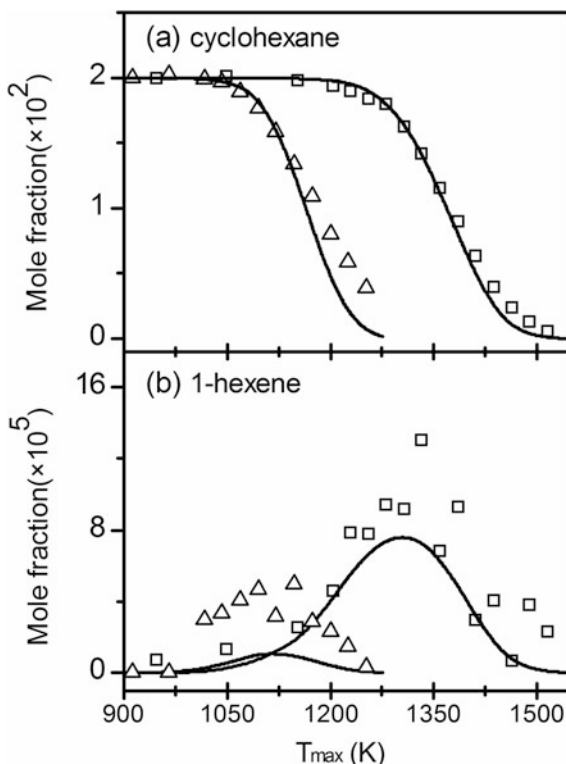
Figures 3.10 and 3.11 present the measured and simulated mole fraction profiles of cyclohexane, 1-hexene, and C0–C5 pyrolysis products. In general, the model captures well the experimental measurements at both pressures and provides insight to analyze the reaction pathways consuming the reactants and producing important products, and the pressure effect on the species speciation (Table 3.3). The reaction pathway analysis reveals that cyclohexane was consumed by isomerization to

**Fig. 3.9** Photoionization efficiency spectra of  $m/z$  84 measured during cyclohexane pyrolysis at 1440 K and 30 Torr. Symbol and line are experimental results; red line is photoionization efficiency spectra of 1-hexene by Yang et al. [88]. Reprinted from Ref. [84], Copyright 2012, with permission from Elsevier



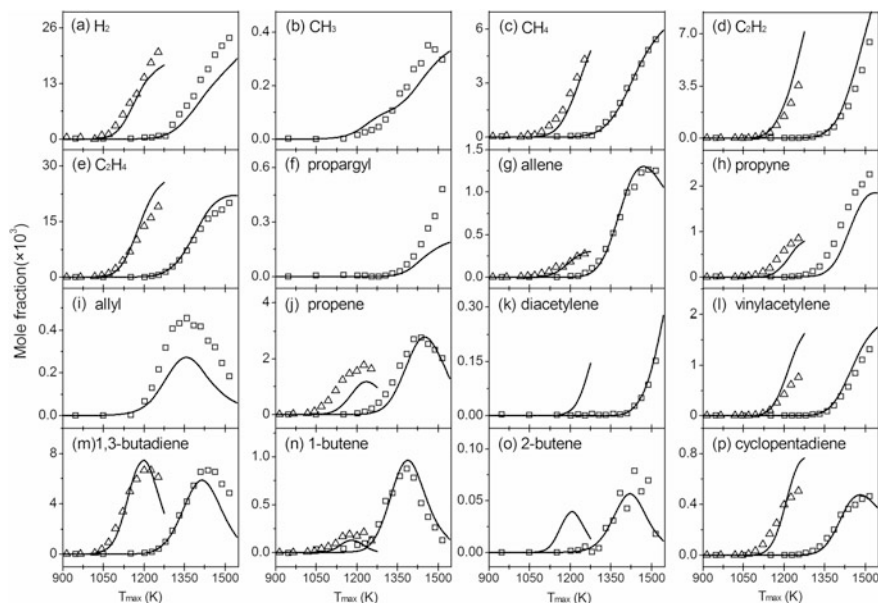


**Fig. 3.10** Mole fraction profiles of cyclohexane and 1-hexene. Symbols are experimental results, lines are simulation results. Square represents 30 Torr, triangle represents 760 Torr experiment



1-hexene and H-atom abstraction to cyclohexyl radical. The contribution of the isomerization pathway to 1-hexene was dominant at 30 Torr pyrolysis while that of H-atom abstraction reactions became more important at 760 Torr. This is the main reason for the higher mole fraction of 1-hexene at 30 Torr than at 760 Torr. Since the subsequent reactions of 1-hexene and cyclohexyl radical were similar at both 30 and 760 Torr, the following discussion focuses on the 30 Torr pyrolysis.

The reaction pathway analysis of cyclohexane pyrolysis at 1360 and 1520 K with 30 Torr pressure is shown in Fig. 3.12. Cyclohexane conversion was 50% at 1360 K, and nearly 100% at 1520 K. Different conversion ratios helped to analyze the effect of conversion ratio (temperature) on the reaction pathways. Analysis for 1360 K in Fig. 3.12a showed that the reaction of cyclohexane isomerizing to 1-hexene (R10) consumed 36% of cyclohexane, while the rest of cyclohexane was consumed via the H-atom abstraction reactions by H atom (R1) and  $\text{CH}_3$  radical (R2). The sensitivity analysis in Fig. 3.13 for cyclohexane reveals that R10 and R1 had large negative sensitivity coefficient at 1360 K, i.e., rate constants of R10 and R1 were increased, promoting cyclohexane consumption. The agreement between experiment and simulation for cyclohexane revealed that the rate constants of R10 and R1 used in this work were reasonable. In the discussions that follow, the values for the reaction flux analysis are for 1360 K, unless specific notes are given.



**Fig. 3.11** Mole fraction profiles of C0–C5 pyrolysis products in cyclohexane pyrolysis. Symbols are experimental results, lines are simulation results. Square represents 30 Torr, triangle represents 760 Torr experiment

1-hexene largely decomposes via the C–C bond scission to form allyl radical and *n*-propyl radical (R20, 93%). The C–C bond scission to form ethyl radical and 3-buten-1-yl radical (R21, 3%) is unimportant. The sensitivity analysis for 1-hexene in Fig. 3.14 shows that R10 had the largest positive sensitivity coefficient, while R20 had the largest negative coefficient at 1310 K. The conclusion from the sensitivity analysis is in accord with the reaction pathway analysis. Two decomposition pathways consume *n*-propyl radical, they are  $\beta$ -C–C scission, to form methyl radical and ethylene, and  $\beta$ -C–H scission, to form H atom and propylene. The former channel dominates *n*-propyl radical consumption ( $\sim 80\%$ ). For the allyl radical, the combination with CH<sub>3</sub> forming 1-butene (36%), the  $\beta$ -C–H scission forming allene (21%), and the combination with H atom forming propene (32%) are the three consumption pathways. The allyl radical was measured from the experiment (Fig. 3.11i); the initial formation temperature was  $\sim 1150$  K and the temperature corresponding to the maximum mole fraction was 1360 K. This observation is similar to that of 1-hexene.

The three consumption channels of allyl radical are the main formation pathways of 1-butene, allene, and propene. The  $\beta$ -C–H scission of *n*-propyl radical also contributes to the formation of propene. The H-atom-assisted isomerization, or direct isomerization of allene, leads to propyne, the main consumption pathway for allene. Propyne has initial formation temperature of  $\sim 50$  K higher than that of allene, but the former has a higher mole fraction. Generally, the model accurately

**Table 3.3** Information of species detected in cyclohexane pyrolysis at 30 and 760 Torr

m/z	Formula	Species	Energy (eV)	PICS (Mb)	X <sub>M</sub> (30 Torr)	X <sub>M</sub> (760 Torr)	References of PICS
2	H <sub>2</sub>	Hydrogen <sup>a</sup>	<sup>e</sup>	<sup>e</sup>	2.37E-2	2.03E-2	<sup>e</sup>
15	CH <sub>3</sub>	Methyl radical <sup>b</sup>	10.00	5.6	3.50E-4	–	[85]
16	CH <sub>4</sub>	Methane <sup>a</sup>	<sup>e</sup>	<sup>e</sup>	5.40E-3	4.30E-3	<sup>e</sup>
26	C <sub>2</sub> H <sub>2</sub>	Acetylene <sup>b</sup>	11.70	24.9	6.43E-3	3.54E-3	[86]
28	C <sub>2</sub> H <sub>4</sub>	Ethylene <sup>b</sup>	11.00	7.8	2.00E-2	1.91E-2	[86]
39	C <sub>3</sub> H <sub>3</sub>	Propargyl radical <sup>c</sup>	10.50	9.0	4.81E-4	–	[87]
40	C <sub>3</sub> H <sub>4</sub>	Allene <sup>b</sup>	10.00	5.7	1.26E-3	2.75E-4	[88]
		Propyne <sup>b</sup>	10.50	23.1	2.26E-3	8.42E-4	[86]
41	C <sub>3</sub> H <sub>5</sub>	Allyl radical <sup>c</sup>	9.50	5.6	4.55E-4	–	[89]
42	C <sub>3</sub> H <sub>6</sub>	Propene <sup>b</sup>	10.50	11.1	2.76E-3	1.77E-3	[90]
50	C <sub>4</sub> H <sub>2</sub>	Diacetylene <sup>b</sup>	10.50	23.8	1.52E-4	–	[86]
52	C <sub>4</sub> H <sub>4</sub>	Vinylacetylene <sup>b</sup>	10.50	22.8	1.32E-3	7.53E-4	[86]
54	C <sub>4</sub> H <sub>6</sub>	1,3-Butadiene <sup>b</sup>	11.00	24.2	6.64E-3	6.66E-3	<sup>f</sup>
56	C <sub>4</sub> H <sub>8</sub>	1-Butene <sup>b</sup>	10.50	10.0	8.73E-4	2.07E-4	[91]
		2-Butene <sup>c</sup>	9.50	5.2	7.84E-5	–	[92]
64	C <sub>5</sub> H <sub>4</sub>	1,3-Pentadiyne <sup>d</sup>	10.00	33.2	2.51E-5	–	[93]
65	C <sub>5</sub> H <sub>5</sub>	Cyclopentadienyl <sup>d</sup>	10.00	9.1	1.33E-4	–	est
66	C <sub>5</sub> H <sub>6</sub>	Cyclopentadiene <sup>d</sup>	9.50	15.7	4.61E-4	5.04E-4	[93]
68	C <sub>5</sub> H <sub>8</sub>	1,3-Pentadiene <sup>c</sup>	9.50	12.7	3.37E-4	1.70E-4	[88]
		Isoprene				6.95E-5	
70	C <sub>5</sub> H <sub>10</sub>	1-Pentene <sup>b</sup>	10.00	14.4	2.19E-5	–	[92]
76	C <sub>6</sub> H <sub>4</sub>	Benzyne <sup>d</sup>	9.50	27.0	2.27E-5	–	est
78	C <sub>6</sub> H <sub>6</sub>	Benzene <sup>b</sup>	9.50	11.05	6.34E-4	8.09E-4	[86]
		Fulvene <sup>d</sup>	8.86	3.9	9.72E-5	2.07E-5	est
80	C <sub>6</sub> H <sub>8</sub>	1,3-Cyclohexadiene <sup>b</sup>	9.50	18.3	1.27E-4	1.14E-4	[92]
82	C <sub>6</sub> H <sub>10</sub>	Cyclohexene <sup>b</sup>	9.50	8.9	2.13E-4	1.58E-4	[92]
		1,3-Hexadiene <sup>c</sup>	8.86	8.7	1.82E-5	1.43E-5	[92]
84	C <sub>6</sub> H <sub>12</sub>	Cyclohexane					[94]
		1-Hexene <sup>c</sup>	9.67	3.7	1.31E-4	4.94E-5	[88]
92	C <sub>7</sub> H <sub>8</sub>	Toluene <sup>b</sup>	9.50	18.5	7.70E-5	1.48E-4	[94]
102	C <sub>8</sub> H <sub>6</sub>	Phenylacetylene <sup>b</sup>	9.50	29.4	2.00E-5	1.84E-5	[94]
104	C <sub>8</sub> H <sub>8</sub>	Styrene <sup>b</sup>	9.50	26.3	4.34E-5	7.84E-5	[94]
106	C <sub>8</sub> H <sub>10</sub>	Ethylbenzene <sup>b</sup>	10.00	25.8	1.65E-5	1.93E-5	[94]
116	C <sub>9</sub> H <sub>8</sub>	Indene <sup>b</sup>	10.50	52.2	1.69E-5	4.66E-5	[94]

Reprinted from Ref. [84], Copyright 2012, with permission from Elsevier

<sup>a</sup>Uncertainty: ±10%

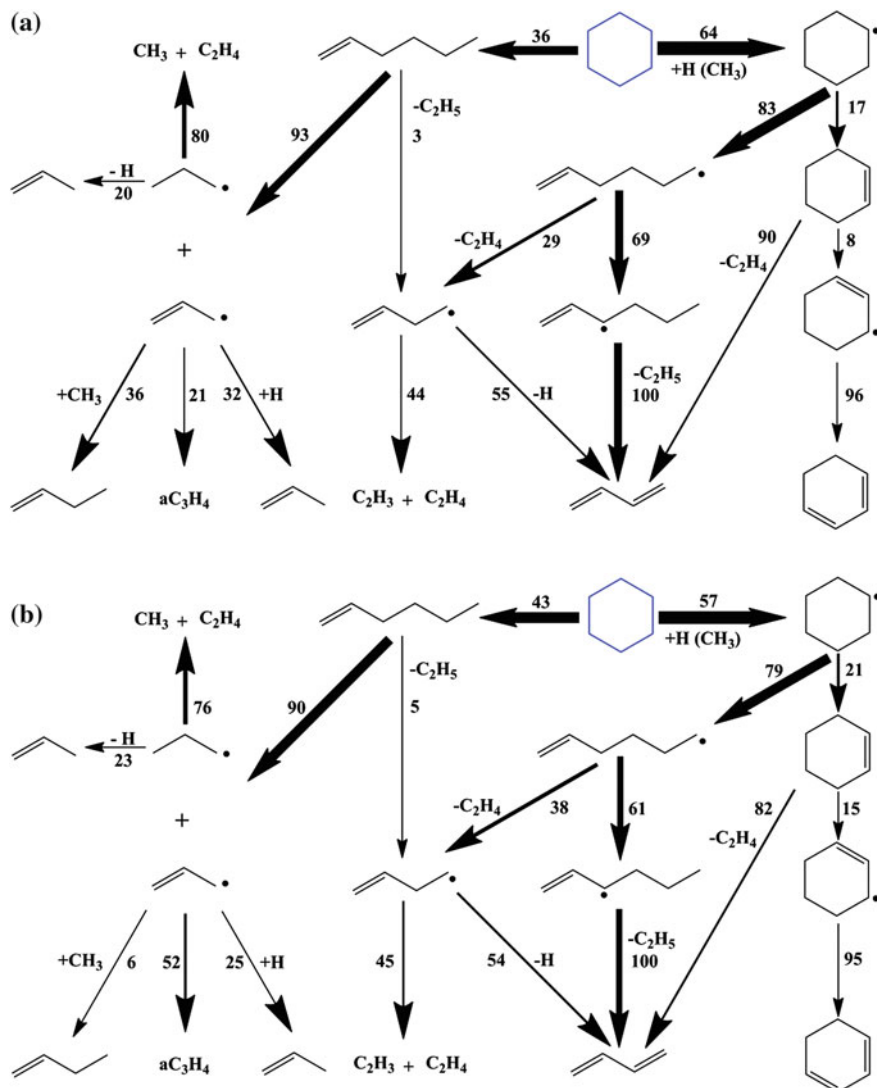
<sup>b</sup>Uncertainty: ±25%

<sup>c</sup>Uncertainty: ±50%

<sup>d</sup>Uncertainty: 2–3

<sup>e</sup>Direct calibration

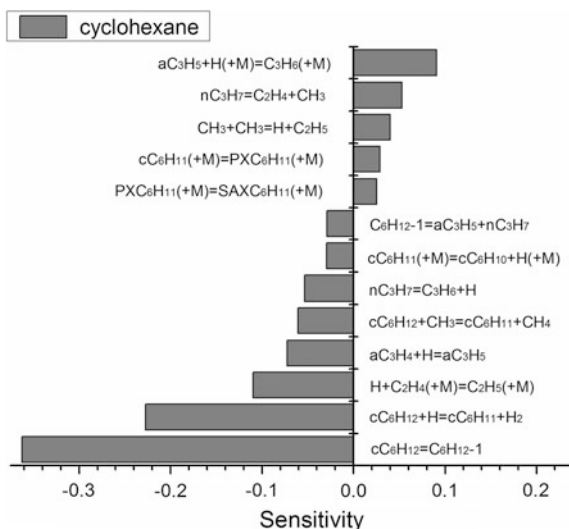
<sup>f</sup>Unpublished result



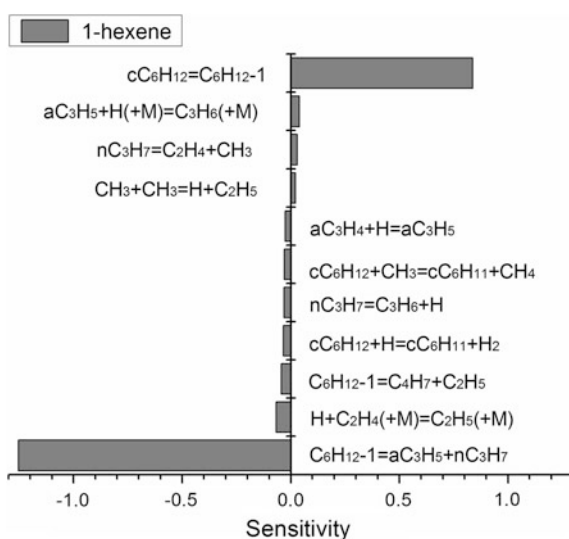
**Fig. 3.12** Reaction pathway analysis of cyclohexane pyrolysis at 30 Torr and temperature of 1360 K (a) and 1520 K (b). Numbers denote percentage of conversion. Reprinted from Ref. [84], Copyright 2012, with permission from Elsevier

predicts the mole fraction profiles of C<sub>3</sub> products (Fig. 3.11f–j) and 1-butene (Fig. 3.11n). As in the discussion above, C<sub>3</sub> products and 1-butene derive mainly from the dissociation of 1-hexene (R20) to allyl radical and *n*-propyl radical. Thus, the amount of 1-hexene affects the formation of C<sub>3</sub> products and 1-butene. At 760 Torr, the formation of 1-hexene is not important because the H-atom

**Fig. 3.13** Sensitivity analysis of cyclohexane pyrolysis at 30 Torr. Temperature is 1360 K. Only reactions with a sensitivity value larger than 0.025 are shown. Reprinted from Ref. [84], Copyright 2012, with permission from Elsevier



**Fig. 3.14** Sensitivity analysis of 1-hexene during cyclohexane pyrolysis at 30 Torr. Temperature is 1310 K. Only reactions with a sensitivity value larger than 0.02 are shown. Reprinted from Ref. [84], Copyright 2012, with permission from Elsevier



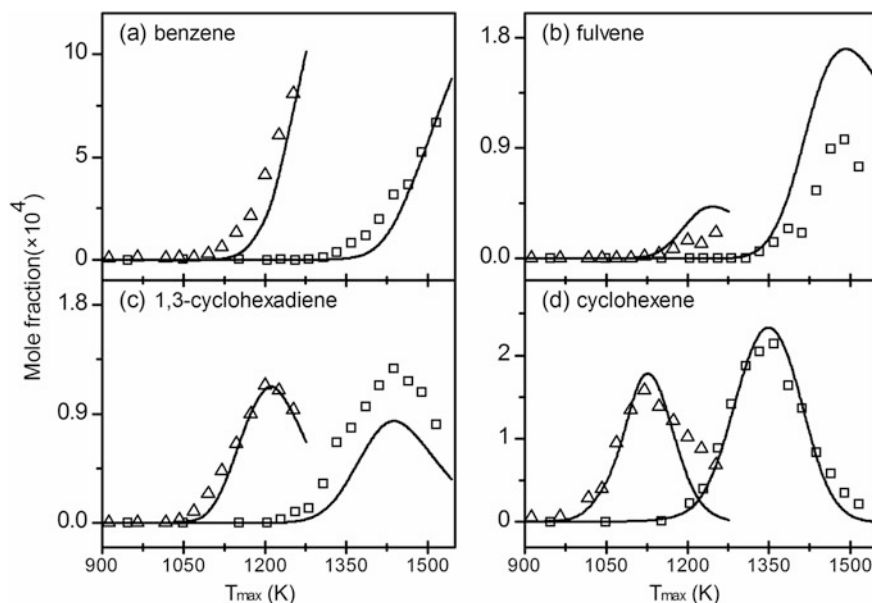
abstraction is the dominant consumption pathway for cyclohexane, leading to less formation of allyl radicals and *n*-propyl radicals, and subsequently less formation of C<sub>3</sub> products and 1-butene during the 760 Torr experiment.

The H-atom abstraction of cyclohexane forms a cyclohexyl radical, which is consumed by two dominant pathways, the ring-opening isomerization to 5-hexen-1-yl radical (R11, 83%) and β-C-H scission to cyclohexene (R12, 17%). For the 5-hexen-1-yl radical, the 1,4-H shift by way of the five-membered ring transition state (TS) leads to 1-hexen-3-yl radical (R46, 69%), which then produces

1,3-butadiene and ethyl radical (R48, 100%) via  $\beta$ -C-C scission. The  $\beta$ -C-C scission to ethylene and 3-buten-1-yl radical (R45, 29%) mainly consumes the residue 5-hexen-1-yl radical. The decomposition of 3-buten-1-yl radical leads to 1,3-butadiene and H atom via  $\beta$ -C-H scission (55%) and to ethylene and vinyl radical via  $\beta$ -C-C scission (44%).

As discussed in Sect. 3.2, the retro-Diels-Alder reaction of cyclohexene forms 1,3-butadiene and ethylene (R51, 90%). The C-H elimination and H-atom abstraction reactions of cyclohexene accounts for only 8% of its consumption, which produces a 2-cyclohexen-1-yl radical. The step-wise dehydrogenation of the 2-cyclohexen-1-yl radical leads to 1,3-cyclohexadiene, 1,3-cyclohexadienyl radical, and benzene. The order of formation for cyclohexene, 1,3-cyclohexadiene and benzene is in accord with the experimental measurement, i.e., the initial formation temperature is in the order of cyclohexene < 1,3-cyclohexadiene < benzene (Fig. 3.15). The model captures the mole fraction profiles of cyclohexene and 1,3-cyclohexadiene. It is noted that the formation of cyclohexene and 1,3-cyclohexadiene is sensitive to the retro-Diels-Alder reaction of cyclohexene (R51). The agreement between experiment and simulation for these species indicates that the rate constants for R51 are reasonable.

Figure 3.12b shows the rate of production analysis of cyclohexane at 1520 K. Compared to the results at 1360 K, more 1-hexene is produced at this higher temperature (43%). The subsequent reactions of 1-hexene and cyclohexyl radicals



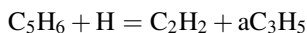
**Fig. 3.15** Mole fraction profiles of benzene, fulvene, 1,3-cyclohexadiene, and cyclohexene. Symbols are experimental measurement, lines are simulation results. Square represents 30 Torr, and triangle represents 760 Torr experiment

at 1520 K are similar to those predicted at 1360 K. The major differences are in the allyl radical, which is consumed by  $\beta$ -C-H scission to allene (52%), and the combination of the H atom (25%) to propene; the carbon flux to 1-butene is much less (6%).

Two reaction pathways consume cyclohexane under these experimental conditions (Fig. 3.12), i.e., cyclohexane  $\rightarrow$  1-hexene  $\rightarrow$  allyl + *n*-propyl radical, and cyclohexane  $\rightarrow$  cyclohexyl radical  $\rightarrow$  5-hexen-1-yl radical  $\rightarrow$  1-butadiene. Most carbon flux goes into 1,3-butadiene, and its prediction is in accordance with the experimental observations. For 1,3-butadiene, the dominant consumption pathway is the H-atom addition to the double bond, and then  $\beta$ -C-C scission to ethylene and vinyl radical. To a much lesser extent, the H-atom abstraction of 1,3-butadiene leads to *i*C<sub>4</sub>H<sub>5</sub> and *n*C<sub>4</sub>H<sub>5</sub>, which are the precursors of diacetylene and vinylacetylene (Fig. 3.11k, l).

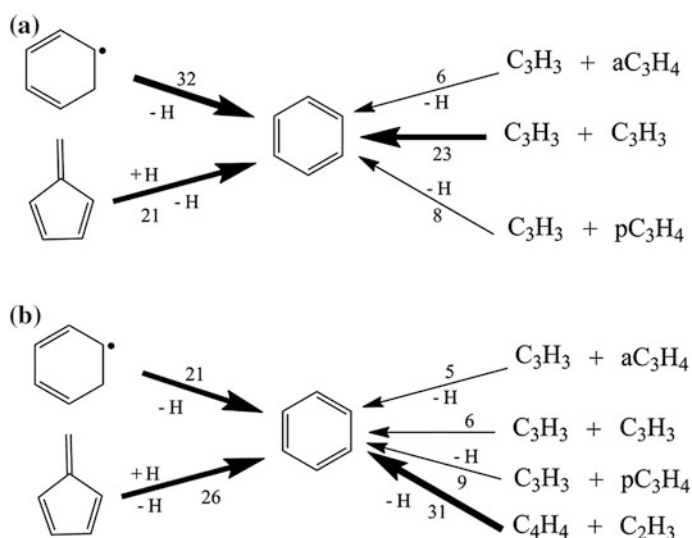
### 3.3.2 Formation and Consumption of Cyclopentadiene and Benzene

Two five-membered ring intermediates, cyclopentadiene and cyclopentadienyl radical, were measured. The model predicts well the mole fraction profiles of cyclopentadiene at both pressures (Fig. 3.11p). The reaction pathways analysis at 30 Torr shows that cyclopentadiene is formed via two channels,  $aC_3H_5 + C_2H_3 \rightarrow IC_5H_7 \rightarrow C_5H_6$  and  $iC_4H_5 + CH_3 \rightarrow IC_5H_7 \rightarrow C_5H_6$ . The H-atom abstraction of the cyclopentadiene forming cyclopentadienyl radical are the main consumption pathways for cyclopentadiene. This pathway is also the dominant precursor for the cyclopentadienyl radical, which then decomposes to C<sub>2</sub>H<sub>2</sub> and C<sub>3</sub>H<sub>3</sub>. Instead, the combination of acetylene and the allyl radical, and ethylene with 2-butylnyl radical, become dominant for cyclopentadiene formation when the pressure is at 760 Torr.



The first aromatic ring (benzene and benzyl radical) is commonly regarded as the rate-controlling step for polycyclic aromatic hydrocarbons and soot. The recent study by Hansen et al. revealed that the molecular structure affects benzene formation [96]. For example, their analysis shows that benzene derives mainly from the reactions of C3 + C3 during 1-hexene flame, because the dissociation of 1-hexene leads to the C3 products. This conclusion was later confirmed by the simulation of 1-hexene flame under the same conditions [97]. Instead, the step-wise dehydrogenation of cyclohexane is important for benzene formation, especially at the preheating zone of the cyclohexane flame.

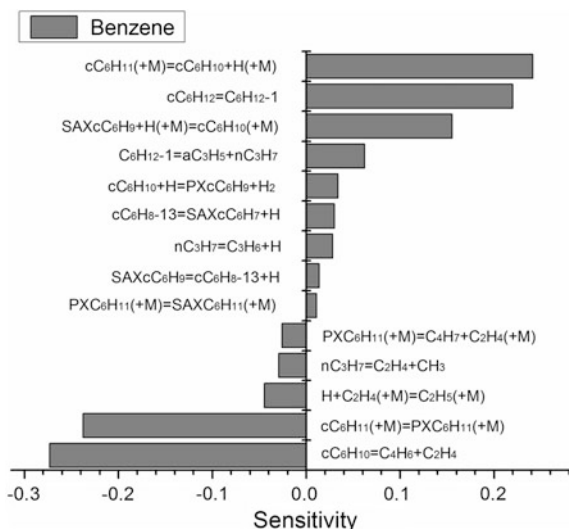
The cyclohexane pyrolysis in this work detected both 1-hexene and cyclohexyl radical, which makes the benzene formation pathways complex. Figure 3.16a presents the rate of production analysis of benzene at 30 Torr and 1520 K. Multiple sources for benzene are predicted, e.g., 32% benzene from the  $\beta$ -C-H scission of cyclohexadienyl radical (R65) and 21% from the isomerization of fulvene. Fulvene derives from the combination of C3 + C3 reactions:  $C_3H_3 + aC_3H_5$  (67%) and  $C_3H_3 + C_3H_3$  (31%). Benzene is also produced from the combination of smaller resonance-stabilized radicals, such as  $C_3H_3 + C_3H_3$ ,  $C_3H_3 + aC_3H_4$ , and  $C_3H_3 + pC_3H_4$ ; the dominant reaction is the self-recombination of  $C_3H_3$  (23%). Considering that fulvene is also produced from the C3 + C3 reactions, the contribution of C3 + C3 reactions to benzene is 58%. Similarly, benzene is produced from multiple channels during cyclohexane pyrolysis at 760 Torr. One distinct difference is that the contribution from the combination of  $C_4H_4$  and  $C_2H_3$  is more evident. As shown in Fig. 3.15, the model prediction for benzene and fulvene is satisfactory, considering the uncertainty of their mole fraction. The sensitivity analysis for benzene at 30 Torr and 1520 K in Fig. 3.17 shows that the H-elimination of cyclohexadienyl radical has the largest positive sensitive coefficient, while its ring-opening isomerization and the retro Diels-Alder reaction of cyclohexene have a large negative sensitive coefficient. The sensitivity analysis is in accord with the reaction pathway analysis. Furthermore, the isomerization of cyclohexane to 1-hexene has a notable effect on benzene formation, indicating the importance of C3 + C3 reactions, since most of the C3 species are produced from 1-hexene.



**Fig. 3.16** Reaction pathway analysis for benzene during cyclohexane pyrolysis at **a** 30 Torr, 1520 K and **b** 760 Torr, 1250 K. Numbers show contribution of each reaction. Reprinted from Ref. [84], Copyright 2012, with permission from Elsevier



**Fig. 3.17** Sensitivity analysis of benzene during cyclohexane pyrolysis at 30 Torr and 1520 K. Reactions with sensitivity value larger than 0.01 are presented. Reprinted from Ref. [84], Copyright 2012, with permission from Elsevier



### 3.4 Laminar Premixed Flame of Cyclohexane

Previous work has investigated the flame of cyclohexane. McEnally and Pfefferl, added 2000 ppm of cyclohexane, cyclohexene, 1,3-cyclohexadiene, and benzene to the non-premixed methane flame. The mole fraction of C1–C12 hydrocarbons, soot, primary combustion products and flame temperature were then measured [23]. Ciajolo et al. [20] investigated the fuel-rich laminar premixed flame of cyclohexane at atmospheric pressure and developed the combustion model for cyclohexane. The model was validated by the major and minor species and soot yield. Law et al. and Li et al. investigated the low pressure premixed flame of cyclohexane with equivalence ratio of 1.0 and 2.0 [21, 22]. More than 40 intermediates during fuel-rich flame were analyzed using the SR-PI-MBMS method. A kinetic model was developed to predict the flame chemistry of cyclohexane at low pressure, with a focus on benzene formation.

The fuel-rich cyclohexane flame of Li et al. [22] was adopted to examine the kinetic model developed in this work. The cyclohexane/ $O_2$ /30%Ar flame ( $\phi = 2.0$ ) was stabilized on a McKenna burner with a diameter of 60 mm. Flame chamber pressure was controlled at 30 Torr. The velocity of the unburned gas mixture at 298 K was 50 cm/s, which corresponded to mass flow rate of  $3.28 \times 10^{-3}$  g/cm<sup>2</sup>/s. The flame temperature, without the interference of a sampling cone, was measured by the OH laser-induced fluorescence near 306 nm. Burner surface temperature was estimated to be 400 K. The uncertainty of the flame temperature at the post flame zone was estimated to be  $\pm 150$  K, while temperature uncertainty near the burner surface was probably even higher.

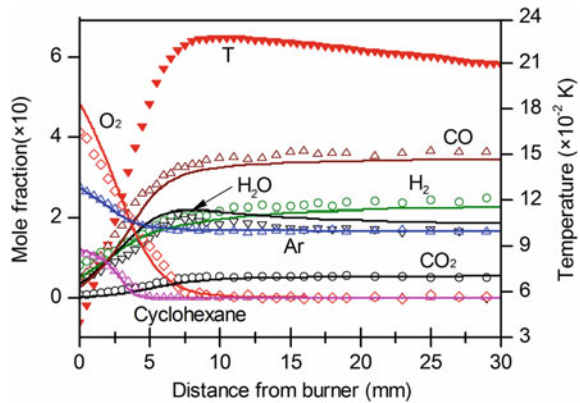
The simulation was conducted using the PREMIX module of CHEMKIN-PRO software [95] under experimental conditions; the measured temperature profile was the boundary condition. Thermal diffusion was considered in the simulation, which

is important for low-molecular weight species (e.g.,  $H_2$ ). For the experiment, mix-averaged transport was adopted (it is less accurate than the multicomponent transport, but normally accelerates calculation and eases convergence).

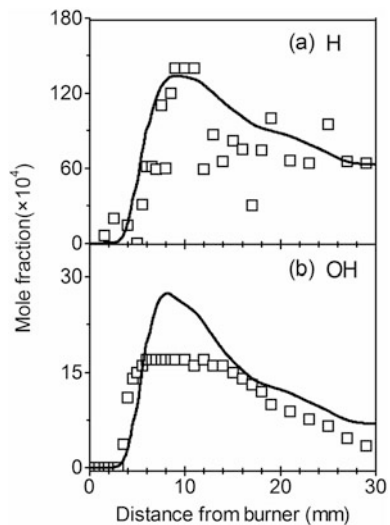
The comparison of experimental and simulated mole fraction profiles of Ar, reactants (i.e., cyclohexane and  $O_2$ ) and major combustion products ( $H_2O$ ,  $CO_2$ ,  $CO$ ,  $H_2$ ) is shown in Fig. 3.18. Cyclohexane was completely consumed earlier than  $O_2$ , which was further consumed in reactions with the flame intermediates. The fuel-rich flame also resulted in large amounts of  $CO$  and  $H_2$ . The cyclohexane model predicted well the consumption of the reactants, formation of the major combustion products and the mole expansion of the flame (i.e., the Ar profile).

H atom and OH radical are important intermediates during low pressure flames. The mole fraction profiles of these two reactive species were measured by Li et al. [22]. As shown in Fig. 3.19, the maximum mole fraction of H atom is a magnitude

**Fig. 3.18** Experimental (symbols) [22] and simulated (lines) mole fraction profiles of reactants, Ar, and major combustion products during fuel-rich laminar premixed flame of cyclohexane. The equivalence ratio is 2.0 and the pressure of 30 Torr



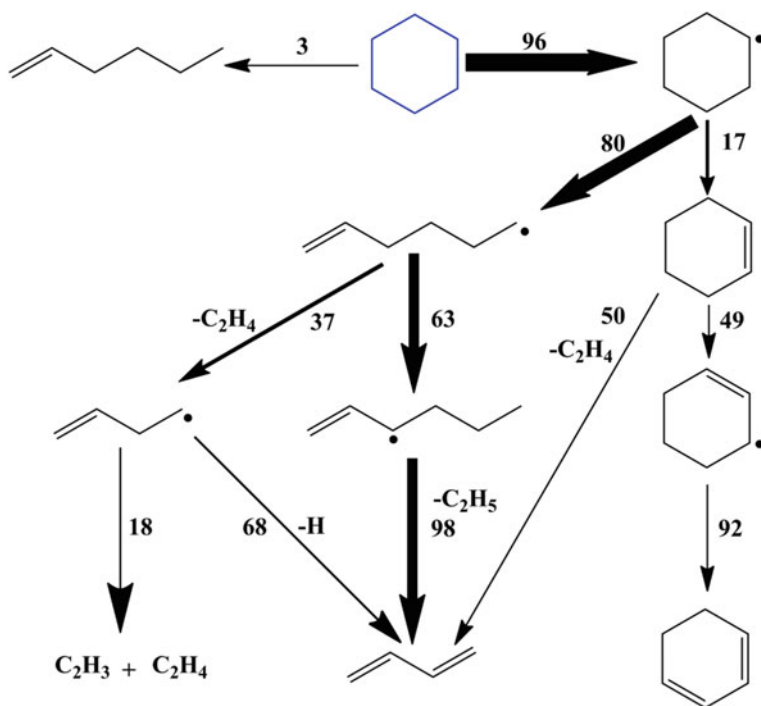
**Fig. 3.19** Experimental (symbols) [22] simulated (lines) mole fraction profiles of H atom and OH radical during fuel-rich laminar premixed flame of cyclohexane with equivalence ratio of 2.0 and pressure of 30 Torr



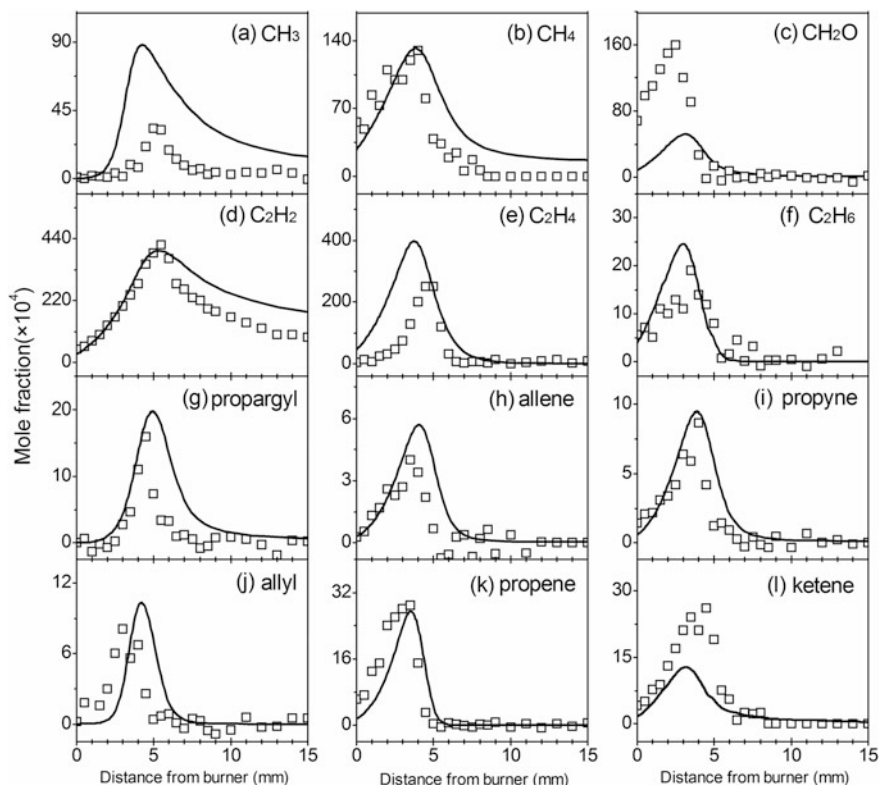
higher than that of the OH radical because of the fuel-rich environment. Although the measured mole fraction of the H atom is scattered, the simulation captures its profile and maximum value. The prediction for OH radical was also satisfactory.

As shown in Fig. 3.20, the rate of production analysis was performed based on the simulation. The consumption of cyclohexane was dominated by the H-atom abstraction by H atom, O atom, and OH radical (H atom, 62%, OH radical, 20%, and O atom, 12%), which differed from the pyrolysis of cyclohexane at 30 Torr. Consequently, 1-hexene was a minor product in the studied flame and was not detected in the experiment [22]. Figures 3.21 and 3.22 present experimental and simulated mole fractions of the C1–C3 intermediates and C4–C6 intermediates, respectively. Apart from the smaller intermediates CH<sub>4</sub>, CH<sub>2</sub>O, C<sub>2</sub>H<sub>2</sub>, and C<sub>2</sub>H<sub>4</sub>, 1,3-butadiene had the highest mole fraction, in agreement with the observation in cyclohexane pyrolysis.

Like the pyrolysis experiment, the dominant consumption pathway for a cyclohexyl radical is ring opening isomerization to form a 5-hexen-1-yl radical, which leads to 1,3-butadiene, vinyl radical, and ethylene. 1,3-butadiene is largely



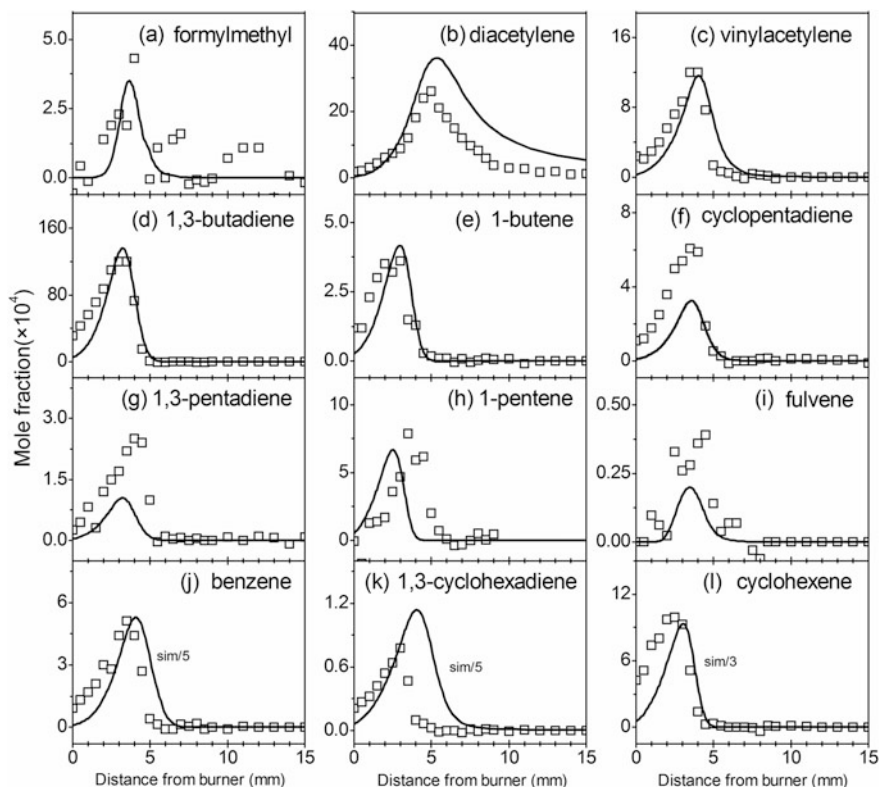
**Fig. 3.20** Production rate analysis of cyclohexane consumption during fuel-rich laminar premixed flame of cyclohexane with equivalence ratio of 2.0 and pressure of 30 Torr. Numbers denote conversion percentage



**Fig. 3.21** Experimental (symbols) [22] and simulated (lines) mole fraction profiles of C1–C3 intermediates during fuel-rich laminar premixed flame of cyclohexane. The equivalence ratio is 2.0 and the pressure of 30 Torr

consumed when it reacts with the H atom, its subsequent decomposition produces vinyl radical and ethylene ( $C_4H_6 + H = C_2H_3 + C_2H_4$ ). This pathway is also an important route for ethylene. Two more important pathways for ethylene are the  $\beta$ -C–C scission of 5-hexen-1-yl radical and  $\beta$ -C–H scission of ethyl radical. The vinyl radical derives mainly from the reaction of 1,3-butadiene with H atom, and its  $\beta$ -C–H scission is the main source for acetylene. The reaction flux analysis explains the large formation of 1,3-butadiene, ethylene, and acetylene in the fuel-rich cyclohexane flame.

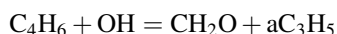
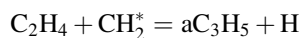
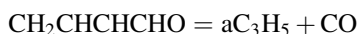
In addition to 1,3-butadiene, other C4 intermediates (diacetylene and vinylacetylene) also have high mole fraction (Fig. 3.22b, c). In the flow reactor pyrolysis of cyclohexane at 30 Torr, these two intermediates derive mainly from the H-elimination of  $C_4H_5$  radicals, which are produced from the H-atom abstraction of 1,3-butadiene. In the flame studied, this pathway is also important for diacetylene and vinylacetylene. Moreover, the combination of smaller radicals, e.g.,



**Fig. 3.22** Experimental (symbols) [22] and simulated (lines) mole fraction profiles of  $\text{CH}_2\text{CHO}$  and C4–C6 intermediates during fuel-rich laminar premixed flame of cyclohexane with equivalence ratio of 2.0 and pressure of 30 Torr

$\text{C}_3\text{H}_2 + \text{CH}_3 = \text{C}_4\text{H}_4 + \text{H}$ ,  $\text{C}_3\text{H}_3 + \text{CH}_2 = \text{C}_4\text{H}_4 + \text{H}$ , and  $\text{C}_3\text{H}_3 + \text{HCCO} = \text{C}_4\text{H}_4 + \text{CO}$  becomes important for vinylacetylene in the flame studied.

In cyclohexane pyrolysis at 30 Torr, the C3 intermediates are produced from the dissociation of 1-hexene and the subsequent reactions. However, the mole fraction of 1-hexene is very low in the studied flame and other pathways contribute to the production of C3 intermediates. For example, the reaction pathway analysis shows that an allyl radical is formed via the following reactions:



For  $\text{CH}_2\text{CHCHCHO}$ , the reaction derives from the oxidation of 1,3-butadiene and the  $n\text{C}_4\text{H}_5$  radical. Subsequent reactions of allyl radical are the main precursors for allene and propene.

Fulvene was measured in the cyclohexane flame with a low mole fraction (Fig. 3.22i). The reaction of  $\text{C}_3\text{H}_3$  with  $a\text{C}_3\text{H}_5$  (R80), and reactions between  $\text{C}_4\text{H}_5$  and  $\text{C}_2\text{H}_2$  (R76 and R77) also contribute to the formation of fulvene.

Another important C6 cyclic compound is cyclohexene, which is produced from the H-elimination of cyclohexyl radical, as shown in Fig. 3.20. However, the prediction overestimates the production of cyclohexene. In the model, only the unimolecular decomposition pathways of cyclohexyl radical are considered; the absence of oxidation pathways may be the reason for cyclohexene over-prediction. The abundance of radicals and atoms in the low pressure flame accelerates the H-atom abstraction of cyclohexene, promoting the formation of 1,3-cyclohexadiene and benzene. Like cyclohexene, the model over-predicts the production of 1,3-cyclohexadiene and benzene. It was noted that cyclohexene, 1,3-cyclohexadiene, and benzene were predicted satisfactorily in the cyclohexane flow reactor pyrolysis. The discrepancy in flame for these three intermediates may be caused by the absence of oxidation and/or other ring-opening pathways for cyclohexyl radical, 2-cyclohexen-1-yl radical, and cyclohexadienyl radical. Further studies on the reaction pathways of these radicals are needed.

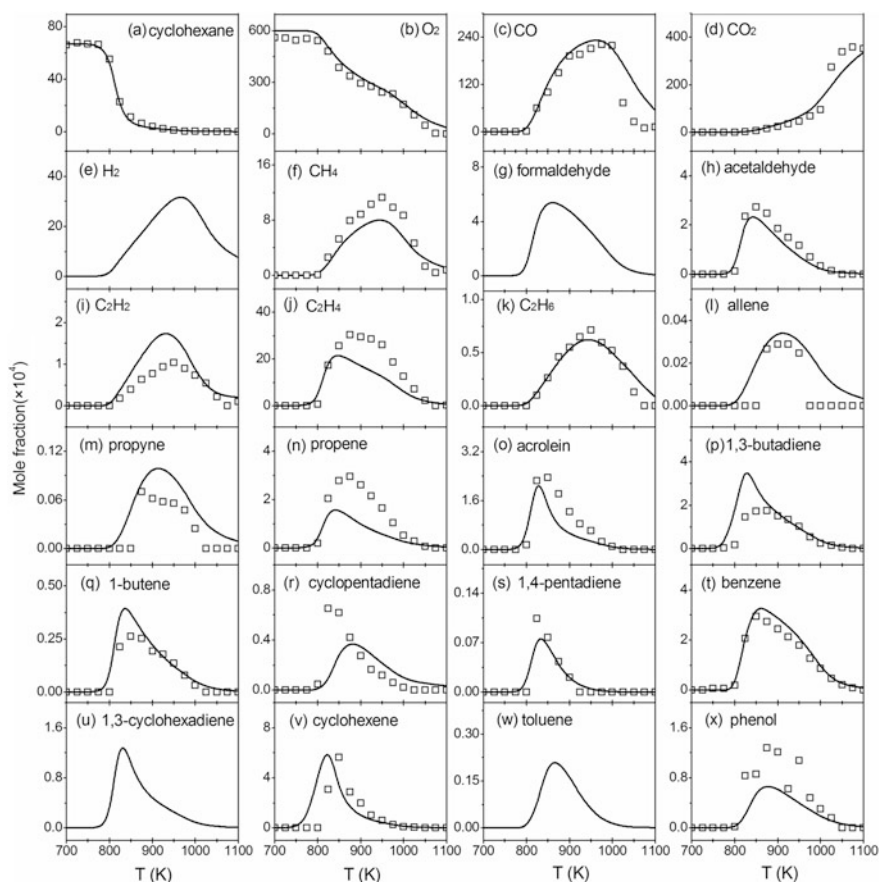
### 3.5 JSR Oxidation of Cyclohexane

Previous studies have reported the JSR oxidation of cyclohexane. In 1998, Viosin et al. investigated the JSR oxidation of cyclohexane in the temperature range of 750–1100 K, at 10 atm, with equivalence ratio of 0.5, 1.0, and 1.5, and residence time of 0.5 s [8]. Later, El-Bakali studied the JSR oxidation of cyclohexane at pressures of 1, 2, and 10 atm, temperatures between 850 and 1100 K, an equivalence ratio of 1.0, and residence time of 0.07 s [9]. Serinyel et al. [10] recently studied the low and intermediate temperature oxidation of cyclohexane in a JSR (500–1100 K), which covers the negative temperature coefficient zone. Equivalence ratios were 0.5, 1.0, and 2.0 and the residence time was 2 s. The measured high temperature oxidation products included  $\text{CO}$ ,  $\text{CO}_2$ ,  $\text{H}_2$ ,  $\text{CH}_2\text{O}$ ,  $\text{CH}_3\text{CHO}$ ,  $\text{C}_2\text{H}_3\text{CHO}$ ,  $\text{CH}_3\text{CH}_2\text{CHO}$ ,  $\text{CH}_4$ ,  $\text{C}_2\text{H}_2$ ,  $\text{C}_2\text{H}_4$ ,  $\text{C}_2\text{H}_6$ ,  $a\text{C}_3\text{H}_4$ ,  $p\text{C}_3\text{H}_4$ ,  $\text{C}_3\text{H}_6$ ,  $\text{C}_3\text{H}_8$ , 1,3-butadiene, 1-butene, 2-butene, cyclopentene, cyclopentadiene, 1,3-cyclohexadiene, cyclohexene, benzene, toluene, and phenol. The convergence of these species under different pressures, equivalence ratios and temperatures is valuable for interpreting the high-temperature oxidation mechanism of cyclohexane, as well as validating the kinetic model.

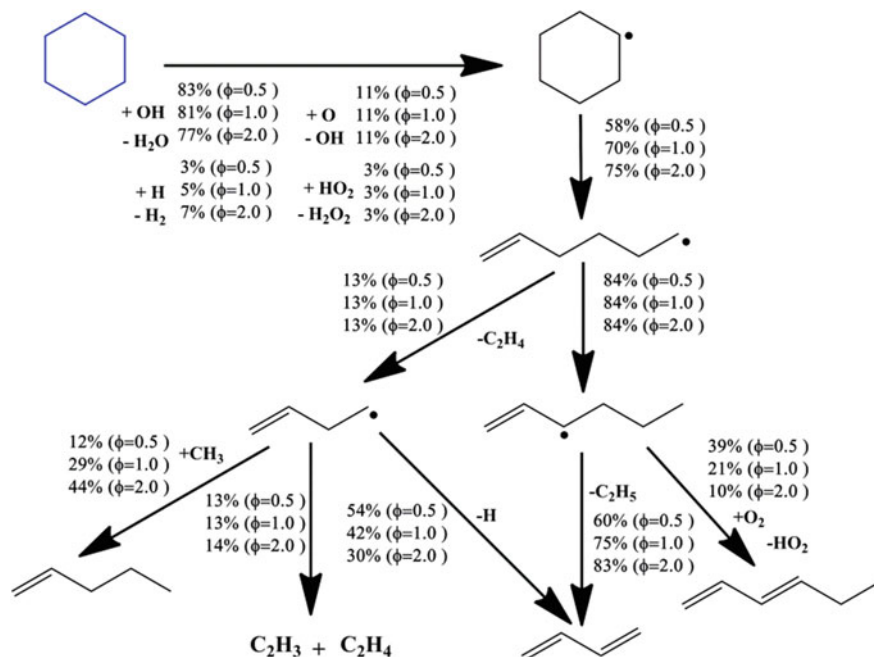
In this work, the experimental data from Serinyel et al. [10] at 1.05 atm and Viosin et al. [8] at 10 atm were adopted to examine the cyclohexane kinetic model. The Perfectly Stirred Reactor Module of the CHEMKIN-PRO software [95], with transient solver, was used in the simulation. Input was the same as the respective

experiment. In Serinyel et al. experiment, the volume of the JSR is  $85 \text{ cm}^3$ , pressure is 1.05 atm, the bath gas is He, the residence time is 2 s. The end time was set as 30 s; In experiments by Viosin et al., the volume of the JSR is  $29.5 \text{ cm}^3$ , pressure is 10 atm, bath gas is  $\text{N}_2$ , and residence time was 0.5 s. In the simulation, the end time was set as 20 s. In this chapter, the comparison between experiment and simulation for the oxidation at stoichiometric condition is presented. The results for other conditions (1.05 atm,  $\phi = 0.5$  and 2.0; 10 atm,  $\phi = 0.5$  and 1.5) are presented in Appendix A.

The experimental and simulated mole fractions of cyclohexane,  $\text{O}_2$ , major products ( $\text{CO}$  and  $\text{CO}_2$ ), and the C1–C7 intermediates for cyclohexane oxidation at 1.05 atm and equivalence ratio of 1.0 are presented in Fig. 3.23.  $\text{H}_2$  and  $\text{H}_2\text{O}$  were not detected because of the limitation of experimental diagnostics. The model



**Fig. 3.23** Experimental (symbols) [10] and simulated (lines) mole fraction profiles of reactants, major products, and C1–C7 intermediates during cyclohexane oxidation with equivalence ratio of 1.0 and pressure of 1.05 atm



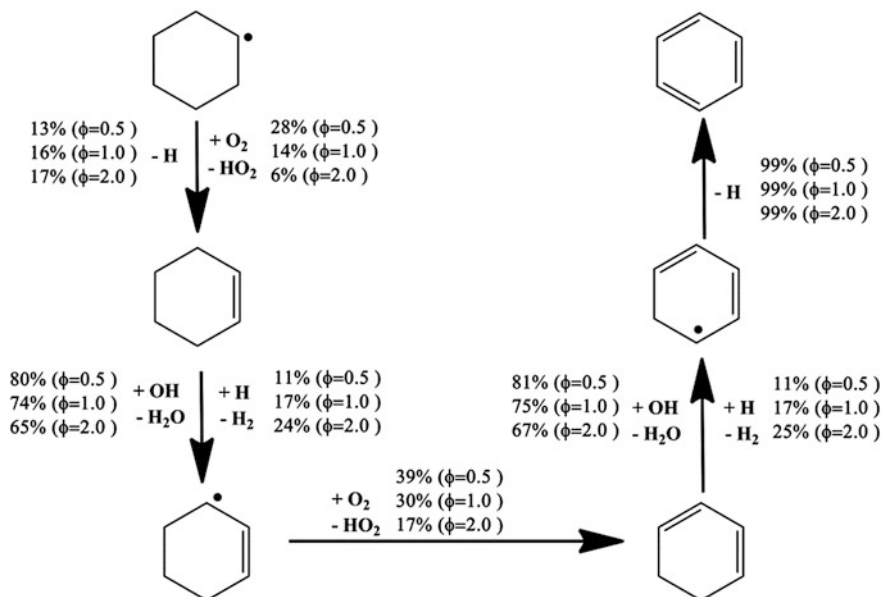
**Fig. 3.24** Rate of production analysis of cyclohexane consumption and ring-opening isomerization of cyclohexyl radical during JSR oxidation of cyclohexane at 1.05 atm and 800 K. Numbers denote conversion percentage

predictions for these species with the three equivalences were satisfactory (Figs. 3.23, A.1 and A.2 in Appendix A). The good agreement between experiment and simulation was the foundation for analysis of cyclohexane consumption and the formation of oxidation intermediates (Figs. 3.24 and 3.25).

Under an oxidation environment, cyclohexane was largely consumed by H-atom abstraction pathways (especially by OH radicals), to form a cyclohexyl radical (Fig. 3.24). The contribution of H-atom abstraction by OH radical decreased with the increase of the equivalence ratio. The dominant route for cyclohexyl radical consumption was ring-opening isomerization to form 5-hexen-1-yl radical; the contribution of this pathway increased with the increase of the equivalence ratio.

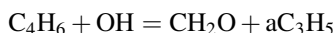
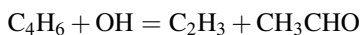
A 5-hexen-1-yl radical undergoes intramolecular H-shift to 1-hexen-3-yl radical and  $\beta$ -C-C scission to 3-buten-1-yl radical and ethylene. Since these pathways do not interact with O<sub>2</sub>, their branching ratio is not affected by the equivalence ratio. The consumption pathways for 1-hexen-3-yl radical are  $\beta$ -C-C scission to 1,3-butadiene and ethyl radical, and reaction with O<sub>2</sub> to form 1,3-hexadiene. The branching ratio for these two pathways is affected by the equivalence ratio, e.g., with the increase of O<sub>2</sub> mole fraction, the contribution of the oxidation pathway increases. There are three pathways for 3-buten-1-yl radical,  $\beta$ -C-H scission to 1,3-butadiene,  $\beta$ -C-C scission to ethylene and vinyl radical, and the combination





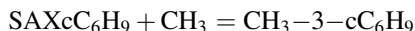
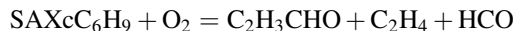
**Fig. 3.25** Reaction pathways from cyclohexyl radical to benzene during JSR oxidation of cyclohexane at 1.05 atm and 800 K. Numbers denote conversion percentage

with  $CH_3$  radical to 1-pentene. Like the pyrolysis and flame of cyclohexane, 1,3-butadiene is also an important intermediate during cyclohexane oxidation (Fig. 3.23p). The consumption of 1,3-butadiene forms the C1–C3 intermediates under the three equivalence ratios.



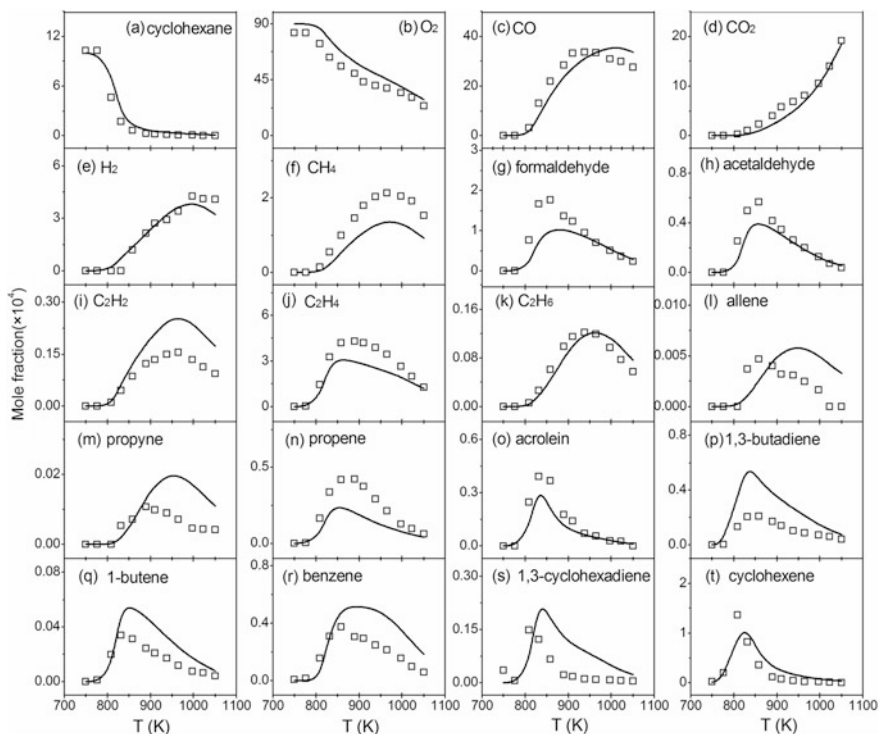
The reaction pathway analysis reveals that 1-pentene and 1,3-hexadiene are produced from cyclohexane oxidation. However, these two intermediates were not detected during the experiment.

On the other hand, the H-elimination of cyclohexyl radical and the H-atom abstraction by  $O_2$  leads to cyclohexene, as shown in Fig. 3.25. The H-atom abstraction pathway is affected by the equivalence ratio because of the mole fraction change of  $O_2$ . Cyclohexene is consumed by H-atom abstraction of OH radical and H atom to produce 2-cyclohexen-1-yl radical, while the retro-Diels-Alder reaction is negligible. For 2-cyclohexen-1-yl radical (apart from the H-atom abstraction by  $O_2$  to produce 1,3-cyclohexadiene in Fig. 3.25), two other important pathways are shown below: reaction with  $O_2$  to smaller intermediates and the combination with  $CH_3$  radical to 3-methylcyclohexene. The contribution of the second pathway is more important at higher equivalence ratios.



The H-atom abstraction of 1,3-cyclohexadiene forms cyclohexadienyl radical, which then undergoes H-elimination, forming benzene. Figure 3.25 shows that the reaction pathways from cyclohexyl radical, cyclohexene, 2-cyclohexen-1-yl radical, 1,3-cyclohexadiene, and cyclohexadienyl radical are the dominant source for benzene (>98%). Compared to cyclohexane pyrolysis, the combination of resonance-stabilized radicals is negligible for benzene in JSR oxidation of cyclohexane.

Figure 3.26 shows the mole fraction profiles of cyclohexane, O<sub>2</sub>, major products (CO and CO<sub>2</sub>), and C1–C6 intermediates, during the JSR oxidation of cyclohexane at equivalence ratio of 1.0 and pressure of 10 atm. Like the JSR experiment at 1 atm, the model prediction for the 10 atm experiment is also satisfactory, as shown in Figs. 3.26, A.3, and A.4 in Appendix A.

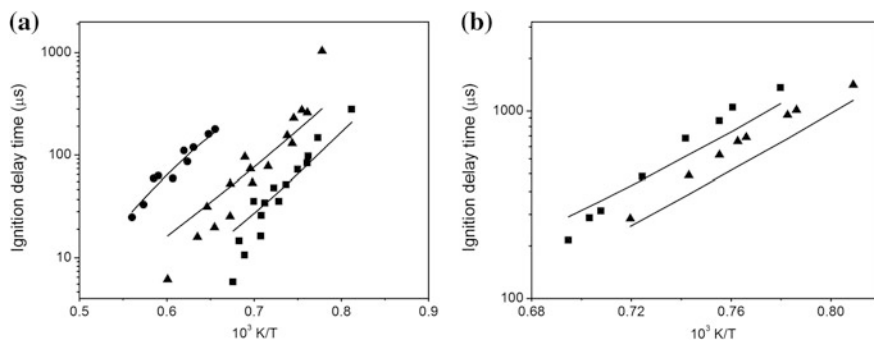


**Fig. 3.26** Experimental (symbols) [8] and simulated (lines) mole fraction profiles of reactants, major products, and C1–C6 intermediates during cyclohexane oxidation with equivalence ratio of 1.0 and pressure of 10 atm

### 3.6 Ignition Delay Time and Laminar Flame Speed of Cyclohexane

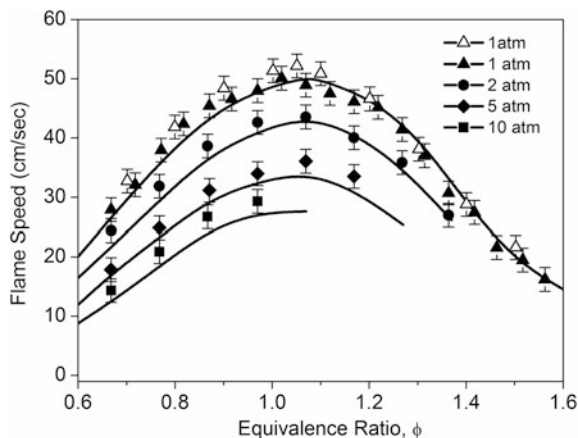
Ignition delay time and laminar flame speed are important combustion properties of fuels and have been widely used to validate the kinetic models. In 2007, Sirjean et al. measured the ignition delay time of cyclohexane/O<sub>2</sub>/Ar mixture in a shock tube with an average pressure of 8 atm. The fuel mole fraction of 0.5% and equivalence ratios of 0.5, 1.0, and 2.0 were obtained by adjusting the ratios between Ar and O<sub>2</sub>. The ignition delay time was determined by the emission of OH\* [11]. Later, Daley et al. [12] measured the ignition delay time of cyclohexane/air mixture at 15 and 50 atm; the equivalence ratios of 0.25, 0.5, and 1.0 were obtained by adjusting the fuel concentration. The ignition delay time was also determined by the emission of OH\*. In 2011, Hong et al. measured the ignition delay time of cyclohexane/O<sub>2</sub>/Ar mixture at 1.5 and 3 atm, equivalence ratio of 0.5 and 1.0. In all the experiments, the mole fraction of O<sub>2</sub> was fixed at 4%. The ignition delay time was also determined by the emission of OH\* [13]. In this work, the experimental data by Sirjean et al. and Hong et al. were adopted to examine the cyclohexane combustion model at various pressures, equivalence ratios and temperature ranges (Fig. 3.27). The ignition delay time was simulated using the Closed Homogenous Batch Reactor in the CHEMKIN-PRO software [95].

Davis et al. [24] and Ji et al. [25] measured the laminar flame speed of cyclohexane at 1 atm with unburnt gas temperature of 298 and 353 K, and equivalence ratios of 0.7–1.7. Later, Wu et al. measured the laminar flame speed of cyclohexane under a wide pressure range (1–20 atm) with unburnt gas temperature of 353 K and equivalence ratios of 0.6–1.6. Recently, in the work of Serinyel et al. [26], the laminar flame speed of cyclohexane at 1 atm and unburnt gas temperature of 298, 358, and 398 K was measured [10]. In this work, the experimental data from Ji et al. and Wu et al. at 1–10 atm and unburnt gas temperature of 353 K was used to



**Fig. 3.27** Ignition delay time of cyclohexane/O<sub>2</sub>/Ar mixture. Symbols are experimental data, lines are model prediction. **a** Experimental data from Sirjean [11], 8 atm; square:  $\phi = 0.5$ , triangle:  $\phi = 1.0$ , and circle:  $\phi = 2.0$ . **b** Experimental data from Hong et al. [13], square: 1.5 atm,  $\phi = 0.5$ , triangle: 3 atm,  $\phi = 1.0$

**Fig. 3.28** Laminar flame speed of cyclohexane/air mixture. Symbols are experimental data, lines are model prediction. Unburnt gas temperature is 353 K. Open triangles are experimental data from Ji et al. [25], solid symbols are experimental data from Wu et al. [26]



examine the model. The premixed module was chosen and the Soret effect and mixture-average transport were included. Considering the uncertainty of the experimental data, the model prediction was good, as shown in Fig. 3.28.

### 3.7 Summary and Conclusions

In this chapter, experimental and kinetic modeling studies were performed to investigate the combustion of cyclohexane. The sub-mechanism of cyclohexane was developed by including the following reaction classes: The ring-opening isomerization and H-atom abstraction of cyclohexane, unimolecular decomposition and H-atom abstraction of 1-hexene, decomposition and isomerization of cyclohexyl radical, decomposition and isomerization of 5-hexen-1-yl radical, decomposition and dehydrogenation of cyclohexene, and reaction pathways to benzene. In most cases, the rate constants of these reactions were adopted from experimental measurements or quantum chemistry calculations. The C0–C4 base model was adopted from the pyrolysis mechanism of butene isomers and USC Mech II. The pressure-dependent rate constants for some unimolecular decomposition pathways—such as those for  $C_3H_5$  isomers, C4 intermediates and  $C_5H_5$ —were considered to simulate the combustion process at a wide range of pressure.

Flow reactor pyrolysis of cyclohexane at atmospheric pressure and low pressure of 30 Torr was performed. More than 30 pyrolysis intermediates were measured with quantified mole fractions. The observation of 1-hexene indicated that ring-opening isomerization of cyclohexane is the initial decomposition pathway of cyclohexane. The species pool detected in both atmospheric and low pressure experiment was similar. However, the formation of 1-hexene, C3 intermediates, 1-butene, and fulvene was promoted at low pressure. The simulation showed that both the isomerization of cyclohexane to 1-hexene and the H-atom abstraction of

cyclohexane are important pathways consuming cyclohexane. However, the H-atom abstraction pathways became dominant when pressure went to 1 atm, consequently the formation of 1-hexene was reduced. Since 1-hexene is the main precursor for C3 intermediates, 1-butene, and fulvene, the production of these three intermediates also decreased when the pressure increased from 30 Torr to atmospheric pressure. Moreover, 1,3-butadiene was produced with high mole fraction during cyclohexane pyrolysis. The ring-opening isomerization of cyclohexyl radical was the main source for 1,3-butadiene. Another important intermediate during cyclohexane pyrolysis is benzene, which is produced from the step-wise dehydrogenation of cyclohexane, the combination of resonance-stabilized radicals and the isomerization of fulvene. More benzene, and other aromatics, were produced during cyclohexane pyrolysis at atmospheric pressure than during the pyrolysis of cyclohexane at 30 Torr.

The kinetic model was further validated by the fuel-rich laminar premixed flame of cyclohexane, including the speciation of reactants, major products and C1–C6 intermediates. The simulation showed that the H-atom abstraction of cyclohexane was the dominant route to consuming cyclohexane, leading to the large formation of 1,3-butadiene, ethylene, and acetylene. Benzene was produced from the step-wise dehydrogenation of cyclohexane. However, the model overpredicted the mole fraction of cyclohexene, 1,3-cyclohexadiene, and benzene. The likely reason could be the absence of high-temperature oxidation pathways for cyclohexyl, 2-cyclohexen-1-yl radical, and cyclohexadienyl radical, or the absence of other ring-opening pathways for these radicals. The reaction mechanism of these radicals should be studied in future work.

The kinetic model was further validated by the JSR oxidation data of cyclohexane at 1.05 atm ( $\phi = 0.5, 1.0, \text{ and } 2.0$ ) and 10 atm ( $\phi = 0.5, 1.0, \text{ and } 1.5$ ). The mole fraction profiles of more than 20 species was used to constrain the kinetic model. Under oxidation environment, the H-atom abstraction by OH radical was the main consumption pathway for cyclohexane and other stable intermediates; the contribution of unimolecular decomposition pathways was negligible. Like pyrolysis and flame of cyclohexane, 1,3-butadiene was an important intermediate during cyclohexane oxidation. The reaction of radical intermediates with  $O_2$  became important during the oxidation environment. The contribution of these pathways increased with the increase of  $O_2$  concentration. Benzene was largely produced from the step-wise dehydrogenation of cyclohexane, while the contribution from the combination of resonance-stabilized radicals was negligible.

The kinetic model for cyclohexane combustion was also validated by the ignition delay time and laminar flame speed of cyclohexane. In summary, the model predicted the reactivity of cyclohexane under pyrolysis, flame, and oxidation environments; the prediction for most of the pyrolysis, oxidation, and flame intermediates were also satisfactory. The model can be applied to predict combustion properties of cyclohexane under a wide range of experimental condition and it is the basis for developing a kinetic model for mono-alkylated cycloalkanes.

## References

1. Prosen, E. J., Johnson, W. H., & Rossini, F. D. (1946). Heats of formation and combustion of the normal alkylcyclopentanes and cyclohexanes and the increment per  $\text{CH}_2$  group for several homologous series of hydrocarbons. *The Journal of Research of the National Institute of Standards*, 37, 51–56.
2. Beckett, C. W., Pitzer, K. S., & Spitzer, R. (1947). The thermodynamic properties and molecular structure of cyclohexane, methylcyclohexane, ethylcyclohexane and the seven dimethylcyclohexanes. *Journal of the American Chemical Society*, 69(10), 2488–2495.
3. Fernández-Alonso, M. D. C., Cañada, J., Jiménez-Barbero, J., & Cuevas, G. (2005) Theoretical study of inversion and topomerization processes of substituted cyclohexanes: The relevance of the energy 3D hypersurface. *ChemPhysChem*, 6(4), 671–680.
4. Tsang, W. (1978). Thermal stability of cyclohexane and 1-hexene. *International Journal of Chemical Kinetics*, 10, 1119–1138.
5. Aribike, D. S., Susu, A. A., & Ogunye, A. F. (1981). Mechanistic and mathematical modeling of the thermal decomposition of cyclohexane. *Thermochimica Acta*, 51(2–3), 113–127.
6. Brown, T. C., King, K. D., & Nguyent, T. T. (1986). Kinetics of primary processes in the pyrolysis of cyclopentanes and cyclohexanes. *Journal of Physical Chemistry*, 90, 419–424.
7. Kiefer, J. H., Gupte, K. S., Harding, L. B., & Klippenstein, S. J. (2009). Shock tube and theory investigation of cyclohexane and 1-hexene decomposition. *Journal of Physical Chemistry A*, 113(48), 13570–13583.
8. Voisin, D., Marchal, A., Reuillon, M., Boettner, J. C., & Cathonnet, M. (1998). Experimental and kinetic modeling study of cyclohexane oxidation in a JSR at high pressure. *Combustion Science and Technology*, 138(1–6), 137–158.
9. El Bakali, A., Braun-Unkloff, M., Dagaut, P., Frank, P., & Cathonnet, M. (2000). Detailed kinetic reaction mechanism for cyclohexane oxidation at pressure up to ten atmospheres. *Proceedings of the Combustion Institute*, 28, 1631–1638.
10. Serinyel, Z., Herbinet, O., Frottier, O., Dirrenberger, P., Warth, V., Glaude, P. A., et al. (2013). An experimental and modeling study of the low- and high-temperature oxidation of cyclohexane. *Combustion and Flame*, 160, 2319–2332.
11. Sirjean, B., Buda, F., Hakka, H., Glaude, P. A., Fournet, R., Warth, V., et al. (2007). The autoignition of cyclopentane and cyclohexane in a shock tube. *Proceedings of the Combustion Institute*, 31, 277–284.
12. Daley, S. M., Berkowitz, A. M., & Oehlschlaeger, M. A. (2008). A shock tube study of cyclopentane and cyclohexane ignition at elevated pressures. *International Journal of Chemical Kinetics*, 40(10), 624–634.
13. Hong, Z., Lam, K.-Y., Davidson, D. F., & Hanson, R. K. (2011). A comparative study of the oxidation characteristics of cyclohexane, methylcyclohexane, and n-butylcyclohexane at high temperatures. *Combustion and Flame*, 158(8), 1456–1468.
14. Lemaire, O., Ribaucour, M., Carlier, M., & Minetti, R. (2001). The production of benzene in the low-temperature oxidation of cyclohexane, cyclohexene, and cyclohexa-1,3-diene. *Combustion and Flame*, 127(1–2), 1971–1980.
15. Vranckx, S., Lee, C., Chakravarty, H. K., & Fernandes, R. X. (2013). A rapid compression machine study of the low temperature combustion of cyclohexane at elevated pressures. *Proceedings of the Combustion Institute*, 34(1), 377–384.
16. Yang, Y., & Boehman, A. L. (2009). Experimental study of cyclohexane and methylcyclohexane oxidation at low to intermediate temperature in a motored engine. *Proceedings of the Combustion Institute*, 32, 419–426.
17. Silke, E. J., Pitz, W. J., Westbrook, C. K., & Ribaucour, M. (2007). Detailed chemical kinetic modeling of cyclohexane oxidation. *Journal of Physical Chemistry A*, 111(19), 3761–3775.
18. Bennett, P. J., Gregory, D., & Jackson, R. A. (1996). Mechanistic studies on the combustion of isotopically labelled cyclohexanes within a single cylinder internal combustion engine. *Combustion Science and Technology*, 115(1–3), 83–103.

19. Billaud, F., Chaverot, P., Berthelin, M., & Freund, E. (1988). Thermal decomposition of cyclohexane at approximately 810 °C. *Industrial and Engineering Chemistry Research*, 27, 759–764.
20. Ciajolo, A., Tregrossi, A., Mallardo, M., Faravelli, T., & Ranzi, E. (2009). Experimental and kinetic modeling study of sooting atmospheric-pressure cyclohexane flame. *Proceedings of the Combustion Institute*, 32, 585–591.
21. Law, M. E., Westmoreland, P. R., Cool, T. A., Wang, J., Hansen, N., Taatjes, C. A., et al. (2007). Benzene precursors and formation routes in a stoichiometric cyclohexane flame. *Proceedings of the Combustion Institute*, 31, 565–573.
22. Li, W., Law, M. E., Westmoreland, P. R., Kasper, T., Hansen, N., & Kohse-Höinghaus, K. (2011). Multiple benzene-formation paths in a fuel-rich cyclohexane flame. *Combustion and Flame*, 158(11), 2077–2089.
23. McEnally, C. S., & Pfefferle, L. D. (2004). Experimental study of fuel decomposition and hydrocarbon growth processes for cyclohexane and related compounds in nonpremixed flames. *Combustion and Flame*, 136(1–2), 155–167.
24. Davis, S. G., & Law, C. K. (1998). Determination of and fuel structure effects on laminar flame speeds of C1–C8 hydrocarbons. *Combustion Science and Technology*, 140, 427–449.
25. Ji, C., Dames, E., Sirjean, B., Wang, H., & Egolfopoulos, F. N. (2011). An experimental and modeling study of the propagation of cyclohexane and mono-alkylated cyclohexane flames. *Proceedings of the Combustion Institute*, 33, 971–978.
26. Wu, F., Kelley, A. P., & Law, C. K. (2012). Laminar flame speeds of cyclohexane and mono-alkylated cyclohexanes at elevated pressures. *Combustion and Flame*, 159(4), 1417–1425.
27. Granata, S., Faravelli, T., & Ranzi, E. (2003). A wide range kinetic modeling study of the pyrolysis and combustion of naphthenes. *Combustion and Flame*, 132(3), 533–544.
28. Wang, H., Dames, E., Sirjean, B., Sheen, D. A., Tangko, R., Violi, A., et al. (2010) *A high-temperature chemical kinetic model of n-alkane (up to n-dodecane), cyclohexane, and methyl-, ethyl-, n-propyl and n-butyl-cyclohexane oxidation at high temperatures*, JetSurF version 2.0, September 19, 2010. (<http://melchior.usc.edu/JetSurF/JetSurF2.0>).
29. Buda, F., Heyberger, B., Fournet, R., Glaude, P. A., Warth, V., & Battin-Leclerc, F. (2006). Modeling of the gas-phase oxidation of cyclohexane. *Energy & Fuels*, 20(4), 1450–1459.
30. Sirjean, B., Glaude, P. A., Ruiz-López, M. F., & Fournet, R. (2009). Theoretical kinetic study of the reactions of cycloalkylperoxy radicals. *Journal of Physical Chemistry A*, 113(25), 6924–6935.
31. Tsang, W. (1988). Chemical kinetic data base for combustion chemistry. Part 3: Propane. *Journal of Physical and Chemical Reference Data*, 17(2), 887–951.
32. Sirjean, B., Glaude, P. A., Ruiz-Lopez, M. F., & Fournet, R. (2006). Detailed kinetic study of the ring opening of cycloalkanes by CBS-QB3 calculations. *Journal of Physical Chemistry A*, 110(46), 12693–12704.
33. Sivaramakrishnan, R., & Michael, J. V. (2009). Shock tube measurements of high temperature rate constants for OH with cycloalkanes and methylcycloalkanes. *Combustion and Flame*, 156(5), 1126–1134.
34. Cohen, N., & Westberg, K. R. (1986). The use of transition-state theory to extrapolate rate coefficients for reactions of O atoms with alkanes. *International Journal of Chemical Kinetics*, 18(1), 99–140.
35. Handford-Styring, S. M., & Walker, R. W. (2001). Arrhenius parameters for the reaction HO<sub>2</sub> + cyclohexane between 673 and 773 K, and for H atom transfer in cyclohexylperoxy radicals. *Physical Chemistry Chemical Physics*, 3(11), 2043–2052.
36. Knepp, A. M., Meloni, G., Jusinski, L. E., Taatjes, C. A., Cavallotti, C., & Klippenstein, S. J. (2007). Theory, measurements, and modeling of OH and HO<sub>2</sub> formation in the reaction of cyclohexyl radicals with O<sub>2</sub>. *Physical Chemistry Chemical Physics*, 9(31), 4315–4331.
37. Sirjean, B., Glaude, P. A., Ruiz-Lopèz, M. F., & Fournet, R. (2008). Theoretical kinetic study of thermal unimolecular decomposition of cyclic alkyl radicals. *Journal of Physical Chemistry A*, 112(46), 11598–11610.

38. Iwan, I., McGivern, W. S., Manion, J. A., & Tsang, W. (2007). The decomposition and isomerization of cyclohexyl and 1-hexenyl radicals. In *Proceedings of 5th US Combustion Meeting*, San Diego, CA 2007, CO<sub>2</sub>.
39. Wang, Z., Ye, L., Yuan, W., Zhang, L., Wang, Y., Cheng, Z., et al. (2014). Experimental and kinetic modeling study on methylcyclohexane pyrolysis and combustion. *Combustion and Flame*, *161*, 84–100.
40. Tsang, W., Walker, J. A., & Manion, J. A. (1998). Single-pulse shock-tube study on the decomposition of 1-pentyl radicals. *Symposium (International) on Combustion*, *27*(1), 135–142.
41. Tsang, W. (2005). Mechanism and rate constants for the decomposition of 1-pentenyl radicals. *Journal of Physical Chemistry A*, *110*(27), 8501–8509.
42. Tsang, W., Walker, J. A., & Manion, J. A. (2007). The decomposition of normal hexyl radicals. *Proceedings of the Combustion Institute*, *31*(1), 141–148.
43. Tsang, W., McGivern, W. S., & Manion, J. A. (2009). Multichannel decomposition and isomerization of octyl radicals. *Proceedings of the Combustion Institute*, *32*(1), 131–138.
44. Gong, C., Li, Z., & Li, X. (2012). Theoretical kinetic study of thermal decomposition of cyclohexane. *Energy & Fuels*, *26*(5), 2811–2820.
45. Kiefer, J. H., & Shah, J. N. (1987). Unimolecular dissociation of cyclohexene at extremely high temperatures: Behavior of the energy-transfer collision efficiency. *Journal of Physical Chemistry*, *91*(11), 3024–3030.
46. Pitz, W. J., Naik, C. V., Mhaoldúin, T. N., Westbrook, C. K., Curran, H. J., Orme, J. P., et al. (2007). Modeling and experimental investigation of methylcyclohexane ignition in a rapid compression machine. *Proceedings of the Combustion Institute*, *31*, 267–275.
47. Orme, J. P., Curran, H. J., & Simmie, J. M. (2006). Experimental and modeling study of methyl cyclohexane pyrolysis and oxidation. *Journal of Physical Chemistry A*, *110*(1), 114–131.
48. Dayma, G., Glaude, P. A., Fournet, R., & Battin-Leclerc, F. (2003). Experimental and modeling study of the oxidation of cyclohexene. *International Journal of Chemical Kinetics*, *35*(7), 273–285.
49. Sirjean, B., Glaude, P. A., Ruiz-Lopez, M. F., Fournet, R. *Theoretical kinetic study of the ring opening and dehydrogenation of cyclic alkenes*. Manuscript in preparation.
50. Zhang, L., Cai, J., Zhang, T., & Qi, F. (2010). Kinetic modeling study of toluene pyrolysis at low pressure. *Combustion and Flame*, *157*(9), 1686–1697.
51. Li, Y., Cai, J., Zhang, L., Yang, J., Wang, Z., & Qi, F. (2011). Experimental and modeling investigation on premixed ethylbenzene flames at low pressure. *Proceedings of the Combustion Institute*, *33*(1), 617–624.
52. Li, Y., Cai, J., Zhang, L., Yuan, T., Zhang, K., & Qi, F. (2011). Investigation on chemical structures of premixed toluene flames at low pressure. *Proceedings of the Combustion Institute*, *33*(1), 593–600.
53. Wang, Z., Li, Y., Zhang, F., Zhang, L., Yuan, W., Wang, Y., et al. (2013). An experimental and kinetic modeling investigation on a rich premixed n-propylbenzene flame at low pressure. *Proceedings of the Combustion Institute*, *34*(1), 1785–1793.
54. Hansen, N., Miller, J. A., Westmoreland, P. R., Kasper, T., Kohse-Höinghaus, K., Wang, J., et al. (2009). Isomer-specific combustion chemistry in allene and propyne flames. *Combustion and Flame*, *156*(11), 2153–2164.
55. Miller, J. A., & Klippenstein, S. J. (2003). The recombination of propargyl radicals and other reactions on a C<sub>6</sub>H<sub>6</sub> potential. *Journal of Physical Chemistry A*, *107*(39), 7783–7799.
56. Georgievskii, Y., Miller, J. A., & Klippenstein, S. J. (2007). Association rate constants for reactions between resonance-stabilized radicals: C<sub>3</sub>H<sub>3</sub> + C<sub>3</sub>H<sub>3</sub>, C<sub>3</sub>H<sub>3</sub> + C<sub>3</sub>H<sub>5</sub>, and C<sub>3</sub>H<sub>5</sub> + C<sub>3</sub>H<sub>5</sub>. *Physical Chemistry Chemical Physics*, *9*(31), 4259–4268.
57. Scherer, S., Just, T., & Frank, P. (2000). High-temperature investigations on pyrolytic reactions of propargyl radicals. *Proceedings of the Combustion Institute*, *28*(2), 1511–1518.



58. Fernandes, R. X., Hippler, H., & Olzmann, M. (2005). Determination of the rate coefficient for the  $C_3H_3 + C_3H_3$  reaction at high temperatures by shock-tube investigations. *Proceedings of the Combustion Institute*, 30(1), 1033–1038.
59. D'Anna, A., & Kent, J. H. (2003). Aromatic formation pathways in non-premixed methane flames. *Combustion and Flame*, 132(4), 715–722.
60. Wu, C. H., & Kern, R. D. (1987). Shock-tube study of allene pyrolysis. *Journal of Physical Chemistry*, 91(24), 6291–6296.
61. Senosiain, J. P., & Miller, J. A. (2007). The reaction of n- and i- $C_4H_5$  radicals with acetylene. *Journal of Physical Chemistry A*, 111(19), 3740–3747.
62. Lindstedt, R. P., & Skevis, G. (1997). Chemistry of acetylene flames. *Combustion Science and Technology*, 125(1–6), 73–137.
63. Marinov, N. M., Castaldi, M. J., Melius, C. F., & Tsang, W. (1997). Aromatic and polycyclic aromatic hydrocarbon formation in a premixed propane flame. *Combustion Science and Technology*, 128(1–6), 295–342.
64. Miller, J. A., Georgievskii, Y., Allen, W. D., & Klippenstein, S. J. Unpublished data.
65. Hansen, N., Miller, J. A., Kasper, T., Kohse-Höinghaus, K., Westmoreland, P. R., Wang, J., et al. (2009). Benzene formation in premixed fuel-rich 1,3-butadiene flames. *Proceedings of the Combustion Institute*, 32(1), 623–630.
66. Violi, A., Truong, T. N., & Sarofim, A. F. (2004). Kinetics of hydrogen abstraction reactions from polycyclic aromatic hydrocarbons by H atoms. *Journal of Physical Chemistry A*, 108(22), 4846–4852.
67. Seta, T., Nakajima, M., & Miyoshi, A. (2006). High-temperature reactions of OH radicals with benzene and toluene. *Journal of Physical Chemistry A*, 110(15), 5081–5090.
68. Roy, K., Horn, C., Frank, P., Slutsky, V. G., & Just, T. (1998). High-temperature investigations on the pyrolysis of cyclopentadiene. *Symposium (International) on Combustion*, 27(1), 329–336.
69. Bacskay, G. B., & Mackie, J. C. (2001). The pyrolysis of cyclopentadiene: quantum chemical and kinetic modelling studies of the acetylene plus propyne/allene decomposition channels. *Physical Chemistry Chemical Physics*, 3(12), 2467–2473.
70. Wang, H., You, X., Joshi, A. V., Davis, S. G., Laskin, A., & Egolfopoulos, F., et al. (2007). *High-temperature combustion reaction model of  $H_2/CO/CI-C_4$  compounds*. [http://ignis.usc.edu/USC\\_Mech\\_II.htm](http://ignis.usc.edu/USC_Mech_II.htm).
71. Richter, H., Granata, S., Green, W. H., & Howard, J. B. (2005). Detailed modeling of PAH and soot formation in a laminar premixed benzene/oxygen/argon low-pressure flame. *Proceedings of the Combustion Institute*, 30(1), 1397–1405.
72. Moskaleva, L. V., & Lin, M. C. (2000). Unimolecular isomerization/decomposition of cyclopentadienyl and related bimolecular reverse process: ab initio MO/statistical theory study. *Journal of Computational Chemistry*, 21(6), 415–425.
73. Zhong, X., & Bozzelli, J. W. (1998). Thermochemical and kinetic analysis of the H, OH,  $HO_2$ , O, and  $O_2$  association reactions with cyclopentadienyl radical. *Journal of Physical Chemistry A*, 102(20), 3537–3555.
74. Zhang, Y., Cai, J., Zhao, L., Yang, J., Jin, H., Cheng, Z., et al. (2012). An experimental and kinetic modeling study of three butene isomers pyrolysis at low pressure. *Combustion and Flame*, 159, 905–917.
75. Laskin, A., Wang, H., & Law, C. K. (2000). Detailed kinetic modeling of 1,3-butadiene oxidation at high temperatures. *International Journal of Chemical Kinetics*, 32(10), 589–614.
76. Miller, J. A., Senosiain, J. P., Klippenstein, S. J., & Georgievskii, Y. (2008). Reactions over multiple, interconnected potential wells: unimolecular and bimolecular reactions on a  $C_3H_5$  potential. *Journal of Physical Chemistry A*, 112(39), 9429–9438.
77. Davis, S. G., Law, C. K., & Wang, H. (1999). Propyne pyrolysis in a flow reactor: An experimental, RRKM, and detailed kinetic modeling study. *Journal of Physical Chemistry A*, 103(30), 5889–5899.
78. Wang, H., & Frenklach, M. (1997). A detailed kinetic modeling study of aromatics formation in laminar premixed acetylene and ethylene flames. *Combustion and Flame*, 110, 173–221.

79. Miller, J. A. *Private communication*.
80. Tokmakov, I. V., Park, J., Gheyas, S., & Lin, M. C. (1999). Experimental and theoretical studies of the reaction of the phenyl radical with methane. *Journal of Physical Chemistry A*, 103(19), 3636–3645.
81. Asaba, T., & Fujii, N. (1971). High temperature oxidation of benzene. *Proceedings of the International Symposium Shock Tubes Waves*, 8, 1–12.
82. Alzueta, M. U., Glarborg, P., & Dam-Johansen, K. (2000). Experimental and kinetic modeling study of the oxidation of benzene. *International Journal of Chemical Kinetics*, 32(8), 498–522.
83. Baulch, D. L., Cobos, C. J., Cox, R. A., Esser, C., Frank, P., Just, T., et al. (1992). Evaluated kinetic data for combustion modelling. *Journal of Physical and Chemical Reference Data*, 21(3), 411–734.
84. Wang, Z., Cheng, Z., Yuan, W., Cai, J., Zhang, L., Zhang, F., et al. (2012). An experimental and kinetic modeling study of cyclohexane pyrolysis at low pressure. *Combustion and Flame*, 159(7), 2243–2253.
85. Taatjes, C. A., Osborn, D. L., Selby, T. M., Meloni, G., Fan, H. Y., & Pratt, S. T. (2008). Absolute photoionization cross-section of the methyl radical. *Journal of Physical Chemistry A*, 112(39), 9336–9343.
86. Cool, T. A., Wang, J., Nakajima, K., Taatjes, C. A., & McIlroy, A. (2005). Photoionization cross sections for reaction intermediates in hydrocarbon combustion. *International Journal of Mass Spectrometry*, 247(1–3), 18–27.
87. Robinson, J. C., Sveum, N. E., & Neumark, D. M. (2003). Determination of absolute photoionization cross sections for vinyl and propargyl radicals. *The Journal of Chemical Physics*, 119(11), 5311–5314.
88. Yang, B., Wang, J., Cool, T. A., Hansen, N., Skeen, S., & Osborn, D. L. (2012). Absolute photoionization cross-sections of some combustion intermediates. *International Journal of Mass Spectrometry*, 309, 118–128.
89. Robinson, J. C., Sveum, N. E., & Neumark, D. M. (2004). Determination of absolute photoionization cross sections for isomers of C<sub>3</sub>H<sub>5</sub>: Allyl and 2-propenyl radicals. *Chemical Physics Letters*, 383(5–6), 601–605.
90. Cool, T. A., Nakajima, K., Mostefaoui, T. A., Qi, F., McIlroy, A., Westmoreland, P. R., et al. (2003). Selective detection of isomers with photoionization mass spectrometry for studies of hydrocarbon flame chemistry. *The Journal of Chemical Physics*, 119(16), 8356–8365.
91. Koizumi, H. (1991). Predominant decay channel for superexcited organic molecules. *The Journal of Chemical Physics*, 95(8), 5846–5852.
92. Wang, J., Yang, B., Cool, T. A., Hansen, N., & Kasper, T. (2008). Near-threshold absolute photoionization cross-sections of some reaction intermediates in combustion. *International Journal of Mass Spectrometry*, 269(3), 210–220.
93. Hansen, N., Klippenstein, S. J., Miller, J. A., Wang, J., Cool, T. A., Law, M. E., et al. (2006). Identification of C<sub>5</sub>H<sub>x</sub> isomers in fuel-rich flames by photoionization mass spectrometry and electronic structure calculations. *Journal of Physical Chemistry A*, 110(13), 4376–4388.
94. Zhou, Z., Zhang, L., Xie, M., Wang, Z., Chen, D., & Qi, F. (2010). Determination of absolute photoionization cross-sections of alkanes and cyclo-alkanes. *Rapid Communications in Mass Spectrometry*, 24(9), 1335–1342.
95. CHEMKIN-PRO 15092. (2009). *Reaction design*. San Diego.
96. Hansen, N., Kasper, T., Yang, B., Cool, T. A., Li, W. J., Westmoreland, P. R., et al. (2011). Fuel-structure dependence of benzene formation processes in premixed flames fueled by C<sub>6</sub>H<sub>12</sub> isomers. *Proceedings of the Combustion Institute*, 33(1), 585–592.
97. Hansen, N., Li, W., Law, M. E., Kasper, T., Westmoreland, P. R., Yang, B., et al. (2010). The importance of fuel dissociation and propargyl plus allyl association for the formation of benzene in a fuel-rich 1-hexene flame. *Physical Chemistry Chemical Physics*, 12(38), 12112–12122.

# Chapter 4

## Experimental and Modeling Study of Methylcyclohexane Combustion

### 4.1 Background

Methylcyclohexane ( $C_7H_{14}$ ) has the following properties: molar mass of 98.18 g/mol, boiling point of 373 K, melting point of 147 K, density of 0.771 g/mL, standard enthalpy of formation of  $-154.8$  kJ/mol [1], standard molar entropy of 343.3 J/mol/K [2], and ionization potential of  $9.64 \pm 0.10$  eV.

The motivation to study the combustion properties of methylcyclohexane is not only that this molecule is an important component of fossil fuels, but it is also a surrogate component, widely adopted in surrogate formulation. Moreover, methylcyclohexane is the simplest branched cycloalkane and the model compound to study combustion properties of cycloalkanes with long side chains, or multiple side chains. Pyrolysis and catalyst-assisted pyrolysis of methylcyclohexane also provides the heat sink to cool hypersonic aircraft [3]; although the high tendency of methylcyclohexane to form aromatics increases soot production in the combustion process.

Compared to the large number of experimental and modeling studies of cyclohexane combustion, studies on alkyl-cyclohexanes are scarce. In 1989, Brown and King studied the unimolecular decomposition of methylcyclohexane using the technique of very low pressure pyrolysis (VLPP); the rate constants for methylcyclohexane ring-opening isomerization and dissociation were reported [4]. Zeppieri et al. investigated the pyrolysis and oxidation of methylcyclohexane in the Princeton Turbulent Flow Reactor at 1 atm and temperature range of 1050–1200 K. The major products were methane, ethylene, propene, and 1,3-butadiene. The conversion of methylcyclohexane at 1058, 1108, 1154, and 1192 K was measured during methylcyclohexane pyrolysis. Formation of pyrolysis products versus residence time was measured at 1155 K during methylcyclohexane pyrolysis, and the formation of oxidation products versus residence time was measured at 1160 K during methylcyclohexane oxidation with an equivalence ratio of 1.3 [5].

The ignition delay time of methylcyclohexane was investigated under a wide range of temperature, pressure, and equivalence ratios. Hawthorn and Nixon [6] measured the ignition delay time of methylcyclohexane/O<sub>2</sub>/dilution gas mixture in a shock tube at 0.61, 1.02, and 1.70 atm, equivalence ratio of 0.1–2.1, and temperature range of 1200–1480 K. In 2007, Orme et al. measured the shock tube ignition delay time of methylcyclohexane/O<sub>2</sub>/Ar mixture at 1.0, 2.0, and 4.0 atm, equivalence ratio of 0.5, 1.0, and 2.0, and temperatures of 1200–2100 K. The ignition delay time was determined by the emission of CH\* and the endwall pressure [7]. Later, Vasu measured the shock tube ignition delay time of methylcyclohexane/O<sub>2</sub>/dilution gas mixture from 1 to 50 atm, temperature range 795–1560 K, and equivalence ratio of 0.5–2.0. The dilution gas was Ar and N<sub>2</sub>. The ignition delay time was determined by measuring the endwall pressure and the emission of CH\* and OH\* [8].

The time histories of OH radical during methylcyclohexane/O<sub>2</sub>/Ar mixture oxidation in the shock tube were also measured by Vasu et al. [9] in the temperature range of 1205–1332 K, pressure of 15 atm, and equivalence ratio of 0.5. In the same year, Vanderover and Oehlschlaeger measured the ignition delay time of methylcyclohexane/air mixture in a high pressure shock tube. The pressure was 12 and 50 atm, and equivalence ratio 0.25, 0.5, and 1.0. The endwall OH\* emission and sidewall pressure was used to determine ignition delay time [10]. The H-atom abstraction rate constants of methylcyclohexane with OH radical was also measured by Sivaramakrishnan and Michael in a shock tube from 836 to 1273 K; the rate constants from 250 to 2000 K were obtained from quantum chemistry calculations [11]. Furthermore, a rapid compression machine (RCM) was adopted to measure the ignition delay time of methylcyclohexane at lower temperatures. For example, Pitz et al. [12] measured the ignition delay time of methylcyclohexane/O<sub>2</sub>/dilution gas mixture at 10, 15, and 20 atm. The negative temperature coefficient (NTC) zone of low temperature oxidation of methylcyclohexane was observed. In 2009, Mittal et al. measured the RCM ignition delay time of methylcyclohexane/O<sub>2</sub>/Ar/N<sub>2</sub> mixture at 15.1 and 25.5 bar, temperature range of 680–905 K and equivalence ratio of 0.5, 1.0, and 1.5 [13]; two-stage ignition with an evident NTC zone was observed. Recently, Weber et al. extended the RCM oxidation of methylcyclohexane/O<sub>2</sub>/Ar/N<sub>2</sub> mixture to 50 bar. The ignition delay time was measured in a temperature range of 690–900 K and equivalence ratio of 0.5, 1.0, and 1.5 [14].

A flame study of methylcyclohexane was also reported in the literature. McEnally and Pfefferle measured the centerline distribution of C<sub>3</sub>–C<sub>12</sub> hydrocarbons in co-flow non-premixed methane flames doped with 2000 ppm methylcyclohexane [15]. The results showed that unimolecular decomposition pathways were the dominant consuming route for methylcyclohexane; benzene was formed from the combination of smaller intermediates, while the step-wise dehydrogenation of methylcyclohexane was not important. Ji et al. [16] and Wu et al. [17] measured the laminar flame speed of methylcyclohexane from 1 to 10 atm; and Skeen et al. recently investigated the laminar premixed flame of methylcyclohexane

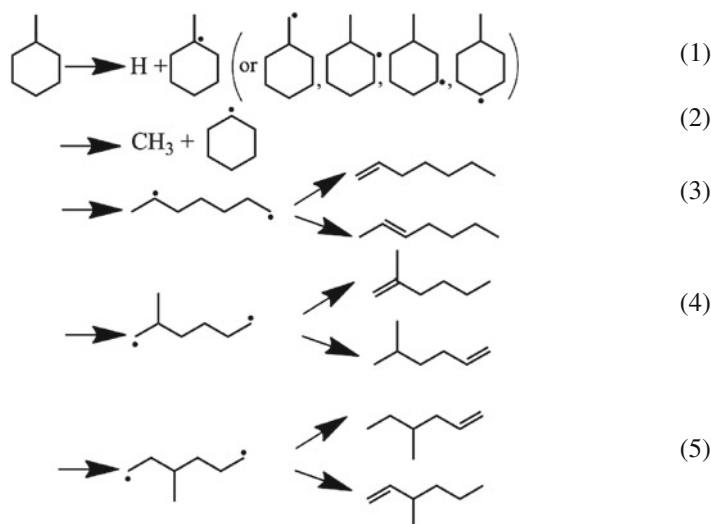
at 15, 20, and 30 Torr with equivalence ratio of 1.0, 1.75, and 1.9 [18]. Discussion focused on the initial decomposition of methylcyclohexane and the reaction mechanism of benzene and toluene.

In addition to experimental study, the kinetic model of methylcyclohexane combustion was also developed. Orme et al. [7] and Pitz et al. [12] developed a high and low temperature oxidation model of methylcyclohexane, respectively. The models were validated by shock tube and RCM ignition delay time and species speciation in flow reactor pyrolysis and oxidation. The JetSurF model by Wang et al. [19] also included the high-temperature pyrolysis and oxidation mechanism of methylcyclohexane, which was validated by laminar premixed flame and shock tube ignition delay time.

Previous studies of methylcyclohexane focused on the measurement of ignition delay time. Experimental data of methylcyclohexane pyrolysis and oxidation with detailed species speciation were seldom reported in the literature. Moreover, the reaction mechanism for the initial decomposition of methylcyclohexane is not well understood and some dispute exists in the literature. In this chapter, species speciation was measured during the flow reactor pyrolysis and laminar premixed flame of methylcyclohexane. The kinetic model of methylcyclohexane was developed with the help of quantum chemistry calculations of reaction pathways and rate constants. This chapter is organized in the following order: (i) reaction pathways and rate constant calculations of methylcyclohexane decomposition; (ii) reaction pathways and rate constant calculations of H-atom abstraction of methylcyclohexane by H atom; (iii) reaction pathways and rate constant calculations of methylcyclohexane radical decomposition and isomerization (theoretical calculation helps develop the sub-mechanism of methylcyclohexane); (iv) estimation of thermodynamic data and kinetic model development. (v) validation of the kinetic model by species speciation from flow reactor pyrolysis and laminar premixed flame, ignition delay time, and laminar flame speed of methylcyclohexane. Discussion focuses on decomposition of methylcyclohexane and the reaction mechanism of benzene and toluene.

## 4.2 Decomposition and Isomerization of Methylcyclohexane

The unimolecular reaction of methylcyclohexane may proceed via the elimination of a C–H bond, losing the methyl side-chain, or ring-opening isomerization to heptene isomers, shown in Fig. 4.1. These pathways are the initial reaction channels of methylcyclohexane combustion. Similar initial reactions may occur for alkyl-cyclohexanes. Thus, clarifying the pressure- and temperature- dependent rate constants of these pathways, and the corresponding branching ratios, is a prerequisite to developing a kinetic model of methylcyclohexane. Examination of the literature on cyclohexane shows that rate constants of C–H bond elimination are



**Fig. 4.1** Decomposition and isomerization pathways of methylcyclohexane. Reprinted with permission from Ref. [24]. Copyright 2013 by American Chemical Society

much slower than isomerization via ring opening because of the high dissociation threshold and high entropy change of the variational transition state [20–22].

Recently, Skeen et al. investigated unimolecular reactions of methylcyclohexane in low pressure laminar premixed flame [18]. They deduced from reaction pathway calculation that production of the six heptene isomers in Fig. 4.1 is comparable. The overall rate constants of ring-opening isomerization are likely to be similar to those of the methyl loss channel [18]. However, this conclusion differs from previous study, wherein the authors suggested that the methyl loss channel is negligible; the dominant isomerization pathway is via the C–C bond scission adjacent to the methyl group and leads to 1-heptene and 2-heptene [4, 15]. This discrepancy for the initial reactions of methylcyclohexane motivated additional quantum calculation in this chapter; the aim was to determine the pressure- and temperature- dependent rate constants and reveal branching ratios of the seven unimolecular reactions in Fig. 4.1. The reasonable prediction of these branching ratios is important in order to analyze the soot formation tendency and other combustion properties of alkyl-cycloalkanes (e.g., ignition delay time and laminar flame speed).

In this work, the methyl loss channel and the isomerization via ring opening of methylcyclohexane were investigated using high-level *ab initio* calculation. From the calculated potential energy surface, we calculated the rate constants of these pathways using the Rice-Ramsperger-Kassel-Marcus (RRKM)/master equation method [23] at temperatures of 800–2000 K and pressures of 7.6–76,000 Torr.

### 4.2.1 Theoretical Method

In this work, multi-reference calculations were adopted in consideration of the unstable diradical intermediates formed in the ring-opening isomerization reactions. The configurations of long C–C bond length in the dissociation reactions also need multi-reference calculations. To this end, the complete active space self-consistent field method (CASSCF) [25] with the 6-31+g(d,p) basis set was used to optimize the stationary points of reactants, transition states and products in the isomerization pathways. For diradical intermediates from channels four and five in Fig. 4.1, the chosen active space was six electrons occupying six orbitals, which included four  $\sigma_{\text{C-H}}$  and corresponding  $\sigma^*_{\text{C-H}}$  molecular orbitals and two singly-occupied molecular orbitals. Another  $\sigma_{\text{C-H}}$  orbital and its  $\sigma^*_{\text{C-H}}$  orbital were considered for channel three. This is because this diradical intermediate undergoes three probable H-migration pathways. Therefore, channel three used CAS(8e, 8o) while channels four and five used CAS(6e, 6o). For the methyl loss channel, the minimum active space of CAS(2e, 2o) was used. In the calculation of single point energies, correction by the multi-reference configuration interaction (MRCI) method was considered; the 1s and 2s orbitals of carbon atoms frozen was considered in Davidson correction [26, 27]. A scaling factor of 0.93 was used to correct the zero-point energies, which were calculated by the CASSCF method. This factor was determined after comparing the zero-point energies of methylcyclohexane calculated at CASSCF/6-31+g(d,p) and B3LYP/CBSB7 level of theory. For CBS-QB3, the well-recognized zero point energy scaled factor of 0.99 was applied [28]. Because they do not require multireference calculations, optimization of the products in Fig. 4.1 was not performed by the CASSCF method. Thus, CBS-QB3 level of theory obtained reaction energies [28] are presented. The software for multi-reference calculations was the Molpro package [29]; for CBS-QB3 calculations the Gaussian 09 program [30] was used. Rate constant calculations are not affected by the reaction energies when the tunneling effect is not considered.

In rate constant calculations with multiple steps of isomerization, an accurate RRKM treatment is challenging, for example, the ring-opening isomerization followed by the intramolecular H-shift for the methylcyclohexane isomerization channels in Fig. 4.1. In this work, a simple one-transition state model was used to estimate rate constants of the isomerization channels. The ring-opening isomerization was treated as the rate-controlling step; the branching ratios for the subsequent H-shift channels were then estimated by calculating the partition functions of each transition states.

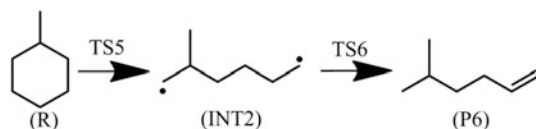
The one-transition state model was also suggested by Kiefer et al. [21], who studied the isomerization of cyclohexane; the resulting high pressure-limit rate constant is reasonable with an uncertainty factor less than 3. For the barrierless methyl loss channel, the variational transition state theory was applied, i.e., the position of the transition state with temperature was determined variationally [31, 32]. In the rate-constant falloff calculation, Lennard–Jones parameters for methylcyclohexane with empirical value of  $\sigma_{\text{MCH}} = 5.982 \text{ \AA}$ ,  $\varepsilon_{\text{MCH}} = 477 \text{ K}$ ,

were used. The value for Ar (the bath gas) was  $\sigma_{\text{Ar}} = 3.542 \text{ \AA}$ , and  $\varepsilon_{\text{Ar}} = 114 \text{ K}$ . A single-parameter exponential down model,  $\langle \Delta E \rangle_{\text{down}} = 0.4 T$ , was applied for the collision energy transfer. This treatment is like the value used for cyclohexane, in which a constant value of  $600 \text{ cm}^{-1}$  was used from 1300 to 2000 K [21]. Finally, the rate constants for channels two to five varying with pressure and temperature were computed using the RRKM/ME method. The software is ChemRate program [33].

## 4.2.2 Results and Discussion

### 4.2.2.1 Potential Energy Surface

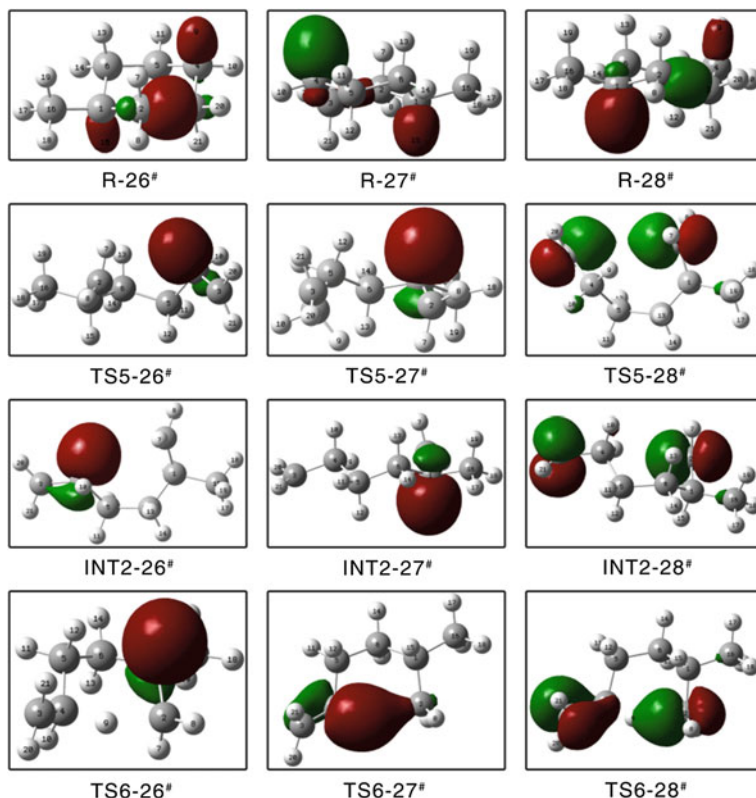
The potential energy surface starts from the lowest energy conformer of methylcyclohexane. In the work of Skeen et al., the isomerization of methylcyclohexane via ring-opening was investigated using the CASPT2/cc-pVDZ method; the minimum active space was used [18]. To reduce the effect of different active spaces on the calculated energies, in each isomerization channel, it was kept consistent for the active space of all stationary points. As an example, the active space for the reaction below is illustrated in Fig. 4.2.



The three antibonding molecular orbitals are not shown in Fig. 4.2. There are 28 doubly-occupied molecular orbitals for methylcyclohexane. The 26–31 orbitals are for the active orbitals in CAS(6e, 6o). The same rule was used for other isomerization channels in Fig. 4.1.

The calculated potential energy surfaces for the above reaction channel are presented in Fig. 4.3. The calculation is at MRCI+Q//CAS(6,6)/6-31+g(d,p) level of theory. The energy barriers of TS6 and TS7 (the intramolecular H-shift of the diradical intermediate), are lower than the energy of INT2. This result differs from the computation by CASPT2/cc-pVDZ, with minimum active spaces, which results in 2–3 kcal/mol barrier heights for TS6 and TS7 [18] (Table 4.1). The isomerizations of dioxane via ring-open were studied by Yang et al. They used multiple multi-reference methods and a large basis set [34]. The calculation resulted in unreliable barrier height for dioxane ring-opening isomerization when they applied small (2e, 2o) active space in the MRCI+Q method. However, Table 4.1 shows that calculations by this group do not have a similar tendency. In MRCI calculations by this group, we frozen the 1s and 2s orbitals of carbon atoms. However, the default

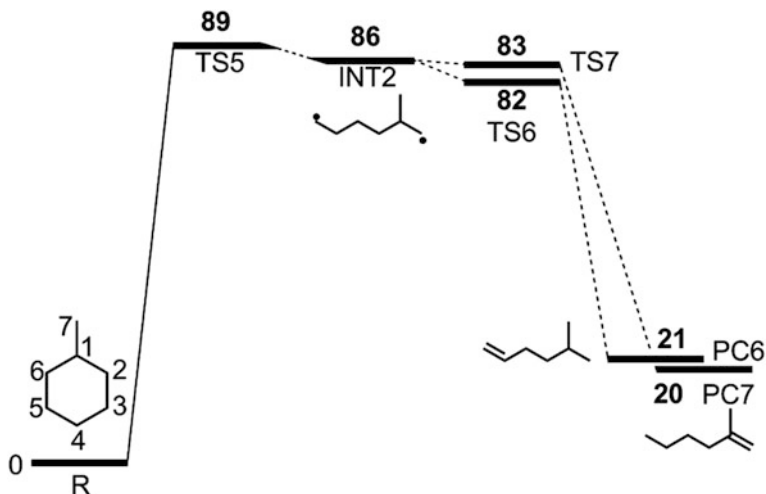




**Fig. 4.2** Molecular orbitals showing only the bonding orbitals, in active space of an isomerization channel for methylcyclohexane. Reprinted with permission from Ref. [24]. Copyright 2013 by American Chemical Society

procedure of Molpro frozen only the C 1s orbitals. The comparison for the reaction pathway  $R \rightarrow P6$  with and without C 2s orbitals frozen (in Table 4.1) shows that no significant error is introduced when C 2s orbital was frozen.

Figure 4.4 shows potential energy surfaces in the RRKM/ME calculation. The energies in brackets are from computations of Skeen et al. [18], using the CASPT2 method. As in the discussion in Sect. 4.2.1, the rate constant calculation only considered the transition states via ring-opening. The branching fractions to the consequent isomerization products were estimated from partition functions of the H-shift transition states from the diradical intermediates. A noticeable difference was observed between calculations by this group and the work of Skeen et al. [18], i.e., the energy barrier of TS1 was 4 kcal/mol lower than that of TS5 and TS8 in our calculation. Instead, the barrier height of the three TSs was the same from the calculation of Skeen et al. Results from this group support the earlier study [4, 15], in which the methyl side-chain causes the C–C bond adjacent to the side-chain to dissociate more easily, but—unlike the conclusion by Skeen et al. [18]—that the



**Fig. 4.3** Potential energy surfaces for ring-opening isomerization of methylcyclohexane by C2–C3 bond dissociation. The calculation was conducted at MRCI/6-31+g(d,p)//CAS(6,6)/6-31+g(d,p) level of theory (energy unit: kcal/mol). Reprinted with permission from Ref. [24]. Copyright 2013 by American Chemical Society

**Table 4.1** Relative energies of stationary points for methylcyclohexane ring-opening isomerization by C2–C3 bond dissociation

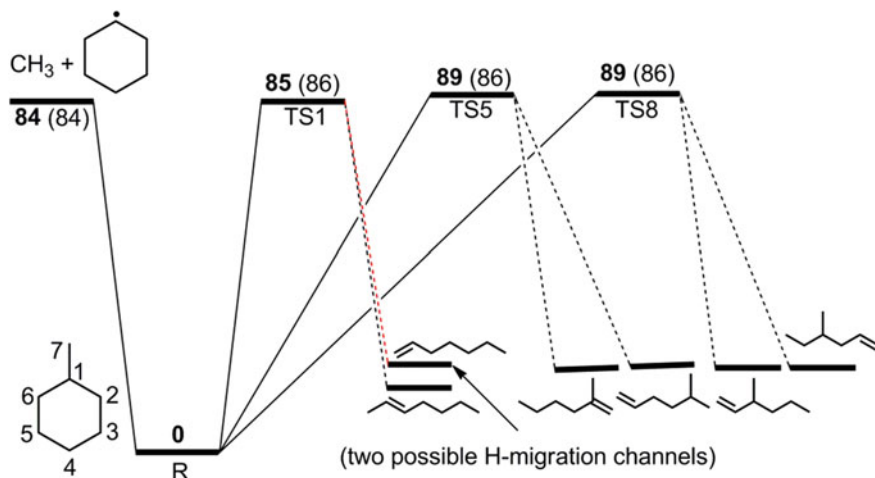
	MRCI(+Q)/CAS(6,6) <sup>a</sup>		MRCI(+Q)/CAS(2,2) <sup>a</sup>	CASPT2/CAS(6,6) <sup>a</sup>	CASPT2(2,2)/cc-pVDZ <sup>b</sup>
	C1s frozen	C1s and C2s frozen	C1s frozen	C1s and C2s frozen	C1s frozen
INT2	83.4 (85.3)	83.7 (85.5)	81.2 (85.4)	84.5	85
TS5	87.1 (89.0)	87.3 (89.1)	87.0 (89.0)	88.0	86
TS6	81.8 (82.3)	81.3 (81.6)	–	78.6	87
TS7	83.5 (83.6)	82.8 (82.6)	–	79.5	88

Reprinted with permission from Ref. [24]. Copyright 2013 by American Chemical Society

<sup>a</sup>6-31+g(d,p) basis set in this work; bracketed values are relative MRCI energies with Davidson correction

<sup>b</sup>Ref. [18]

methyl side-chain insignificantly effects the ring-opening isomerization. On the other hand, calculations of this group and the work of Skeen et al. both show that the methyl loss channel was energetically the most favorable pathway. The estimation from Skeen et al. suggested that the overall rate constant of methylcyclohexane isomerization via ring-opening was likely to be close to the methyl loss



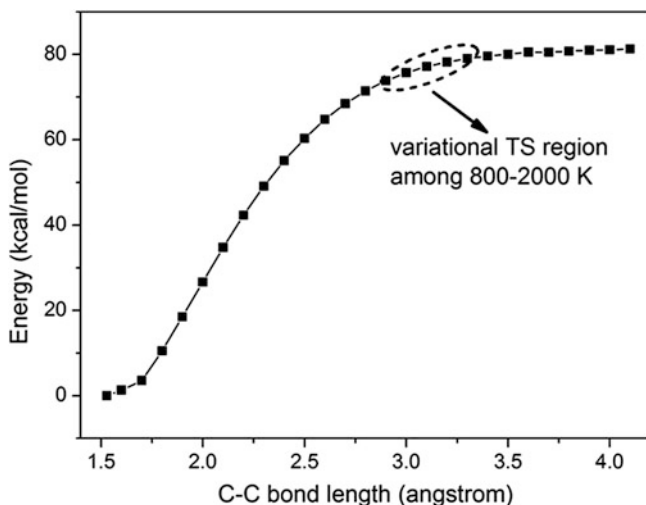
**Fig. 4.4** Potential energy surfaces for RRKM/ME calculation at MRCI+Q/6-31+g(d,p) level of theory. Bracketed values computed at CASPT2/cc-pVDZ level of theory by Skeen et al. [18]. Dashed lines indicate neglected diradical intermediates and H-migration transition states. Red dashed line indicates two possible H-migration channels for 1-heptene. Reprinted with permission from Ref. [24]. Copyright 2013 by American Chemical Society

channel. However, Brown and King suggested that the methyl loss channel was negligible compared to the ring-opening isomerization pathways [4].

The step-wise optimized potential energy curve for methylcyclohexane dissociation via methyl loss is presented in Fig. 4.5. Using methodology in the literature [31, 32], the barrier height of variational transition states was in the range of 74–78 kcal/mol from 800 to 2000 K. Correspondingly, C–C bond stretching varied from 2.9 to 3.2 Å. The lower energy height of the methyl loss channel indicates that this pathway should not be neglected. The kinetics of the methyl loss channel and the ring-opening isomerization pathways will be addressed in the rate constant calculation.

#### 4.2.2.2 Rate Constants Calculation

The first step for rate constant calculation is to validate the rate-controlling assumption, to this end, high pressure limit rate for the two-step isomerization reaction in  $R \rightarrow P6$  were calculated. The result showed that in the studied temperature range of 800–2000 K, the rate constants of  $R \rightarrow INT2$  varied from  $10^{-9}$  to  $10^6$  s $^{-1}$  while the rate constants of  $INT2 \rightarrow P6$  was around  $10^{11}$  s $^{-1}$ . It was noted that the energy barrier of TS6 artificially increased to 87 kcal/mol in this calculation. This comparison indicates that RRKM/ME methods reliably calculate rate constants for potential energy surfaces in Fig. 4.4 for the following reactions (R1–R7).

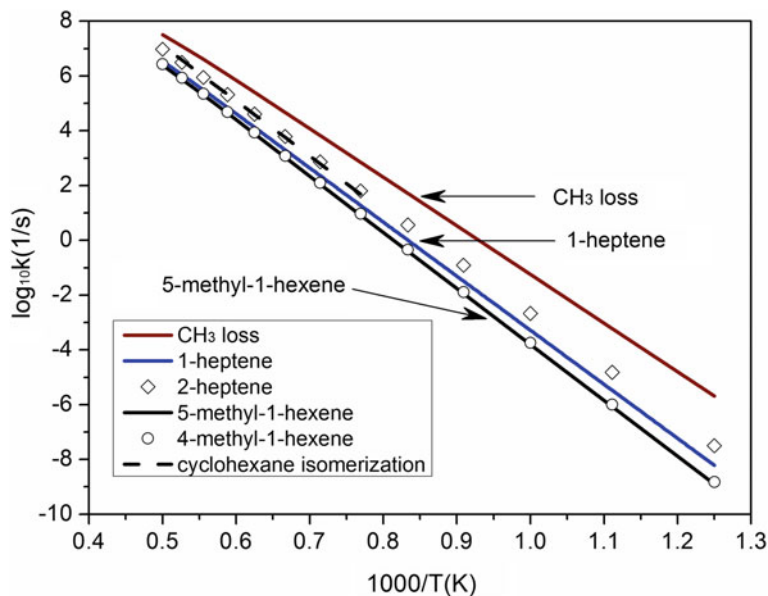


**Fig. 4.5** Step-wise optimized potential energy curve of methylcyclohexane dissociation via methyl loss. The calculation was conducted at MRCI/6-31+g(d,p)//CAS(2e,2o)/6-31+g(d,p) level of theory. Reprinted with permission from Ref. [24]. Copyright 2013 by American Chemical Society



High pressure limit rate constants of **R1–R4** and **R6** are displayed in Fig. 4.6; **R5** and **R7** are not shown because the rate constants of **R4–R7** were nearly identical.

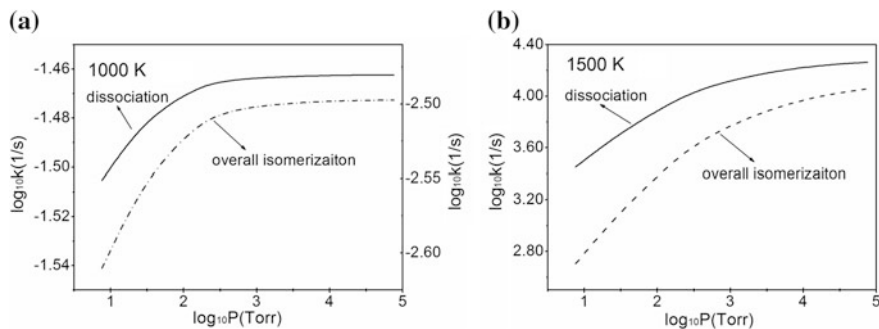
*First*, although two H-migration pathways produce to 1-heptene, the rate constant of **R3** to 2-heptene was higher than that of **R2** because the energy barrier of the saddle point connecting INT1 and 2-heptene was lower. *Second*, the rate constants of **R2** and **R3** were higher than those of the other isomerization pathways of **R4–R7**. This may be due to the lower barrier height to dissociate the C–C bond adjacent to the side-chain (Fig. 4.4). However, even when the temperature was 2000 K, the high pressure limit rate constant of **R3** was a factor of 3 faster than that of **R4**. The difference in the barrier height of these two pathways were probably insufficient to



**Fig. 4.6** High pressure limit rate constants for methylcyclohexane isomerization and dissociation. High pressure limit rate constant of cyclohexane isomerization presented for comparison; considering degeneracy, values are reduced by six. Reprinted with permission from Ref. [24]. Copyright 2013 by American Chemical Society

explain this observation. Another explanation may be that the more flexible structure of TS1 gives it higher entropy than TS5 and TS8. The distinguishable rate constants of R2 and R3 indicate that the production of branched heptene isomers was insignificant during methylcyclohexane pyrolysis at high pressure.

*Third*, the dominant unimolecular reaction of methylcyclohexane is the methyl loss channel. However, with increased temperature, the significance of this pathway decreased, evidently because that the isomerization pathways have high A-factor. Our calculation is in accord with the quantum chemistry calculation of Skeen et al. [18], in which the methyl loss channel was important during methylcyclohexane pyrolysis. This result does not support previous study by Brown and King [4] who suggested that the methyl loss channel is unimportant in methylcyclohexane pyrolysis. Furthermore, this group compared the high pressure limit rate constant of cyclohexane isomerization with those for methylcyclohexane. The A factor of the Arrhenius equation calculated by Kiefer et al. [21] was divided by six, in consideration of the degeneracy. As in the dashed line in Fig. 4.6, the rate constant for cyclohexane isomerization was very close to that of R3, but much higher than those of other isomerization pathways. The higher rate constants of cyclohexane isomerization were probably caused by the reduction of the barrier height from 88.7 to 86.0 kcal/mol, resulting in a better fit with the experimental data by Kiefer et al. [21].



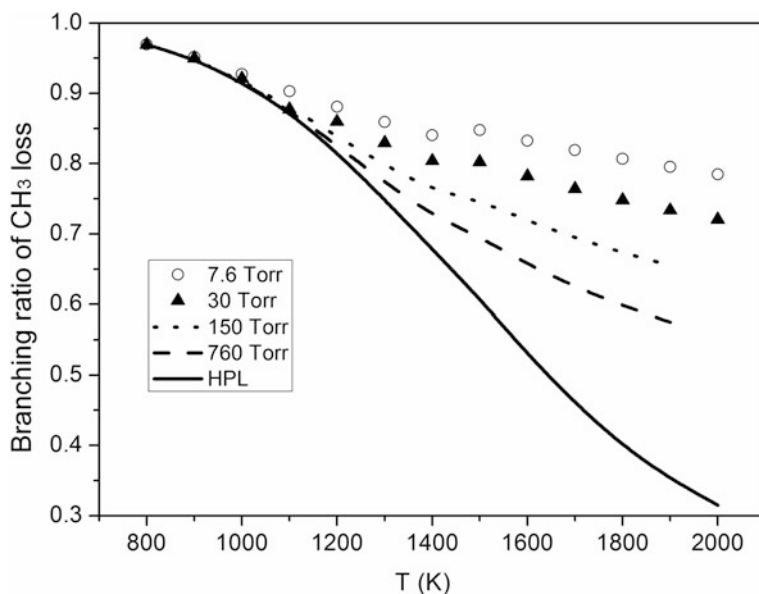
**Fig. 4.7** Rate constants of methylcyclohexane dissociation and isomerization as a function of temperature at **a** 1000 K and **b** 1500 K. Left vertical coordinate is dissociation pathway, right is isomerization pathways in Fig. 4.7a. Reprinted with permission from Ref. [24]. Copyright 2013 by American Chemical Society

The pressure-dependent rate constants of methylcyclohexane dissociation (i.e., R1) and the total rate constants of methylcyclohexane isomerization of R2–R7 at 1000 and 1500 K are presented in Fig. 4.7. *First*, pressure dependence of rate constants is more evident at higher temperatures for both channels. This can be explained by the strong collision model [35, 36]. *Second*, isomerization pathways are more pressure-dependent on rate constants than are dissociation pathways. For example, the rate constant of methylcyclohexane isomerizations at 7.6 Torr and 1500 K is 22.5 times lower than at 76,000 Torr. However, this ratio is only 6.5 for the dissociation channel. When the temperature is increased, it causes the branching ratio to decrease for the dissociation channel, from low to high pressure limits, as shown in Fig. 4.8. For a given temperature, the importance of dissociation channel drops with increased pressure because of the less pressure-dependent dissociation channel.

As discussed above, the canonical variational transition state theory was used to estimate the rate constant of methylcyclohexane dissociation via methyl loss. The rate constants as functions of pressure and temperature were obtained from a rough rigid rotor harmonic oscillator (RRHO) assumption and a simple energy transfer model. It was expected that this methodology could cause large uncertainty within an order of magnitude.

### 4.3 H-atom Abstraction of Methylcyclohexane

In addition to the unimolecular decomposition of methylcyclohexane, this work also calculates the H-atom abstraction rate constant of methylcyclohexane via H atom at CBS-QB3 level of theory [28]. In the calculation, the geometry optimization and vibration analysis were performed at B3LYP/6-311G(2d,d,p) level. A series of high accuracy methods, including a complete basis set extrapolation,

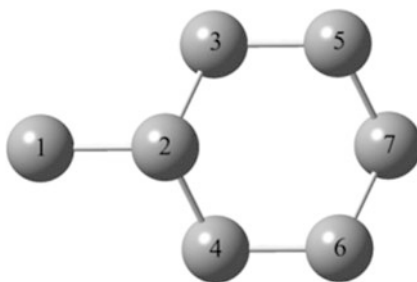


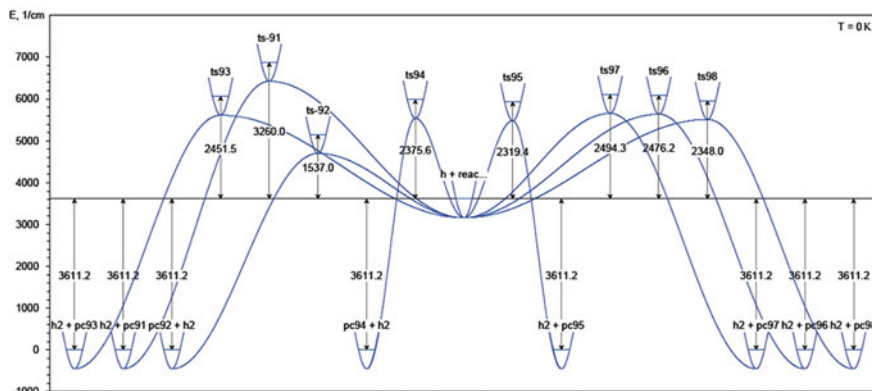
**Fig. 4.8** Branching ratio of methyl loss channel with pressure (e.g., 7.6 Torr to HPL) and temperature (e.g., 800–2000 K). *HPL* High pressure limit. Reprinted with permission from Ref. [24]. Copyright 2013 by American Chemical Society

were then adopted to correct the single potential energy [37]. The Gaussian 09 program was used to conduct the theoretical calculation [30].

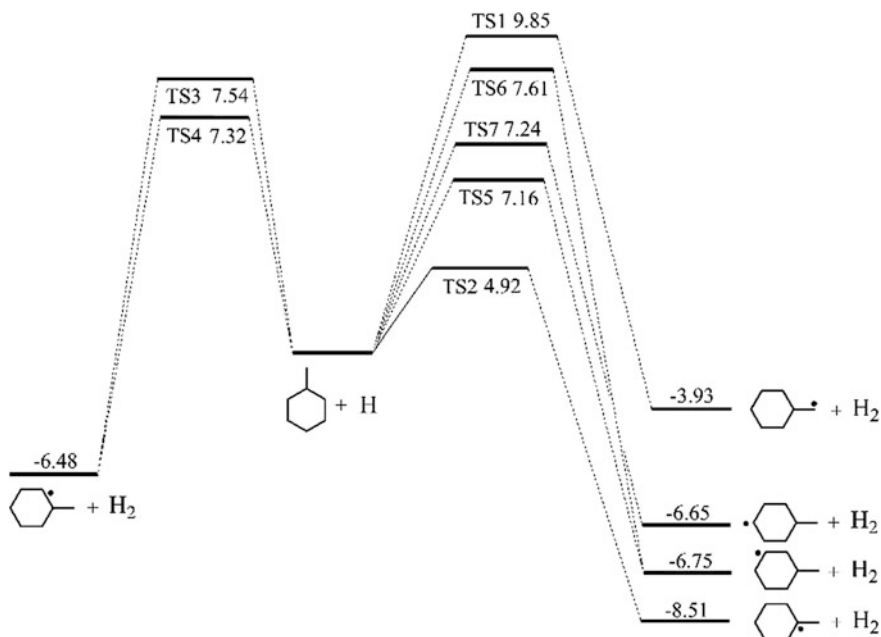
Figure 4.9 shows the structure of methylcyclohexane. Its asymmetric structure causes the differences among the six carbon atoms; the two H-atoms in carbon seven are also different. Thus, in the potential energy surface calculation, eight H-atom abstraction pathways were considered: H+C1(H), degeneracy is 3, H+C2(H), degeneracy is 1, H+C3(H), degeneracy is 2, H+C4(H), degeneracy is 2, H+C5(H), degeneracy is 2, H+C6(H), degeneracy is 2, H+C7(H1), degeneracy is 1 and H+C7(H2), degeneracy is 1, as shown in Fig. 4.10. The potential energy surface of the reaction pathways is shown in Fig. 4.11. Energy barriers for these reactions are very low; the lowest channel is the H-atom abstraction at the tertiary carbon.

**Fig. 4.9** Structure of methylcyclohexane. Only carbon atoms shown





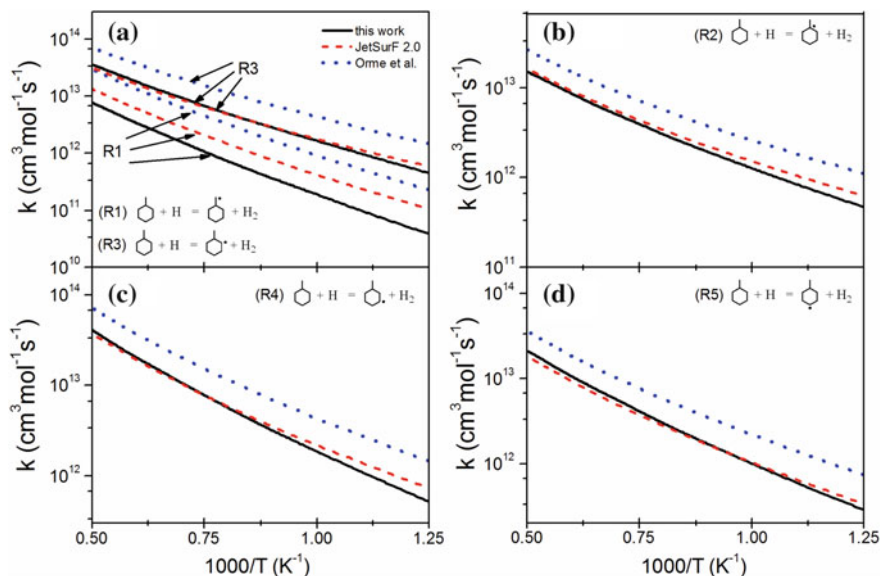
**Fig. 4.10** Detailed reaction pathways for H-atom abstraction reactions of methylcyclohexane by H atom (unit:  $\text{cm}^{-1}$ )



**Fig. 4.11** Reaction pathways for H-atom abstraction reactions of methylcyclohexane by H atom (unit: kcal/mol). Reprinted from Ref. [38], Copyright 2014, with permission from Elsevier

Temperature-dependent rate constants for the reaction pathways in Fig. 4.11 were calculated using the transition state theory. Special consideration was applied for the vibration mode of the internal rotation of the methyl group. It was treated like a hindered rotor, using a symmetric hindrance potential function. The rate



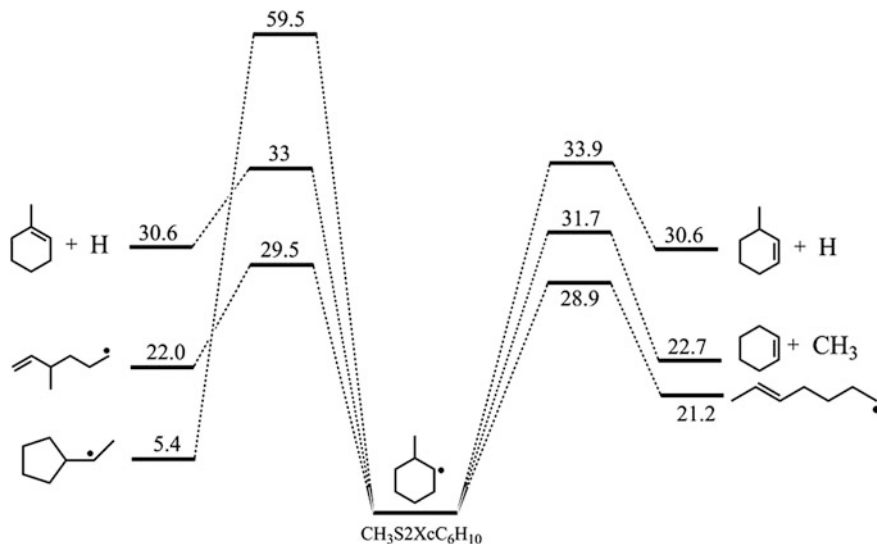


**Fig. 4.12** Rate constants of H-atom abstraction of methylcyclohexane from H atom. Solid lines (this work), dashed lines (JetSurF 2.0 [19]), dotted lines (Orme et al. [7]). Reprinted from Ref. [38], Copyright 2014, with permission from Elsevier

constants were calculated by the ChemRate program [33], and are shown in Fig. 4.12, with rate estimation from JetSurF 2.0 [19] and Orme et al. [7]. The comparison indicates that the three datasets were only slightly different; the calculated rate constants were closer to those from JetSurF 2.0 [19].

#### 4.4 Unimolecular Reactions of Methylcyclohexane Radicals

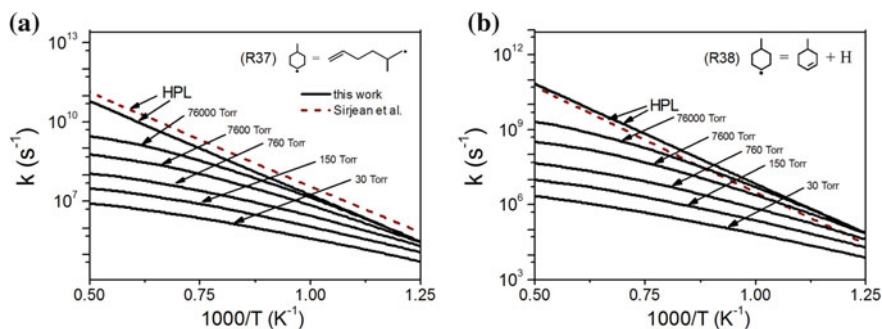
The H-atom abstraction of methylcyclohexane leads to five methylcyclohexane radicals, as shown in Fig. 4.11. The unimolecular reactions of these radicals—dissociation and isomerization—were computed at CBS-QB3 level of theory. The transition state of the calculated reaction pathways was checked by the intrinsic reaction coordinate (IRC) analysis [39]. Figure 4.13 shows the reaction pathways of 2-methyl-cyclohexyl radical, including dissociation via  $\beta$ -C-C scission, or  $\beta$ -C-H scission, and isomerization via  $\beta$ -C-C scission, to open the six-membered ring, or via intramolecular H-shift. The energy barriers of the two ring-opening isomerization pathways are lower than other pathways. Furthermore, ring-opening isomerization, via the dissociation of the C-C bond adjacent to the methyl side-chain, has the lowest energy barrier. Compared to the ring-opening isomerization



**Fig. 4.13** Reaction pathways of 2-methyl-cyclohexyl radical dissociation and isomerization (unit: kcal/mol). Reprinted from Ref. [38], Copyright 2014, with permission from Elsevier

pathways, the dissociation to loss of the methyl group had a slightly higher energy barrier, while the energy barrier of dissociation via the  $\beta$ -C-H scission was 3–4 kcal/mol higher. Another isomerization pathway, shown in Fig. 4.13, leads to a five-membered ring radical; however, the energy barrier for this pathway was quite high and this pathway can be neglected. The potential energy surface for the unimolecular reactions of the other four methylcyclohexane radicals is shown in Appendix B, Figs. B.1a–B.4a. In the rate constant calculation, the conventional transition state theory was applied for reactions with distinct barriers, while barrierless reactions were treated using the variational transition state theory [31]. For barrierless reactions, the critical structure controlling the kinetics in direct bond breaking varies with temperature. Thus, the canonical variational rate constant at high pressure limit was calculated, which is a function of both position and temperature. In the fall-off calculation, the bath gas was Ar. An exponential-down model, i.e.,  $\langle E_{\text{down}} \rangle = 0.4 T$ , was applied in the collisional energy transfer calculation. This is in accord with the computation for dissociation and isomerization of methylcyclohexane. The rate constants at 30, 150, 760, 7600, 76000 Torr and temperatures of 800–2000 K were calculated by the method of RRKM/Master Equation. The program for rate constant calculation was ChemRate [33].

As an example, the pressure-dependent rate constants of 4-methyl-cyclohexyl radical isomerization via  $\beta$ -C-C scission and decomposition via  $\beta$ -C-H scission are presented in Fig. 4.14. The high pressure limit rate constants of similar reactions from cyclohexyl radical, computed by Sirjean et al. [40], are also presented. Although the rate constants calculated in this work were close to those of the same



**Fig. 4.14** Pressure-dependent rate constants for 4-methyl-cyclohexyl radical dissociation and isomerization (solid lines). High pressure limit rate constants of cyclohexyl radical dissociation and isomerization from Sirjean et al. [40] (dashed lines). Reprinted from Ref. [38], Copyright 2014, with permission from Elsevier

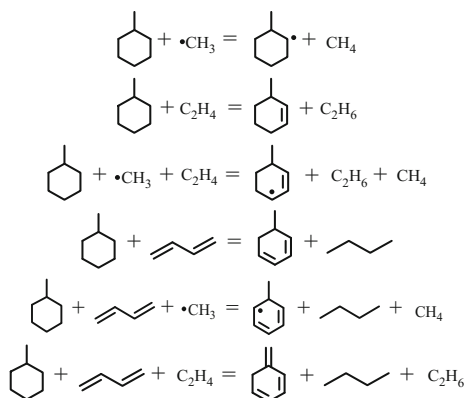
reaction type by Sirjean et al., their branching ratio was different. This may be due to the difference of the calculated energy barrier. For example, the barrier height of the ring-opening isomerization and the H-loss pathways calculated by Sirjean et al. was 29.5 and 35.3 kcal/mol, respectively. For 4-methyl-cyclohexyl radical, the energy barrier for these two pathways was calculated to be 30.2 and 33.6 kcal/mol, respectively. The barrier height difference for these two pathways was 5.8 kcal/mol from the calculation of Sirjean et al. However, this difference was only 3.4 kcal/mol in this work. As discussed in Fig. 3.7 in Sect. 3.2.5, the calculated branching ratio was closer to the experimental measurement by Iwan et al. [41].

## 4.5 Estimation of Thermodynamic Data

Studies of low pressure laminar premixed flame of methylcyclohexane in the literature have shown that the step-wise dehydrogenation of methylcyclohexane are important routes for toluene [18]. The reaction pathways of  $C_7H_{14} \rightarrow C_7H_{13} \rightarrow C_7H_{12} \rightarrow C_7H_{11} \rightarrow C_7H_{10} \rightarrow C_7H_9 \rightarrow C_7H_8$  must be included in the kinetic model to predict aromatic formation in methylcyclohexane combustion. Models in the literature usually treated this reaction route using a lumping method, which did not include all the possible reaction intermediates. This treatment is useful in the model construction, but may increase uncertainty in the model prediction. In this work, detailed reaction pathways for the step-wise dehydrogenation were considered. The thermodynamic data in NASA polynomials of the targeted species were fitted using the FitDat of CHEMKIN-PRO software [42]. The input for this fitting were standard enthalpy of formation, standard molar entropy, and frequency of targeted species. The quantum chemistry calculation at CBS-QB3 level of theory was applied to compute frequencies and standard molar entropy of the species.

In most cases internal degrees of freedom were treated as rigid rotor harmonic oscillators. For internal rotations the hindered rotor treatment was applied.

The standard enthalpy of formation of the intermediate species was obtained by constructing isodesmic reactions for the  $C_7H_{13} \rightarrow C_7H_8$  isomers, as shown below.



The standard enthalpies of reaction for these isodesmic reactions were obtained from the theoretical calculation, while the standard enthalpies of formation for other intermediates in the isodesmic reactions were obtained from an online database, as shown in Table 4.2.

Table 4.3 presents the molecular formula, nomenclature, structure and thermodynamic data for the step-wise dehydrogenation intermediates. The standard enthalpies of formation for selected intermediates, e.g., cyclic  $C_7H_{13}$  and  $C_7H_{12}$ , are compared with the estimation from Orme et al. [7]. In most cases, the discrepancies are about 0.5 kcal/mol. The largest discrepancy of about 1.3 kcal/mol was observed for 3-methyl-cyclohexene.

**Table 4.2** Standard enthalpies of formation for species in isodesmic reactions

	MCH	CH <sub>3</sub>	CH <sub>4</sub>	C <sub>2</sub> H <sub>4</sub>	C <sub>2</sub> H <sub>6</sub>	1,3-butadiene	1-butene
$\Delta_f H^0$ (298 K)	-154.8	146.7	-74.6	52.4	-84	109.2	-125.79
Unit	kJ/mol	kJ/mol	kJ/mol	kJ/mol	kJ/mol	kJ/mol	kJ/mol
Reference	NIST	CCCBDB	CCCBDB	CCCBDB	CCCBDB	CCCBDB	CCCBDB

Reprinted from Ref. [38], Copyright 2014, with permission from Elsevier

Note NIST [43], CCCBDB [44]

Table 4.3 Thermodynamic data of step-wise dehydrogenation intermediates from methylcyclohexane

Formula	Nomenclature	Structure	$\Delta_f H^\circ$ (298 K)	$\Delta_f H^\circ$ (298 K)	$S^\circ$ (298 K)	$C_p$						
						300 K	400 K	500 K	600 K	800 K	1000 K	1500 K
C <sub>7</sub> H <sub>13</sub>	PXCH <sub>2</sub> cC6H <sub>11</sub>		12.75	12.25 <sup>a</sup>	84.78	31.69	42.34	52.00	60.15	72.79	81.99	96.02
C <sub>7</sub> H <sub>13</sub>	CH <sub>3</sub> TXcC6H <sub>10</sub>		8.18	7.65 <sup>a</sup>	85.59	30.98	41.45	51.13	59.41	72.33	81.73	96.00
C <sub>7</sub> H <sub>13</sub>	CH <sub>3</sub> S2XcC6H <sub>10</sub>		10.17	9.6 <sup>a</sup>	84.37	31.48	42.03	51.66	59.85	72.59	81.87	96.00
C <sub>7</sub> H <sub>13</sub>	CH <sub>3</sub> S3XcC6H <sub>10</sub>		9.91	9.6 <sup>a</sup>	84.31	31.56	42.07	51.70	59.89	72.61	81.89	96.02
C <sub>7</sub> H <sub>13</sub>	CH <sub>3</sub> S4XcC6H <sub>10</sub>		10.00	9.6 <sup>a</sup>	84.21	31.50	42.03	51.66	59.85	72.59	81.89	96.02
C <sub>7</sub> H <sub>12</sub>	CH <sub>3</sub> -4-cC <sub>6</sub> H <sub>9</sub>		-8.67	-9.37 <sup>a</sup>	80.61	29.35	39.50	48.76	56.63	68.79	77.64	91.05
C <sub>7</sub> H <sub>12</sub>	CH <sub>3</sub> -3-cC <sub>6</sub> H <sub>9</sub>		-8.19	-9.54 <sup>a</sup>	80.66	29.27	39.46	48.72	56.59	68.77	77.62	91.03
C <sub>7</sub> H <sub>12</sub>	CH <sub>3</sub> -1-cC <sub>6</sub> H <sub>9</sub>		-10.12	-10.65 <sup>a</sup>	81.23	29.49	39.52	48.70	56.53	68.71	77.58	91.03
C <sub>7</sub> H <sub>12</sub>	CH <sub>2</sub> cC <sub>6</sub> H <sub>10</sub>		-8.12	-7.71 <sup>a</sup>	79.59	28.79	39.25	48.62	56.55	68.75	77.60	91.01
C <sub>7</sub> H <sub>11</sub>	CH <sub>3</sub> -5-SAxcC <sub>6</sub> H <sub>8</sub>		22.32		81.84	29.43	39.23	47.93	55.22	66.41	74.46	86.68
C <sub>7</sub> H <sub>11</sub>	CH <sub>3</sub> -4-SAxcC <sub>6</sub> H <sub>8</sub>		22.77		81.86	29.35	39.15	47.89	55.18	66.37	74.42	86.64
C <sub>7</sub> H <sub>11</sub>	CH <sub>3</sub> -3-SAxcC <sub>6</sub> H <sub>8</sub>		20.65		83.08	29.47	39.07	47.73	55.02	66.25	74.38	86.66
C <sub>7</sub> H <sub>11</sub>	CH <sub>3</sub> -2-SAxcC <sub>6</sub> H <sub>8</sub>		22.37		86.10	29.77	39.36	47.97	55.22	66.37	74.42	86.66
C <sub>7</sub> H <sub>11</sub>	CH <sub>3</sub> -1-SAxcC <sub>6</sub> H <sub>8</sub>		20.66		83.14	29.47	39.07	47.73	55.02	66.25	74.38	86.66
C <sub>7</sub> H <sub>11</sub>	CH <sub>2</sub> SAXcC <sub>6</sub> H <sub>9</sub>		25.40		81.32	29.17	39.13	47.91	55.22	66.39	74.44	86.66
C <sub>7</sub> H <sub>10</sub>	CH <sub>2</sub> -3-cC <sub>6</sub> H <sub>8</sub>		15.96		78.37	27.32	36.78	45.11	52.06	62.63	70.22	81.71
C <sub>7</sub> H <sub>10</sub>	CH <sub>3</sub> -2-cC <sub>6</sub> H <sub>7</sub> -13		16.35		79.94	28.16	37.24	45.39	52.22	62.71	70.30	81.77
C <sub>7</sub> H <sub>10</sub>	CH <sub>3</sub> -1-cC <sub>6</sub> H <sub>7</sub> -13		15.66		79.83	28.08	37.18	45.33	52.18	62.71	70.30	81.77
C <sub>7</sub> H <sub>10</sub>	CH <sub>3</sub> -5-cC <sub>6</sub> H <sub>7</sub> -13		17.99		79.29	27.88	37.16	45.39	52.26	62.79	70.34	81.77
C <sub>7</sub> H <sub>9</sub>	CH <sub>3</sub> -5-SAxcC <sub>6</sub> H <sub>6</sub>		37.45		80.93	27.66	36.44	44.13	50.51	60.17	67.06	77.40
C <sub>7</sub> H <sub>9</sub>	CH <sub>3</sub> -6-SAxcC <sub>6</sub> H <sub>6</sub>		40.38		80.33	27.38	36.40	44.21	50.59	60.21	67.02	77.32
C <sub>7</sub> H <sub>9</sub>	CH <sub>3</sub> -2-SAxcC <sub>6</sub> H <sub>6</sub>		38.68		81.48	27.86	36.64	44.31	50.65	60.25	67.08	77.40

(continued)

Table 4.3 (continued)

Formula	Nomenclature	Structure	$\Delta_f H^0$ (298 K)	$\Delta_f H^0$ (298 K)	$S^0$ (298 K)	$C_p$									
						300 K	400 K	500 K	600 K	800 K	1000 K	1500 K			
$C_7H_9$	$CH_3$ -3-SAXcC <sub>6</sub> H <sub>6</sub>		38.85		85.73	27.78	36.50	44.15	50.51	60.17	67.06	77.40			
$C_7H_9$	$CH_3$ -4-SAXcC <sub>6</sub> H <sub>6</sub>		38.68		81.48	27.86	36.64	44.31	50.65	60.25	67.08	77.40			
$C_7H_9$	$CH_3$ -1-SAXcC <sub>6</sub> H <sub>6</sub>		37.42		80.99	27.68	36.46	44.15	50.53	60.19	67.06	77.42			
$C_7H_9$	$CH_2$ -6-SAXcC <sub>6</sub> H <sub>7</sub>		43.07		79.26	27.30	36.42	44.25	50.65	60.25	67.06	77.34			
$C_7H_9$	$CH_2$ -3-PXcC <sub>6</sub> H <sub>7</sub>		50.10		79.79	27.82	36.76	44.51	50.87	60.41	67.16	77.30			
$C_7H_8$	$CH_2$ -5-cC <sub>6</sub> H <sub>6</sub> -13		42.96		77.81	25.91	34.44	41.73	47.69	56.61	62.95	72.45			
$C_7H_8$	$CH_2$ -3-cC <sub>6</sub> H <sub>6</sub> -14		39.02		76.68	25.75	34.28	41.57	47.55	56.51	62.89	72.45			

Reprinted from Ref. [38], Copyright 2014, with permission from Elsevier

<sup>a</sup>Estimation from Orme et al. [7]; The unit for  $\Delta_f H^0$ ,  $S^0$ ,  $C_p$  is kcal/mol, cal/mol/K, and cal/mol/K, respectively

## 4.6 Kinetic Model for Methylcyclohexane Combustion

The kinetic model for cyclohexane combustion, including the sub-mechanism of cyclohexane and the C0–C4 base model, was discussed in detail in Chap. 3. The sub-mechanism of methylcyclohexane was developed in this chapter and added to the kinetic model of cyclohexane. The reaction class of methylcyclohexane combustion includes:

- (a) Unimolecular decomposition and isomerization of methylcyclohexane
- (b) Dissociation of heptenes and methyl-hexenes
- (c) H-atom abstraction of methylcyclohexane
- (d) Decomposition and isomerization of methylcyclohexane radicals
- (e) Decomposition and isomerization of heptenyl radicals and methyl-hexenyl radicals
- (f) Decomposition and step-wise dehydrogenation of cyclic  $C_7H_{12}$  intermediates.

Pressure and temperature dependent rate constants of methylcyclohexane dissociation and isomerization were specifically adopted from high-level quantum chemistry calculation, as discussed in Sect. 4.2. The isomerization of methylcyclohexane forms two heptene isomers (1-heptene and 2-heptene) and four methyl-hexenes (2-methyl-1-hexene, 3-methyl-1-hexene, 4-methyl-1-hexene, and 5-methyl-1-hexene). The dominant unimolecular decomposition pathway of these alkenes occurs by breaking the allylic C–C bond. Rate constants for this reaction class were estimated from unimolecular decomposition of 1-hexene to allyl radical and *n*-propyl radical. For the H-atom abstraction reactions of these alkenes, the rate constants were estimated from the rate rules proposed by Pitz et al. [7, 12]. The methyl loss of methylcyclohexane forms cyclohexyl radical, whose reaction pathways have also been included in the sub-mechanism of cyclohexane in Sect. 3.2.4.

For H-atom abstractions of methylcyclohexane, the rate constants of H-atom abstraction by H atom were calculated in this work. Those by OH radical, O atom,  $O_2$ ,  $HO_2$  radical and  $CH_3$  radical were adopted from JetSurF 2.0 [19]. The rate constants of subsequent reactions of methylcyclohexane radicals—dissociation and ring-opening isomerization—were adopted from the quantum chemistry calculation in this work. The ring-opening isomerization of five methylcyclohexane radicals led to heptenyl radicals and/or methyl-hexenyl radicals, which underwent intramolecular H-shift isomerization and  $\beta$ -C–C scission dissociation. The rate constants for these reactions in the format of Troe parameters were also taken from the JetSurF 2.0 model [19].

In the flame experiment of methylcyclohexane by Skeen et al. [18], a series of C6 and C7 cyclic compounds were detected. These intermediates were also measured in the flame experiment in this work and are evidence that the step-wise dehydrogenation of methylcyclohexane leads to aromatics like benzene and toluene. In this work, a detailed reaction mechanism from methylcyclohexane to benzene and toluene (including the important step-wise dehydrogenation intermediates of  $C_7H_{12}$ ,  $C_7H_{11}$ ,  $C_7H_{10}$ ,  $C_7H_9$  and  $C_7H_8$ ) was developed. The rate constants of H-elimination

of  $C_7H_{12}$  and  $C_7H_{10}$  were estimated from that of propene ( $C_3H_6$ ), while the rate constants of  $\beta$ -C-H scission of 1-buten-3-yl radical ( $SAXC_4H_7$ ) were applied for  $C_7H_{11}$  and  $C_7H_9$  radicals. For  $C_7H_{12}$  and  $C_7H_{10}$ , H-atom abstraction reactions were also considered, and the rate rule from Pitz et al. [7, 12] was utilized. Like cyclohexene, the retro-Diels-Alder reaction dissociates methylcyclohexenes into smaller intermediates. The rate constants for this process referred to those of cyclohexene. In the step-wise dehydrogenation process of methylcyclohexane, the isomers of toluene, *o*-isotoluene and *p*-isotoluene ( $cC_7H_8$ ) are formed. Similar to toluene, the H-elimination of these intermediates forms benzyl radical ( $C_7H_7$ ). The rate constants for this reaction were from theoretical calculation by Klippenstein et al. [45]. Table 4.4 shows the sub-mechanism of methylcyclohexane.

## 4.7 Flow Reactor Pyrolysis

The flow reactor pyrolysis of methylcyclohexane at 30, 150, and 760 Torr was performed with a total flow rate of 1000 sccm at standard temperature and pressure (STP). The inlet mole fraction of methylcyclohexane and Ar was 0.02 and 0.98, respectively. These experimental conditions were similar to the cyclohexane pyrolysis experiment. The quantification of some intermediates, such as 2-methyl-1,3-butadiene, 2-heptene,  $cC_7H_8$ ,  $C_7H_{10}$ ,  $C_7H_{12}$ , cyclopentadienyl radical ( $C_5H_5$ ), cyclopentadiene ( $C_5H_6$ ) and fulvene, required estimation of the photoionization cross sections. These values were obtained from species with similar structure, or taken from estimations in the literature.

Previous study of methylcyclohexane by Zippieri et al. [5] detected and quantified  $\sim 15$  species; ethylene, 1,3-butadiene, methane and propene are the major products. This work measured more than 30 pyrolysis intermediates. The newly detected intermediates include the initial dissociation and isomerization products (methyl radical and 2-heptene) of methylcyclohexane, cyclic compounds fulvene, 1,3-cyclohexadiene,  $C_7H_8$  (*o*-isotoluene and *p*-isotoluene),  $C_7H_{10}$  and  $C_7H_{12}$ , etc. In the steam pyrolysis of methylcyclohexane [46], 2-heptene and some cyclic  $C_7H_{12}$  compounds were also detected in a tubular reactor. However, the species pool in methylcyclohexane pyrolysis were quite different under supercritical conditions [47].

### 4.7.1 Consumption of Methylcyclohexane

The mole fraction profiles of methylcyclohexane, 2-heptene, 1-heptene and methyl radical are presented in Fig. 4.15. The pyrolysis experiment at 30 Torr favored the formation of 2-heptene and methyl radical, which were detected from the experiment. With increased pressure, their concentration was below the detection limit of



**Table 4.4** Sub-mechanism of methylcyclohexane in this work

No.	Reactions	A	n	E	Pressure (Torr)	Refs.
<i>Reactions of methylcyclohexane</i>						
1	$\text{CH}_3\text{C}_6\text{H}_{11} + \text{H} = \text{PXCH}_2\text{cC}_6\text{H}_{11} + \text{H}_2$	6.66E+06	2.13	8895		This work
2	$\text{CH}_3\text{C}_6\text{H}_{11} + \text{H} = \text{CH}_3\text{TXcC}_6\text{H}_{10} + \text{H}_2$	4.53E+06	2.11	4099		This work
3	$\text{CH}_3\text{C}_6\text{H}_{11} + \text{H} = \text{CH}_3\text{S2XcC}_6\text{H}_{10} + \text{H}_2$	2.08E+07	2.10	6474		This work
4	$\text{CH}_3\text{C}_6\text{H}_{11} + \text{H} = \text{CH}_3\text{S3XcC}_6\text{H}_{10} + \text{H}_2$	2.07E+07	2.12	6441		This work
5	$\text{CH}_3\text{C}_6\text{H}_{11} + \text{H} = \text{CH}_3\text{S4XcC}_6\text{H}_{10} + \text{H}_2$	1.16E+07	2.11	6339		This work
6	$\text{CH}_3\text{C}_6\text{H}_{11} + \text{OH} = \text{PXCH}_2\text{cC}_6\text{H}_{11} + \text{H}_2\text{O}$	5.33E+03	2.90	504		[19]
7	$\text{CH}_3\text{C}_6\text{H}_{11} + \text{OH} = \text{CH}_3\text{TXcC}_6\text{H}_{10} + \text{H}_2\text{O}$	6.69E+03	2.82	2966		[19]
8	$\text{CH}_3\text{C}_6\text{H}_{11} + \text{OH} = \text{CH}_3\text{S2XcC}_6\text{H}_{10} + \text{H}_2\text{O}$	8.13E+03	2.84	-1479		[19]
9	$\text{CH}_3\text{C}_6\text{H}_{11} + \text{OH} = \text{CH}_3\text{S3XcC}_6\text{H}_{10} + \text{H}_2\text{O}$	9.50E+03	2.85	-1023		[19]
10	$\text{CH}_3\text{C}_6\text{H}_{11} + \text{OH} = \text{CH}_3\text{S4XcC}_6\text{H}_{10} + \text{H}_2\text{O}$	5.82E+03	2.85	-1011		[19]
11	$\text{CH}_3\text{C}_6\text{H}_{11} + \text{CH}_3 = \text{PXCH}_2\text{cC}_6\text{H}_{11} + \text{CH}_4$	3.75E+01	3.27	13,516		[19]
12	$\text{CH}_3\text{C}_6\text{H}_{11} + \text{CH}_3 = \text{CH}_3\text{TXcC}_6\text{H}_{10} + \text{CH}_4$	1.91E+01	3.27	9022		[19]
13	$\text{CH}_3\text{C}_6\text{H}_{11} + \text{CH}_3 = \text{CH}_3\text{S2XcC}_6\text{H}_{10} + \text{CH}_4$	6.68E+01	3.21	11,418		[19]
14	$\text{CH}_3\text{C}_6\text{H}_{11} + \text{CH}_3 = \text{CH}_3\text{S3XcC}_6\text{H}_{10} + \text{CH}_4$	7.18E+01	3.26	11,303		[19]
15	$\text{CH}_3\text{C}_6\text{H}_{11} + \text{CH}_3 = \text{CH}_3\text{S4XcC}_6\text{H}_{10} + \text{CH}_4$	1.82E+01	3.36	10,931		[19]
16	$\text{CH}_3\text{C}_6\text{H}_{11} = \text{cC}_6\text{H}_{11} + \text{CH}_3$	1.85E+105	-26.15	129,214	7.6	This work
		1.19E+92	-22.23	122,595	30	This work
		1.50E+80	-18.67	116,938	150	This work
		5.93E+64	-14.15	108,486	760	This work
		3.59E+45	-8.56	97,430	7600	This work
		1.66E+33	-4.99	90,100	76,000	This work
		1.10E+27	-3.20	86,385	HPL	This work

(continued)

Table 4.4 (continued)

No.	Reactions	A	n	E	Pressure (Torr)	Refs.
17	$\text{CH}_3\text{cC}_6\text{H}_{11} = \text{C}_7\text{H}_{14+1}$	5.49E+115	-29.26	143,180	7.6	This work
		1.03E+104	-25.68	138,280	30	This work
		1.92E+88	-20.96	130,954	150	This work
		5.57E+69	-15.49	121,178	760	This work
		4.90E+44	-8.17	107,073	7600	This work
		7.98E+26	-3.02	96,627	76,000	This work
		1.09E+17	-0.16	90,732	HPL	This work
18	$\text{CH}_3\text{cC}_6\text{H}_{11} = \text{C}_7\text{H}_{14+2}$	9.52E+114	-28.98	140,737	7.6	This work
		1.74E+103	-25.40	135,829	30	This work
		3.34E+87	-20.68	128,511	150	This work
		9.66E+68	-15.21	118,735	760	This work
		8.51E+43	-7.89	104,630	7600	This work
		1.38E+26	-2.74	94,184	76,000	This work
		1.90E+16	0.12	88,289	HPL	This work
19	$\text{CH}_3\text{cC}_6\text{H}_{11} = \text{CH}_3\text{-2-1C}_6\text{H}_{11}$	2.25E+132	-34.10	155,250	7.6	This work
		1.46E+109	-27.20	144,350	30	This work
		4.09E+93	-22.49	137,505	150	This work
		3.27E+74	-16.83	127,710	760	This work
		3.09E+47	-8.92	112,705	7600	This work
		2.18E+27	-3.08	100,948	76,000	This work
		6.04E+15	0.27	94,051	HPL	This work
20	$\text{CH}_3\text{cC}_6\text{H}_{11} = \text{CH}_3\text{-5-1C}_6\text{H}_{11}$	1.99E+132	-34.11	154,207	7.6	This work
		1.28E+109	-27.20	143,306	30	This work

(continued)

Table 4.4 (continued)

No.	Reactions	A	n	E	Pressure (Torr)	Refs.
		3.61E+93	-22.49	136,462	150	This work
		2.89E+74	-16.83	126,667	760	This work
		2.73E+47	-8.93	111,662	7600	This work
		1.93E+27	-3.08	99,905	76,000	This work
		5.34E+15	0.27	93,008	HPL	This work
21	$\text{CH}_3\text{cC}_6\text{H}_{11} = \text{CH}_3\text{-3-IC}_6\text{H}_{11}$	1.70E+119	-30.34	147,025	7.6	This work
		1.77E+108	-26.94	142,902	30	This work
		4.67E+92	-22.23	136,004	150	This work
		3.71E+73	-16.58	126,164	760	This work
		5.09E+46	-8.72	111,220	7600	This work
		6.68E+26	-2.95	99,619	76,000	This work
		2.53E+15	0.36	92,802	HPL	This work
22	$\text{CH}_3\text{cC}_6\text{H}_{11} = \text{CH}_3\text{-4-IC}_6\text{H}_{11}$	1.87E+119	-30.34	146,825	7.6	This work
		1.95E+108	-26.95	142,703	30	This work
		5.13E+92	-22.24	135,803	150	This work
		4.07E+73	-16.58	125,964	760	This work
		5.59E+46	-8.72	111,019	7600	This work
		7.33E+26	-2.95	99,418	76,000	This work
		2.78E+15	0.35	92,602	HPL	This work
<i>Reactions of cC<sub>7</sub>H<sub>13</sub> radicals</i>						
23	$\text{PXCH}_2\text{cC}_6\text{H}_{11} = \text{PXC}_7\text{H}_{13}$	8.92E+18	-2.94	19,897	30	This work
		6.83E+22	-3.82	23,511	150	This work
		1.56E+29	-5.39	29,211	760	This work

(continued)

Table 4.4 (continued)

No.	Reactions	A	n	E	Pressure (Torr)	Refs.
		4.15E+37	-7.44	37,753	7600	This work
		1.92E+39	-7.58	42,286	76,000	This work
		2.53E+13	0.16	29,785	HPL	This work
24	PXCH <sub>2</sub> cC <sub>6</sub> H <sub>11</sub> = CH <sub>2</sub> cC <sub>6</sub> H <sub>10</sub> + H	8.14E+14	-2.42	21,719	30	This work
		1.23E+20	-3.61	26,095	150	This work
		1.18E+28	-5.58	32,946	760	This work
		1.31E+39	-8.28	43,693	7600	This work
		4.67E+42	-8.87	50,298	76,000	This work
		1.60E+11	0.59	35,447	HPL	This work
25	CH <sub>3</sub> TXcC <sub>6</sub> H <sub>10</sub> = CH <sub>3</sub> -2-PXC <sub>6</sub> H <sub>10</sub>	7.77E+21	-3.78	22,330	30	This work
		2.46E+23	-3.98	24,528	150	This work
		3.46E+31	-6.06	31,348	760	This work
		3.04E+40	-8.25	40,204	7600	This work
		3.40E+43	-8.78	45,692	76,000	This work
		2.51E+13	0.24	31,344	HPL	This work
26	CH <sub>3</sub> TXcC <sub>6</sub> H <sub>10</sub> = CH <sub>2</sub> cC <sub>6</sub> H <sub>10</sub> + H	5.68E+24	-4.98	28,465	30	This work
		4.63E+25	-4.97	30,017	150	This work
		2.67E+34	-7.20	37,107	760	This work
		4.39E+44	-9.70	46,944	7600	This work
		1.12E+49	-10.55	53,815	76,000	This work
		1.18E+14	-0.04	37,343	HPL	This work
27	CH <sub>3</sub> TXcC <sub>6</sub> H <sub>10</sub> = CH <sub>3</sub> -1-cC <sub>6</sub> H <sub>9</sub> + H	1.47E+22	-4.09	24,874	30	This work
		1.57E+23	-4.12	26,671	150	This work
		7.83E+31	-6.33	33,844	760	This work

(continued)

Table 4.4 (continued)

No.	Reactions	A	n	E	Pressure (Torr)	Refs.
		6.83E+41	-8.76	43,572	7600	This work
		7.93E+45	-9.52	50,174	76,000	This work
		5.80E+12	0.46	34,881	HPL	This work
28	$\text{CH}_3\text{S2XcC}_6\text{H}_{10} = \text{CH}_3\text{-3-PXC}_6\text{H}_{10}$	1.24E+22	-4.01	22,066	30	This work
		4.17E+22	-3.93	23,430	150	This work
		1.01E+28	-5.23	28,271	760	This work
		2.14E+37	-7.54	37,062	7600	This work
		1.11E+43	-8.81	44,209	76,000	This work
		1.59E+13	0.22	31,118	HPL	This work
29	$\text{CH}_3\text{S2XcC}_6\text{H}_{10} = \text{PX7-2C}_7\text{H}_{13}$	2.99E+22	-4.04	21,843	30	This work
		8.66E+22	-3.95	23,164	150	This work
		1.44E+28	-5.21	27,888	760	This work
		1.61E+37	-7.45	36,452	7600	This work
		4.39E+42	-8.66	43,334	76,000	This work
		2.37E+13	0.19	30,429	HPL	This work
30	$\text{CH}_3\text{S2XcC}_6\text{H}_{10} = \text{CH}_3\text{-1-cC}_6\text{H}_9 + \text{H}$	2.06E+20	-3.80	23,117	30	This work
		1.50E+21	-3.78	24,651	150	This work
		2.14E+27	-5.27	30,013	760	This work
		8.88E+37	-7.90	39,841	7600	This work
		9.49E+44	-9.50	48,246	76,000	This work
		5.69E+11	0.60	34,004	HPL	This work
31	$\text{CH}_3\text{S2XcC}_6\text{H}_{10} = \text{CH}_3\text{-3-cC}_6\text{H}_9 + \text{H}$	1.82E+20	-3.68	23,447	30	This work
		1.92E+21	-3.70	25,053	150	This work
		5.62E+27	-5.27	30,610	760	This work

(continued)

Table 4.4 (continued)

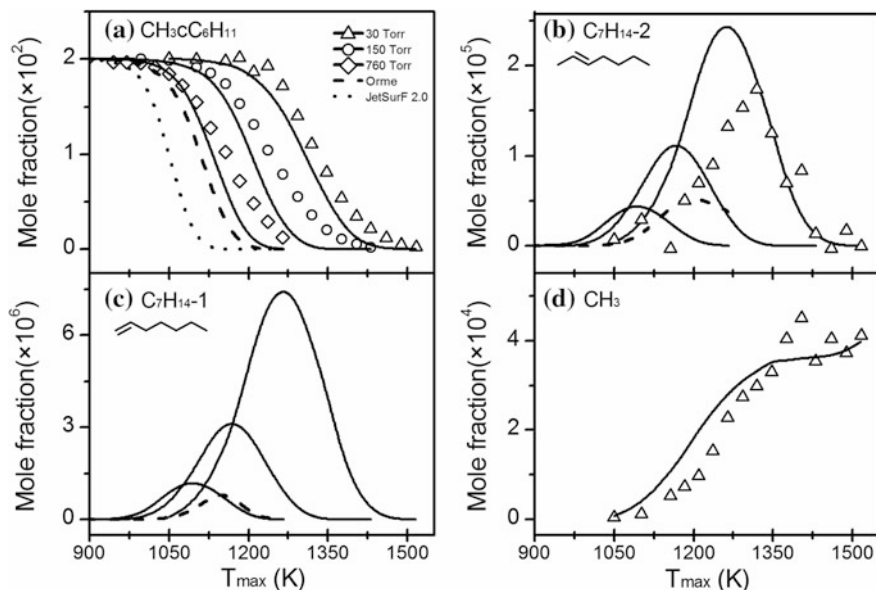
No.	Reactions	A	n	E	Pressure (Torr)	Refs.
		7.34E+38	-8.02	40,816	7600	This work
		2.67E+46	-9.75	49,698	76,000	This work
		2.01E+12	0.63	35,196	HPL	This work
32	$\text{CH}_3\text{S2XcC}_6\text{H}_{10} = \text{cC}_6\text{H}_{10} + \text{CH}_3$	4.24E+21	-3.89	22,867	30	This work
		2.58E+22	-3.86	24,360	150	This work
		2.27E+28	-5.30	29,571	760	This work
		4.14E+38	-7.84	39,088	7600	This work
		1.94E+45	-9.36	47,105	76,000	This work
		6.35E+13	0.20	33,524	HPL	This work
33	$\text{CH}_3\text{S3XC}_6\text{H}_{10} = \text{CH}_3\text{-4-PXC}_6\text{H}_{10}$	1.21E+18	-2.84	19,903	30	This work
		7.98E+21	-3.70	23,365	150	This work
		2.52E+28	-5.31	28,978	760	This work
		8.05E+37	-7.66	38,033	7600	This work
		6.13E+42	-8.70	44,718	76,000	This work
		1.68E+13	0.21	31,241	HPL	This work
34	$\text{CH}_3\text{S3XC}_6\text{H}_{10} = \text{SXC}_7\text{H}_{13}$	5.23E+18	-2.93	19,555	30	This work
		2.06E+22	-3.73	22,876	150	This work
		3.29E+28	-5.27	28,275	760	This work
		3.31E+37	-7.49	36,918	7600	This work
		8.80E+41	-8.42	43,157	76,000	This work
		2.55E+13	0.17	30,061	HPL	This work
35	$\text{CH}_3\text{S3XC}_6\text{H}_{10} = \text{CH}_3\text{-4-cC}_6\text{H}_9 + \text{H}$	1.19E+16	-2.44	20,998	30	This work
		5.50E+20	-3.50	24,928	150	This work
		1.93E+28	-5.37	31,247	760	This work

(continued)

Table 4.4 (continued)

No.	Reactions	A	n	E	Pressure (Torr)	Refs.
		3.19E+39	-8.14	41,683	7600	This work
		1.03E+46	-9.58	49,952	76,000	This work
		1.87E+12	0.63	34,980	HPL	This work
36	$\text{CH}_3\text{S3XcC}_6\text{H}_{10} = \text{CH}_3\text{-3-cC}_6\text{H}_9 + \text{H}$	6.78E+14	-2.23	21,396	30	This work
		8.10E+19	-3.39	25,518	150	This work
		8.05E+27	-5.38	32,106	760	This work
		6.73E+39	-8.33	43,061	7600	This work
		1.12E+47	-9.95	51,964	76,000	This work
		1.64E+12	0.61	36,658	HPL	This work
37	$\text{CH}_3\text{S4XcC}_6\text{H}_{10} = \text{PXCH}_2\text{-5-1C}_6\text{H}_{11}$	1.26E+22	-3.85	22,627	30	This work
		3.57E+26	-4.89	26,638	150	This work
		2.59E+32	-6.32	32,020	760	This work
		2.07E+41	-8.51	40,814	7600	This work
		5.79E+44	-9.15	46,530	76,000	This work
		3.87E+13	0.20	31,782	HPL	This work
38	$\text{CH}_3\text{S4XcC}_6\text{H}_{10} = \text{CH}_3\text{-4-cC}_6\text{H}_9 + \text{H}$	8.38E+20	-3.63	23,771	30	This work
		8.32E+25	-4.80	28,120	150	This work
		5.73E+32	-6.47	34,206	760	This work
		1.37E+43	-9.02	44,242	7600	This work
		7.21E+47	-9.98	51,272	76,000	This work
		3.78E+12	0.63	34,881	HPL	This work

Reprinted from Ref. [38]. Copyright 2014, with permission from Elsevier  
 Note k =  $\text{AT}^n \exp(-E/RT)$ , unit is  $\text{cm}^3$ , mol, s, cal; HPL High pressure limit



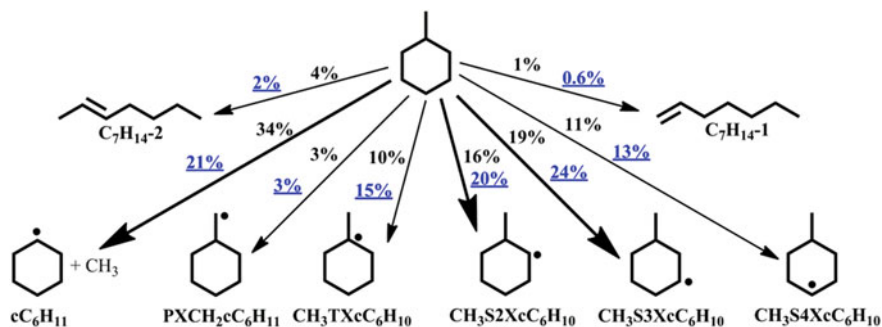
**Fig. 4.15** Mole fraction profiles of **a** methylcyclohexane, **b** 2-heptene, **c** 1-heptene and **d**  $\text{CH}_3$  during methylcyclohexane pyrolysis at 30, 150 and 760 Torr. Symbols are experimental data. Solid lines are model prediction in this work, dashed lines are model prediction at 760 Torr by Orme et al. [7], and dotted lines are model prediction at 760 Torr by JetSurF 2.0 [19]. Reprinted from Ref. [38], Copyright 2014, with permission from Elsevier

the mass spectrometer. The quantum chemistry calculation showed that the dominant isomerization product of methylcyclohexane was 2-heptene. This conclusion was in accord with the experiment that measured 2-heptene. The simulation also showed that the mole fraction of other isomerization products (1-heptene in Fig. 4.15c) was much lower than that of 2-heptene.

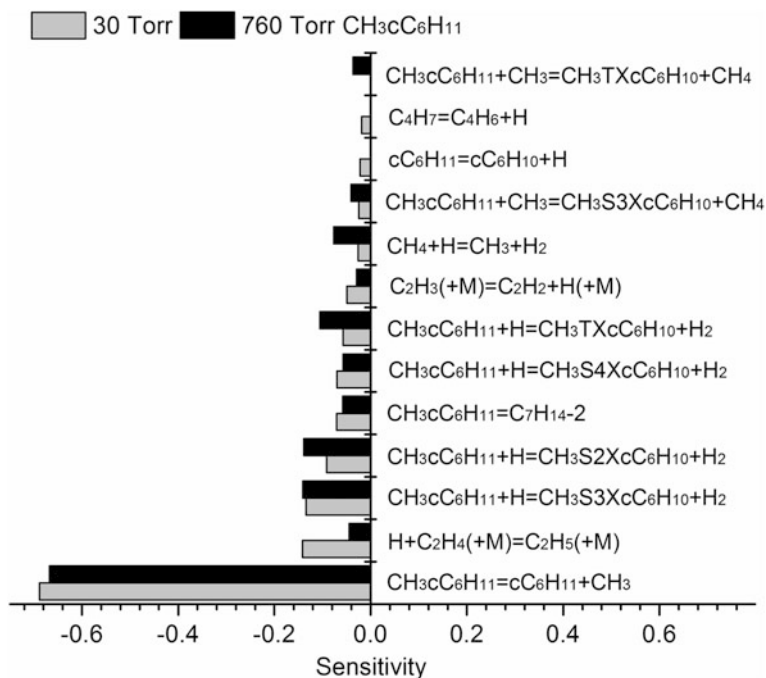
Figure 4.16 shows the reaction flux of methylcyclohexane at 30 and 760 Torr. In conversion of approximately 80%, methylcyclohexane is mostly consumed by unimolecular dissociation, isomerization, and H-atom abstraction by H atom and methyl radical. The contribution of unimolecular dissociation and isomerization was more important at 30 Torr (i.e., 40%); the dominant route was methylcyclohexane dissociation. However, H-atom abstraction reactions became more important at 760 Torr, which led to five methylcyclohexane radicals.

To further clarify the effect of unimolecular decomposition and H-atom abstraction reactions on methylcyclohexane consumption, the sensitivity analysis of methylcyclohexane was conducted at both 30 and 760 Torr. Selected conditions were the same as the reaction flux analysis in Fig. 4.16. Results in Fig. 4.17 indicate that both unimolecular dissociation and H-atom abstraction reactions had a positive effect in consuming methylcyclohexane. The most sensitive reaction was the dissociation of methylcyclohexane to methyl radical and cyclohexyl radical.





**Fig. 4.16** Reaction pathways consuming methylcyclohexane at 30 and 760 Torr with methylcyclohexane conversion of approximately 80%. Black numbers are 30 Torr experiment. Blue numbers and underlines are 760 Torr experiment. Numbers obtained by dividing pathway carbon flux by total carbon flux of methylcyclohexane consumption. Reprinted from Ref. [38], Copyright 2014, with permission from Elsevier



**Fig. 4.17** Normalized sensitivity analysis of methylcyclohexane at both 30 and 760 Torr pyrolysis experiment with fuel conversion of approximately 80%. Reactions shown have absolute sensitivity coefficients larger than 0.02 for 30 Torr experiment and 0.03 for 760 Torr experiment, respectively. Reprinted from Ref. [38], Copyright 2014, with permission from Elsevier

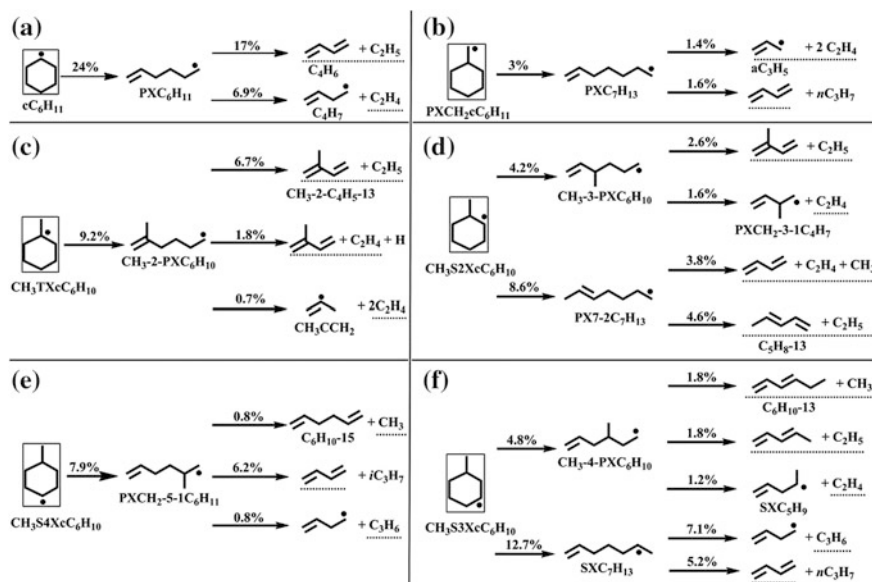
The positive effects of these reactions on methylcyclohexane consumption occurred because these reactions directly consume methylcyclohexane. Furthermore, the cyclohexyl radical and the methylcyclohexane radicals formed from these pathways were the precursors of the H atom by way of reactions like the  $\beta$ -C-H scission of  $C_2H_5$  radical and  $C_4H_7$  radical, etc. H-atom abstraction reactions of methylcyclohexane were promoted when more H-atoms were added into the system. This explanation is in accord with the positive effect of  $\beta$ -C-H scission of  $C_2H_5$  and  $C_4H_7$  radicals on methylcyclohexane consumption.

The kinetic model in this work was also compared with a methylcyclohexane combustion model by Orme et al. [7] and JetSurF 2.0 [19]. In the JetSurF 2.0 model, an over-prediction of methylcyclohexane consumption was observed (dotted lines in Fig. 4.15) at 760 Torr. Analysis showed that the dominant pathways to methylcyclohexane consumption were its isomerization to heptenes. However, the estimated rate constants were much larger than the calculation in this work, this is the probable reason for the over-prediction of methylcyclohexane consumption. However, the prediction of methylcyclohexane by the kinetic model of Orme et al. is closer to the simulation in this work (dashed line in Fig. 4.15); but the predicted mole fraction of 2-heptene and 1-heptene appears at a higher temperature. This discrepancy is probably due to the different reaction mechanism for these isomerization products.

Isomerization pathways of methylcyclohexane in the model of Orme et al. considered two-step reactions. The ring-opening of methylcyclohexane formed three  $C_7H_{14}$  bi-radicals, which then underwent intramolecular H-shift isomerization and/or  $\beta$ -C-C scission decomposition. The theoretical study by Skeen et al. [18], and this work, both showed that dominant pathways for these biradicals are intramolecular H-shift to produce heptenes and methyl-hexenes; the  $\beta$ -C-C scission pathways were energetically unfavorable. Instead, the dominant pathways for these biradicals was the unfavorable  $\beta$ -C-C scission channels in the model by Orme et al.

#### ***4.7.2 Isomerization of Cyclohexyl Radical and Methylcyclohexane Radicals***

The cyclohexyl and methylcyclohexane radicals produced from the unimolecular decomposition and H-atom abstraction of methylcyclohexane are not stable and were not detected in the experiment. As shown in Fig. 4.18, the dominant consumption pathways for these radicals are ring-opening isomerization. The ring-opening isomerization in the cyclohexyl radical led to a 5-hexen-1-yl radical ( $PXC_6H_{11}$ ), which then formed 1-hexen-3-yl radical ( $SAXC_6H_{11}$ ) by way of intramolecular 1,4-H shift, and ethylene and 3-buten-1-yl radical ( $C_4H_7$ ) via direct  $\beta$ -C-C scission. As discussed in cyclohexane pyrolysis, the  $\beta$ -C-C scission of 1-hexen-3-yl radical formed 1,3-butadiene and ethyl radical. Apart from these two

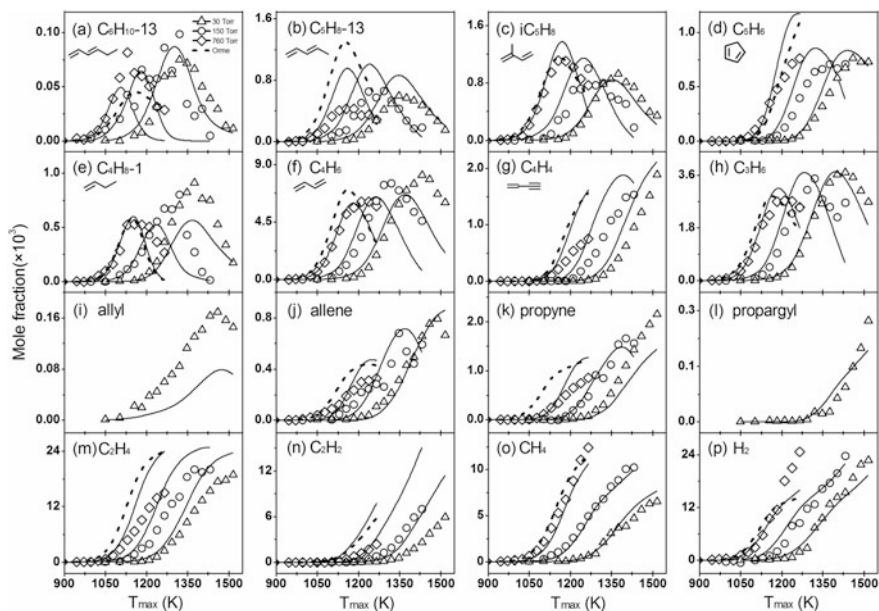


**Fig. 4.18** Reaction flux of ring-opening isomerization of cyclohexyl radical and methylcyclohexane radicals during methylcyclohexane pyrolysis at 30 Torr with fuel conversion of about 80%. Numbers obtained by dividing pathway carbon flux by total carbon flux of methylcyclohexane consumption. Underlined species detected in this work. Reprinted from Ref. [38], Copyright 2014, with permission from Elsevier

pathways, 5-hexen-1-yl radical also isomerized to a five-membered ring intermediate cyclopentylmethyl radical  $CH_2cC_5H_9$  [48] ( $\text{C}_5$ ). However, the simulation showed that this pathway was negligible among the pathways consuming the 5-hexen-1-yl radical.

The ring-opening isomerization of methylcyclohexane radicals leads to  $C_7H_{13}$  alkenyl radicals, which then mainly undergoes two kinds of reactions. By abstracting the allylic hydrogen atom, the intramolecular H-shift formed a conjugate radical intermediate (not shown in Fig. 4.18). The  $\beta$ -C-C scission of this intermediate which followed, produced diene and a small radical. The  $\beta$ -C-C scission of the  $C_7H_{13}$  alkenyl radicals led to alkenes and small radicals. Like the 5-hexen-1-yl radical ( $PXC_6H_{11}$ ), isomerization of the  $C_7H_{13}$  alkenyl radicals also yielded five-membered ring intermediates. However, this reaction class was not included in the kinetic model since it has been shown to be insignificant in consuming the 5-hexen-1-yl radical.

Figure 4.19 shows measured and simulated mole fraction profiles of important C0-C6 species in methylcyclohexane pyrolysis at 30, 150, and 760 Torr. Here, focus was on the reaction kinetics of cyclohexyl radical and methylcyclohexane radicals in 30 Torr pyrolysis because their reaction flux is similar at both 30 Torr and 760 Torr. Mole fraction profiles of 1,3-hexadiene, C5 dienes (1,3-pentadiene



**Fig. 4.19** Mole fraction profiles of important C0–C6 species during methylcyclohexane pyrolysis at 30, 150, and 760 Torr. Symbols and solid lines are experimental measurement and model prediction in this work. Dashed lines are model prediction by Orme et al. [7] at 760 Torr. Reprinted from Ref. [38], Copyright 2014, with permission from Elsevier

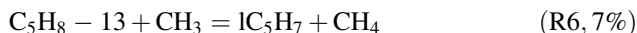
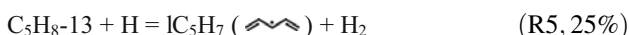
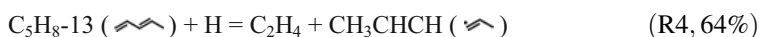
and 2-methyl-1,3-butadiene), 1,3-butadiene, and allyl radical were also compared with those formed in cyclohexane pyrolysis at 30 Torr, as shown in Fig. 4.20. The mole fraction of 1,3-hexadiene in methylcyclohexane pyrolysis was three times higher than in cyclohexane pyrolysis. The reaction pathway analysis shows that 1,3-hexadiene was formed from the 5-hexen-1-yl radical ( $\text{PXC}_6\text{H}_{11}$ ) in cyclohexane pyrolysis. In methylcyclohexane pyrolysis, however, this pathway was negligible; the dominant source for 1,3-hexadiene resulted from the decomposition of the 3-methyl-5-hexen-1-yl radical ( $\text{CH}_3\text{-4-PXC}_6\text{H}_{10}$ ), which was produced from 3-methyl-cyclohexyl radical ( $\text{CH}_3\text{S3XcC}_6\text{H}_{10}$ ).

In addition to 1,3-hexadiene in Fig. 4.19a, this work measured two other important C5 dienes, 1,3-pentadiene ( $\text{C}_5\text{H}_8\text{-13}$ ) in Fig. 4.19b and 2-methyl-1,3-butadiene ( $\text{CH}_3\text{-2-C}_4\text{H}_5\text{-13}$ ) in Fig. 4.19c. The mole fraction of the C5 dienes in methylcyclohexane pyrolysis was also much higher than in cyclohexane pyrolysis. This difference was caused by the different reaction pathways, which are related to the molecular structure of the two cycloalkanes. The C5 dienes in cyclohexane pyrolysis were produced from secondary reactions of smaller intermediates. However, in methylcyclohexane pyrolysis, the C5 dienes are formed from the decomposition of the methylcyclohexane radicals. For example, the dissociation of 3-methyl-1-hexen-6-yl radical ( $\text{CH}_3\text{-3-PXC}_6\text{H}_{10}$ , 24%) and 2-methyl-1-hexen-6-yl radical ( $\text{CH}_3\text{-2-PXC}_6\text{H}_{10}$ , 69%) are the

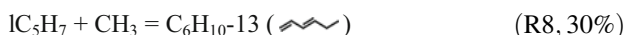
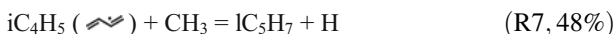
two main pathways for 2-methyl-1,3-butadiene. The following three reactions (R1–R3) are the dominant route to consuming 2-methyl-1,3-butadiene.



There are also two main pathways for 1,3-pentadiene, the dissociation of 5-hepten-1-yl radical (PX7-2C<sub>7</sub>H<sub>13</sub>, 65%) and 3-methyl-5-hexen-1-yl radical (CH<sub>3</sub>-4-PXC<sub>6</sub>H<sub>10</sub>, 32%). The following three reactions (R4–R6) compose the dominant route to consuming 1,3-pentadiene.



The H-atom abstractions of 1,3-pentadiene (R5 and R6) led to 1C<sub>5</sub>H<sub>7</sub>. Another two important pathways for 1C<sub>5</sub>H<sub>7</sub> are reactions R7 and R8, 30%. The dominant reactions of 1C<sub>5</sub>H<sub>7</sub> led to cyclopentadiene in Fig. 4.19d.



The most important diene in methylcyclohexane pyrolysis is 1,3-butadiene (Fig. 4.19f), which is also the most important diene in cyclohexane pyrolysis. As shown in Fig. 4.20c, the mole fraction of 1,3-butadiene in the two cycloalkane pyrolysis is similar. The dominant pathway for 1,3-butadiene in cyclohexane pyrolysis is from 5-hexen-1-yl radical (PXC<sub>6</sub>H<sub>11</sub>). This pathway is also important for 1,3-butadiene formation in methylcyclohexane pyrolysis (Fig. 4.18a), while other pathways from 1-hepten-6-yl radical (SXC<sub>7</sub>H<sub>13</sub>), 2-methyl-5-hexen-1-yl radical (PXCH<sub>2</sub>-5-1C<sub>6</sub>H<sub>11</sub>) and 5-hepten-1-yl radical (PX7-2C<sub>7</sub>H<sub>13</sub>) also lead to 1,3-butadiene. The H-atom addition to the double bond of 1,3-butadiene, and subsequent decomposition, forms ethylene and C<sub>2</sub>H<sub>3</sub>; and the H-atom abstraction of 1,3-butadiene produces *n*C<sub>4</sub>H<sub>5</sub> and *i*C<sub>4</sub>H<sub>5</sub> radicals. The β-C–H scission of these two radicals are the dominant source for vinylacetylene (C<sub>4</sub>H<sub>4</sub>) in Fig. 4.19g.

The profiles of C3 intermediates in methylcyclohexane pyrolysis are shown in Fig. 4.19h–l. Three important reaction pathways lead to propene: dissociation of 1-hepten-6-yl radical (SXC<sub>7</sub>H<sub>13</sub>); H-elimination of *i*C<sub>3</sub>H<sub>7</sub>, from the 2-methyl-5-hexen-1-yl radical (PXCH<sub>2</sub>-5-1C<sub>6</sub>H<sub>11</sub>); and the reaction of CH<sub>3</sub> radical with C<sub>2</sub>H<sub>3</sub> radical. The major reaction pathways for propene are by way of the reaction with H atom to form ethylene and methyl radical.

Another important C3 intermediate is allyl radical ( $aC_3H_5$ ), produced mainly from R9 to R11:

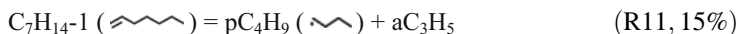
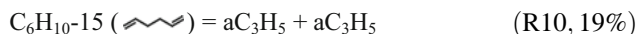
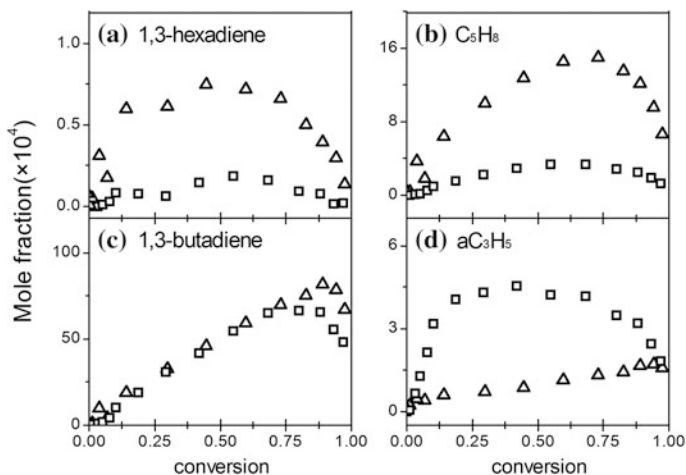


Figure 4.20d shows that its mole fraction is much lower than in cyclohexane pyrolysis, indicating that the production of allyl radical is not favorable in methylcyclohexane pyrolysis. In cyclohexane pyrolysis, the allyl radical is largely produced from the decomposition of 1-hexene, an important intermediate from the initial isomerization of cyclohexane (Sect. 3.3.1). The initial isomerization of methylcyclohexane forms 1-heptene, which also decomposes into allyl radical (R11). However, 1-heptene is not the major dissociation product of methylcyclohexane, and the contribution to allyl radical from 1-heptene is much less than 1-hexene in cyclohexane pyrolysis.

In summary, the ring-opening isomerization of cyclohexyl radical and methylcyclohexane radicals forms 5-hexen-1-yl radical and various  $C_7H_{13}$  alkenyl radicals. They lead to dienes of 1,3-hexadiene, 1,3-pentadiene, 2-methyl-1,3-butadiene, and 1,3-butadiene, alkenes of  $C_3H_6$  and  $C_2H_4$ , radicals of  $C_4H_7$ ,  $C_3H_7$ , and  $C_2H_5$ . Compared to cyclohexane, the pyrolysis of methylcyclohexane favors the formation of C5 (1,3-pentadiene and 2-methyl-1,3-butadiene) and C6 (1,3-hexadiene) dienes. Instead, the production of allyl radical is much lower than in cyclohexane pyrolysis.



**Fig. 4.20** Mole fraction profiles of 1,3-hexadiene, C5 dienes (1,3-pentadiene and 2-methyl-1,3-butadiene), 1,3-butadiene, and allyl radical during methylcyclohexane (triangle) and cyclohexane (square) pyrolysis at 30 Torr. Horizontal axis is conversion of methylcyclohexane and cyclohexane, respectively

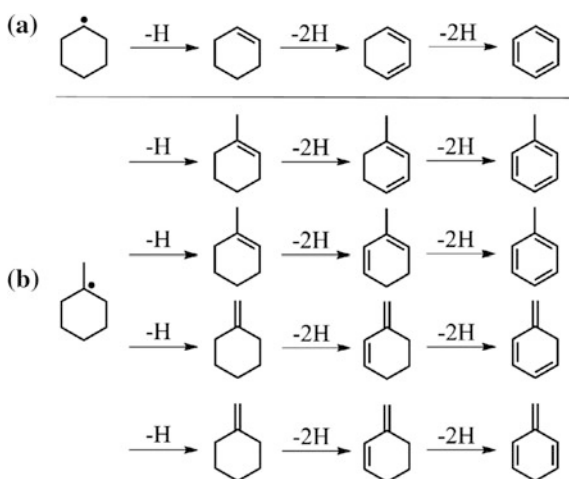
These differences reflect the chemical structure of the reactant on the distribution of pyrolysis intermediates. Generally, model prediction for the pyrolysis of methylcyclohexane, as shown in Figs. 4.15 and 4.19, is satisfactory. The model by Orme et al. [7] also satisfactorily predicts the C0–C6 species at 760 Torr.

### 4.7.3 Dissociation of Cyclohexyl and Methylcyclohexane Radicals

Apart from ring-opening isomerization pathways, the dissociation of cyclohexyl radical and methylcyclohexane radicals by step-wise dehydrogenation and/or dealkylation forms C6 and C7 cyclic compounds. The step-wise dehydrogenation of cyclohexyl radical and 1-methyl-cyclohexyl radical are shown in Fig. 4.21 as examples. This work measured C6 cyclic compounds of cyclohexene ( $cC_6H_{10}$ ), 1,3-cyclohexadiene ( $cC_6H_8$ -13), benzene (A1), C7 cyclic compounds of  $C_7H_{12}$ ,  $C_7H_{10}$ , *o*-isotoluene and *p*-isotoluene ( $cC_7H_8$ ), and toluene (A1CH<sub>3</sub>).

Table 4.5 shows ionization energy of the cyclic  $C_7H_{12}$ ,  $C_7H_{10}$  and  $C_7H_8$  molecule from NIST [43], as well as theoretical calculation in this work and in the literature. The most probable isomers of these intermediates were considered here. In the experiment by this group, the photoionization efficiency spectra of  $m/z$  78, 92, 94, and 96 were measured and are presented in Fig. 4.22, with the ionization energy and the structure of the most probable isomers. For  $m/z$  78, clear ionization energy onset of benzene and fulvene is observed. For  $m/z$  92, the ionization energy onset of toluene is observed at 8.84 eV. Another onset is observed for this  $m/z$  at approximately 7.96 eV, indicating the formation of isomers of toluene, e.g., *o*-isotoluene and *p*-isotoluene from Fig. 4.21b. The calculated ionization energy of

**Fig. 4.21** Benzene and toluene isomers from step-wise dehydrogenation of cyclohexyl radical and 1-methyl-cyclohexyl radical. H-loss pathways include direct C–H scission and H-atom abstractions. Reprinted from Ref. [38], Copyright 2014, with permission from Elsevier

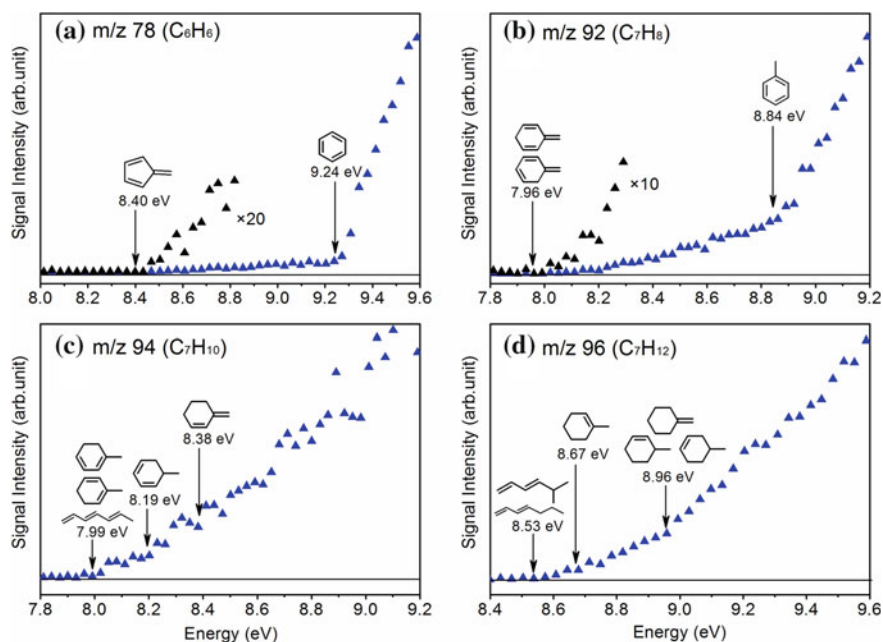


**Table 4.5** Adiabatic ionization energy of cyclic  $C_7H_{12}$ ,  $C_7H_{10}$ , and  $C_7H_8$  species

Formula	Species	Structure	IE/eV	Refs.
$C_7H_{12}$	Methylenecyclohexane		8.93	<sup>a</sup>
	1-methyl-cyclohexene		8.67	<sup>a</sup>
	3-methyl-cyclohexene		8.89	<sup>a</sup>
	4-methyl-cyclohexene		8.91	<sup>a</sup>
$C_7H_{10}$	3-methylene-cyclohexene		8.38	<sup>b</sup>
	2-methyl-1,3-cyclohexadiene		8.05 (8.05)	<sup>b</sup>
	1-methyl-1,3-cyclohexadiene		7.96 (7.95)	<sup>b</sup>
	5-methyl-1,3-cyclohexadiene		8.23 (8.21)	<sup>b</sup>
$C_7H_8$	5-methylene-1,3-cyclohexadiene		7.81	<sup>b</sup>
	3-methylene-1,4-cyclohexadiene		8.11	<sup>b</sup>
	Toluene		8.83	<sup>a</sup>

Reprinted from Ref. [38], Copyright 2014, with permission from Elsevier

<sup>a</sup>NIST database [43]; <sup>b</sup>calculation in this work; bracketed value from Skeen et al. [18]



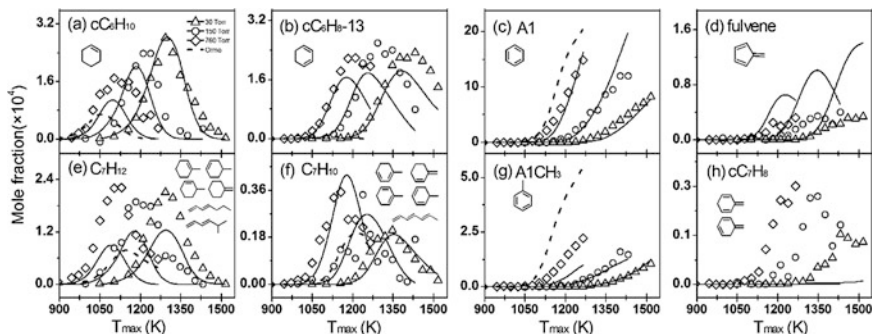
**Fig. 4.22** Photoionization efficiency spectra of  $m/z$  78, 92, 94, 96 in methylcyclohexane pyrolysis. Reprinted from Ref. [38], Copyright 2014, with permission from Elsevier



*o*-isotoluene and *p*-isotoluene is, respectively, 7.81 and 8.11 eV, which is close to the experimental measurement. It was noted that the ionization energy of *o*-isotoluene in the NIST database was 7.9 eV, slightly higher than our theoretical calculation. In cyclohexane pyrolysis, fulvene, benzene, and toluene were also observed, but  $m/z$  corresponding to  $C_7H_{12}$  and  $C_7H_{10}$  was not detected. This indicates that  $C_7H_{12}$  and  $C_7H_{10}$  species were produced directly from the dissociation of methylcyclohexane.

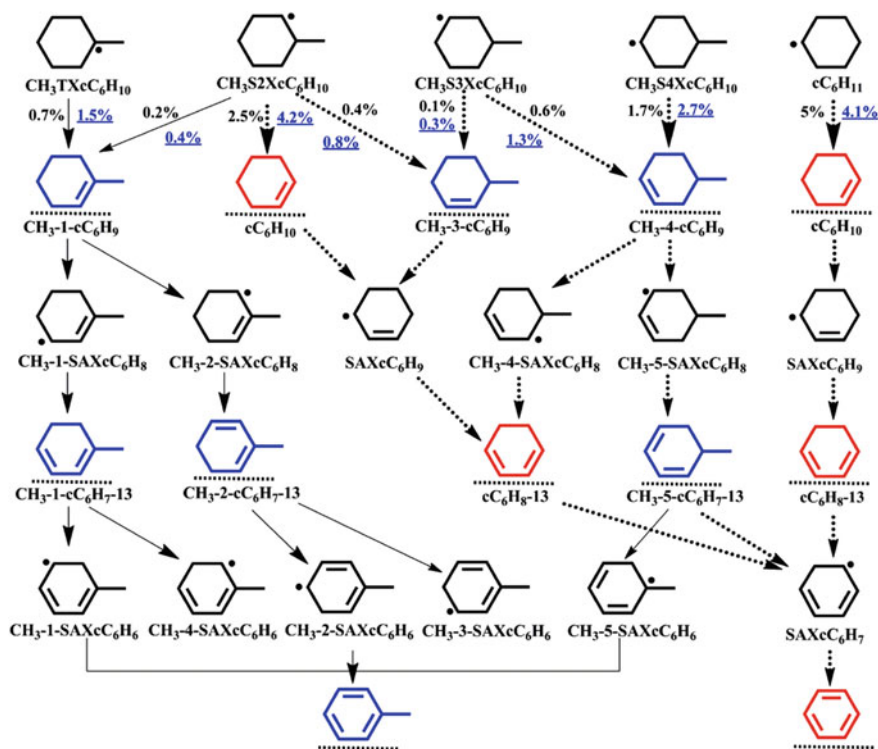
Figure 4.23 shows mole fraction profiles of the C6 and C7 intermediates. The experiment by this group did not separate the isomers for  $C_7H_{10}$  and  $C_7H_{12}$ , so the estimated mole fractions of these two intermediates are the summation of all probable isomers. Accordingly, the simulated mole fractions of these two intermediates also included all the possible isomers (cyclic and/or chain compounds). The simulation revealed that the dominant isomer for  $C_7H_{12}$  was 4-methylcyclohexene. The production of other isomers, such as 1,3-heptadiene and 5-methyl-1,3-hexadiene, was much less under the three pressure pyrolysis. For  $C_7H_{10}$ , the cyclic compounds in Table 4.4 were the major constituent at 30 Torr. However, the contribution of 1,3,5-heptatriene was dominant at higher pressures, constituting  $\sim 70\%$  of the total mole fraction of  $C_7H_{10}$  at 760 Torr, for example. The buildup reaction of 1,3-pentadiene with a vinyl radical was the main source for 1,3,5-heptatriene. For  $C_7H_8$ , the mole fraction of toluene and  $cC_7H_8$  was separated, as shown in Fig. 4.23g, h. The model satisfactorily predicted the formation of the C6 and C7 intermediates, except for  $cC_7H_8$ . Analysis revealed that the step-wise dehydrogenation of 1-methyl-cyclohexyl ( $CH_3TXcC_6H_{10}$ ) and  $PXCH_2cC_6H_{11}$  ( $\text{C}_6\text{H}_{11}$ ) radicals were the source of  $cC_7H_8$ , which included *o*-isotoluene and *p*-isotoluene. The decomposition of these two intermediates led to benzyl radical ( $A1CH_2$ ). The kinetic model of  $cC_7H_8$  needs to be further developed to reduce the discrepancy between experiment and simulation.

Apart from  $cC_7H_8$ , benzene and toluene are two other intermediates from the decomposition of cyclohexyl radical and methylcyclohexane radicals. Figure 4.23c, g



**Fig. 4.23** Mole fraction profiles of C6 and C7 intermediates in methylcyclohexane pyrolysis at 30, 150, and 760 Torr. Symbols and solid lines are experimental measurement and prediction in this work. Dashed lines are model predictions from Orme et al. [7] at 760 Torr. Reprinted from Ref. [38], Copyright 2014, with permission from Elsevier

show that production of benzene was higher than toluene from low to atmospheric pressure pyrolysis. A similar trend was also observed between 1,3-cyclohexadiene (Fig. 4.23b) and cyclic  $C_7H_{10}$  dienes (Fig. 4.23f). Here we focused on the decomposition pathways of cyclohexyl radical and methylcyclohexane radicals to benzene and toluene, as shown in Fig. 4.24. On one hand, toluene is produced from  $C_7$  cyclic alkene 1-methyl-cyclohexene ( $CH_3-1-cC_6H_9$ ), as well as  $C_7$  cyclic diene 1-methyl-1,3-cyclohexadiene ( $CH_3-1-cC_6H_7-13$ ) and 2-methyl-1,3-cyclohexadiene ( $CH_3-2-cC_6H_7-13$ ). These  $C_7$  cyclic alkene and dienes are from the step-wise dehydrogenation of 1-methyl-cyclohexyl radical ( $CH_3TXcC_6H_{10}$ ) and 2-methyl-cyclohexyl radical ( $CH_3S2XcC_6H_{10}$ ). On the other hand, benzene is formed from cyclohexene ( $cC_6H_{10}$ ), 3-methyl-cyclohexene ( $CH_3-3-cC_6H_9$ ), 4-methyl-cyclohexene ( $CH_3-4-cC_6H_9$ ), 5-methyl-1,3-cyclohexadiene ( $CH_3-5-cC_6H_7-13$ ) and 1,3-cyclohexadiene ( $cC_6H_8-13$ ). These  $C_6$  and  $C_7$  cyclic compounds leading to benzene are from the step-wise dehydrogenation and/or dealkylation of

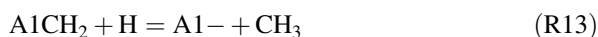


**Fig. 4.24** Major reactions of cyclohexyl radical and methylcyclohexane radical decomposition via step-wise dehydrogenation and/or dealkylation in methylcyclohexane pyrolysis. Methylcyclohexane conversion is  $\sim 80\%$  for 30 and 760 Torr pyrolysis. Black numbers are 30 Torr experiment. Blue numbers and underlines are 760 Torr, obtained by dividing pathway carbon flux by methylcyclohexane consumption total carbon flux. Species detected in this work are colored and underlined. Reprinted from Ref. [38], Copyright 2014, with permission from Elsevier

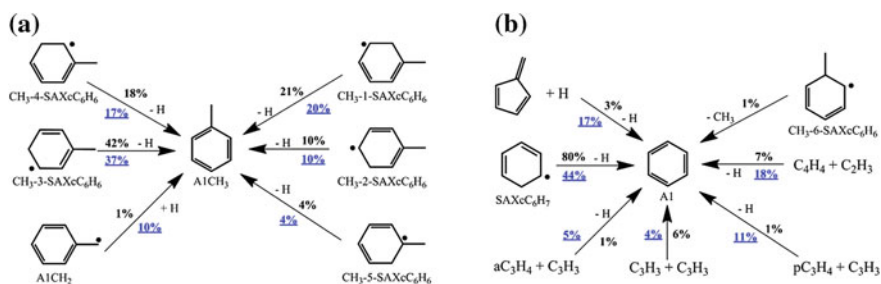
2-methyl-cyclohexyl ( $\text{CH}_3\text{S2XcC}_6\text{H}_{10}$ ), 3-methyl-cyclohexyl ( $\text{CH}_3\text{S3XcC}_6\text{H}_{10}$ ) and 4-methyl-cyclohexyl ( $\text{CH}_3\text{S4XcC}_6\text{H}_{10}$ ) radicals. Furthermore, the decomposition of methylcyclohexane forms cyclohexyl radical, whose further step-wise dehydrogenation is another important source for benzene. In summary, the analysis from the kinetic model revealed that more carbon flux goes into C6 cyclic compounds than the C7 cyclic compounds. This explains the higher production of benzene than toluene.

#### 4.7.4 Reaction Pathway Analysis for Toluene and Benzene

Figure 4.25 shows the reaction pathway analysis of toluene and benzene with methylcyclohexane conversion of  $\sim 80\%$  at both 30 and 760 Torr pyrolysis. The dominant source of toluene is the H-elimination of five cyclic  $\text{C}_7\text{H}_9$  radicals. They were produced from the step-wise dehydrogenation of 1-methyl-cyclohexyl radical ( $\text{CH}_3\text{TXcC}_6\text{H}_{10}$ ) and 2-methyl-cyclohexyl radical ( $\text{CH}_3\text{S2XcC}_6\text{H}_{10}$ ). Among the five cyclic  $\text{C}_7\text{H}_9$  radicals, the contribution from 3-methyl-1,3-cyclohexadienyl ( $\text{CH}_3\text{-3-SAXcC}_6\text{H}_6$ ) radical is more important. Another pathway to producing toluene is the association of H atom with benzyl radical; this reaction mechanism for toluene in methylcyclohexane pyrolysis is different from that in cyclohexane pyrolysis. For example, the self-combination of propargyl radical ( $\text{C}_3\text{H}_3$ ) in cyclohexane pyrolysis is the dominant source of toluene via the following reaction pathways.

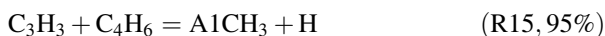


Here the toluene formation pathways in the kinetic model of Orme et al. [7] are considered; the reaction mechanism of cyclic  $\text{C}_7\text{H}_{12}$  and  $\text{C}_7\text{H}_{10}$  intermediates from



**Fig. 4.25** Reaction pathway analysis of toluene and benzene in methylcyclohexane pyrolysis at 30 and 760 Torr with methylcyclohexane conversion of  $\sim 80\%$ . Black numbers are 30 Torr, blue numbers and underlines are for 760 Torr are contribution percentages. Reprinted from Ref. [38], Copyright 2014, with permission from Elsevier

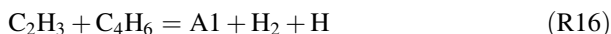
their simulation was analyzed first. As the dashed line in Fig. 4.23e indicates, all the probable isomers of  $C_7H_{12}$  were included. Like the model prediction in this work, the four cyclic  $C_7H_{12}$  alkenes were also formed from the decomposition of methylcyclohexane; however, no subsequent reactions were considered for these cyclic  $C_7H_{12}$  alkenes in the model from Orme et al. Although their predicted mole fraction of  $C_7H_{12}$  was close to the simulation in this work, the value was expected to be lower when the subsequent reactions of cyclic  $C_7H_{12}$  alkenes were included. Consequently, cyclic  $C_7H_{10}$  dienes and toluene cannot be produced from the decomposition of methylcyclohexane in the model by Orme et al. As shown in Fig. 4.23g, their predicted mole fraction of toluene was much higher than the experimental measurement. Analysis reveals that the reaction of 1,3-butadiene with  $C_3H_3$  was the dominant route for toluene (R15).



Like cyclohexane pyrolysis, benzene is produced from multiple channels in methylcyclohexane pyrolysis (Fig. 4.25b). The contribution of different reaction pathways is affected by the pressure of pyrolysis. For example, the most important benzene formation route is the H-loss of cyclohexadienyl (SAXcC<sub>6</sub>H<sub>7</sub>) radical under 30 Torr pyrolysis. As shown in Fig. 4.24, the step-wise dehydrogenation of cyclohexyl radical and the dissociation of 2-methyl-cyclohexyl (CH<sub>3</sub>S2XcC<sub>6</sub>H<sub>10</sub>), 3-methyl-cyclohexyl (CH<sub>3</sub>S3XcC<sub>6</sub>H<sub>10</sub>) and 4-methyl-cyclohexyl (CH<sub>3</sub>S4XcC<sub>6</sub>H<sub>10</sub>) radicals are the source of the cyclohexadienyl radical. The contribution to benzene from β-C-H scission of the cyclohexadienyl radical decreases when the pressure is 760 Torr.

Other important reactions for benzene are from resonance stabilized radicals, such as reactions  $C_4H_4 + C_2H_3$ ,  $C_3H_3 + C_3H_3$ ,  $C_3H_3 + aC_3H_4$ , and  $C_3H_3 + pC_3H_4$ . These reaction pathways—as well as the H-assisted isomerization of fulvene—are more important for benzene at 760 Torr pyrolysis, another reason for the higher mole fraction of benzene than toluene.

The kinetic model by Orme et al. [7] also predicted well the mole fraction of benzene (A1) at 760 Torr. However, the production of 1,3-cyclohexadiene was largely under-predicted. Analysis revealed that the H-loss of cyclohexadienyl radical was also the main source for benzene. However, the cyclohexadienyl radical was produced from the reactions of  $nC_4H_5$  with  $C_2H_2$ , not from the decomposition of methylcyclohexane. Moreover, another important route for benzene in the Orme et al. model was the reaction of 1,3-butadiene with vinyl radical.

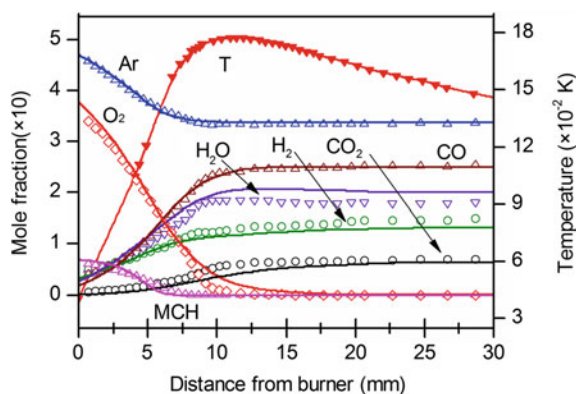


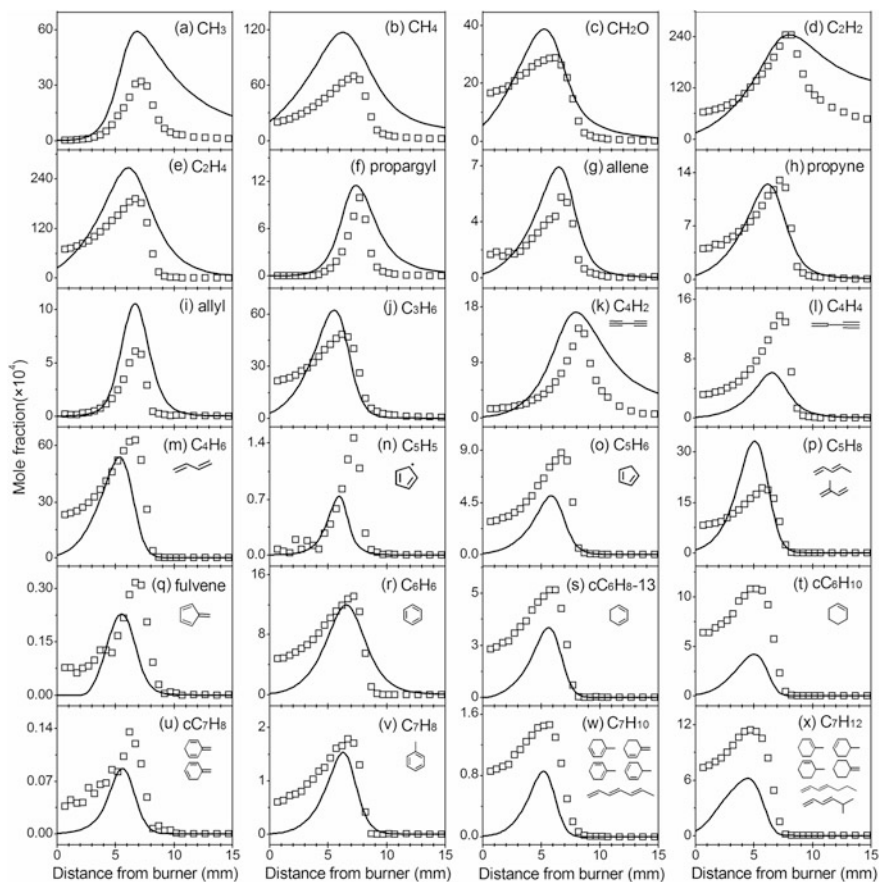
## 4.8 Low-Pressure Premixed Flame of Methylcyclohexane

To further validate the kinetic model of methylcyclohexane combustion, the laminar premixed flame of methylcyclohexane with equivalence ratio of 1.75 at 30 Torr was studied in this work. The flame of methylcyclohexane/O<sub>2</sub>/50% Ar mixture was stabilized on a McKenna burner. The diameter of the burner was 60 mm. The velocity and mass flow rate of the unburnt gas at 300 K was 35 cm/s and  $2.28 \times 10^{-3}$  g/cm<sup>2</sup>/s, respectively. The flow rates of methylcyclohexane, Ar, and O<sub>2</sub> were 152, 1066, and 914 sccm, respectively. In the CHEMKIN simulation, the temperature profile obtained from the experiment was used as input. The mixture-average transport, including Soret diffusion, was considered. The simulation was converged with solution gradient of 0.19 and curvature of 0.39, respectively. Figure 4.26 displays the temperature profile and the mole fraction profiles of the major combustion products. The model satisfactorily captured the flame structure of methylcyclohexane, which is similar to the fuel-rich cyclohexane flame at low pressure.

Mole fraction profiles of C1–C7 combustion intermediates are presented in Fig. 4.27. A large discrepancy is observed between experiment and simulation at distances shorter than 2 mm from the burner surface; this was caused by the perturbation of the sampling nozzle. Thus, within this range, the measured mole fraction might not be used to examine the kinetic model. Analysis shows that the unimolecular reactions of methylcyclohexane were not important for the consumption of methylcyclohexane in a flame environment. Instead, the bimolecular reactions of methylcyclohexane with OH radical and H atom controlled the consumption of methylcyclohexane and produced methylcyclohexane radicals. The yield of 3-methyl-cyclohexyl (CH<sub>3</sub>S3XcC<sub>6</sub>H<sub>10</sub>) and 2-methyl-cyclohexyl (CH<sub>3</sub>S2XcC<sub>6</sub>H<sub>10</sub>) radicals was especially higher than other radicals. The reaction pathways for methylcyclohexane radicals were like those in methylcyclohexane pyrolysis, e.g., ring-opening isomerization to form long-chain alkenyl radicals. The further decomposition of these alkenyl radicals constitutes the species pool of the

**Fig. 4.26** Mole fraction profiles of reactants and major combustion products in methylcyclohexane flame with equivalence ratio of 1.75 and pressure of 30 Torr. Symbol is experiment measurement. Line is model prediction. Solid symbol and line is temperature profile in this work. Reprinted from Ref. [38], Copyright 2014, with permission from Elsevier



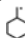


**Fig. 4.27** Mole fraction profiles of C1–C7 combustion intermediates in methylcyclohexane flame with equivalence ratio of 1.75 and pressure of 30 Torr. Symbol is experiment measurement. Line is model prediction. Reprinted from Ref. [38], Copyright 2014, with permission from Elsevier

combustion intermediates. On the other hand, the decomposition of the methylcyclohexane radicals via  $\beta$ -C–H scission and  $\beta$ -C–C scission were the source for cyclohexene and methylcyclohexene isomers. The formation of some key combustion intermediates is highlighted in the following discussion.

Like cyclohexane flame, 1,3-butadiene is an important intermediate in methylcyclohexane flame (Fig. 4.27m). However, the reaction flux for 1,3-butadiene in the methylcyclohexane flame studied was much more complex. More than 50% of 1,3-butadiene is from the decomposition of alkenyl  $C_7H_{13}$  radicals such as 2-methyl-5-hexen-1-yl radical ( $PXCH_2-5-1C_6H_{11}$ , 18%), 1-hepten-6-yl radical ( $SXC_7H_{13}$ , 17%), 5-hepten-1-yl radical ( $PX7-2C_7H_{13}$ , 11%) and 6-hepten-1-yl radical ( $PXC_7H_{13}$ , 8%). Another source was the decomposition of 5-hexen-1-yl radical ( $PXC_6H_{11}$ , 15%). The contribution of this channel to 1,3-butadiene was less important

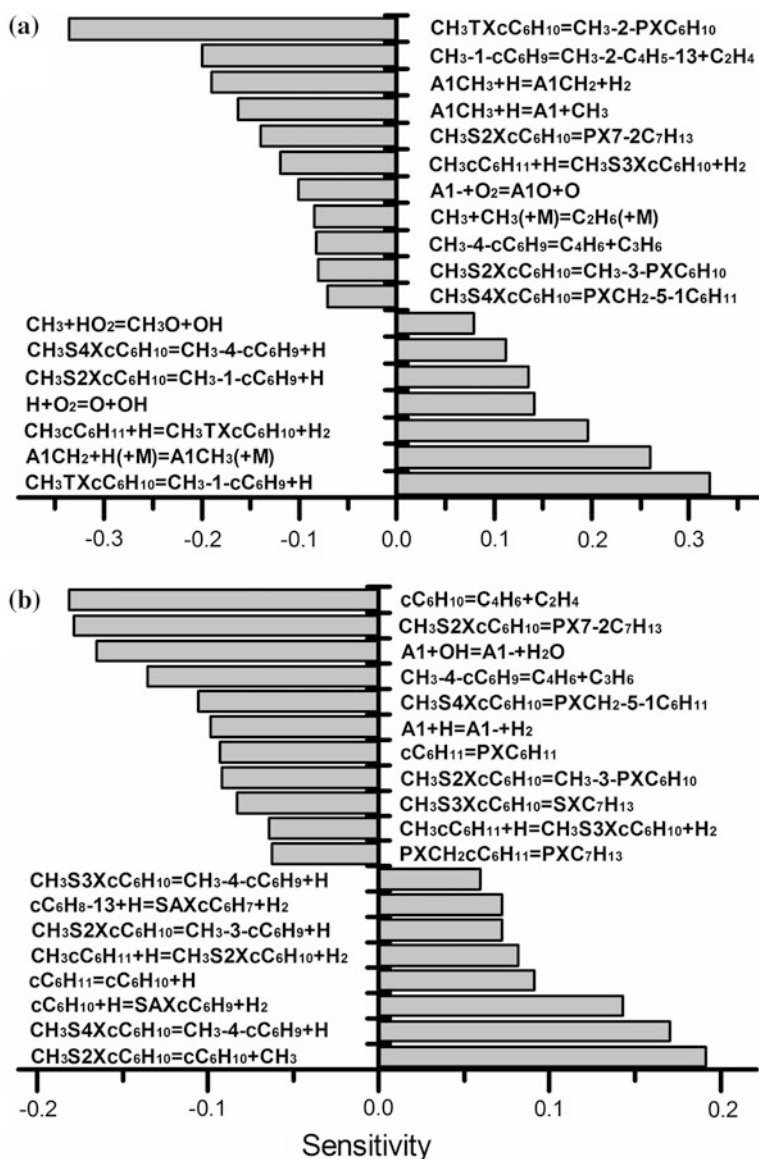
than in methylcyclohexane pyrolysis because the unimolecular decomposition of methylcyclohexane from the loss of  $\text{CH}_3$  side-chain is not important in flame. Another important intermediate is  $\text{C}_5\text{H}_8$  dienes, including 1,3-pentadiene and 2-methyl-1,3-butadiene (Fig. 4.27p). The decomposition of the  $\text{C}_7\text{H}_{13}$  alkenyl radicals is the major source for these two intermediates. Experiments by this group did not separate these two species. According to the experimental observation of Skeen et al. [18], the mole fraction of 1,3-pentadiene is slightly lower than that of 2-methyl-1,3-butadiene.

Mole fraction profiles of the cyclic C6–C7 species are shown in Fig. 4.27q–x; model prediction for these intermediates was generally satisfactory. The photoionization efficiency spectra of these cyclic C6–C7 species were similar to the observation in methylcyclohexane pyrolysis. These intermediates were also detected by Skeen et al. [18]; photoionization efficiency spectra for species in the two experiments were also similar. For  $\text{C}_7\text{H}_{10}$  and  $\text{C}_7\text{H}_{12}$ , all the probable isomers in the simulated mole fraction profiles were considered, as shown in Fig. 4.27w, x. Like methylcyclohexane pyrolysis,  $c\text{C}_7\text{H}_8$  (*o*-isotoluene and *p*-isotoluene), the isomers of toluene, were also detected in methylcyclohexane flame. The measured ionization onset for  $c\text{C}_7\text{H}_8$  was  $\sim 7.91$  eV, which is close to the ionization energy of *o*-isotoluene (7.81 eV). Although the formation of  $c\text{C}_7\text{H}_8$  was significantly under-predicted in methylcyclohexane pyrolysis, the model satisfactorily predicted its mole fraction in a flame environment. The step-wise dehydrogenation of 1-methylcyclohexyl radical ( $\text{CH}_3\text{TXcC}_6\text{H}_{10}$ ) and cyclohexylmethyl radical ( $\text{PXCH}_2\text{cC}_6\text{H}_{11}$ , ) was the main source for  $c\text{C}_7\text{H}_8$ . The higher concentration of radicals in flame environment promoted the H-abstraction reactions and is the probable reason for the better prediction of  $c\text{C}_7\text{H}_8$ .

The model prediction for fulvene was also good. The analysis revealed that fulvene was formed mainly from R16. Like the observation of methylcyclohexane pyrolysis, the mole fraction of  $\text{C}_6\text{H}_8$  and  $\text{C}_6\text{H}_6$  was higher than  $\text{C}_7\text{H}_{10}$  and  $\text{C}_7\text{H}_8$  in the flame environment; this phenomenon can also be explained by the flux analysis in Fig. 4.24. In the following, discussion focuses on the kinetics of benzene and toluene.

In the studied flame, the direct H-elimination of the five cyclic  $\text{C}_7\text{H}_9$  radicals was the dominant source for toluene, while the five cyclic  $\text{C}_7\text{H}_9$  radicals were produced from the step-wise dehydrogenation of methylcyclohexane. This observation for toluene was similar to methylcyclohexane pyrolysis. Multiple pathways led to benzene, e.g., H-elimination from cyclohexadienyl radical ( $\text{SAXcC}_6\text{H}_7$ , 76%), H-atom assisted isomerization of fulvene (9%), and the reaction of H atom with toluene (7%). Unlike methylcyclohexane pyrolysis, the reaction pathways from small resonance stabilized radicals had a negligible contribution on benzene formation.

For clarification of toluene and benzene reaction kinetics, a sensitivity analysis was calculated for toluene at 6.3 mm from the burner surface and for benzene at 6.6 mm, as shown in Fig. 4.28. Results showed that the reactions with C7- and C6- cyclic intermediates affected the formation of toluene and benzene. For example, the H-elimination of methylcyclohexane radicals to methylcyclohexenes positively affected the formation of toluene, such as those of 1-methyl-cyclohexyl,



**Fig. 4.28** Normalized sensitivity analysis of **a** toluene and **b** benzene in methylcyclohexane flame at 6.3 and 6.6 mm from burner surface, respectively. Reactions with absolute sensitivity coefficients larger than 0.09 are shown for toluene. Reactions with absolute sensitivity coefficients larger than 0.06 are shown for benzene. Reprinted from Ref. [38], Copyright 2014, with permission from Elsevier

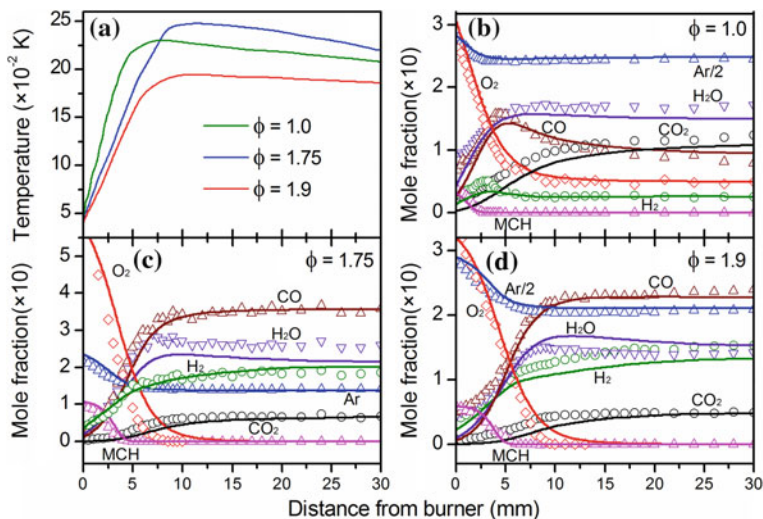


2-methyl-cyclohexyl and 4-methyl-cyclohexyl radicals. But their ring-opening isomerization had a negative effect on toluene formation. Furthermore, the decomposition of methyl-cyclohexenes, e.g., 1-methyl-cyclohexene and 4-methyl-cyclohexene, via the retro-Diels-Alder reaction, also had a negative effect on toluene formation. The result also revealed that the H-atom abstraction of toluene to benzyl radical had a considerable negative effect on toluene formation, since this pathway is the dominant consumption channel for toluene. The combination of benzyl radical with H atom is another source for toluene, and this reaction had a substantial positive effect on toluene formation.

The sensitivity analysis for benzene showed that the reactions of 2-methyl-cyclohexyl radical had the greatest effect on benzene formation. For example, the  $\beta$ -C-C scission of 2-methyl-cyclohexyl radical to methyl radical and cyclohexene had the most positive effect, while its isomerization via ring-opening had the most negative effect. Other methylcyclohexane radicals, such as 4-methyl-cyclohexyl, 2-methyl-cyclohexyl and 3-methyl-cyclohexyl radicals, also affect benzene formation; the direct H-elimination of these radicals have positive effects while their isomerization via ring-opening has negative effects. Apart from the reactions involving methylcyclohexane radicals, benzene formation was also affected by reactions of cyclohexyl radical, cyclohexene and 1,3-cyclohexadiene.

The kinetic model developed in this work was further validated by methylcyclohexane flame data from Skeen et al. [18]. In their work, the methylcyclohexane flames at equivalence ratios of 1.0, 1.75 and 1.9, and pressure of 10, 15, and 30 Torr were investigated using an experimental method similar to this work. Valuable information on the consumption of methylcyclohexane, and formation of aromatic intermediates such as benzene and toluene was provided. Figure 4.29 presents the temperature profiles of the three methylcyclohexane flames, and the mole fraction profiles of the reactants and the major combustion products. The model prediction captured well the consumption of the reactants (i.e., methylcyclohexane and O<sub>2</sub>) and the formation of the major combustion products. As in the discussion in Sect. 4.7.1 and the work of Skeen et al. [18], the unimolecular decomposition, isomerization and H-abstraction were the three types of reactions consuming methylcyclohexane. Simulation by this group showed that under stoichiometric flame, the H-atom abstraction reactions by H atom, OH radical and O atom consumed 97% of methylcyclohexane. The unimolecular decomposition and isomerization of methylcyclohexane became more important in the fuel-rich flame of  $\phi = 1.75$  and 1.9.

Mole fraction profiles of some combustion intermediates, e.g., 1,3-pentadiene, 2-methyl-1,3-butadiene, benzene, 1,3-cyclohexadiene, cyclohexene, and toluene, are presented in Fig. 4.30. In general, the model prediction for most of these species was satisfactory. The largest difference was observed for 1,3-pentadiene and 2-methyl-1,3-butadiene in the flame with equivalence ratio of 1.75, as well as cyclohexene and toluene in flames with equivalence ratio of 1.0 and 1.9. The experimental uncertainties for the mole fractions could be a factor of 2 in the work by Skeen et al. [18]. The kinetic model in this work may also need improvement for better prediction of these intermediates.

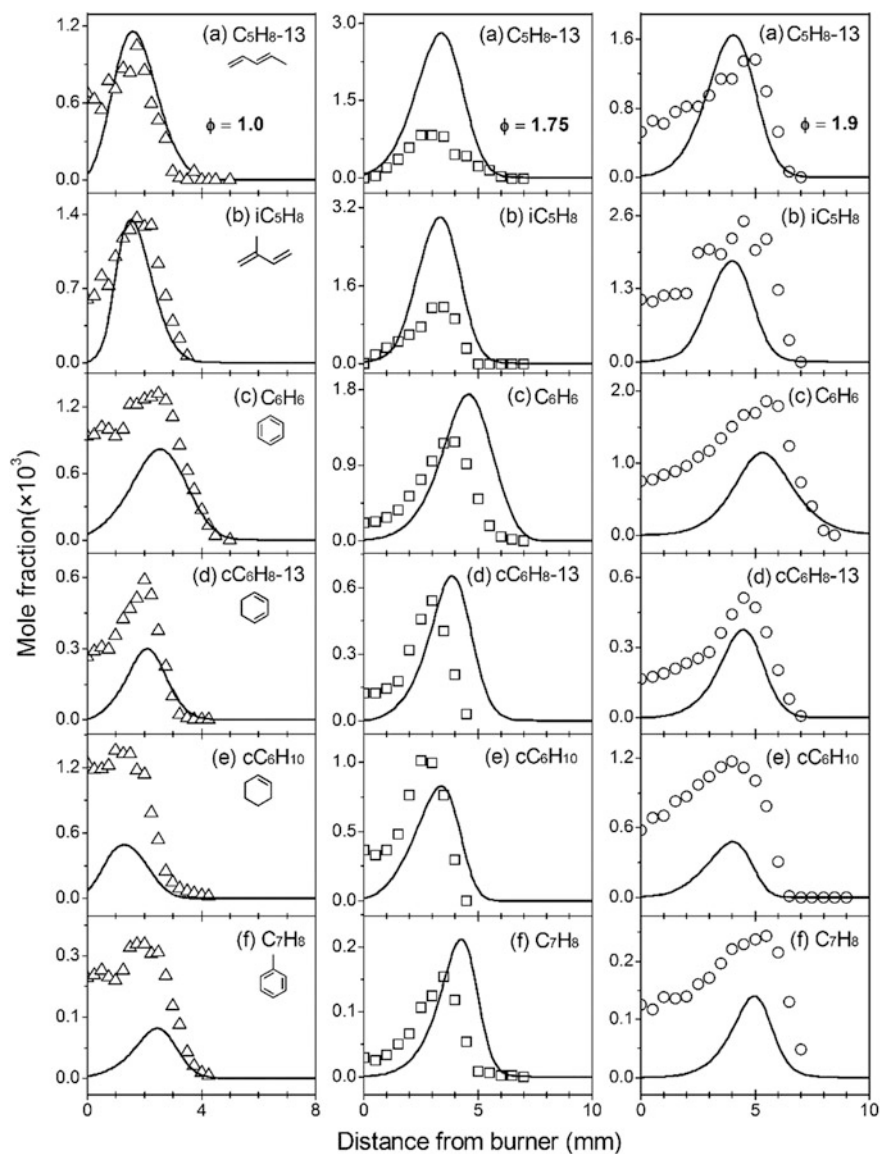


**Fig. 4.29** a Flame temperature profiles in three methylcyclohexane flame with equivalence ratio of 1.0, 1.75, and 1.9. **b–d** Mole fraction profiles of reactants and major combustion products. Experimental data (open symbol) from Skeen et al. [18]. Lines are model simulation in this work. Reprinted from Ref. [38], Copyright 2014, with permission from Elsevier

Analysis revealed that multiple pathways lead to benzene. One important route is the sequential dehydrogenation of the cyclohexyl radical. However, this pathway is not the dominant route for benzene, especially for the stoichiometric flame. This conclusion differed from the assumption by Skeen et al. [18], who suggested that benzene production is dominantly from sequential dehydrogenation of cyclohexyl radical.

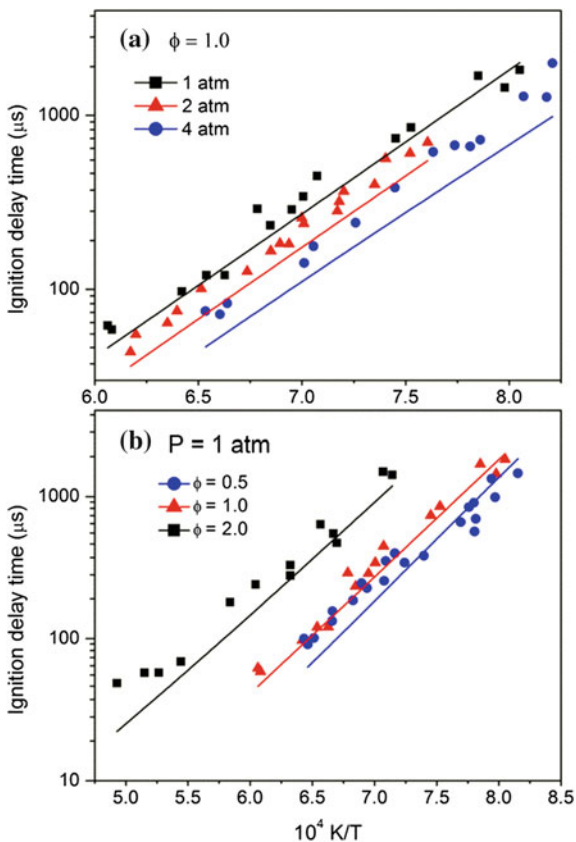
## 4.9 Ignition Delay Time and Laminar Flame Speed

The kinetic model in this work was further validated by the macroscopic combustion properties of methylcyclohexane combustion, e.g. ignition delay times and laminar flame speeds. The method for CHEMKIN simulation can be found in Sect. 3.6 of Chap. 3. Figure 4.31 compares ignition delay times of methylcyclohexane between the model prediction and the measurement by Orme et al. [7] at various equivalence ratios and pressures. Figure 4.32 shows simulated laminar flame speed and experimental measurement by Wu et al. [17] at various pressures and equivalence ratios. The uncertainty for the flame speed measurement is  $\pm 2$  cm/s. The model in this work satisfactorily predicted ignition and flame speed at the conditions studied.

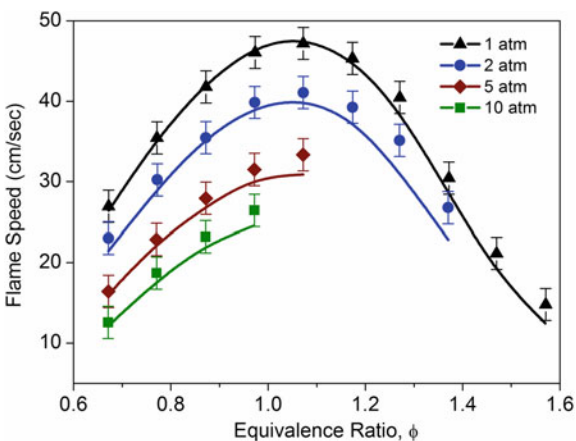


**Fig. 4.30** Mole fraction profiles of selected combustion intermediates in three methylcyclohexane flames. Experimental data (open symbol) from Skeen et al. [18]. Lines are model prediction in this work. Reprinted from Ref. [38], Copyright 2014, with permission from Elsevier

**Fig. 4.31** Ignition delay times for methylcyclohexane oxidation. **a**  $\phi = 1.0$  and 1.0% methylcyclohexane/Ar/ $O_2$  mixture. Pressure is 1, 2, and 4 atm. **b** Methylcyclohexane/ $O_2$ /Ar mixture at 1 atm with  $\phi = 0.5$  (0.5% MCH, 10.5%  $O_2$ ), 1.0 (1.0% MCH, 10.5%  $O_2$ ) and 2.0 (1.0% MCH, 5.25%  $O_2$ ). Experimental data (symbols) from Orme et al. [7]. Model predictions (lines) from this work. Reprinted from Ref. [38], Copyright 2014, with permission from Elsevier



**Fig. 4.32** Laminar flame speeds of methylcyclohexane/air mixture at 1, 2, 5, and 10 atm. Unburnt gas temperature is 353 K. Experimental data (symbols) from Wu et al. [17]. Model predictions (lines) from this work. Reprinted from Ref. [38], Copyright 2014, with permission from Elsevier



## 4.10 Summary and Conclusions

In this chapter, the combustion kinetics of methylcyclohexane were investigated from quantum chemistry calculations of reaction pathways and rate constants, experimental measurement of methylcyclohexane pyrolysis and flame, and detailed kinetic modeling.

The reaction pathways of methylcyclohexane unimolecular decomposition and their rate constants were calculated, which is the starting point for developing a combustion model of methylcyclohexane and alkyl-cyclohexanes. Isomerization of methylcyclohexane via ring-opening forms heptene isomers and methyl-hexene isomers. The dissociation of the methyl side-chain forms cyclohexyl radical. The temperature-dependent (800–2000 K) and pressure-dependent (7.6–76,000 Torr) rate constants for these unimolecular decomposition reactions were obtained and the results showed that the dissociation channel from the loss of the methyl group was competitive with the isomerization pathways. The isomerization via C–C bond scission adjacent to the methyl side-chain was more favorable than other isomerization pathways. The bimolecular reactions of methylcyclohexane with H atom were studied at the CBS-QB3 level of theory. Rate constants were calculated from the transition state theory and were in good agreement with the values from the literature. Finally, the unimolecular decomposition of methylcyclohexane radicals from H-abstraction of methylcyclohexane, was also computed at a CBS-QB3 level of theory. Pressure-dependent rate constants were computed based on the RRKM/ME theory in the temperature range of 800–2000 K.

The sub-mechanism of methylcyclohexane combustion was developed from calculated unimolecular decomposition pathways, H-abstraction reactions by H atom, and unimolecular decomposition of methylcyclohexane radicals, and review of the literature. A detailed kinetic model of methylcyclohexane was built by adding its sub-mechanism to a cyclohexane kinetic model (Chap. 3). Detailed reaction pathways to benzene and toluene were also included, from the step-wise dehydrogenation and/or dealkylation of methylcyclohexane; and the thermodynamic data for the intermediate species in this process were estimated from the quantum chemistry calculation and building of isodesmic reactions.

The flow reactor pyrolysis of methylcyclohexane at 30, 150, and 760 Torr was investigated; more than 30 pyrolysis intermediates, including the initial isomerization product from methylcyclohexane (e.g. 2-heptene), were measured. The model captured well the consumption of methylcyclohexane and the production of important intermediates. Analysis from the kinetic model showed that both the unimolecular dissociation to methyl and cyclohexyl radical and the H-atom abstraction of methylcyclohexane are important to the consumption of methylcyclohexane; the decomposition of cyclohexyl radical and methylcyclohexane radicals constitute the abundant pyrolysis intermediates. Compared to cyclohexane pyrolysis, higher production of 1,3-pentadiene, 2-methyl-1,3-butadiene, and 1,3-hexadiene was observed in methylcyclohexane pyrolysis; but the production of

allyl radical was much less than in cyclohexane pyrolysis. The production of 1,3-butadiene was high in both cyclohexane and methylcyclohexane pyrolysis.

The pyrolysis experiment of methylcyclohexane detected a series C6 and C7 cyclic compounds, the intermediates from the decomposition of methylcyclohexane and precursors to benzene and toluene. Multiple benzene formation channels were predicted, such as the H-elimination of cyclohexadienyl radical (from the step-wise dehydrogenation of cyclohexyl radical and dealkylation of methylcyclohexane), the combination of resonance stabilized radicals, and the isomerization of fulvene. The contribution from the isomerization of fulvene and the combination of resonance stabilized radicals increased with the pressure of pyrolysis. Toluene was dominantly produced from the H-elimination of cyclic C<sub>7</sub>H<sub>9</sub> radicals, which are from the step-wise dehydrogenation of 1-methyl-cyclohexyl and 2-methyl-cyclohexyl radical. The production of benzene was much higher than toluene since more carbon flux goes into benzene.

The model was validated by the fuel-rich laminar premixed flame ( $\phi = 1.75$ ) in this work, and flames reported in the literature with equivalence ratio of 1.0, 1.7, and 1.9. The model satisfactorily predicted the mole fraction profile of the reactants, major combustion products, and the C1–C7 intermediates. Model analysis revealed that H-atom abstraction of methylcyclohexane was the dominant consumption pathway for methylcyclohexane, and large amounts of 1,3-butadiene is produced. Like methylcyclohexane pyrolysis, cyclic C6 and C7 intermediates were also formed in methylcyclohexane flames. The simulation showed that these cyclic C6 and C7 intermediates are the major source for benzene and toluene; the contribution from the combination of resonance stabilized radicals was insignificant. The model was also validated by the macroscopic combustion properties of methylcyclohexane, e.g., ignition delay time and laminar flame speed.

## References

1. Prosen, E. J., Johnson, W. H., & Rossini, F. D. (1946). Heats of formation and combustion of the normal alkylcyclopentanes and cyclohexanes and the increment per CH<sub>2</sub> group for several homologous series of hydrocarbons. *Journal of Research of the National Bureau of Standards*, 37, 51–56.
2. Beckett, C. W., Pitzer, K. S., & Spitzer, R. (1947). The thermodynamic properties and molecular structure of cyclohexane, methylcyclohexane, ethylcyclohexane and the seven dimethylcyclohexanes. *Journal of the American Chemical Society*, 69(10), 2488–2495.
3. Taylor, P. H., & Rubey, W. A. (1988). Evaluation of the gas-phase thermal decomposition behavior of future jet fuels. *Energy & Fuels*, 2(6), 723–728.
4. Brown, T. C., & King, K. D. (1989). Very low-pressure pyrolysis (VLPP) of methyl- and ethynyl-cyclopentanes and cyclohexanes. *International Journal of Chemical Kinetics*, 21(4), 251–266.
5. Zeppieri, S., Brezinsky, K., & Glassman, I. (1997). Pyrolysis studies of methylcyclohexane and oxidation studies of methylcyclohexane and methylcyclohexane/toluene blends. *Combustion and Flame*, 108(3), 266–286.

6. Hawthorn, R. D., & Nixon, A. C. (1966). Shock tube ignition delay studies of endothermic fuels. *AIAA Journal*, 4(3), 513–520.
7. Orme, J. P., Curran, H. J., & Simmie, J. M. (2006). Experimental and modeling study of methyl cyclohexane pyrolysis and oxidation. *Journal of Physical Chemistry A*, 110(1), 114–131.
8. Vasu, S. S., Davidson, D. F., Hong, Z., & Hanson, R. K. (2009). Shock tube study of methylcyclohexane ignition over a wide range of pressure and temperature. *Energy & Fuels*, 23(1), 175–185.
9. Vasu, S. S., Davidson, D. F., & Hanson, R. K. (2009). OH time-histories during oxidation of n-heptane and methylcyclohexane at high pressures and temperatures. *Combustion and Flame*, 156(4), 736–749.
10. Vanderover, J., & Oehlschlaeger, M. A. (2009). Ignition time measurements for methylcyclohexane- and ethylcyclohexane-air mixtures at elevated pressures. *International Journal of Chemical Kinetics*, 41(2), 82–91.
11. Sivaramakrishnan, R., & Michael, J. V. (2009). Shock tube measurements of high temperature rate constants for OH with cycloalkanes and methylcycloalkanes. *Combustion and Flame*, 156(5), 1126–1134.
12. Pitz, W. J., Naik, C. V., Mhaoldúin, T. N., Westbrook, C. K., Curran, H. J., Orme, J. P., et al. (2007). Modeling and experimental investigation of methylcyclohexane ignition in a rapid compression machine. *Proceedings of the Combustion Institute*, 31, 267–275.
13. Mittal, G., & Sung, C. J. (2009). Autoignition of methylcyclohexane at elevated pressures. *Combustion and Flame*, 156(9), 1852–1855.
14. Weber, B. W., Pitz, W. J., Mehl, M., Silke, E. J., Davis, A. C., & Sung, C.-J. (2014). Experiments and modeling of the autoignition of methylcyclohexane at high pressure. *Combustion and Flame*, 161, 1972–1983.
15. McEnally, C. S., & Pfefferle, L. D. (2005). Fuel decomposition and hydrocarbon growth processes for substituted cyclohexanes and for alkenes in nonpremixed flames. *Proceedings of the Combustion Institute*, 30, 1425–1432.
16. Ji, C., Dames, E., Sirjean, B., Wang, H., & Egolfopoulos, F. N. (2011). An experimental and modeling study of the propagation of cyclohexane and mono-alkylated cyclohexane flames. *Proceedings of the Combustion Institute*, 33, 971–978.
17. Wu, F., Kelley, A. P., & Law, C. K. (2012). Laminar flame speeds of cyclohexane and mono-alkylated cyclohexanes at elevated pressures. *Combustion and Flame*, 159(4), 1417–1425.
18. Skeen, S. A., Yang, B., Jasper, A. W., Pitz, W. J., & Hansen, N. (2011). Chemical structures of low-pressure premixed methylcyclohexane flames as benchmarks for the development of a predictive combustion chemistry model. *Energy & Fuels*, 25, 5611–5625.
19. Wang, H., Dames, E., Sirjean, B., Sheen, D. A., Tangko, R., Violi, A., et al. (2010). A high-temperature chemical kinetic model of n-alkane (up to n-dodecane), cyclohexane, and methyl-, ethyl-, n-propyl and n-butyl-cyclohexane oxidation at high temperatures. JetSurF version 2.0. September 19, 2010 (<http://melchior.usc.edu/JetSurF/JetSurF2.0>).
20. Gong, C., Li, Z., & Li, X. (2012). Theoretical kinetic study of thermal decomposition of cyclohexane. *Energy & Fuels*, 26(5), 2811–2820.
21. Kiefer, J. H., Gupte, K. S., Harding, L. B., & Klippenstein, S. J. (2009). Shock tube and theory investigation of cyclohexane and 1-hexene decomposition. *Journal of Physical Chemistry A*, 113(48), 13570–13583.
22. Sirjean, B., Glaude, P. A., Ruiz-Lopez, M. F., & Fournet, R. (2006). Detailed kinetic study of the ring opening of cycloalkanes by CBS-QB3 calculations. *Journal of Physical Chemistry A*, 110(46), 12693–12704.
23. Holbrook, K. A., Pilling, M. J., & Robertson, S. H. (1996). *Unimolecular reactions* (2nd ed.). Chichester: John Wiley & Sons.

24. Zhang, F., Wang, Z., Wang, Z., Zhang, L., Li, Y., & Qi, F. (2013). Kinetics of decomposition and isomerization of methylcyclohexane: Starting point for kinetic modeling mono-alkylated cyclohexanes. *Energy & Fuels*, *27*(3), 1679–1687.
25. Werner, H. J., & Knowles, P. J. (1985). A second order multiconfiguration SCF procedure with optimum convergence. *Journal of Chemical Physics*, *82*(11), 5053–5063.
26. Werner, H. J., & Knowles, P. J. (1988). An efficient internally contracted multiconfiguration-reference configuration interaction method. *Journal of Chemical Physics*, *89*(9), 5803–5814.
27. Davidson, E. R., & Silver, D. W. (1977). Size consistency in the dilute helium gas electronic structure. *Chemical Physics Letters*, *52*(3), 403–406.
28. Montgomery, J. A., Jr., Frisch, M. J., Ochterski, J. W., & Petersson, G. A. (1999). A complete basis set model chemistry. VI. Use of density functional geometries and frequencies. *Journal of Chemical Physics*, *110*, 2822–2827.
29. Werner, H. J., Knowles, P. J., Knizia, G., Manby, F. R., Schutz, M., & Celani, P. MOLPRO, a package of ab initio programs.
30. Frisch, M. J., Trucks, G. W., Schlegel, H. B., & Scuseria, G. E. (2009). *Gaussian 09, Revision B.01*. Wallingford, CT: Gaussian, Inc.
31. da Silva, G., & Bozzelli, J. W. (2008). Variational analysis of the Phenyl+O<sub>2</sub> and Phenoxy+O reactions. *The Journal of Physical Chemistry A*, *112*(16), 3566–3575.
32. Zhao, L., Ye, L., Zhang, F., & Zhang, L. (2012). Thermal decomposition of 1-pentanol and its isomers: A theoretical study. *The Journal of Physical Chemistry A*, *116*(37), 9238–9244.
33. Mokrushin, V., Bedanov, V., Tsang, W., Zachariah, M., & Knyazev, V. (2009). *ChemRate, Version 1.5.8*. Gaithersburg, MD: National Institute of Standard and Technology.
34. Yang, X., Jasper, A. W., Giri, B. R., Kiefer, J. H., & Tranter, R. S. (2011). A shock tube and theoretical study on the pyrolysis of 1,4-dioxane. *Physical Chemistry Chemical Physics*, *13*(9), 3686–3700.
35. Gilbert, R. G., & Smith, S. C. (1990). *Theory of unimolecular and recombination reactions*. Carlton, Australia: Blackwell Scientific.
36. Zhang, S., & Truong, T. N. (2001). Branching ratio and pressure dependent rate constants of multichannel unimolecular decomposition of gas-phase  $\alpha$ -HMX: An Ab Initio dynamics study. *The Journal of Physical Chemistry A*, *105*(11), 2427–2434.
37. Montgomery, J. A., Ochterski, J. W., & Petersson, G. A. (1994). A complete basis set model chemistry. IV. An improved atomic pair natural orbital method. *The Journal of Chemical Physics*, *101*(7), 5900–5909.
38. Wang, Z., Ye, L., Yuan, W., Zhang, L., Wang, Y., Cheng, Z., et al. (2014). Experimental and kinetic modeling study on methylcyclohexane pyrolysis and combustion. *Combustion and Flame*, *161*, 84–100.
39. Raghavachari, K., Trucks, G. W., Pople, J. A., & Head-Gordon, M. (1989). A fifth-order perturbation comparison of electron correlation theories. *Chemical Physics Letters*, *157*(6), 479–483.
40. Sirjean, B., Glaude, P. A., Ruiz-Lopèz, M. F., & Fournet, R. (2008). Theoretical kinetic study of thermal unimolecular decomposition of cyclic alkyl radicals. *The Journal of Physical Chemistry A*, *112*(46), 11598–11610.
41. Iwan, I., McGivern, W. S., Manion, J. A., & Tsang, W. (2007). The decomposition and isomerization of cyclohexyl and 1-hexenyl radicals. In *Proceedings of 5th US Combustion Meeting*, San Diego, CA, 2007, CO<sub>2</sub>.
42. CHEMKIN-PRO 15092. (2009). San Diego: Reaction Design.
43. Linstrom, P. J., & Mallard, W. G. (2005). *NIST chemistry webbook*. Gaithersburg, MD: National Institute of Standard and Technology, Number 69. <http://webbook.nist.gov/>.
44. Russell, D., & Johnson, I. (2013). *NIST computational chemistry comparison and benchmark database*. NIST Standard Reference Database Number 101, Release 16a, August 2013. <http://cccbdb.nist.gov/>.
45. Klippenstein, S. J., Harding, L. B., & Georgievskii, Y. (2007). On the formation and decomposition of C<sub>7</sub>H<sub>8</sub>. *Proceedings of the Combustion Institute*, *31*(1), 221–229.



46. Pant, K. K., & Kunzru, D. (1997). Pyrolysis of methylcyclohexane: Kinetics and modelling. *Chemical Engineering Journal*, 67(2), 123–129.
47. Kim, J., Park, S. H., Lee, C. H., Chun, B.-H., Han, J. S., Jeong, B. H., et al. (2012). Coke formation during thermal decomposition of methylcyclohexane by alkyl substituted C5 ring hydrocarbons under supercritical conditions. *Energy & Fuels*, 26(8), 5121–5134.
48. Knepp, A. M., Meloni, G., Jusinski, L. E., Taatjes, C. A., Cavallotti, C., & Klippenstein, S. J. (2007). Theory, measurements, and modeling of OH and HO<sub>2</sub> formation in the reaction of cyclohexyl radicals with O<sub>2</sub>. *Physical Chemistry Chemical Physics*, 9(31), 4315–4331.

# Chapter 5

## Experimental and Modeling Study of Ethylcyclohexane Combustion

### 5.1 Background

Ethylcyclohexane ( $C_8H_{16}$ ) has the following properties: molar mass of 112.21 g/mol, boiling point of 405 K, melting point of 162 K, density of 0.789 g/mL, standard enthalpy of formation of  $-171.8 \pm 1.5$  kJ/mol [1], standard molar entropy of 382.67 J/mol/K [2], and ionization potential of  $9.54 \pm 0.10$  eV.

Compared to methylcyclohexane, the longer side chain of ethylcyclohexane is closer to the cycloalkane components in transport fuels. It is beneficial to study the side-chain length effect on the combustion properties and aromatics formation in cycloalkane combustion; but literature on ethylcyclohexane is scarce. The ignition delay time of ethylcyclohexane/air mixture was measured by Vanderover and Oehlschlaeger [3] in a shock tube from 10.8 to 52.5 atm, 896 to 1241 K, and with equivalence ratios of 0.25, 0.5 and 1.0. The laminar flame speed of ECH/air mixtures was measured by Ji et al. [4] and Wu et al. [5] from 1 to 5 atm, with unburnt gas temperature of 353 K. In addition to its macroscopic combustion properties, Husson et al. [6] investigated the low and intermediate temperature oxidation of ethylcyclohexane in a jet-stirred reactor (JSR) at 500–1100 K and 800 Torr. Dozens of hydrocarbons and oxygenated intermediates, including 47 intermediates with molecular weight less than ethylcyclohexane, and several isomers of  $C_8H_{14}O$ , were measured by gas chromatography in ethylcyclohexane oxidation with equivalence ratios of 0.25, 1.0 and 2.0. These data serve as targets for kinetic model validation and are valuable to understand the combustion properties of ethylcyclohexane. For example, Wang et al. [7] developed the JetSurF 2.0 model, which includes the high-temperature pyrolysis and oxidation sub-mechanism of ethylcyclohexane. These experimental data of ignition delay time and laminar flame speed were adopted to validate the sub-mechanism of ethylcyclohexane.

In this chapter, experimental and kinetic modeling study of ethylcyclohexane combustion was carried out to investigate the chemical kinetics of ethylcyclohexane

pyrolysis and oxidation. In Sect. 5.2, the flow reactor pyrolysis of ethylcyclohexane at atmospheric pressure was probed using synchrotron radiation photoionization mass spectrometry. To interpret the large number of isomers formed in ethylcyclohexane pyrolysis, we combined the flow reactor with GC/GC-MS and carried out pyrolysis experiments of ethylcyclohexane under the same conditions. The initial decomposition of ethylcyclohexane, as well as the reaction mechanism of important pyrolytic intermediates, were discussed in this preliminary study. In Sects. 5.3–5.5, a more detailed study of ethylcyclohexane pyrolysis and oxidation was carried out by developing a novel detailed combustion model of ethylcyclohexane, which was validated by pyrolysis data at 30, 150, and 760 Torr, laminar premixed flame data at 30 Torr, JSR oxidation data at atmospheric pressure, ignition delay time and laminar flame speed.

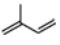
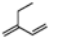

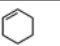
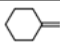
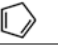
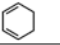
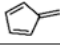

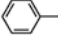
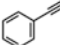
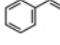
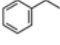
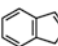
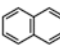
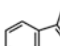
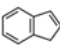
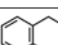
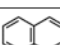
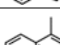
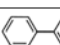
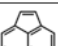
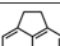
## 5.2 Preliminary Investigation of Ethylcyclohexane Decomposition

This work first examined the pyrolysis of ethylcyclohexane in the flow reactor at 1 atm. The initial mole fraction of fuel and argon is 0.02 and 0.98, respectively. More than 40 pyrolysis intermediates were analyzed with synchrotron radiation photoionization molecular beam mass spectrometry (SR-PI-MBMS) and GC/GC-MS. The two analytical methods separated most of the isomeric components. Table 5.1 presents the major species detected in ethylcyclohexane pyrolysis. The measurement of  $C_8H_{16}$  alkenes, chain and branched dienes, and cyclic alkenes aided in clarifying the pyrolysis mechanism of ethylcyclohexane. The JetSurF 2.0 model [7] was adopted to predict the experimental measurement and help analyze the ethylcyclohexane pyrolysis mechanism. The discussion following will focus on the initial dissociation and isomerization of ethylcyclohexane, isomerization of ethylcyclohexane radicals, and dissociation of ethylcyclohexane radicals.

### 5.2.1 *Dissociation and Isomerization of Ethylcyclohexane*

The initial reactions of ethylcyclohexane include both dissociation and isomerization, which are in accord with the decomposition of methylcyclohexane [9]. Figure 5.1 shows these reaction pathways via the opening of the C–C bonds for ethylcyclohexane. Direct C–H scission channels for ethylcyclohexane are not included here because they have a high dissociation threshold and lower reaction entropy. The dissociation of the side chain forms cyclohexyl + ethyl radical (R1) and cyclohexylmethyl radical + methyl radical (R2), while the ring-opening isomerization forms  $C_8H_{16}$  alkenes (R3–R9). The ring-opening, by way of the C–C bonds adjacent to the ethyl side chain, was expected to be the dominant route for

**Table 5.1** Major pyrolysis products during ethylcyclohexane pyrolysis in a flow reactor at 1 atm

Name	Structure	Name	Structure	Name	Structure	Name	Structure
H <sub>2</sub>	—	CH <sub>4</sub>	—	C <sub>2</sub> H <sub>2</sub>	C≡C	C <sub>2</sub> H <sub>4</sub>	C=C
C <sub>2</sub> H <sub>6</sub>	C—C	C <sub>3</sub> H <sub>4</sub>	C=C=C	C <sub>3</sub> H <sub>4</sub>	C≡C—C	C <sub>3</sub> H <sub>6</sub>	C=C—C
C <sub>4</sub> H <sub>4</sub>	C≡C— C = C	C <sub>4</sub> H <sub>6</sub>	C=C— C=C	C <sub>4</sub> H <sub>8</sub>	C=C—C—C	C <sub>4</sub> H <sub>8</sub>	C—C=C—C
C <sub>5</sub> H <sub>8</sub>	C=C—C=C— C	C <sub>5</sub> H <sub>8</sub>		C <sub>5</sub> H <sub>10</sub>	C=C—C—C—C	C <sub>5</sub> H <sub>10</sub>	C—C=C—C— C
C <sub>6</sub> H <sub>10</sub>	C=C—C=C— C—C	C <sub>6</sub> H <sub>10</sub>		C <sub>7</sub> H <sub>12</sub>	C=C—C=C— C—C—C	C <sub>8</sub> H <sub>16</sub>	C—C—C=C— C—C—C—C
C <sub>5</sub> H <sub>8</sub>		C <sub>6</sub> H <sub>10</sub>		C <sub>7</sub> H <sub>12</sub>		C <sub>8</sub> H <sub>14</sub>	— <sup>a</sup>
C <sub>5</sub> H <sub>6</sub>		C <sub>6</sub> H <sub>8</sub>		C <sub>6</sub> H <sub>6</sub>		C <sub>6</sub> H <sub>6</sub>	
C <sub>7</sub> H <sub>8</sub>		C <sub>8</sub> H <sub>6</sub>		C <sub>8</sub> H <sub>8</sub>		C <sub>8</sub> H <sub>10</sub>	
C <sub>9</sub> H <sub>8</sub>		C <sub>10</sub> H <sub>8</sub>		C <sub>10</sub> H <sub>10</sub>		C <sub>10</sub> H <sub>10</sub>	
C <sub>10</sub> H <sub>10</sub>		C <sub>11</sub> H <sub>10</sub>		C <sub>11</sub> H <sub>10</sub>		C <sub>12</sub> H <sub>10</sub>	
C <sub>12</sub> H <sub>8</sub>		C <sub>12</sub> H <sub>10</sub>					

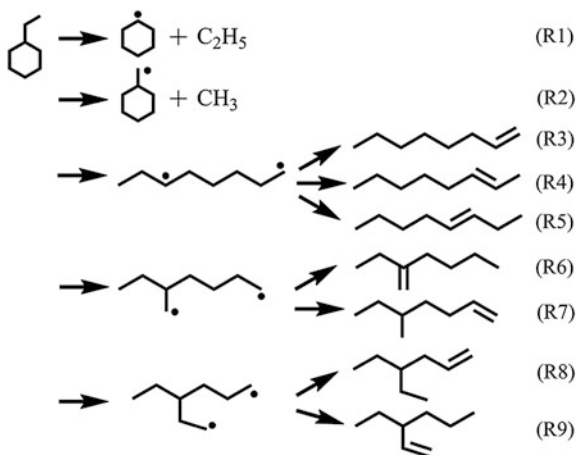
Reprinted from Ref. [8], Copyright 2015, with permission from Elsevier

Note <sup>a</sup>Many isomers and their identification appear in the text

ethylcyclohexane isomerization, which leads to 1-octene, 2-octene and 3-octene (R3–R5). Similar isomerization channels have been confirmed in cyclohexane and methylcyclohexane pyrolysis [9, 10]; however, in the oxidation of ethylcyclohexane, the C<sub>8</sub>H<sub>16</sub> alkenes were not detected [6], probably due to the low concentration of these intermediates in the oxidation environment. In SR-PI-MBMS analysis of ethylcyclohexane pyrolysis by this group, the signal corresponding to the C<sub>8</sub>H<sub>16</sub> alkenes was detected, however, it was scattered and the quantification was not available. In the GC analysis, 3-octene was measured. The GC analysis did not detect other isomers and the probable reason is that their concentration was too low. It was noted that 3-octene had the *cis*- and *trans*- forms, but only one peak appeared in this GC analysis.

The mole fraction profiles of ethylcyclohexane and 3-octene are presented in Fig. 5.2. Dashed lines are simulation results from JetSurF 2.0, which significantly over-predicts the conversion of ethylcyclohexane; it also over-predicts the formation of 3-octene by a factor of 100. In the JetSurF 2.0 model, four isomerization channels in Fig. 5.1 were included, i.e., R1, R2, R5 and R6. The analysis of the reaction flux indicated that R5 and R6 were the dominant channels to consume ethylcyclohexane at 1100 K. The reaction mechanism of ethylcyclohexane to

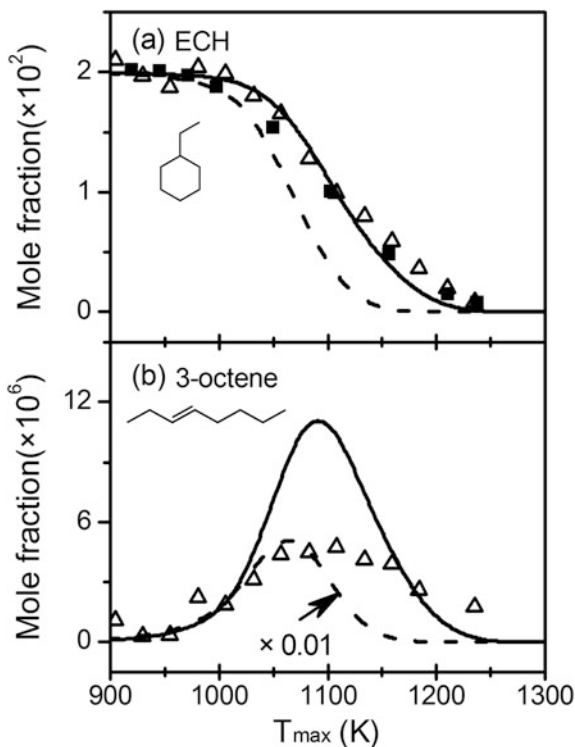
**Fig. 5.1** Initial dissociation and isomerization of ethylcyclohexane. Reprinted from Ref. [8], Copyright 2015, with permission from Elsevier



3-octene (R5) and 2-ethyl-1-hexene (R6) was similar to reactions forming 2-heptene and 2-methyl-1-hexene in methylcyclohexane isomerization. It was expected that the rate constants of the similar reactions would be comparable; instead, the estimated rate constant of R5 in JetSurF 2.0 model was a factor of 60 faster than the isomerization of methylcyclohexane to 2-heptene. The rate constant of R6 was even larger—about a factor of 1000 higher than the isomerization of methylcyclohexane to 2-methyl-1-hexene. The rapid consumption of ethylcyclohexane may be explained by the overly large rate constants of R5 and R6 in the JetSurF 2.0 model.

Based on the analysis above, a revised model of JetSurF 2.0 was developed by modifying the initial reactions of ethylcyclohexane. Specifically, the rate constants of R5 and R6 were estimated from analogous reactions of methylcyclohexane [11]. The rate constant of R1 was estimated from the dissociation of methylcyclohexane to methyl radical and cyclohexyl radical [11]. The rate constant of R2 was estimated from the dissociation of propane, which has been measured by Oehlschlaeger et al. [12] in the shock tube experiment. The rate constant of propane dissociation was reduced by a factor of two, considering the degeneracy. The revised model also included other isomerization channels of ethylcyclohexane, i.e., R3, R4, R7–R9. The rate constants of R3 and R4 were estimated from the isomerization of methylcyclohexane to 1-heptene [11], and the rate constants were divided by two, considering the degeneracy. The isomerization of methylcyclohexane to 5-methyl-1-hexene, 4-methyl-1-hexene and 3-methyl-1-hexene was used to estimate rate constants of R7–R9, respectively [11]. The prediction of ethylcyclohexane and 3-octene by the revised JetSurF 2.0 model appears as solid lines in Fig. 5.2. The model satisfactorily predicted the conversion of ethylcyclohexane; however, the model prediction for 3-octene was greatly improved, although a discrepancy factor of two remained. The estimated rate constants of ethylcyclohexane dissociation and isomerization from methylcyclohexane and propane was

**Fig. 5.2** Experimental (solid symbols) and simulated mole fraction profiles (lines) of ethylcyclohexane and 3-octene during ethylcyclohexane pyrolysis at atmospheric pressure. Solid symbol: SR-PI-MBMS data; open symbol: GC data. Dashed and solid lines are simulation by JetSurF 2.0 [7] and revised JetSurF 2.0 model, respectively. Reprinted from Ref. [8], Copyright 2015, with permission from Elsevier

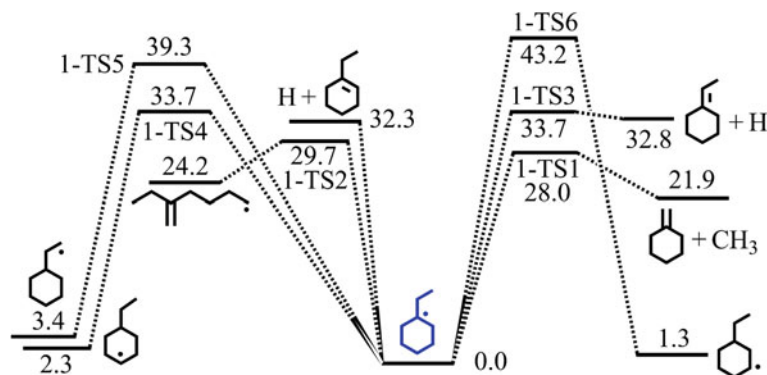


found to be reasonable. In the following, comparison between experimental measurement and prediction by the revised JetSurF 2.0 model is presented.

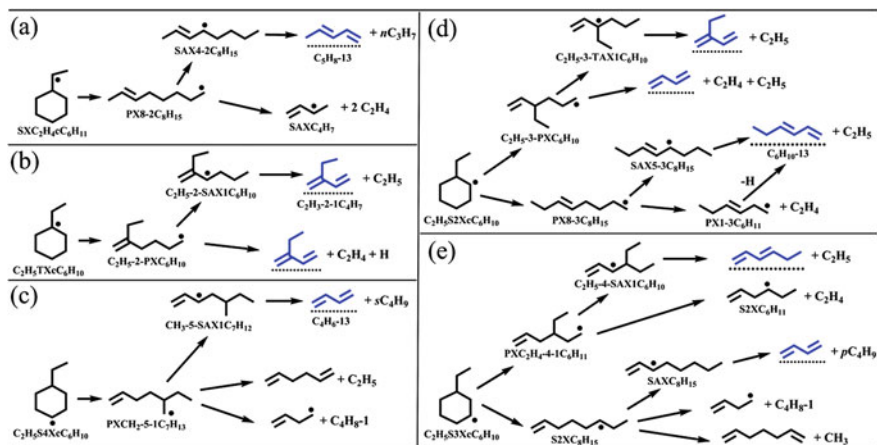
### 5.2.2 Ring-Opening Isomerization of Ethylcyclohexane Radicals

The H-atom abstraction of ethylcyclohexane is also an important pathway consuming ethylcyclohexane, which leads to six ethylcyclohexane radicals. As shown in Fig. 5.3 for 1-ethyl-cyclohexyl radical, these radicals have three types of subsequent reactions, isomerization to alkenyl radicals by ring-opening, dissociation by  $\beta$ -C-C or  $\beta$ -C-H scission, and isomerization to other ethylcyclohexane radicals by intramolecular H-atom shift.

Figure 5.4 shows the ring-opening isomerization pathways of the ethylcyclohexane radicals in the JetSurF 2.0 model, which led to chain or branched alkenyl radicals. Two kinds of reactions were considered for these alkenyl radicals, forming resonance stabilized radical intermediates by intramolecular H-shift via five- or six-membered-ring transition state, and forming alkene and a radical intermediate



**Fig. 5.3** Potential energy surface of 1-ethyl-cyclohexyl radical computed at CBS-QB3 level of theory. (0 K, unit: kcal/mol). Reprinted from Ref. [8], Copyright 2015, with permission from Elsevier

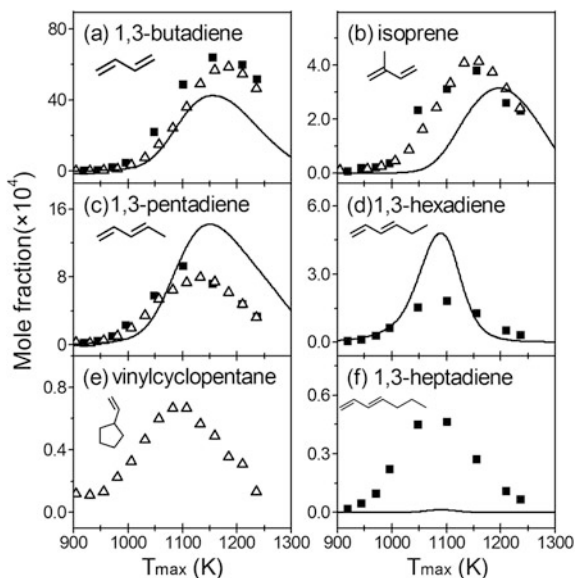


**Fig. 5.4** Ring-opening isomerization pathways of ethylcyclohexane radicals in JetSurF 2.0 model [7]. Reprinted from Ref. [8], Copyright 2015, with permission from Elsevier

by direct  $\beta$ -C-C scission. Further decomposition of the resonance stabilized radical intermediates formed chain and branched dienes, as shown in Fig. 5.5 for the C4-C7 dienes.

Vinylcyclopentane was also measured in the experiment. Among these unsaturated intermediates, the mole fraction of 1,3-butadiene (Fig. 5.5a) was very high. The maximum mole fraction of 1,3-butadiene was comparable to the maximum mole fraction of 1,3-butadiene in methylcyclohexane pyrolysis [9]. The measurement of these unsaturated intermediates is valuable to clarify the branching ratios of

**Fig. 5.5** Experimental (solid symbols) and simulated mole fraction profiles (lines) of C4–C7 unsaturated intermediates during ethylcyclohexane pyrolysis at atmospheric pressure. Solid symbol: SR-PI-MBMS data; open symbol: GC data. Solid lines simulated by revised JetSurF 2.0 model. Reprinted from Ref. [8], Copyright 2015, with permission from Elsevier

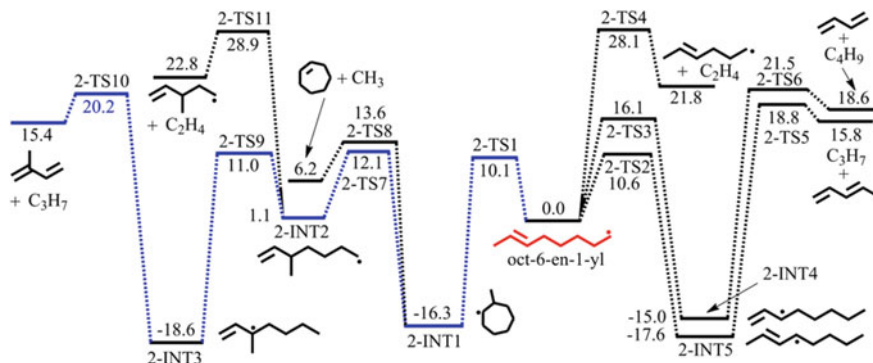


these long-chain alkenyl radicals. The following discussion focuses on the novel formation pathways of 2-methyl-1,3-butadiene (isoprene) and vinylcyclopentane.

2-methyl-1,3-butadiene is an important branched diene in methylcyclohexane pyrolysis; this intermediate can be produced directly from the ring-opening isomerization of the methylcyclohexane radicals. In ethylcyclohexane pyrolysis, the initial formation temperature of 2-methyl-1,3-butadiene is close to other dienes, indicating that 2-methyl-1,3-butadiene may also be produced from the ring-opening isomerization of the ethylcyclohexane radicals. The revised JetSurF 2.0 model captured well the maximum mole fraction of 2-methyl-1,3-butadiene (isoprene in Fig. 5.5b). However, the formation began at a higher temperature than the experimental observation. Figure 5.4 shows that no reactions from ethylcyclohexane radicals led to 2-methyl-1,3-butadiene; instead, reaction flux analysis revealed that the combination of methyl radical with  $iC_4H_5$  radical was the dominant source for 2-methyl-1,3-butadiene. However, the buildup reactions of smaller radicals could not start the early formation of 2-methyl-1,3-butadiene.

This group has explored the reaction pathways of  $C_8H_{15}$  alkenyl radicals, which may produce 2-methyl-1,3-butadiene through reactions not reported before. Figure 5.6 shows the computed pathways of 6-octen-1-yl radical, the dominant ring-opening isomerization product of 1-cyclohexyl-ethyl radical. Note that H-elimination pathways of the radical intermediates in Fig. 5.6 are not presented because of their higher energy barrier. The two reaction pathways via  $2-TS2 \rightarrow 2-INT5 \rightarrow 2-TS5$ , and  $2-TS4$  were included in the JetSurF 2.0 model, as shown in Fig. 5.4a. The calculation also found other reactions with lower energy barriers. The reactions labeled in blue in Fig. 5.6 are one of the newly found reaction pathways to 2-methyl-1,3-butadiene. The reaction began with the radical



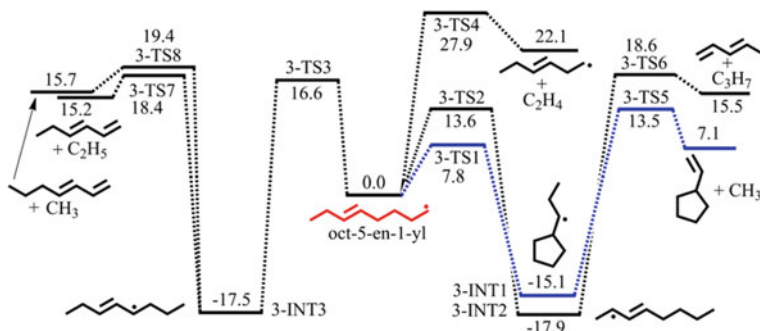


**Fig. 5.6** Potential energy surface of 6-octen-1-yl radical at CBS-QB3 level of theory. (0 K, unit: kcal/mol). Reprinted from Ref. [8], Copyright 2015, with permission from Elsevier

addition to the double bond via 2-TS1, which led to a seven-membered-ring intermediate (2-INT1) with a ring-opening that formed a branched  $C_8H_{15}$  alkenyl radical (2-INT2). The intramolecular 1,5-H-migration of 2-INT2 then formed a resonance stabilized radical intermediate 2-INT3, which underwent  $\beta$ -C-C scission and formed 2-methyl-1,3-butadiene and *n*-propyl radical. This pathway may explain the early formation of 2-methyl-1,3-butadiene at lower temperatures. Because of the complex reaction network in the ethylcyclohexane pyrolysis, there could be other pathways to producing 2-methyl-1,3-butadiene. From the viewpoint of energy barriers, the route to 2-methyl-1,3-butadiene and *n*-propyl radical might be completed with the route to 1,3-pentadiene (2-TS2  $\rightarrow$  2-INT5  $\rightarrow$  2-TS5). Including this previously unconsidered pathway is expected to reduce the formation of 1,3-pentadiene and achieve a better prediction of the experimental measurement.

The reaction mechanism of vinylcyclopentane (Fig. 5.5e) is unclear because this intermediate has not been examined in previous ethylcyclohexane studies. Like the computed 6-octen-1-yl radical pathways, the probable reactions to form a five-membered-ring intermediate could also come from other  $C_8H_{15}$  alkenyl radicals. For example, the radical addition to the double bond of 5-octen-1-yl radical (the ring-opening isomerization product of 2-ethyl-cyclohexyl radical), forms a five-membered-ring intermediate. Further  $\beta$ -C-C scission of this radical could produce vinylcyclopentane. Figure 5.7 shows the reaction pathways calculated for 5-octen-1-yl radical. The H-elimination pathways are also not shown because of their higher energy barrier. The reaction channel with the lowest energy barrier is highlighted in blue. Reaction initiates from the radical addition to the double bond of the 5-octen-1-yl radical via 3-TS1, which led to a five-membered-ring intermediate 3-INT1. The  $\beta$ -C-C scission of 5-octen-1-yl radical via 3-TS5 forms vinylcyclopentane and methyl radical. This reaction channel to vinylcyclopentane is feasible considering the low energy barrier.

On the other hand, the intramolecular H-atom isomerization of 5-octen-1-yl radical formed resonance stabilized radical intermediates 3-INT2 and 3-INT3 via



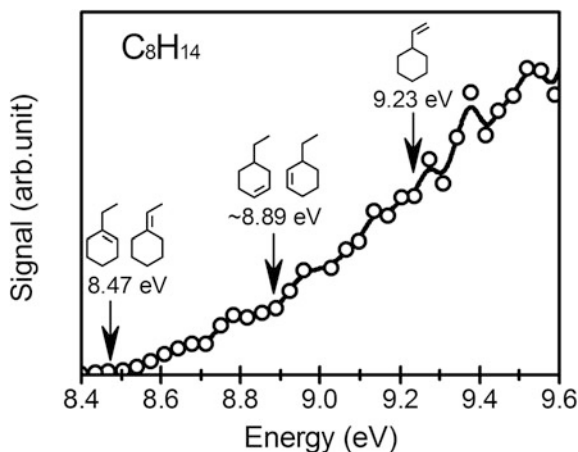
**Fig. 5.7** Potential energy surface of 5-octen-1-yl radical at CBS-QB3 level of theory. (0 K, unit: kcal/mol). Reprinted from Ref. [8], Copyright 2015, with permission from Elsevier

3-TS2 (1,7-H-migration) and 3-TS3 (1,4-H-migration), respectively. The energy barrier of 1,7-H-migration was 3 kcal/mol lower than the 1,4-H-migration channel, indicating that the 1,7-H-migration is also feasible. The  $\beta$ -C-C scission of 3-INT2 and 3-INT3 via 3-TS6, 3-TS7 and 3-TS8 led to 1,3-pentadiene, 1,3-hexadiene, and 1,3-heptadiene, respectively. As shown in Fig. 5.4, the JetSurF 2.0 model included only the two pathways of 5-octen-1-yl radical, i.e., via 3-TS3  $\rightarrow$  3-INT3  $\rightarrow$  3-TS7 and 3-TS4. Including other reaction pathways in Fig. 5.7 may reduce the carbon flux to 1,3-hexadiene (Fig. 5.5d) and achieve a better prediction of its formation. Moreover, the prediction for 1,3-heptadiene in Fig. 5.5f is also expected to improve when the reaction channel via 3-TS8 is included in the model.

It is necessary to revisit the reaction mechanism and clarify the branching ratios of the reactions of  $C_8H_{15}$  alkenyl radicals, such as those in Figs. 5.6 and 5.7 computed for 5-octen-1-yl and 6-octen-1-yl radicals. To this end, temperature- and pressure-dependent rate constants are desired; the reactions involving radical addition to the double bond could also proceed for other  $C_8H_{15}$  alkenyl radicals in ethylcyclohexane pyrolysis. Further experiment and theoretical study is required, and the preliminary results for 5-octen-1-yl and 6-octen-1-yl radicals in this work have shed light on this project.

### 5.2.3 Dissociation of Ethylcyclohexane Radicals

The dissociation of ethylcyclohexane radicals leads to C6-C8 cyclic alkenes, such as cyclohexene, methylenecyclohexane ( $C_7H_{12}$ ), and cyclic  $C_8H_{14}$  intermediates. Figure 5.8 presents the photoionization efficiency spectra of the  $m/z$  corresponding to  $C_8H_{14}$ . The structure and ionization energies of the five probable isomers of cyclic  $C_8H_{14}$  intermediates are shown in Table 5.2. These values are from the NIST database [13] and calculations from this work.



**Fig. 5.8** Photoionization efficiency spectra of  $C_8H_{14}$  intermediates measured in ethylcyclohexane atmospheric pressure pyrolysis. Reprinted from Ref. [8], Copyright 2015, with permission from Elsevier

**Table 5.2** Structure and adiabatic ionization energies of the probable cyclic  $C_8H_{14}$  intermediates in ethylcyclohexane atmospheric pressure pyrolysis

Formula	Species	Structure	IE/eV	Refs.
$C_8H_{14}$	Vinylcyclohexane		9.19	This work
	Ethylidenecyclohexane		8.47	[13]
	1-ethylcyclohexene		8.48	[13]
	3-ethylcyclohexene		8.83	[13]
	4-ethylcyclohexene		8.88	[13]

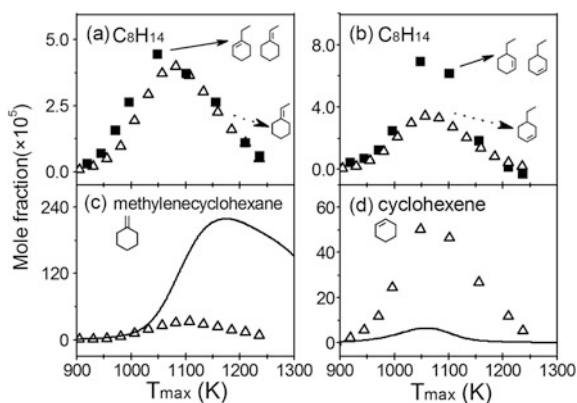
Reprinted from Ref. [8], Copyright 2015, with permission from Elsevier

The mole fractions of C6–C8 cyclic alkenes are shown in Fig. 5.9. Considering the uncertainties of the experimental measurement, the mole fractions of cyclic  $C_8H_{14}$  intermediates in Fig. 5.9a, b measured by SR-PI-MBMS and GC analysis were consistent. The mole fraction of methylenecyclohexane and cyclohexene analyzed by the GC is shown in Fig. 5.9c, d. The mole fraction of methylenecyclohexane was comparable to that of the C5 dienes and higher than the mole fractions of the  $C_7H_{12}$  intermediates in methylcyclohexane pyrolysis. The longer side chain of ethylcyclohexane easily formed methylenecyclohexane. For example, the H-atom abstraction of ethylcyclohexane forms 1-ethyl-cyclohexyl radical, whose  $\beta$ -C–C scission leads to methylenecyclohexane (Fig. 5.3); and, the dissociation of ethylcyclohexane by way of R2 forms cyclohexylmethyl radical, whose  $\beta$ -C–H scission also forms methylenecyclohexane. The simulation shows that  $\beta$ -C–C scission of 1-ethyl-cyclohexyl radical is the dominant source for

methylenecyclohexane. However, the model significantly over-predicted the mole fraction profiles of methylenecyclohexane, most likely because model did not predict the branching ratio of the 1-ethyl-cyclohexyl radical decomposition. According to Fig. 5.3, both the ring-opening isomerization of 1-ethyl-cyclohexyl radical to alkenyl radical and the dissociation of 1-ethyl-cyclohexyl radical to methylenecyclohexane are important. However, 1-ethyl-cyclohexyl radical was dominantly consumed by the dissociation channel to form methylenecyclohexane. The absence of subsequent reactions of methylenecyclohexane could be another reason for the over-prediction of its mole fraction.

Figure 5.8d shows the mole fraction profile of cyclohexene, which is dominantly produced from  $\beta$ -C-C scission of 2-ethyl-cyclohexyl radical and the  $\beta$ -C-H scission of cyclohexyl radical. The 2-ethyl-cyclohexyl radical derives from the H-atom abstraction of ethylcyclohexane, while cyclohexyl radical is produced from the dissociation of ethylcyclohexane via R1. The step-wise dehydrogenation of cyclohexene is an important source for benzene [9, 10]. Similar reactions of cyclic  $C_8H_{14}$  alkenes could promote the formation of ethylbenzene. Moreover, the step-wise dehydrogenation of methylenecyclohexane forms *o*-isotoluene and *p*-isotoluene; and subsequent reactions of *o*-isotoluene and *p*-isotoluene (direct H-elimination and H-atom abstraction) lead to benzyl radical [14], an important precursor for aromatics. The formation of these cyclic C6-C8 intermediates plays an important role in the high sooting tendency of ethylcyclohexane. Many aromatics were measured in this work (Table 5.1).

Preliminary study indicates that the combination of SR-PI-MBMS and GC analysis separates many isomers, and the results obtained from the two different analytical methods are in good agreement. The measurement of 3-octene confirms that ring-opening isomerization of ethylcyclohexane is the initial decomposition



**Fig. 5.9** Experimental (solid symbols) and simulated mole fraction profiles (lines) of C6-C8 cyclic intermediates during ethylcyclohexane pyrolysis at atmospheric pressure. Solid symbol: SR-PI-MBMS data; open symbol: GC data. Solid lines are simulation from revised JetSurF 2.0 model. Solid arrows in Fig. 5.9a, b are species measured by SR-PI-MBMS. Dashed lines are species measured by the GC. Reprinted from Ref. [8], Copyright 2015, with permission from Elsevier

step of ethylcyclohexane. Possible reactions for 2-methyl-1,3-butadiene and vinylcyclopentane is discussed—a guide to further kinetic model development. The kinetics for the C4–C7 chain and branched dienes, and C6–C8 cyclic alkenes are discussed with the aid of model prediction from the JetSurF 2.0 model.

To further examine the combustion chemistry of ethylcyclohexane, its pyrolysis was investigated at 30 and 150 Torr. Low-pressure pyrolysis is more responsive to the study of initial decomposition pathways of ethylcyclohexane; therefore the low-pressure premixed flame of ethylcyclohexane/O<sub>2</sub>/Ar was studied at 30 Torr, which provided sufficient data to investigate the reaction mechanism, decomposition and the formation of aromatics at flame conditions in ethylcyclohexane. The detailed kinetic combustion model was developed with the help of quantum chemistry calculations of reaction pathways, and examined with the pyrolysis and flame data in this work, as well as JSR speciation and flame speed data in the literature.

### 5.3 Kinetic Model of Ethylcyclohexane

Compared to the kinetic model of methylcyclohexane, the reaction class for the sub-mechanism of ethylcyclohexane includes:

- (a) Dissociation and isomerization of ethylcyclohexane
- (b) Dissociation of octene and ethyl-hexene isomers
- (c) H-atom abstraction of ethylcyclohexane
- (d) Dissociation and isomerization of ethylcyclohexane radicals
- (e) Dissociation and isomerization of octenyl radicals and ethyl-hexenyl radicals
- (f) Dissociation and step-wise dehydrogenation of C<sub>8</sub>H<sub>14</sub> cyclic alkenes.

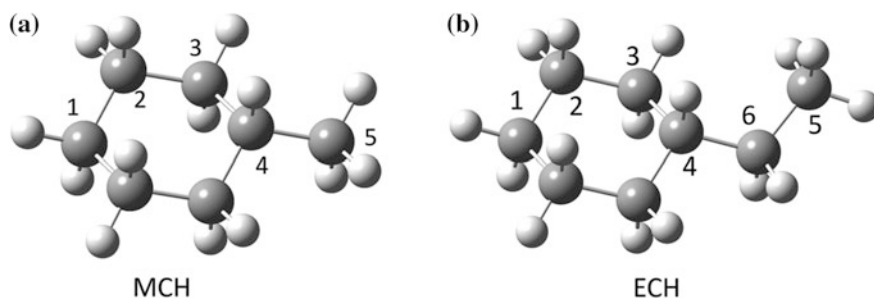
In the preliminary study on the initial decomposition of ethylcyclohexane in Sect. 5.2, its decomposition rate constant was estimated from the analogous reactions of methylcyclohexane and propane. The prediction for the reactivity of ethylcyclohexane atmospheric pyrolysis was satisfactory. Experimental study and theoretical calculation of the unimolecular decomposition pathways of ethylcyclohexane is scarce, especially pressure-dependent rate constants. Like the preliminary study in Sect. 5.2, the pressure- and temperature- dependent rate constants of ethylcyclohexane decomposition are estimated from those of methylcyclohexane (R1, R3–R9 in Fig. 5.1) and propane (R2 in Fig. 5.1).

The ring-opening isomerization of ethylcyclohexane forms three octene isomers (1-octene, 2-octene, and 3-octene, R3-R5) and four ethyl-hexenes (2-ethyl-1-hexene, 3-ethyl-1-hexene, 4-ethyl-1-hexene, and 5-ethyl-1-hexene, R6–R9). In the model from this group, the unimolecular reactions of these alkenes by way of the allylic C–C bond scission led to resonance-stabilized radicals. The rate constants of these reactions were estimated from the allylic C–C bond fission of 1-hexene, which forms allyl radical and n-propyl radical [15]. The H-atom abstraction rate constants of these alkene intermediates were estimated from the rate rules proposed by Pitz et al. [16, 17].

H-atom abstractions by H, O, OH, HO<sub>2</sub>, CH<sub>3</sub> and O<sub>2</sub> are important routes that consume ethylcyclohexane. The site-specific rate constants of these H-atom abstraction reactions were adopted from the JetSurF 2.0 model [7], with several modifications, as discussed below. First, the optimized structures of methylcyclohexane and ethylcyclohexane were compared, which were computed at CBS-QB3 level of theory with the B3LYP/CBSB7 basis set. Figure 5.10 shows that the chair configuration of the cyclohexane ring with alkyl substitution at the equatorial position was the stable conformer for methylcyclohexane and ethylcyclohexane. The degeneracy of carbon sites two and three were two, since they had another quasi-identical carbon. The similar structure of methylcyclohexane and ethylcyclohexane indicated that rate constants of H-atom abstraction on the analogous carbon site should be similar. For instance, the H-atom abstraction rate constants of methylcyclohexane-C1 and ethylcyclohexane-C1 (i.e., radical on carbon site 1) by OH radical. Here, the H-atom abstraction rate constants on the analogous carbon site were compared with the methylcyclohexane model in Chap. 4 and the ethylcyclohexane sub-mechanism of the JetSurF 2.0 model in a temperature range of 800–2000 K. Except for the H-atom abstraction by the H atom, the H-atom abstraction rate constants by way of O, OH, HO<sub>2</sub>, CH<sub>3</sub> and O<sub>2</sub> in the methylcyclohexane model in Chap. 4 were taken from the JetSurF 2.0 model.

The results show that the H-atom abstraction rate constants by the H atom for carbon site one to carbon site four (i.e., methylcyclohexane-C1 vs. ethylcyclohexane-C1, methylcyclohexane-C2 vs. ethylcyclohexane-C2, etc.), were very close between the two molecules. However, the H-atom abstraction rate constants for carbon site five were different; the rate constants in ethylcyclohexane model were about a factor of two faster than those in methylcyclohexane model. In ethylcyclohexane, both C1 and C6 are the secondary carbon site; and their H-atom abstraction rate constants by the H atom were very close.

For H-atom abstractions by OH radical, the difference at C1–C3 between methylcyclohexane and ethylcyclohexane was 10–30%. Like the H-atom abstraction by H atom, the rate constant of the H-atom abstraction by OH radical at the



**Fig. 5.10** Optimized structure of methylcyclohexane and ethylcyclohexane at CBS-QB3 level of theory. Reprinted from Ref. [18], Copyright 2015, with permission from Elsevier

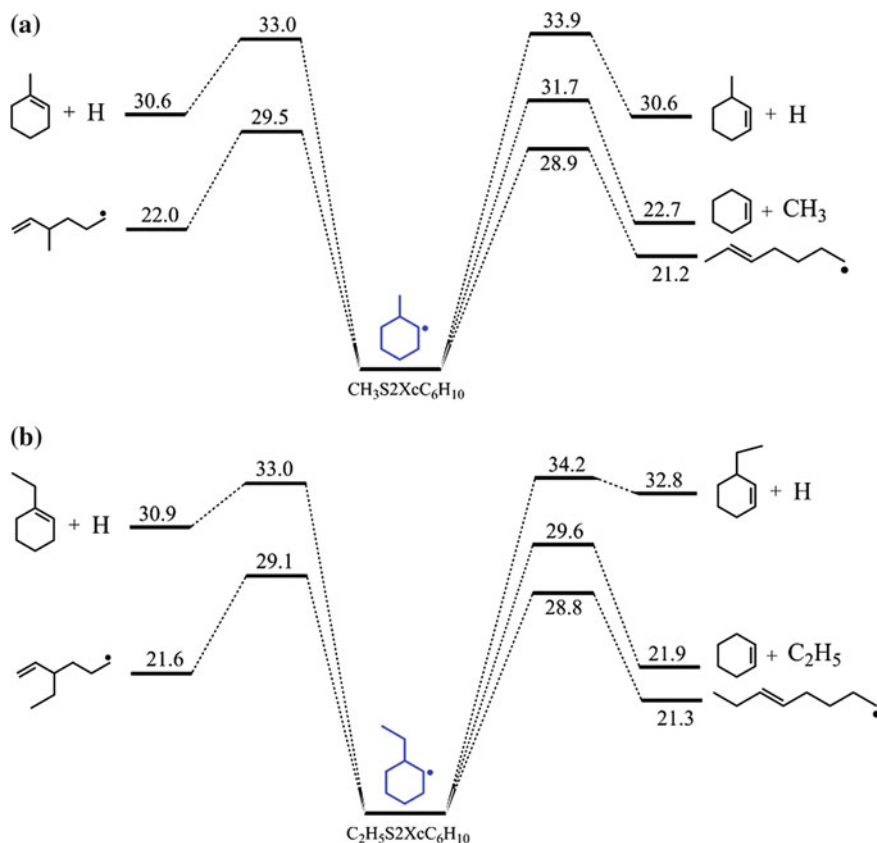
primary carbon site (C5) of ethylcyclohexane was twice as large as that of methylcyclohexane, the largest difference being the H-atom abstraction at the tertiary carbon site (C4), the rate constant of methylcyclohexane was two to eight times greater than the rate constant of ethylcyclohexane.

For the H-atom abstractions by  $\text{CH}_3$  radical, the difference in the H-atom abstraction at C1–C3 between methylcyclohexane and ethylcyclohexane was 10–50%. In the H-atom abstractions at the primary carbon site (C5) and the tertiary carbon site (C4), the rate constant of ethylcyclohexane was three and 2.5 times greater than that of methylcyclohexane, respectively.

The rate constants of H-atom abstractions by the O atom,  $\text{O}_2$  and  $\text{HO}_2$  radical were estimated from similar carbon sites of propane, isobutane and cyclohexane in the JetSurF 2.0 model. The same estimation was adopted to find the H-atom abstraction rate constants by these radicals in the methylcyclohexane sub-mechanism. Compared to the methylcyclohexane sub-mechanism, the discrepancy for rate constants in the H-atom abstraction reactions of ethylcyclohexane sub-mechanism in the JetSurF 2.0 model was not large, the major difference being H-atom abstractions at the primary carbon (C5) and tertiary carbon sites (C4) by the H atom, OH and  $\text{CH}_3$  radicals. However, these differences are not expected to be significant for ethylcyclohexane consumption since the hydrogen numbers of the primary C–H and tertiary C–H were not high in comparison with the total C–H numbers of ethylcyclohexane. In this work, H-atom abstraction rate constants of ethylcyclohexane by H atom, OH and  $\text{CH}_3$  radicals were estimated from those of analogous reactions of methylcyclohexane. The rate constants of the H-atom abstractions at the C6 site in ethylcyclohexane were adopted from the JetSurF 2.0 model.

H-atom abstraction of ethylcyclohexane forms six ethylcyclohexane radicals, whose reaction pathways were calculated in this work at CBS-QB3 level. Figure 5.11 shows the potential energy surface of the major reactions of 2-ethyl-cyclohexyl radical. The reaction pathways of other ethylcyclohexane radicals are presented in Figs. B.1, B.2, B.3 and B.4 in Appendix B. Like the reaction pathways of methylcyclohexane radicals, these reactions include three classes: isomerizing to long-chain alkenyl radicals via  $\beta$ -C–C scission, decomposing to cyclic alkenes and small radicals via  $\beta$ -C–C scission, and decomposing to cyclic alkenes and H atom via  $\beta$ -C–H scission. The energy barriers of the  $\beta$ -C–C scission channels (28–30.2 kcal/mol) were slightly lower than  $\beta$ -C–H scission channels (32.3–35.5 kcal/mol), indicating that the former reaction is more favorable.

To estimate the rate constants of ethylcyclohexane radical decomposition, potential energy surfaces of the unimolecular reactions of methylcyclohexane radicals and ethylcyclohexane radicals were compared, as shown in Fig. 5.11 and Figs. B.1, B.2, B.3 and B.4 in Appendix B. In most cases, the barrier height difference for the analogous reaction class of methylcyclohexane radical and ethylcyclohexane radical was very small, which is lower than the uncertainty of the CBS-QB3 method (1 kcal/mol). The largest discrepancy of 2.1 kcal/mol was for the  $\beta$ -C–C scission between the ring and the side-chain of the 2-ethyl-cyclohexyl radical and the 2-methyl-cyclohexyl radical. This comparison shows that the



**Fig. 5.11** Potential energy surfaces for unimolecular reactions of 2-methyl-cyclohexyl radical and 2-ethyl-cyclohexyl radical. Reprinted from Ref. [18], Copyright 2015, with permission from Elsevier

reaction kinetics of methylcyclohexane radicals can be used to estimate the rate constants of ethylcyclohexane radical decomposition and isomerization. Thus, the reaction kinetics of methylcyclohexane radical decomposition and isomerization were used to estimate those of the same reaction type as ethylcyclohexane radicals. In the case of 2-ethyl-cyclohexyl radical decomposing to ethyl radical and cyclohexene, the rate constants were estimated from the decomposition of 2-methyl-cyclohexyl radical to methyl radical and cyclohexene, but the activation energy was reduced by 2.1 kcal/mol to consider the energy difference caused by the dissimilar length of side-chain. Estimating the reaction kinetics of ethylcyclohexane radicals from methylcyclohexane radicals could lend some uncertainty to the ethylcyclohexane kinetic model since the reaction kinetics of the two radicals may have different pressure dependence.



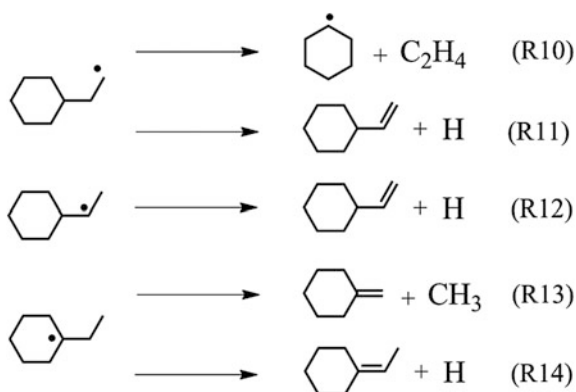
Unimolecular reactions of ethylcyclohexane radical which cannot be estimated from the analogous reactions of methylcyclohexane radicals are shown in Fig. 5.12. Rate constants for R10 in the JetSurF 2.0 model were adopted; and the rate constants of R11–R12 were estimated from the  $\beta$ -C–H scission of *n*-propyl and iso-propyl radicals [19], respectively. The high pressure limit rate constants of R13, i.e., the  $\beta$ -C–C scission of 1-ethyl-cyclohexyl radical to methylenecyclohexane and methyl radical, were estimated from the decomposition of 2-methyl-but-2-yl radical to iso-butene and methyl radical [20]. The pressure dependence of R13 was referred to the radical ring-opening isomerization of the 1-ethyl-cyclohexyl. For R14, the rate constants of the  $\beta$ -C–H scission of 1-ethyl-cyclohexyl radical to 1-ethyl-cyclohexene were used and divided by a factor of two.

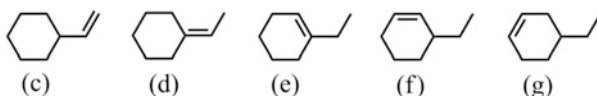
The last reaction type included for the ethylcyclohexane radicals was their intramolecular H-atom migration (isomerization), e.g., 2-cyclohexyl-ethyl to 2-ethyl-cyclohexyl, 3-ethyl-cyclohexyl, and 4-ethyl-cyclohexyl, etc. The reaction pathways of these radicals and their rate constants were included in the JetSurF 2.0 model and used in this work.

The ring-opening isomerization of the ethylcyclohexane radicals led to chain and branched alkenyl radicals, as shown in Fig. 5.4. Subsequent reactions of these radicals, including  $\beta$ -C–C scission and/or intramolecular H-atom migration to resonance stabilized radical intermediates, were adopted from the JetSurF 2.0 model or referred to similar reactions of 5-hexen-1-yl radical. For the  $\beta$ -C–C scission of the resonance-stabilized radical intermediates, the rate constants were estimated from the dissociation of 1-hexen-3-yl radical in the JetSurF 2.0 model. In addition, the reactions of the radical addition to the double bond of the alkenyl radicals (like those leading to 2-methyl-1,3-butadiene and vinylcyclopentane), were included in the model and will be discussed later.

The  $\beta$ -C–H scission of the ethylcyclohexane radicals forms vinylcyclohexane (c), ethylidenecyclohexane (d), and three ethylcyclohexenes (e–g). The rate rules by Pitz et al. [16, 17] was adopted to estimate the H-atom abstraction rate constant of these cyclic intermediates.

**Fig. 5.12** Specific unimolecular reaction type of ethylcyclohexane radicals that cannot proceed from methylcyclohexane radicals. Reprinted from Ref. [18], Copyright 2015, with permission from Elsevier





The ring-opening of vinylcyclohexane (c) via the C–C scission adjacent to the side-chain, formed 1,3-octadiene. The rate constant of this reaction was estimated from the ring-opening isomerization of methylcyclohexane to 2-heptene [11]. The retro-Diels-Alder reaction of 1-ethylcyclohexene (c), 3-ethylcyclohexene (f), and 4-ethylcyclohexene (g) led to 2-ethyl-1,3-butadiene and ethylene, 1,3-hexadiene and ethylene, and 1,3-butadiene and 1-butene. Rate constants of these reactions were estimated from the analogous reactions of cyclohexene [19]. The step-wise dehydrogenation of vinylcyclohexane, ethylidenecyclohexane, and ethylcyclohexenes formed cyclic dienes (C<sub>8</sub>H<sub>12</sub>) and cyclic trienes (C<sub>8</sub>H<sub>10</sub>); and the H-atom abstraction reactions for these species were also adopted from the rate rules of Pitz et al. [16, 17]. H-atom elimination reactions of cyclic dienes (C<sub>8</sub>H<sub>12</sub>) and cyclic trienes were adopted from the analogous reactions of propene [19]. For radical intermediates during the step-wise dehydrogenation process, such as C<sub>8</sub>H<sub>13</sub>, C<sub>8</sub>H<sub>11</sub>, and C<sub>8</sub>H<sub>9</sub>, the rate constants for the β–C–H scission were estimated from the analogous reaction of 1-buten-3-yl radical (SAXC<sub>4</sub>H<sub>7</sub>) [7].

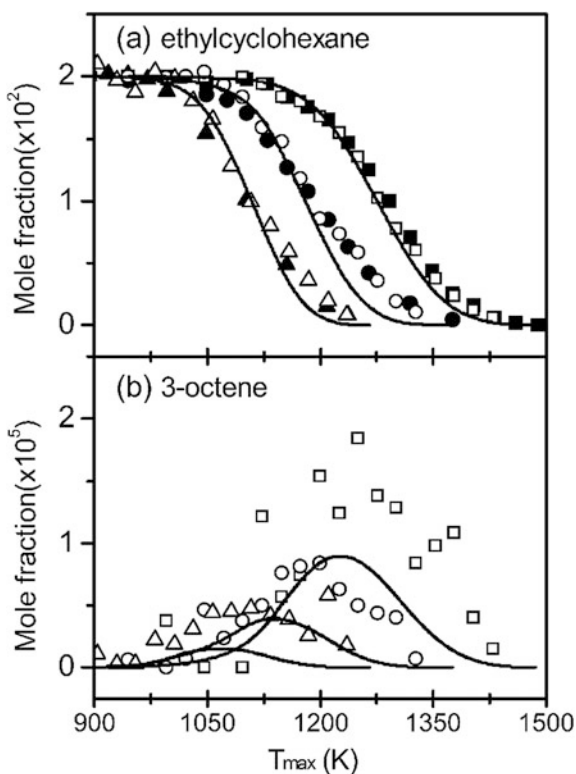
The detailed kinetic model for ethylcyclohexane high-temperature pyrolysis and oxidation were developed by adding the sub-mechanism of ethylcyclohexane to the cyclohexane and methylcyclohexane kinetic model. The kinetic model was examined by the species speciation in the flow reactor pyrolysis at 30, 150, and 760 Torr, in laminar premixed flame at 30 Torr, and in the atmospheric pressure jet-stirred reactor oxidation, as well as the laminar flame speed of ethylcyclohexane. The reaction kinetics of ethylcyclohexane pyrolysis and oxidation under different combustion environments were discussed, focusing on the aromatic formation mechanism.

## 5.4 Pyrolysis of Ethylcyclohexane

The flow reactor pyrolysis of ethylcyclohexane at atmospheric pressure has been examined in Sect. 5.2. Here, ethylcyclohexane pyrolysis at 30 and 150 Torr has been extended. The experimental conditions are the same as in the atmospheric pressure experiment, the fuel mole fraction is 0.02 and the residue is the dilution gas Ar. Pyrolysis products were measured using SR-PI-MBMS and GC analysis; those detected at lower pressure were similar to the atmospheric pressure experiment, except that radicals like methyl, propargyl, and allyl were measured at lower pressure pyrolysis. Because the secondary reactions were mitigated, the production of aromatics was also lower during low pressure experiments.

Mole fraction profiles of ethylcyclohexane and 3-octene at 30, 150, and 760 Torr pyrolysis are shown in Fig. 5.13. The model captures well the consumption of ethylcyclohexane, and the formation of 3-octene. From the preliminary study in Sect. 5.2, octene was confirmed as the initial decomposition product of ethylcyclohexane, which was also detected in 30 and 150 Torr pyrolysis experiments. Experiments and simulation both showed that the mole fraction of this intermediate decreased with increasing pressure; the trend was also observed for the initial decomposition product during the pyrolysis of cyclohexane and methylcyclohexane [9, 10]. This phenomenon can be explained by the pressure-dependent competitive relationship between the unimolecular decomposition and H-atom abstraction reactions. With the decrease of pressure, the collision of the molecule was mitigated. Consequently, the contribution of H-atom abstraction reaction was reduced at lower pressures. The relatively lower contribution of the H-atom abstraction reactions led to the relatively higher contribution of the unimolecular decomposition channels and the higher mole fraction of the initial decomposition products. Comparison of ethylcyclohexane mole fraction profiles in Fig. 5.13, and other pyrolysis intermediates, show that SR-PI-MBMS data is nearly identical to the GC data. In the discussion on the reaction kinetics of ethylcyclohexane pyrolysis, the analysis was based on the SR-PI-MBMS data.

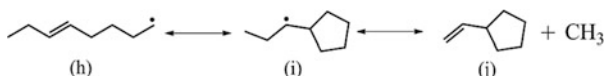
**Fig. 5.13** Mol fraction profiles of ethylcyclohexane and its initial decomposition product 3-octene in ethylcyclohexane pyrolysis at 30, 150, and 760 Torr. Solid symbol is from SR-PI-MBMS data. Open symbol is from GC data, lines are from simulation. Square represents 30 Torr. Circle is 150 Torr. Triangle is 760 Torr data



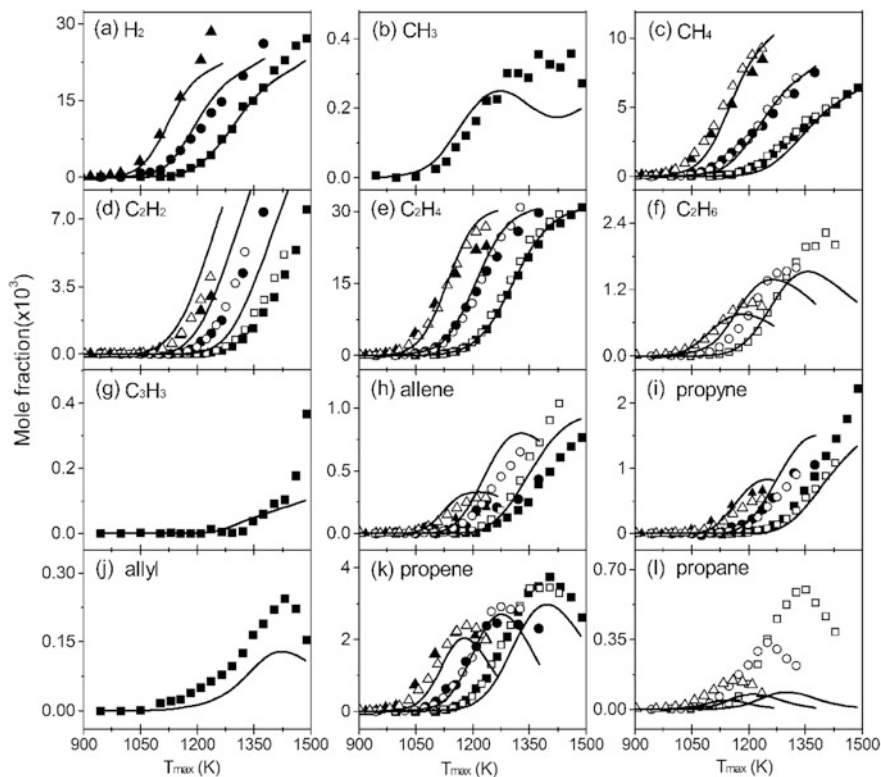
The sensitivity analysis for ethylcyclohexane consumption was performed at 30 Torr with fuel conversion of 86% and at 760 Torr, with fuel conversion of 83%. Similar to methylcyclohexane pyrolysis [9], the sensitivity analysis showed that the dissociation of ethylcyclohexane to ethyl radical and cyclohexyl radical (R1 in Fig. 5.1) had the largest positive sensitivity coefficient; this is because R1 is an important reaction consuming ethylcyclohexane. More importantly, the subsequent reactions of cyclohexyl and ethyl radical are an important source for H-atoms. This is in accord with the reaction of  $C_2H_5 = C_2H_4 + H$ , and it also has a large positive sensitive coefficient, since the  $\beta$ -C-H scission of ethyl radical is an important source for H atom. The H-atom abstraction reactions by H atom also have large positive sensitivity coefficients. The good agreement between experiments and simulation indicates that the estimated rate constants for the unimolecular and H-atom abstraction reactions of ethylcyclohexane were reasonable.

The unimolecular decomposition and H-atom abstraction reactions of ethylcyclohexane form cyclohexyl and ethylcyclohexane radicals. The isomerization of these radicals by way of the  $\beta$ -C-C scission ring-opening forms  $C_6H_{11}$  alkenyl radical (Fig. 4.18a) and  $C_8H_{15}$  alkenyl radicals (Fig. 5.4). Further reactions of these radicals are the source of abundant pyrolysis intermediates observed in this work. Figures 5.14 and 5.15 show the measured and model-predicted mole fraction profiles of the C0-C7 intermediates. In most cases, the model prediction for these pyrolysis species was satisfactory. The following section focuses on the reaction kinetics of some representative intermediates.

Figure 5.15l shows mole fraction profiles of vinylcyclopentane. Reaction pathways calculated for 5-octen-1-yl radical in Fig. 5.7 were included in the kinetic model, as shown below.



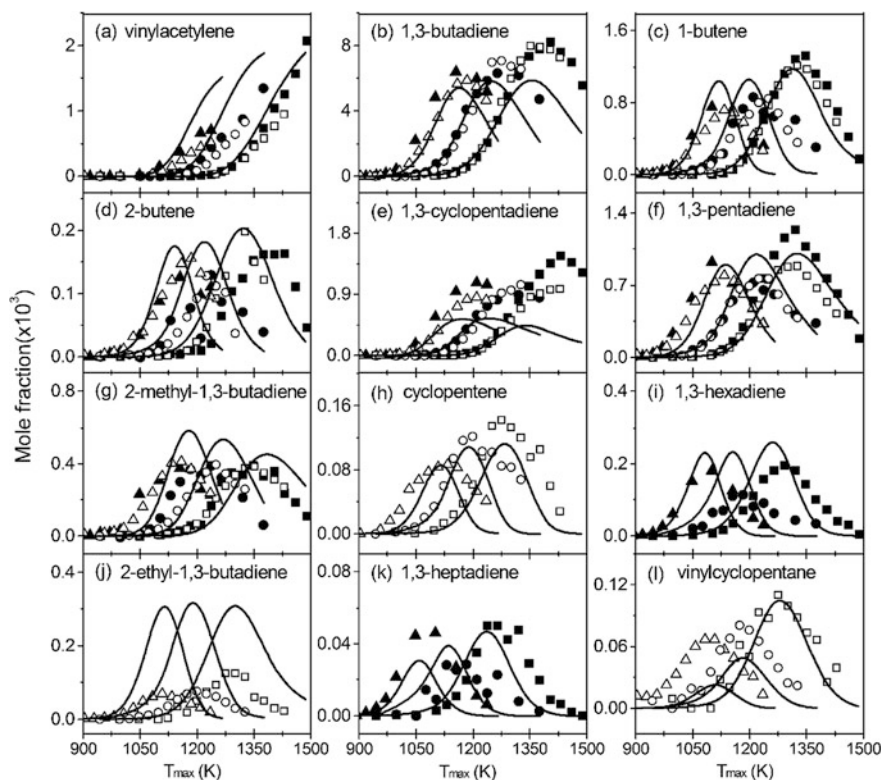
In the model development, the ring-opening isomerization and dissociation reactions of 1-cyclopentylpropyl radical were considered. Rate constants for the ring-opening isomerization ( $i \rightarrow h$ ) were estimated from the analogous reaction of the cyclopentylmethyl radical ( $\text{C}_5\text{H}_9\text{CH}_2\cdot$ ) [21]; and the rate constants for the dissociation by way of  $\beta$ -C-C scission of 1-cyclopentylpropyl radical ( $i \rightarrow j$ ) were estimated from the analogous reactions of 2-butyl radical [20]. For subsequent reactions of vinylcyclopentane, the ring-opening isomerization via the C-C bond scission adjacent to the side chain formed 1,3-heptadiene; the rate constants for this reaction were estimated from the ring-opening isomerization of cyclopentane [22]. Rate constants of H-atom abstraction reactions on the tertiary and secondary C-H were estimated from the rate rule proposed by Pitz et al. [16, 17]. The experimental observation that the mole fraction of vinylcyclopentane decreases with pressure was well predicted by the model; however, the mole fraction of vinylcyclopentane was under-predicted at



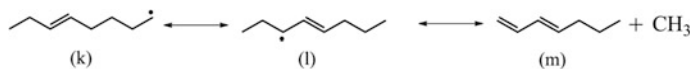
**Fig. 5.14** Mol fraction profiles of C0–C3 products in ethylcyclohexane pyrolysis at 30, 150, and 760 Torr. Solid symbol is from SR-PI-MBMS data, open symbol from GC data, lines from simulation. Square is 30 Torr, circle is 150 Torr, triangle is 760 Torr data

760 Torr. Further study of the rate constants of 5-octen-1-yl reactions is needed to improve the prediction of vinylcyclopentane.

Mole fraction profiles of 1,3-heptadiene are presented in Fig. 5.15k. In the discussion in Sect. 5.2, the mole fraction of this intermediate was under-predicted by the JetSurF 2.0 model (Fig. 5.5f). The reaction pathway calculation in Fig. 5.7 shows that the following reactions of 5-octen-1-yl radical (k), i.e., intramolecular H-migration to 4-octen-3-yl radical (k → l) and subsequent decomposition via  $\beta$ -C–C scission led to 1,3-heptadiene (l → m). However, only the  $\beta$ -C–C scission of 4-octen-3-yl radical to 1,3-hexadiene and ethyl radical was included in the JetSurF 2.0 model. In the ethylcyclohexane kinetic model in this work, the  $\beta$ -C–C scission of 5-octen-1-yl radical to 1,3-heptadiene and methyl radical (l → m) was considered. The model predicted the mole fraction profiles of 1,3-heptadiene well after including this reaction channel.



**Fig. 5.15** Mol fraction profiles of C4–C7 products in ethylcyclohexane pyrolysis at 30, 150, and 760 Torr. Solid symbol is SR-PI-MBMS data, open symbol is GC data, lines are simulation. Square is 30 Torr, circle is 150 Torr, triangle is 760 Torr data

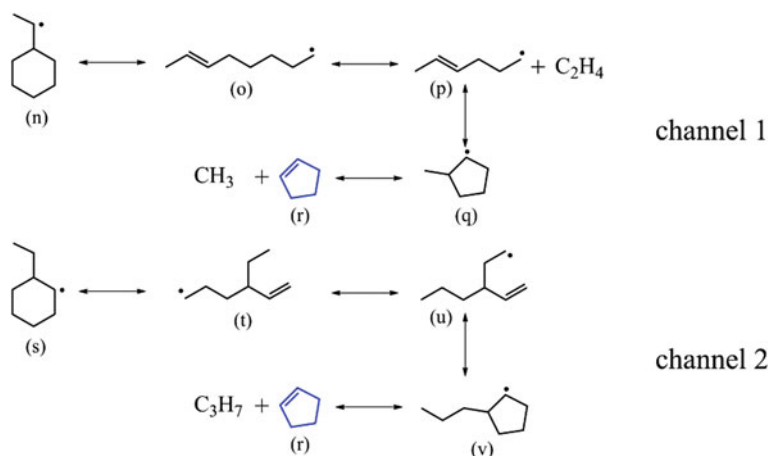


Mole fraction profiles of 2-ethyl-1,3-butadiene are presented in Fig. 5.15j. The reaction pathway analysis in Fig. 5.4 shows that there were three channels leading to 2-ethyl-1,3-butadiene. The dominant contribution coming from the decomposition of 2-ethyl-1-hexen-6-yl radicals. The association of 2-methylene-3-buten-1-yl radical with methyl radical, and the retro-Diels-Alder reaction of 1-ethylcyclohexene also formed 2-ethyl-1,3-butadiene. Although it is an abundant source for 2-ethyl-1,3-butadiene, the experimentally measured mole fraction for this species was not very high. The large discrepancy between experiment and simulation indicates that the reaction kinetics to 2-ethyl-1,3-butadiene may need to be improved and/or the experimental data for this intermediate double-checked.

Another C6 diene measured in the experiment was 1,3-hexadiene, as shown in Fig. 5.15i. This intermediate was produced from the decomposition of  $C_8H_{15}$  alkenyl radicals; two pathways are shown in Fig. 5.4d, e. The contribution of these two channels to 1,3-hexadiene was close. In the discussion of Sect. 5.2, the model prediction for 1,3-hexadiene by the JetSurF 2.0 model was a factor of two higher than the experiment. Analysis showed that the absence of other consumption channels for 5-octen-1-yl and 3-octen-5-yl radicals led to over-prediction of 1,3-hexadiene. On the other hand, the model prediction of vinylcyclohexane and 1,3-heptadiene was much lower than the experimental measurement. In the kinetic model in this work, absent reaction pathways to vinylcyclohexane and 1,3-heptadiene were included and the branching ratios for the unimolecular reactions of 5-octen-1-yl and 3-octen-5-yl radicals were better predicted. This explains the improved prediction of vinylcyclopentane (Fig. 5.15l), 1,3-heptadiene (Fig. 5.15k), and 1,3-hexadiene (Fig. 5.15i). 1,3-Hexadiene was also measured in the pyrolysis of methylcyclohexane, but the mole fraction was twice as low as that measured in ethylcyclohexane pyrolysis. Reaction pathway analysis showed that 1,3-hexadiene was also produced from the alkenyl radicals in the decomposition of the methylcyclohexane radicals; however, only one reaction channel led to 1,3-hexadiene in methylcyclohexane pyrolysis, while two reaction channels with an equal contribution led to 1,3-hexadiene in ethylcyclohexane pyrolysis.

In the GC analysis, cyclopentene was measured, as shown in Fig. 5.15h. The initial formation temperature of this intermediate was close to the chain and branched dienes, indicating that cyclopentene should not be produced from the built-up reactions of smaller intermediates.

We have proposed two possible pathways for cyclopentene, as shown in Fig. 5.16. The first reaction pathway started from the ring-opening isomerization of



**Fig. 5.16** Possible reaction pathways for cyclopentene. Reprinted from Ref. [18], Copyright 2015, with permission from Elsevier

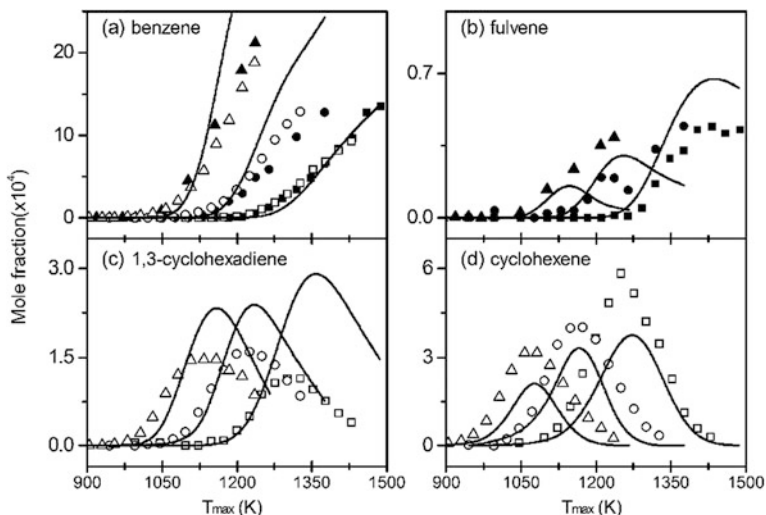
1-cyclohexylethyl radical (n) to 6-octen-1-yl radical (o), which decomposed into 4-hexen-1-yl radical via  $\beta$ -C-C scission (p). The radical addition to the double bond of 4-hexen-1-yl radical formed 2-methyl-cyclopentyl radical (q), which then produced cyclopentene and methyl radical (r) via  $\beta$ -C-C scission. The reaction pathway of  $p \rightarrow q \rightarrow r$  was not included in the JetSurF 2.0 model. In this model, the rate constants of 2-methyl-cyclopentyl radical decomposition ( $q \rightarrow r$ ) and isomerization ( $q \rightarrow p$ ) were adopted from the quantum chemistry of Sirjean et al. [21].

The second reaction pathway for cyclopentene starts from the 2-ethyl-cyclohexyl radical, which isomerized to 3-ethyl-1-hexen-6-yl radical by way of the ring opening ( $s \rightarrow t$ ). In addition to the reaction pathways in Fig. 5.4d, the 1,6-H migration of 3-ethyl-1-hexen-6-yl radical forms 3-propyl-4-penten-1-yl radical (u). The radical addition on the double bond of 3-propyl-4-penten-1-yl radical led to 2-propyl-cyclopentyl radical (v), which decomposed into cyclopentene (r) and n-propyl radical through  $\beta$ -C-C scission. The rate constants of  $t \rightarrow u$  referred to the 1,6-H intramolecular isomerization of 1-octyl radical [7]. Rate constants of ring-opening isomerization and dissociation of 2-propyl-cyclopentyl radical were estimated from the analogous reactions of 2-methyl-cyclopentyl radical [21]. Model prediction with these two reaction pathways agreed well with the experimental measurement of cyclopentene. Further analysis revealed that the contributions of channels one and two were close at 30 Torr pyrolysis, while channel one was dominant at 760 Torr pyrolysis. The dominant consumption channel for cyclopentene was the unimolecular hydrogen elimination and the H-atom abstraction by H atom.

Mole fractions of two C5 dienes—1,3-pentadiene and 2-methyl-1,3-butadiene—appear in Fig. 5.15f, g. The mole fraction profiles obtained from the SR-PI-MBMS analysis and GC analysis were in good agreement. As shown in Fig. 5.4, 1,3-pentadiene was produced largely from the  $\beta$ -C-C scission of 2-hepten-4-yl radical. The 2-methyl-1,3-pentadiene, was mainly produced from the bimolecular reactions of H atom with 2-ethyl-1,3-butadiene, the recombination of H atom with 2-vinyl-3-buten-1-yl radical, and the recombination of methyl radical with  $iC_4H_5$  radical. In Sect. 5.2, a possible reaction pathway for 2-methyl-1,3-butadiene (blue lines in Fig. 5.6), was proposed; this reaction pathway was also included, with rate constant estimation from reactions of molecules like 2-methyl-cyclohexyl radical, 5-hexen-1-yl radical, and 1-hexen-3-yl radical, etc. The reaction flux analysis revealed that the proposed reaction pathway contributed to 2-methyl-1,3-butadiene, especially at 30 Torr with a contribution of 10%. Although the contribution of the new proposed reaction pathways was not high, they did start earlier than other formation channels of 2-methyl-1,3-butadiene.

Like pyrolysis of cyclohexane and methylcyclohexane, large amounts of 1,3-butadiene were formed in the pyrolysis of ethylcyclohexane. The main source for 1,3-butadiene included the ring-opening isomerization of cyclohexyl radical (Fig. 4.18a), 3-methyl-cyclohexyl radical (Fig. 5.4 e), 4-methyl-cyclohexyl radical (Fig. 5.4 c), and 2-methyl-cyclohexyl radical (Fig. 5.4 d). The retro-Diels-Alder reaction of cyclohexene also contributed to 1,3-butadiene. 1,3-butadiene was





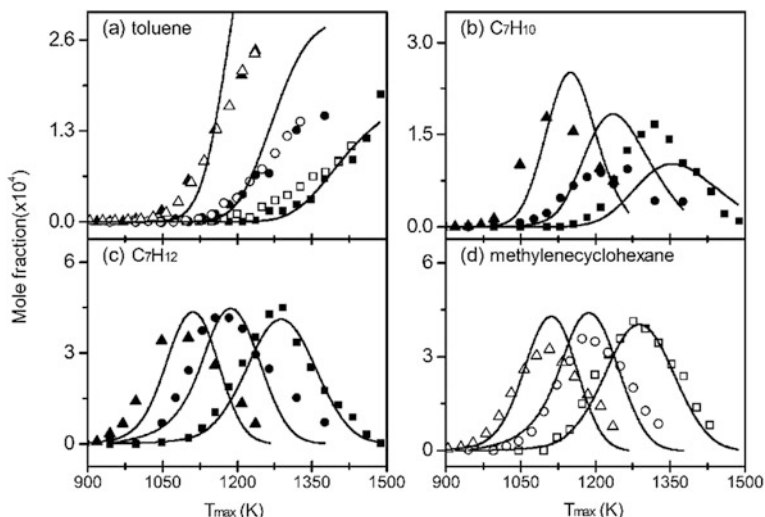
**Fig. 5.17** Mol fraction profiles of C6 cyclic intermediates in ethylcyclohexane pyrolysis at 30, 150, and 760 Torr. Solid symbol is SR-PI-MBMS data, open symbol is GC data, lines are simulation. Square is 30 Torr, circle is 150 Torr, triangle is 760 Torr data

consumed by the bimolecular reactions of 1,3-butadiene with H atom, leading to ethylene and vinyl radical, and the H-atom abstraction, to form  $nC_4H_5$  and  $iC_4H_5$  radicals. The H-elimination of  $nC_4H_5$  and  $iC_4H_5$  radicals is the source of vinylacetylene in Fig. 5.15a.

Section 5.2 discusses the decomposition of cyclohexyl radical and ethylcyclohexane radicals which led to C6–C8 cyclic intermediates. The mole fraction profiles of C6 cyclic intermediates, benzene, fulvene, and 1,3-cyclohexadiene, and cyclohexene, are shown in Fig. 5.17.

Decomposition of cyclohexyl and ethylcyclohexane radicals via the formation of cyclohexene, 4-ethyl-cyclohexene, and 3-ethyl-cyclohexene is important for benzene. Another major source of benzene is the H-atom-assisted isomerization of fulvene. There are two sources for fulvene, the recombination of methyl radical with cyclopentadienyl radical, and recombination of allyl radical with propargyl radical; the contribution of the former reaction pathway is dominant.

Figure 5.18 presents C7 cyclic intermediates measured in ethylcyclohexane pyrolysis at 30, 150, and 760 Torr. In the GC analysis, methylenecyclohexane was measured (Fig. 5.18d). In the SR-PI-MBMS experiment, the  $m/z$  corresponding to  $C_7H_{12}$  was also observed. The quantified mole fraction of  $C_7H_{12}$  with an estimated photoionization cross section of methylenecyclohexane (Fig. 5.18c) was close to that of the GC measurement of methylenecyclohexane, indicating that methylenecyclohexane was the dominant composition of  $C_7H_{12}$  signal in the SR-PI-MBMS experiment. The simulation showed that methylenecyclohexane was produced largely from the  $\beta$ -C–C scission of 1-ethyl-cyclohexyl radical and



**Fig. 5.18** Mol fraction profiles of C7 cyclic intermediates in ethylcyclohexane pyrolysis at 30, 150, and 760 Torr. Solid symbol is SR-PI-MBMS data, open symbol is GC data, lines are simulation. Square is 30 Torr, circle is 150 Torr, triangle is 760 Torr data

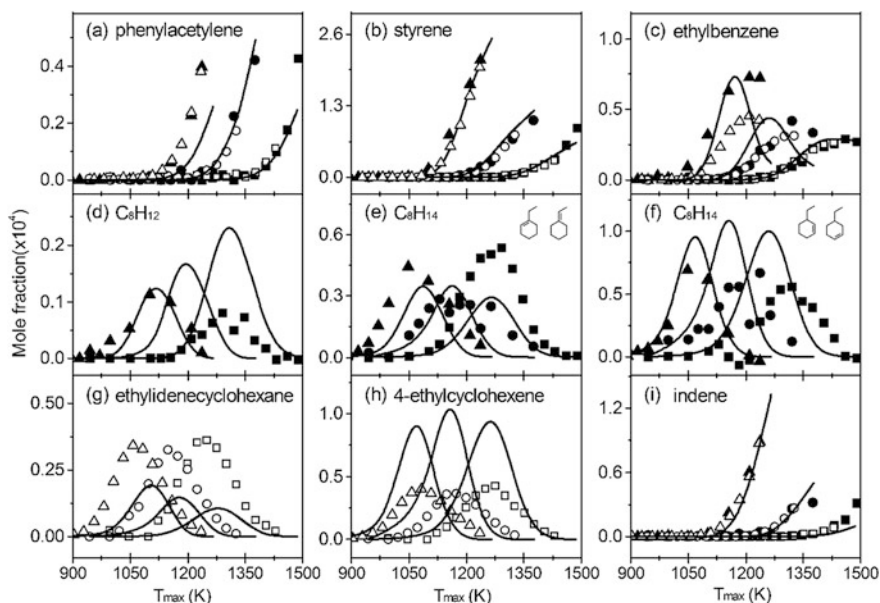
consumed by the H-atom abstraction to form three cyclic  $C_7H_{11}$  isomers. The ring-opening isomerization of these radicals led to diene radicals, while the H-atom elimination reaction led to cyclic dienes, especially 3-methylene-cyclohexene ( $=\text{C}_6\text{H}_9$ ). In the SR-PI-MBMS experiment, the signal corresponding to  $C_7H_{10}$  was recorded and the mole fraction was evaluated by estimating the photoionization cross-section of 3-methylene-cyclohexene. The model prediction showed that the major component for  $C_7H_{10}$  was 3-methylene-cyclohexene.

Another  $C_7$  cyclic intermediate is toluene (Fig. 5.18), an important precursor to polycyclic aromatic hydrocarbons. Analysis from the model showed that two important channels contributed to toluene, i.e., the reaction of propargyl radical with 1,3-butadiene and the recombination of H atom with benzyl radical. In contrast to ethylcyclohexane pyrolysis, the benzyl radical in methylcyclohexane pyrolysis resulted from the dehydrogenation of toluene, product from the step-wise dehydrogenation of methylcyclohexane. Considering the step-wise dehydrogenation of ethylcyclohexane, ethylbenzene can be produced, but not toluene. In the ethylcyclohexane model, the source for benzyl radical was H-atom abstraction reactions of  $cC_7H_8$  (*o*-isotoluene and *p*-isotoluene), produced from the step-wise dehydrogenation of methylenecyclohexane (Fig. 4.21b). Methylenecyclohexane can also be produced from the  $\beta$ -C-H scission of methylcyclohexane radical, e.g., 1-methyl-cyclohexyl radical and cyclohexylmethyl radical in methylcyclohexane pyrolysis. However, the  $\beta$ -C-H scission was much more unfavorable than the  $\beta$ -C-C scission; for example the  $\beta$ -C-C scission of 1-ethyl-cyclohexyl radical easily produced methylenecyclohexane (Fig. 5.3). Thus, the step-wise

dehydrogenation of methylenecyclohexane was a novel pathway for benzyl radical, and subsequently for aromatic formation in ethylcyclohexane pyrolysis.

The mole fraction profiles for the cyclic C<sub>8</sub> intermediates are presented in Fig. 5.19. Discussion in Sect. 5.2 determined that the H-elimination of ethylcyclohexane radicals forms five cyclic C<sub>8</sub>H<sub>14</sub> alkenes. In the GC analysis, ethylidenecyclohexane and 4-ethyl-cyclohexene were measured, as shown in Fig. 5.19g, h. Other isomers were not detected or were difficult to identify. In the SR-PI-MBMS experiment, an attempt was also made to separate the isomers, as shown in Fig. 5.19e, f. Considering the experimental uncertainties, the GC and SR-PI-MBMS measurement for these species were in agreement. The model prediction also agreed with these measurements. The step-wise dehydrogenation of cyclic C<sub>8</sub>H<sub>14</sub> alkenes formed cyclic C<sub>8</sub>H<sub>12</sub> dienes. The SR-PI-MBMS experiment was unable to separate the isomers, and the mole fraction for C<sub>8</sub>H<sub>12</sub> in Fig. 5.19d included all the possible isomers. Similarly, the mole fraction for the simulation included all the possible isomers of C<sub>8</sub>H<sub>12</sub> in the model. The further step-wise dehydrogenation of cyclic C<sub>8</sub>H<sub>12</sub> dienes also resulted in ethylbenzene, especially during the 30 Torr pyrolysis.

The mole fraction of styrene in Fig. 5.19b was much higher than that of ethylbenzene. In ethylbenzene flame, styrene is dominantly produced from the radical initiated two-step H-elimination pathways of ethylbenzene [23, 24]. Similarly, this reaction pathway also led to styrene. Another source for styrene



**Fig. 5.19** Mol fraction profiles of C<sub>8</sub> cyclic intermediates and indene in ethylcyclohexane pyrolysis at 30, 150, and 760 Torr. Solid symbol is SR-PI-MBMS data, open symbol is GC data, lines are simulation. Square is 30 Torr, circle is 150 Torr, triangle is 760 Torr data

includes the reaction of benzene with vinyl radical. Moreover, the reaction of phenyl radical with acetylene also contributes to styrene. The step-wise dehydrogenation of ethylcyclohexane is a group of specific reactions leading to styrene; one example is shown below. Reaction pathway analysis revealed that the step-wise dehydrogenation of ethylcyclohexane to styrene is favorable at 30 Torr pyrolysis.

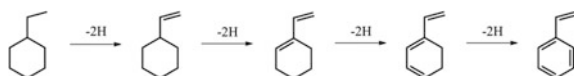
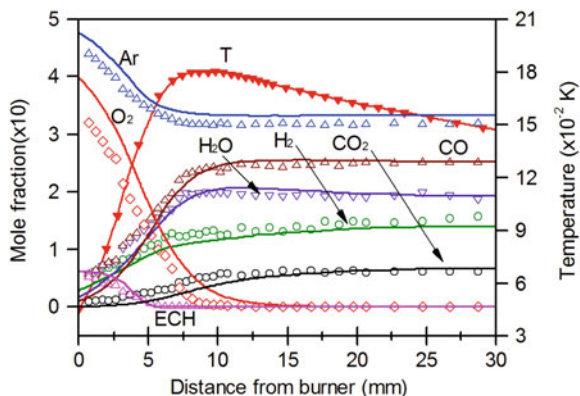


Figure 5.19a presents mole fraction profiles of phenylacetylene, produced from the combination of phenyl radical with acetylene and the H-atom abstraction of styrene with subsequent H-elimination. A large amount of indene was also formed in ethylcyclohexane pyrolysis (Fig. 5.19i), which is predominantly produced from the reaction of the cyclopentadienyl radical with 1,3-butadiyne at 760 Torr. At 30 Torr, the reaction of phenyl radical with propargyl radical becomes more important.

## 5.5 Premixed Flame of Ethylcyclohexane

The low-pressure laminar premixed flame of ethylcyclohexane at 30 Torr was studied in this work on a McKenna burner with a diameter of 60 mm. The flame of ethylcyclohexane/ $O_2$ /50% Ar mixture has equivalence ratio of 1.75. Velocity and mass flow rate of the unburnt gas at 300 K was 50 cm/s and  $3.29 \times 10^{-3}$  g/cm<sup>2</sup>/s, respectively. The flow rates of ethylcyclohexane, Ar, and  $O_2$  were 194, 1523, and 1330 sccm, respectively. In the CHEMKIN simulation, the temperature profile from the experiment was used as input. The mixture-average transport, including Soret diffusion, was considered. Simulation was converged with a solution gradient of 0.1 and curvature of 0.1, respectively. The mole fraction profiles of the reactants and major combustion products are presented in Fig. 5.20, along with measured temperature profiles. Ethylcyclohexane was consumed at  $\sim 6.5$  mm, slightly closer to the burner surface than the methylcyclohexane flame. These two flames have the same equivalence ratio and pressure. The main reason for this discrepancy was the cold gas velocity of the ethylcyclohexane flame; at 50 cm/s@300 K it was greater than the methylcyclohexane flame at 35 cm/s@300 K. Like the methylcyclohexane flame, the consumption of  $O_2$  was also slower than ethylcyclohexane and large amounts of incomplete combustion products  $H_2$  and CO were formed. The ethylcyclohexane kinetic model satisfactorily predicted the consumption of ethylcyclohexane, the formation of the major combustion products, and the profile of Ar (mole expansion effect of the flame).

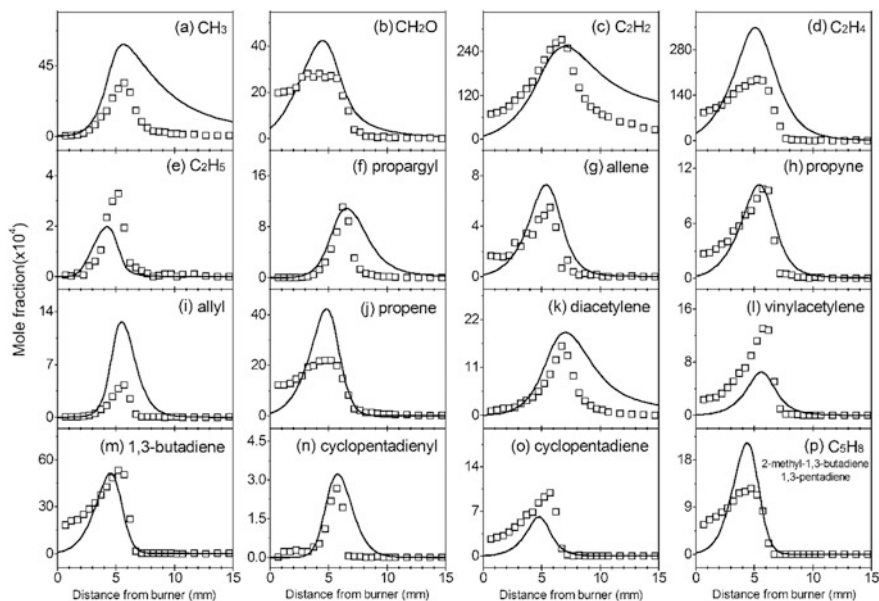
Flame intermediates detected in this work were similar to those measured in ethylcyclohexane pyrolysis. The experimental and simulated mole fraction profiles of the C1–C5 intermediates are displayed in Fig. 5.21. It was noted that the



**Fig. 5.20** Mol fraction profiles of reactants and major combustion products in ethylcyclohexane flame with equivalence ratio of 1.75. Symbol is experimental measurement, line is model prediction. Profile with solid symbol and line is temperature profile measured in this work. Reprinted from Ref. [18], Copyright 2015, with permission from Elsevier

perturbation of the sampling probe was the main reason for the large discrepancy between simulation and experiment close to the burner surface. Model analysis showed that ethylcyclohexane was largely consumed by H-atom abstraction reaction, such as by H atoms and OH radicals. The unimolecular reactions of ethylcyclohexane were insignificant under flame conditions. Thus, the flame intermediates were constituted from the decomposition of ethylcyclohexane radicals, as shown in Fig. 5.4.

Like methylcyclohexane flame, a large amount of 1,3-butadiene (Fig. 5.21m) was formed in the ethylcyclohexane flame studied here. The reaction pathways for 1,3-butadiene are similar to those in ethylcyclohexane pyrolysis. The mole fraction of  $C_5H_8$  intermediates is shown in Fig. 5.21p, including 1,3-pentadiene and 2-methyl-1,3-butadiene. The photon energy selected could not separate the two isomers; therefore the total mole fraction is given. It was noted that large uncertainties may exist for the quantified mole fraction of  $C_5H_8$  intermediates because the photoionization cross-sections were estimated. The simulation showed that the major component of  $C_5H_8$  intermediates was 1,3-pentadiene; the maximum value of its mole fraction was a factor of  $\sim 3$  higher than 2-methyl-1,3-butadiene. The simulated mole fraction ratio of these two intermediates was close to that in the ethylcyclohexane pyrolysis. The reaction pathways for these two intermediates in ethylcyclohexane flame also resembled the ethylcyclohexane pyrolysis: 1,3-pentadiene was produced from the ring-opening isomerization of 1-cyclohexylethyl radical while 2-methyl-1,3-butadiene resulted from secondary reactions such as the combination of H atom with 2-vinyl-3-buten-1-yl radical and the reaction of 2-ethyl-1,3-butadiene with H atom. The new proposed reaction pathways for 2-methyl-1,3-butadiene in Fig. 5.6 also contributed to 2-methyl-1,3-butadiene.

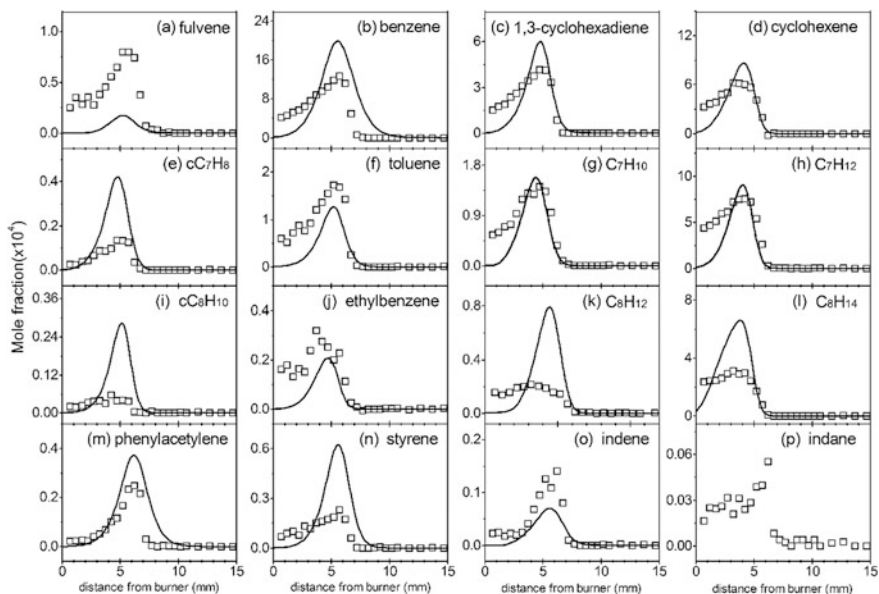


**Fig. 5.21** Mol fraction profiles of C1–C5 flame intermediates in ethylcyclohexane flame at 30 Torr. Symbols are from SR-PI-MBMS data, lines are from simulation. Reprinted from Ref. [18], Copyright 2015, with permission from Elsevier

Figure 5.22 displays the mole fraction profiles of C6–C9 intermediates in ethylcyclohexane flame, including alkenes, cyclic dienes, trienes, and aromatics. These intermediates were also measured in ethylcyclohexane pyrolysis. The total mole fraction for some intermediate is presented, e.g.,  $C_7H_{12}$ ,  $C_7H_{10}$ ,  $cC_7H_8$ ,  $C_8H_{14}$ ,  $C_8H_{12}$ , and  $cC_8H_{10}$ ; they may include many isomers, but the experiment could not separate them. It was noted that an uncertainty factor of 2–3 may be applied to these species since their mole fraction was evaluated from estimated photoionization cross sections.

Mole fraction profiles of the C6 intermediates are shown in Fig. 5.22a–d. The formation pathways for cyclohexene (Fig. 5.22d) in flame condition resembles those in ethylcyclohexane pyrolysis, i.e., the dissociation of 2-ethyl-cyclohexyl radical and cyclohexyl radical. The step-wise dehydrogenation of cyclohexene (Fig. 5.22d) was the main precursor for benzene (Fig. 5.22b). 1,3-cyclohexadiene in Fig. 5.22c was the intermediate bridge connecting cyclohexene and benzene. In the step-wise dehydrogenation process, the H-atom abstraction reactions by H atoms and OH radicals were important because of the abundant radicals in low-pressure flames.

Mole fraction profiles for C7 intermediates are shown in Fig. 5.22e–h. The mole fraction for the  $C_7H_{12}$  intermediate in Fig. 5.22h is slightly higher than that of cyclohexene and may have received a contribution from methylenecyclohexane,

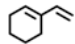
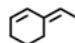
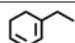
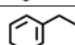
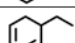
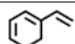
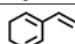
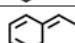
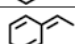
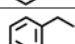


**Fig. 5.22** Mol fraction profiles of C6-C9 flame intermediates in ethylcyclohexane flame at 30 Torr. Symbols are SR-PI-MBMS data, lines are simulation. Reprinted from Ref. [18], Copyright 2015, with permission from Elsevier

1,3-heptadiene, and methylcyclohexenes. Simulation showed that the major component of  $C_7H_{12}$  intermediate was methylenecyclohexane and 1,3-heptadiene. Like ethylcyclohexane pyrolysis, methylenecyclohexane is produced from the  $\beta$ -C-C scission of 1-ethyl-cyclohexyl radical while 1,3-heptadiene is produced from the  $\beta$ -C-C scission of 3-octen-5-yl radical. For  $C_7H_{10}$ , the measured mole fraction may include the contribution of several cyclic diene isomers and 1,3,5-heptatriene. However, the simulation showed that the dominant component for  $C_7H_{10}$  was 3-methylene-cyclohexene (Fig. 5.22g), the product from the two-step dehydrogenation of methylenecyclohexane. 3-methylene-cyclohexene was mainly consumed by the H-atom abstraction to 3-methylene-cyclohexene radicals, which underwent subsequent  $\beta$ -C-H scission, leading to  $cC_7H_8$  (*o*-isotoluene and *p*-isotoluene, in Fig. 5.22e). Further dehydrogenation/H-atom abstraction of  $cC_7H_8$  was the main source of benzyl radical in the ethylcyclohexane flame studied. The combination of benzyl radical with H atom was the main source for toluene (Fig. 5.22f).

In the study of ethylcyclohexane pyrolysis, the step-wise dehydrogenation of ethylcyclohexane formed cyclic  $C_8H_{14}$ ,  $C_8H_{12}$ , and  $C_8H_{10}$  intermediates, which were also measured in the ethylcyclohexane flame, as shown in Fig. 5.22i-l. The ionization energy of the probable isomers of these intermediates is presented in Tables 5.2 and 5.3; they were taken from the NIST database [13], or the

**Table 5.3** Structure and adiabatic ionization energies of probable cyclic  $C_8H_{12}$  and  $C_8H_{10}$  intermediates in ethylcyclohexane flame

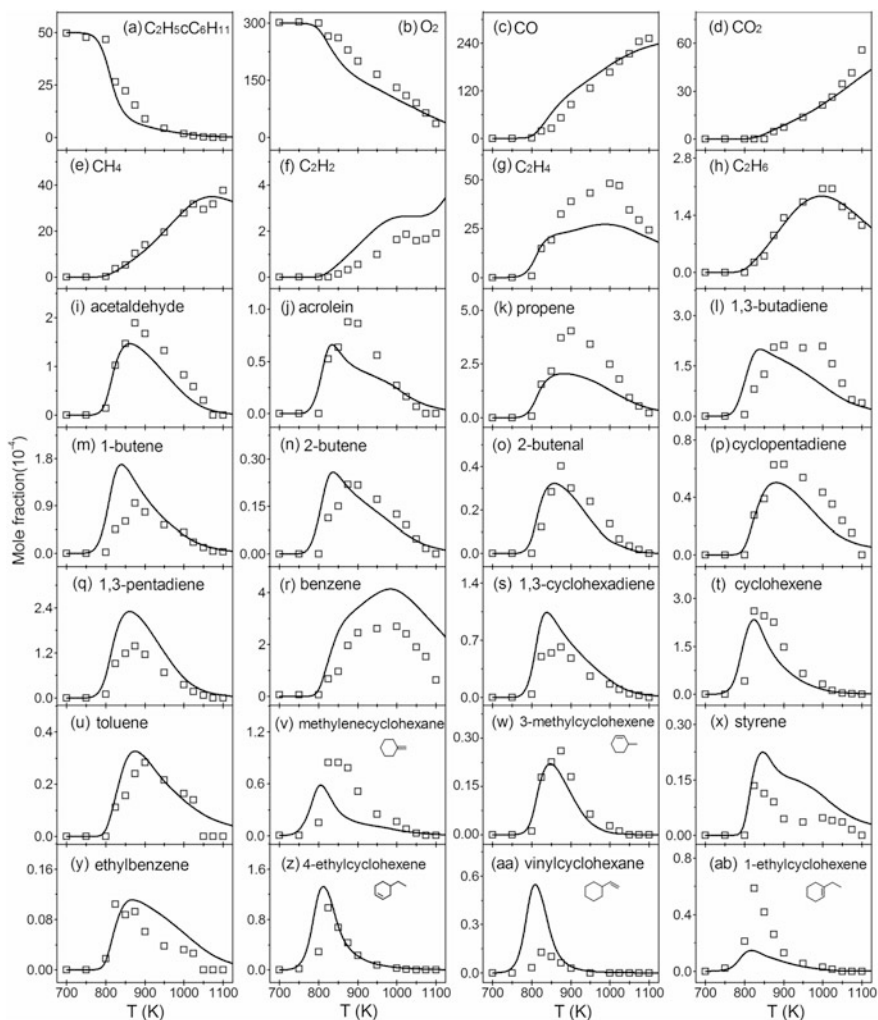
Formula	Species	Structure	IE/eV	Refs.
$C_8H_{12}$	Vinylcyclohexene		8.24	This work
	3-ethylidenecyclohexene		7.98	This work
	1-ethyl-1,3-cyclohexadiene		7.91	This work
	2-ethyl-1,3-cyclohexadiene		7.99	This work
	5-ethyl-1,3-cyclohexadiene		8.17	This work
$C_8H_{10}$	1-ethenyl-1,3-cyclohexadiene		7.79	This work
	2-ethenyl-1,3-cyclohexadiene		7.97	This work
	5-ethylidene-1,3-cyclohexadiene		7.53	This work
	3-ethylidene-1,4-cyclohexadiene		7.75	This work
	Ethylbenzene		8.77	[13]

calculations in this work at the CBS-QB3 level of theory. The experiment by this group could not separate these probable isomers, thus the measured mole fraction may include the contribution from all the isomers. The prediction shows that 4-ethyl-cyclohexene was the major component of  $C_8H_{14}$ . The step-wise dehydrogenation of cyclic  $C_8H_{14}$  intermediates led to cyclic  $C_8H_{12}$  intermediates (Fig. 5.22k), ethylbenzene (Fig. 5.22j), and  $cC_8H_{10}$  (Fig. 5.22i). The subsequent dehydrogenation/H-atom abstraction of  $cC_8H_{10}$  formed cyclic  $C_8H_9$  radicals, which then led to styrene by  $\beta$ -C-H scission. These pathways are the major source for ethylbenzene and styrene (Fig. 5.22n) in the ethylcyclohexane flame studied. In addition, phenylacetylene, indene, and indane were measured in ethylcyclohexane flame, as shown in Fig. 5.22m, o, and p. Like ethylcyclohexane pyrolysis, phenylacetylene is produced from the combination of phenyl radical with acetylene, the H-atom abstraction of styrene with subsequent H-elimination. Indene results from the reaction of cyclopentadienyl radical with 1,3-butadiene and the combination of phenyl radical with propargyl radical. The mole fraction of indane is very low; the current mechanism did not include its reaction pathways.

## 5.6 JSR Oxidation of Ethylcyclohexane

Husson et al. [6] studied the low and intermediate temperature oxidation of ethylcyclohexane in a JSR, covering fuel-lean, stoichiometric, and fuel-rich conditions. These data were very useful for further examination of the ethylcyclohexane





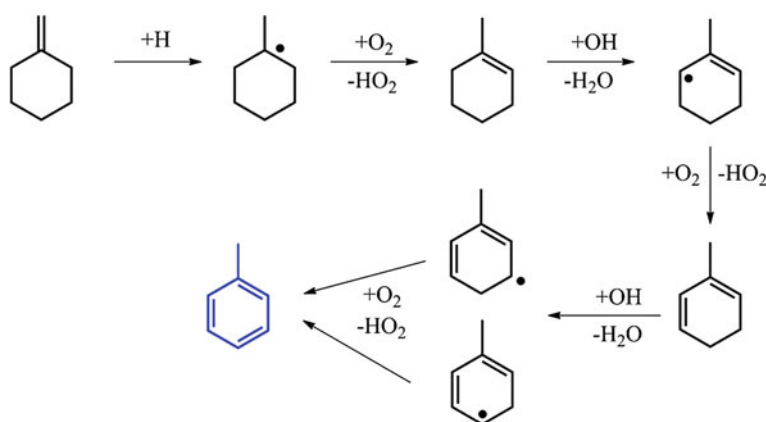
**Fig. 5.23** Mol fraction profiles of reactants, major oxidation products, and C1–C8 intermediates in ethylcyclohexane oxidation at 800 Torr and equivalence of 2.0. Symbols are literature data from Husson et al. [6], lines are simulation. Reprinted from Ref. [18], Copyright 2015, with permission from Elsevier

kinetic model in this work. The simulation method was the same as the JSR oxidation of cyclohexane in Chap. 3. Specifically, the volume of the reactor was  $95 \text{ cm}^3$ , pressure was 800 Torr, dilution gas was He, and the residence time was 2 s. The end time for the transient solver was 30 s. The experiment and simulated results for the reactants and important oxidation intermediates in ethylcyclohexane oxidation with equivalence ratio of 2.0 are displayed in Fig. 5.23. The comparison between experiment and simulation for other conditions (i.e.,  $\phi = 0.25$  and

$\phi = 1.0$ ) is shown in Figs. C.1 and C.2 in Appendix C. Generally, the model prediction for most of the species was satisfactory. The following discussion is focused on ethylcyclohexane decomposition and the formation of some represented products.

Ethylcyclohexane is mainly consumed by H-atom abstraction from OH radicals under an oxidation environment. Subsequent reactions of the ethylcyclohexane radicals led to 1,3-pentadiene (Fig. 5.23q), 1-butene (Fig. 5.23m), 1,3-butadiene (Fig. 5.23l), ethylene (Fig. 5.23g). Smaller radicals of methyl, ethyl, n-propyl, 1-buten-3-yl, 2-butyl, and 1-butyl radicals were also produced in this process. Further reactions of these stable and radical intermediates—including direct decomposition or oxidation—formed C1–C4 oxygenated and hydrocarbon intermediates. For example, 1-butene is produced from the oxidation reactions of butyl radicals (2-butyl and 1-butyl); 2-butene (Fig. 5.23n) is produced from the reactions of 2-butyl radical with  $O_2$ ; the reactions of 1-buten-3-yl radical with  $HO_2$  also contribute to its formation; the main pathway for propene (Fig. 5.23k) is the reaction of  $HO_2$  with allyl radical, the dissociation of 2-butyl radical, and the reactions of propyl radicals (n-propyl and i-propyl radical) with  $O_2$ . The reaction of ethyl radical with  $O_2$  is the main source for ethylene; the oxidation reactions of 2-cyclohexen-1-yl radical and 1-buten-3-yl radical with  $HO_2$  reaction result in acrolein (Fig. 5.23j); the reaction of OH radical with 1,3-butadiene produces acetaldehyde in Fig. 5.23i. Under a pyrolysis environment, reactions of unimolecular decomposition, H-atom abstraction by H atom,  $\beta$ -C–C scission of radicals were prevalent. The reaction mechanism became much more diverse in ethylcyclohexane oxidation however, the main reasons being the participation of oxygen and the formation of a large number of oxygenated radicals.

The decomposition of 2-ethyl-cyclohexyl radical led to ethyl radical and cyclohexene (Fig. 5.23t), which was consumed by H-atom abstractions to form 2-cyclohexen-1-yl radical. The decomposition of 2-cyclohexen-1-yl radical led to



**Fig. 5.24** Reaction pathways for toluene in ethylcyclohexane oxidation with  $\phi = 2.0$  and pressure of 800 Torr

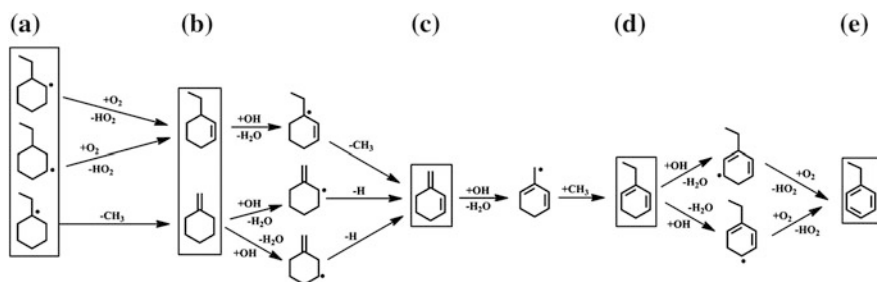
1,3-cyclohexadiene in Fig. 5.23s. Another pathway for 1,3-cyclohexadiene was the decomposition of 4-ethyl-1-cyclohexen-3-yl radical. This is similar to the reaction pathways for 1,3-cyclohexadiene in ethylcyclohexane pyrolysis. 1,3-cyclohexadiene is also produced from the reaction of 2-cyclohexen-1-yl radical with  $O_2$  in ethylcyclohexane oxidation. The subsequent reactions of 1,3-cyclohexadiene were the source of benzene in Fig. 5.23r. For example, its H-atom abstraction by OH radical, H atom, and O atom led to 1,3-cyclohexadienyl radical. The subsequent  $\beta$ -C-H scission of 1,3-cyclohexadienyl radical directly resulted in benzene.

The C7 cyclic alkene, methylenecyclohexane in Fig. 5.23v, was produced from the  $\beta$ -C-C scission of 1-ethyl-cyclohexyl radical and consumed by H-atom abstraction reactions and the H-atom addition to the double bond to form 1-methyl-cyclohexyl radical. The subsequent reactions of 1-methyl-cyclohexyl radical formed toluene (Fig. 5.23u), as shown in Fig. 5.24.

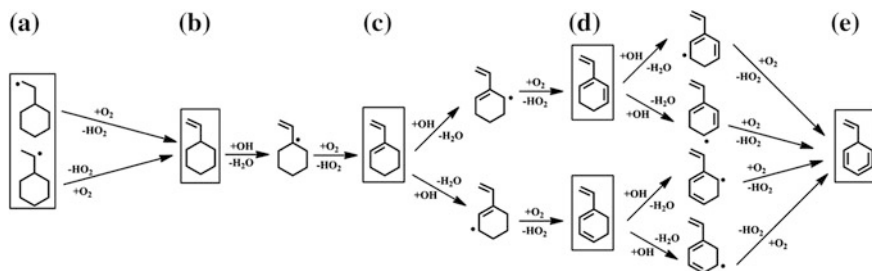
The reactions of ethylcyclohexane radical with  $O_2$  and the direct  $\beta$ -C-H scission of ethylcyclohexane radical formed cyclic  $C_8H_{14}$  alkenes. The three isomers measured from the experiment are shown in Fig. 5.23z, aa, and ab. The mole fraction of 4-ethylcyclohexene was predicted satisfactorily, while large discrepancies existed for the other two isomers, vinylcyclohexane and 1-ethyl-cyclohexene.

Mole fraction profiles of ethylbenzene and styrene are presented in Fig. 5.23x, y. The reaction pathways for ethylbenzene in Fig. 5.25 included four steps: *First*, methylenecyclohexane and 3-ethyl-cyclohexene were formed from the decomposition of 1-ethyl-cyclohexyl radical and the reaction of 2-ethyl-cyclohexyl and 3-ethyl-cyclohexyl radical with  $O_2$ , respectively (a  $\rightarrow$  b). *Second*, the H-atom abstraction of methylenecyclohexane and 3-ethyl-cyclohexene, and subsequent  $\beta$ -C-C and/or  $\beta$ -C-H scission led to 3-methylene-cyclohexene (b  $\rightarrow$  c). *Third*, the H-atom abstraction of 3-methylene-cyclohexene, and subsequent methyl addition to the radical site, produced 2-ethyl-1,3-cyclohexadiene (c  $\rightarrow$  d). *Last*, the H-atom abstraction of 2-ethyl-1,3-cyclohexadiene and subsequent reaction with  $O_2$  led to ethylbenzene (d  $\rightarrow$  e).

The mole fraction of styrene is close to that of ethylbenzene. As shown in Fig. 5.26, styrene is also produced from four reactions steps, which are similar to

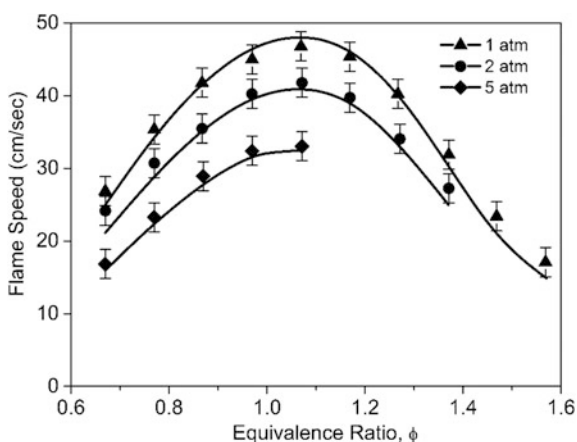


**Fig. 5.25** Reaction pathways for ethylbenzene in ethylcyclohexane oxidation with  $\phi = 2.0$  and pressure of 800 Torr



**Fig. 5.26** Reaction pathways for styrene in ethylcyclohexane oxidation with  $\phi = 2.0$  and pressure of 800 Torr. Reprinted from Ref. [18], Copyright 2015, with permission from Elsevier

**Fig. 5.27** Laminar flame speed of ethylcyclohexane at 1, 2, and 5 atm. Unburnt gas temperature is 353 K. Symbols are experimental measurement by Wu et al. [5], lines are model prediction in this work. Reprinted from Ref. [18], Copyright 2015, with permission from Elsevier



those of ethylbenzene. The first step is the bimolecular reaction of 1-cyclohexyl-ethyl and 2-cyclohexyl-ethyl radical with  $O_2$ , which produce vinylcyclohexane. The step-wise dehydrogenation of vinylcyclohexane, by way of 1-ethenyl-1,3-cyclohexadiene and 2-ethenyl-1,3-cyclohexadiene, forms styrene; this reaction process is similar to the styrene pathways in ethylcyclohexane pyrolysis. However, OH radical and  $O_2$  are important in this process during ethylcyclohexane oxidation.

## 5.7 Laminar Flame Speed of Ethylcyclohexane

The ethylcyclohexane kinetic model was further validated by the laminar flame speed of ethylcyclohexane/air mixture measured by Wu et al. [5]. The simulation method was the same as the laminar flame speed simulation for cyclohexane in Chap. 3: the premixed module was chosen and the Soret diffusion and

mixture-average transport were included. The simulated flame speeds in Fig. 5.27 agree with the experimental measurement at 1, 2, and 5 atm.

## 5.8 Summary and Conclusions

In this chapter, the flow reactor pyrolysis of ethylcyclohexane, from low to 1 atm, and premixed flame of ethylcyclohexane at 30 Torr, were examined. More than 40 pyrolysis and flame species were measured. In the pyrolysis experiment, the combination of SR-PI-MBMS and GC analysis separated many isomers and detected some low-concentration intermediates. The detection of 3-octene confirmed that the initial ring-opening isomerization of ethylcyclohexane was plausible. This type of reaction was also observed during cyclohexane and methylcyclohexane pyrolysis. The decomposition and H-atom abstraction of ethylcyclohexane resulted in cyclohexyl radical and ethylcyclohexane radicals, the source of various chain and branched dienes, such as 1,3-heptadiene, 2-ethyl-1,3-butadiene, 1,3-hexadiene, 2-methyl-1,3-butadiene, 1,3-pentadiene, and 1,3-butadiene. The quantification of these intermediates examined the branching ratios of the ethylcyclohexane radicals and cyclohexyl radical decomposition.

A detailed kinetic model of ethylcyclohexane combustion was developed from this work's theoretical calculations the reaction mechanism of methylcyclohexane pyrolysis and oxidation, and literature review. The ethylcyclohexane kinetic model satisfactorily predicted the species speciation in ethylcyclohexane pyrolysis, oxidation, and flame, revealing that rate analogies to methylcyclohexane were reasonable, and a good starting point for ethylcyclohexane, and possibly for other alkyl-cyclohexane model development. The isomerization of alkenyl radicals, produced from the decomposition of the ethylcyclohexane radicals, via the radical addition on the double bond was highlighted; it explains the formation of five-membered-ring intermediates like vinylcyclopentane and cyclopentane. This reaction mechanism also contributed to the early formation of 2-methyl-1,3-butadiene, especially for the low-pressure experiment.

In the pyrolysis, premixed flame and oxidation of ethylcyclohexane, the C6–C8 cyclic compounds—including alkenes, dienes, trienes, and aromatics—were measured. The reaction kinetics of these intermediates were discussed from experimental observations and with the help of kinetic modeling. The decomposition of ethylcyclohexane and H-atom abstraction of ethylcyclohexane were the source of cyclic alkenes. Further reactions of these cyclic alkenes lead to benzene, toluene, ethylbenzene, and styrene in the ethylcyclohexane flame and JSR oxidation studied here. Secondary reactions, such as the recombination of resonance stabilized radicals and the reactions of methyl radical with cyclopentadienyl radical, are important for aromatics formation during ethylcyclohexane pyrolysis.

Validation of the ethylcyclohexane kinetic model by the broad dataset measured in this work and reported in the literature, is the foundation on which the model can

clarify reaction kinetics and develop kinetic models of other cycloalkanes with complex structures.

## References

1. Prosen, E. J., Johnson, W. H., & Rossini, F. D. (1946). Heats of formation and combustion of the normal alkylcyclopentanes and cyclohexanes and the increment per  $\text{CH}_2$  group for several homologous series of hydrocarbons. *Journal of Research of the National Bureau of Standards*, 37, 51–56.
2. Huffman, H. M., Todd, S. S., & Oliver, G. D. (1949). Low temperature thermal data on eight  $\text{C}_8\text{H}_{16}$  alkylcyclohexanes. *Journal of the American Chemical Society*, 71(2), 584–592.
3. Vanderover, J., & Oehlschlaeger, M. A. (2009). Ignition time measurements for methylcyclohexane- and ethylcyclohexane-air mixtures at elevated pressures. *International Journal of Chemical Kinetics*, 41(2), 82–91.
4. Ji, C., Dames, E., Sirjean, B., Wang, H., & Egolfopoulos, F. N. (2011). An experimental and modeling study of the propagation of cyclohexane and mono-alkylated cyclohexane flames. *Proceedings of the Combustion Institute*, 33, 971–978.
5. Wu, F., Kelley, A. P., & Law, C. K. (2012). Laminar flame speeds of cyclohexane and mono-alkylated cyclohexanes at elevated pressures. *Combustion and Flame*, 159(4), 1417–1425.
6. Husson, B., Herbinet, O., Glaude, P. A., Ahmed, S. S., & Battin-Leclerc, F. (2012). Detailed product analysis during low- and intermediate-temperature oxidation of ethylcyclohexane. *Journal of Physical Chemistry A*, 116(21), 5100–5111.
7. Wang, H., Dames, E., Sirjean, B., Sheen, D. A., Tangko, R., Violi, A., et al. (2010). A high-temperature chemical kinetic model of n-alkane (up to n-dodecane), cyclohexane, and methyl-, ethyl-, n-propyl and n-butyl-cyclohexane oxidation at high temperatures, JetSurF version 2.0, September 19, 2010. (<http://melchior.usc.edu/JetSurF/JetSurF2.0>).
8. Wang, Z., Bian, H., Wang, Y., Zhang, L., Li, Y., Zhang, F., et al. (2015). Investigation on primary decomposition of ethylcyclohexane at atmospheric pressure. *Proceedings of the Combustion Institute*, 35(1), 367–375.
9. Wang, Z., Ye, L., Yuan, W., Zhang, L., Wang, Y., Cheng, Z., et al. (2014). Experimental and kinetic modeling study on methylcyclohexane pyrolysis and combustion. *Combustion and Flame*, 161, 84–100.
10. Wang, Z., Cheng, Z., Yuan, W., Cai, J., Zhang, L., Zhang, F., et al. (2012). An experimental and kinetic modeling study of cyclohexane pyrolysis at low pressure. *Combustion and Flame*, 159(7), 2243–2253.
11. Zhang, F., Wang, Z., Wang, Z., Zhang, L., Li, Y., & Qi, F. (2013). Kinetics of decomposition and isomerization of methylcyclohexane: Starting point for kinetic modeling mono-alkylated cyclohexanes. *Energy & Fuels*, 27(3), 1679–1687.
12. Oehlschlaeger, M. A., Davidson, D. F., & Hanson, R. K. (2005). High-temperature ethane and propane decomposition. *Proceedings of the Combustion Institute*, 30(1), 1119–1127.
13. Linstrom, P. J. & Mallard, W. G. (2005). *NIST Chemistry Webbook*. Gaithersburg, MD: National Institute of Standard and Technology, Number 69. <http://webbook.nist.gov/>.
14. Klippenstein, S. J., Harding, L. B., & Georgievskii, Y. (2007). On the formation and decomposition of  $\text{C}_7\text{H}_8$ . *Proceedings of the Combustion Institute*, 31(1), 221–229.
15. Kiefer, J. H., Gupte, K. S., Harding, L. B., & Klippenstein, S. J. (2009). Shock tube and theory investigation of cyclohexane and 1-hexene decomposition. *Journal of Physical Chemistry A*, 113(48), 13570–13583.

16. Pitz, W. J., Naik, C. V., Mhaoldúin, T. N., Westbrook, C. K., Curran, H. J., Orme, J. P., et al. (2007). Modeling and experimental investigation of methylcyclohexane ignition in a rapid compression machine. *Proceedings of the Combustion Institute*, 31, 267–275.
17. Orme, J. P., Curran, H. J., & Simmie, J. M. (2006). Experimental and modeling study of methyl cyclohexane pyrolysis and oxidation. *Journal of Physical Chemistry A*, 110(1), 114–131.
18. Wang, Z., Zhao, L., Wang, Y., Bian, H., Zhang, L., Zhang, F., et al. (2015). Kinetics of ethylcyclohexane pyrolysis and oxidation: An experimental and detailed kinetic modeling study. *Combustion and Flame*, 162(7), 2873–2892.
19. Tsang, W. (1991). Chemical kinetic data base for combustion chemistry part V. propene. *Journal of Physical and Chemical Reference Data*, 20(2), 221–273.
20. Curran, H. J. (2006). Rate constant estimation for C1 to C4 alkyl and alkoxy radical decomposition. *International Journal of Chemical Kinetics*, 38(4), 250–275.
21. Sirjean, B., Glaude, P. A., Ruiz-Lopèz, M. F., & Fournet, R. (2008). Theoretical kinetic study of thermal unimolecular decomposition of cyclic alkyl radicals. *The Journal of Physical Chemistry A*, 112(46), 11598–11610.
22. Sirjean, B., Glaude, P. A., Ruiz-Lopez, M. F., & Fournet, R. (2006). Detailed kinetic study of the ring opening of cycloalkanes by CBS-QB3 calculations. *Journal of Physical Chemistry A*, 110(46), 12693–12704.
23. Li, Y., Tian, Z., Zhang, L., Yuan, T., Zhang, K., Yang, B., et al. (2009). An experimental study of the rich premixed ethylbenzene flame at low pressure. *Proceedings of the Combustion Institute*, 32, 647–655.
24. Li, Y., Cai, J., Zhang, L., Yang, J., Wang, Z., & Qi, F. (2011). Experimental and modeling investigation on premixed ethylbenzene flames at low pressure. *Proceedings of the Combustion Institute*, 33(1), 617–624.

## Chapter 6

# Combustion Kinetics of Cyclohexane and C1–C2 Mono-alkyl Cyclohexanes

Chapters 3 through 5 examined the flow reactor pyrolysis and laminar premixed flames of cyclohexane, methylcyclohexane and ethylcyclohexane; pyrolysis and flame intermediates were identified and quantified. Based on experimental measurements, quantum chemistry calculations, and literature review, kinetic models for cyclohexane, methylcyclohexane and ethylcyclohexane were developed; additional experimental data from the literature were adopted to further validate the kinetic model. Satisfactory prediction of the experimental data makes the model a useful tool for clarification and discussion of the combustion kinetics of the three fuels.

### 6.1 Flow Reactor Pyrolysis

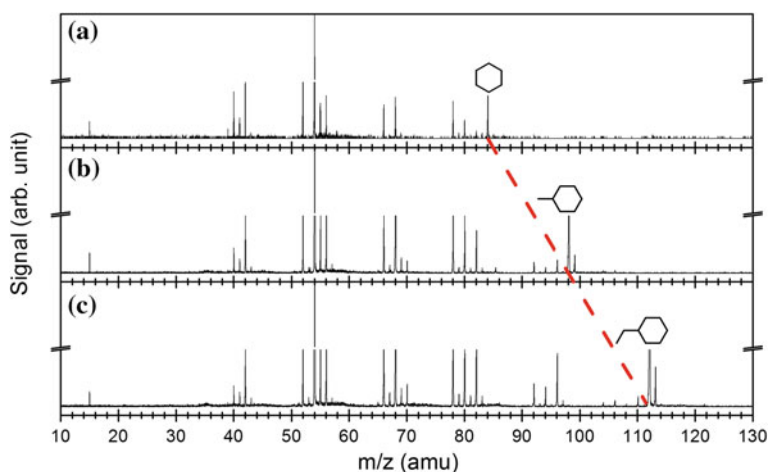
The pyrolysis of cyclohexane and the two mono-alkylated cycloalkanes were investigated using the synchrotron radiation photoionization molecular beam mass spectrometry. The total flow rate of the initial gas was maintained at 1000 sccm at 273.15 K in all the experiments with a fuel concentration of 0.02; moreover, the mole fraction of the pyrolysis intermediates at 30, 150, and 760 Torr pyrolysis was evaluated by the same methodology and the same source of photoionization cross-sections was applied [1–8]. These well-defined experimental conditions and data evaluation were the basis for analysis of the pyrolysis mechanism of cyclohexane, methylcyclohexane, and ethylcyclohexane. In the following, pyrolysis kinetics of the three fuels are discussed, including the species pool and mole fraction distribution of a series of intermediates.



### 6.1.1 Species Pool

Figure 6.1 presents the mass spectra resulting from pyrolysis of cyclohexane, methylcyclohexane and ethylcyclohexane with fuel conversions of 70%. Each mass peak corresponded to one or more hydrocarbon isomer. The mass peaks below mass-to-charge-ratio ( $m/z$ ) of 82 in the three fuels pyrolysis were identical. Due to the existence of a side chain, more intermediates were formed in the mono-alkylated cyclohexanes, for example,  $m/z$  94 and 96 were observed in methylcyclohexane and ethylcyclohexane pyrolysis, while  $m/z$  108 and 110 were detected only in ethylcyclohexane pyrolysis.

Photoionization efficiency (PIE) spectra were scanned to distinguish the species composition of each mass peak. Tables 3.3 and 6.1 show intermediates in the three-fuel pyrolysis, which are mainly linear or cyclic alkenes, linear or cyclic dienes, and aromatics. Radicals such as  $\text{CH}_3$ ,  $\text{C}_2\text{H}_5$ ,  $\text{C}_3\text{H}_3$ ,  $\text{C}_3\text{H}_5$  and  $\text{C}_5\text{H}_5$  were also detected under low pressure. Like the mass spectra shown in Fig. 6.1, the C1–C6 pyrolysis product species detected were similar in the three cyclohexanes, except for  $\text{C}_6\text{H}_{10}$ . Cyclohexene and 1,3-hexadiene are the two  $\text{C}_6\text{H}_{10}$  isomers produced from cyclohexane pyrolysis; in addition to these two isomers, 4-methyl-1,3-pentadiene and 2,4-hexadiene might exist in methylcyclohexane pyrolysis while 2-ethyl-1,3-butadiene is a probable isomer in ethylcyclohexane pyrolysis. In the pyrolysis of these three fuels, the  $\text{C}_6$  cyclic alkene ( $m/z$  82) was cyclohexene. As the side chain increased,  $\text{C}_7$  cyclic alkenes ( $m/z$  96) were produced. The dominant isomers are methylcyclohexenes in methylcyclohexane pyrolysis while the dominant isomers are methylenecyclohexane in ethylcyclohexane pyrolysis; moreover,  $\text{C}_8$  cyclic alkenes ( $m/z$  110) with the same carbon



**Fig. 6.1** Mass spectra of cyclohexane, methylcyclohexane and ethylcyclohexane pyrolysis at 30 Torr with fuel conversions of 70%. Photoionization energy is 10 eV

**Table 6.1** Species detected from the pyrolysis and flame of methylcyclohexane and ethylcyclohexane

m/z	Formula	Species	Measured IE <sup>b</sup>							
			Literature IE <sup>a</sup>	MCH		ECH		Flame		
2	H <sub>2</sub>	Hydrogen	15.43	√	√	√	√	√	√	√
15	CH <sub>3</sub>	Methyl radical	9.84	9.83	√	9.86	9.83	√	9.80	√
16	CH <sub>4</sub>	Methane	12.61	√	√	√	√	√	√	√
26	C <sub>2</sub> H <sub>2</sub>	Acetylene	11.40	√	√	11.42	√	√	√	√
28	C <sub>2</sub> H <sub>4</sub>	Ethylene	10.51	10.50	10.54	10.52	10.50	10.50	10.50	√
29	C <sub>2</sub> H <sub>5</sub>	Ethyl radical	8.12	8.29		8.32	8.30		8.29	
39	C <sub>3</sub> H <sub>3</sub>	Propargyl radical	8.67	8.71		8.67	8.71		8.67	
40	C <sub>3</sub> H <sub>4</sub>	Allene	9.69	9.69	9.70	9.73	9.72	9.70	9.72	9.72
		Propyne	10.36	10.36	10.39	10.38	10.39	10.36	10.36	10.36
41	C <sub>3</sub> H <sub>5</sub>	Allyl radical	8.18	8.19		8.12	8.19		8.10	
42	C <sub>3</sub> H <sub>6</sub>	Propene	9.73	9.76	9.76	9.76	9.76	9.76	9.76	9.72
50	C <sub>4</sub> H <sub>2</sub>	1,3-Butadiyne	10.17			10.18			10.12	
52	C <sub>4</sub> H <sub>4</sub>	1,2,3-Butatriene	9.25	9.17	9.20	9.17	9.20	9.17	9.18	9.18
		Vinylacetylene	9.58	9.59	9.61	9.58	9.59	9.62	9.57	9.57
54	C <sub>4</sub> H <sub>6</sub>	1,3-Butadiene	9.07	9.09	9.07	9.07	9.06	9.06	9.05	9.05
56	C <sub>4</sub> H <sub>8</sub>	1-Butene	9.55	9.59	9.58	9.61	9.59	9.52	9.57	9.57
		2-Butene	9.11	9.10	9.16	9.13	9.13	9.17	9.12	9.12
65	C <sub>5</sub> H <sub>5</sub>	Cyclopentadienyl radical	8.41	8.43		8.43	8.47		8.41	
66	C <sub>5</sub> H <sub>6</sub>	1,3-Cyclopentadiene	8.57	8.60	8.59	8.57	8.57	8.61	8.55	8.55
68	C <sub>5</sub> H <sub>8</sub>	1,3-Pentadiene	8.6	8.64	8.65	8.60	8.64	8.61	8.58	8.58
		2-Methyl-1,3-butadiene	8.86	8.88	8.86	8.84	8.85	8.89	8.82	8.82
70	C <sub>5</sub> H <sub>10</sub>	1-Pentene	9.49	9.52	9.52	9.49	9.45	9.45	9.54	9.54

(continued)

Table 6.1 (continued)

m/z	Formula	Species	Literature IE <sup>a</sup>	Measured IE <sup>b</sup>					
				MCH Py-30	Py-760	Flame	ECH Py-30	Py-760	Flame
78	C <sub>6</sub> H <sub>6</sub>	2-Pentene	9.05	9.09	9.04	9.04	9.03	9.06	8.98
		Benzene	9.24	9.27	9.22	9.24	9.27	9.27	9.22
		Fulvene	8.36	8.40	8.38	8.34	8.36	8.40	8.34
80	C <sub>6</sub> H <sub>8</sub>	1,3-Cyclohexadiene	8.25	8.29	8.29	8.25	8.29	8.29	8.24
82	C <sub>6</sub> H <sub>10</sub>	Cyclohexene	8.95	8.96	8.98	8.94	8.96	8.99	8.92
		2-Ethyl-1,3-butadiene	8.81				8.82	8.82	8.82
		1,3-Hexadiene	8.53	8.50	8.50	8.55	8.50	8.50	8.52
		4-Methyl-1,3-pentadiene	8.26	8.25	8.32	8.23	8.26	8.26	8.21
		2,4-Hexadiene	8.26						
92	C <sub>7</sub> H <sub>8</sub>	Toluene	8.83	8.85	8.86	8.84	8.85	8.81	8.82
		<sup>c</sup>	<sup>c</sup>	7.96	7.93	7.91	7.87	8.01	7.90
94	C <sub>7</sub> H <sub>10</sub>	<sup>c</sup>	<sup>c</sup>	8.02	7.99	7.94	7.94	7.94	7.87
96	C <sub>7</sub> H <sub>12</sub>	<sup>c</sup>	<sup>c</sup>	8.96	8.98	8.94	8.96	8.89	8.86
		(E)-1,3-Heptadiene	8.47	8.54	8.53	-	8.47	8.36	8.52
		5-Methyl-1,3-hexadiene	8.47						
98	C <sub>7</sub> H <sub>14</sub>	Methylcyclohexane	9.64	9.66	9.64	9.67			
		2-Heptene	8.84	8.83	8.83	8.82			
102	C <sub>8</sub> H <sub>6</sub>	Phenylacetylene	8.82	√	8.83	8.84	√	8.78	8.79
104	C <sub>8</sub> H <sub>8</sub>	Styrene	8.46	√	8.50	8.46	√	8.43	8.50
106	C <sub>8</sub> H <sub>10</sub>	Ethylbenzene	8.77	√	8.74	8.74	8.78	8.78	8.82
		<sup>d</sup>	<sup>d</sup>	-	7.76	7.8	7.87	7.87	7.85

(continued)

Table 6.1 (continued)

m/z	Formula	Species	Literature IE <sup>a</sup>	Measured IE <sup>b</sup>					
				MCH		Flame		ECH	
				Py-30	Py-760	Flame	Py-30	Py-760	Flame
108	C <sub>8</sub> H <sub>12</sub>	d	d			7.92	7.87	—	7.90
		d	d				—	—	8.19
110	C <sub>8</sub> H <sub>14</sub>	d	d				8.43	8.47	8.46
112	C <sub>8</sub> H <sub>16</sub>	Ethylcyclohexane	9.54				9.59	9.55	9.58
		2-Octene	8.92 <sup>e</sup>				8.89	—	8.86
		3-Octene	8.86 <sup>c</sup>				8.89	—	8.86
		2-Ethyl-1-hexene	8.92 <sup>c</sup>				8.89	—	8.86
116	C <sub>9</sub> H <sub>8</sub>	Indene	8.14		8.17	8.17	√	8.19	8.13
128	C <sub>10</sub> H <sub>8</sub>	Naphthalene	8.14	—	8.17	8.19	—	8.19	8.10

<sup>a</sup>Ref to NIST [10] except for specific note

<sup>b</sup>Uncertainty is  $\pm 0.05$  eV for species with high signal to noise ratio;  $\pm 0.1$  eV for species with low signal to noise ratio

<sup>c</sup>Refer to Chap. 4

<sup>d</sup>Refer to Chap. 5

<sup>e</sup>Computed at CBS-QB3 level of theory

√ Identified from mass; — ionization energy onset is not evident; *Py-30* pyrolysis at 30 Torr, *Py-760* pyrolysis at 760 Torr; flame pressure is 30 Torr

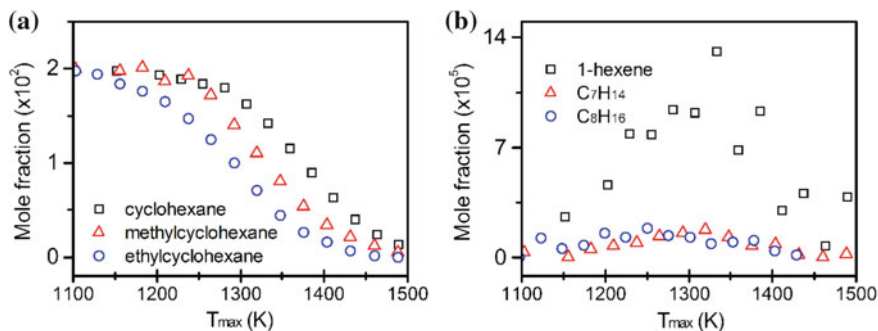
skeleton as ethylcyclohexane were produced in ethylcyclohexane pyrolysis. These C<sub>6</sub>–C<sub>8</sub> cyclic alkenes are precursors of aromatics like benzene, toluene, ethylbenzene, and styrene. The similarities and discrepancies in mass peaks are related to the distinguishing pyrolysis pathways of these cycloalkanes.

In the pyrolysis of cyclohexane and methylcyclohexane, the isomer of the reactant, 1-hexene and 2-heptene, was measured. The measured ionization energy for ethylcyclohexane isomerization products is 8.9 eV, which corresponds to 2-octene, 3-octene, and 2-ethyl-1-hexene. However, only 3-octene was detected in the gas chromatography (GC) analysis of ethylcyclohexane pyrolysis. The observation of the alkene isomers confirmed the ring-opening isomerization of cyclohexane, methylcyclohexane and ethylcyclohexane. The measurement of 2-heptene and 3-octene indicated that ring-opening via the C–C bond adjacent to the side chain was more favorable and is accord with the quantum chemistry calculation [9].

### 6.1.2 Mole Fraction Distribution

The mole fraction distributions of several important intermediates are examined in order to analyze the pyrolysis kinetics of cyclohexane and its mono-alkylated derivatives. Data are from the SR-PI-MBMS analysis at 30 Torr unless otherwise noted. Figure 6.2 presents the mole fraction profiles of the three fuels and the formation of their corresponding isomerization products. Under the same experimental conditions, the reactivity of the three fuels follows the trend: cyclohexane < methylcyclohexane < ethylcyclohexane. This observation indicated that the presence of the alkyl side chain increased reactivity (cyclohexane vs. methylcyclohexane), and increasing the length of the alkyl side chain also increases reactivity (methylcyclohexane vs. ethylcyclohexane). This is in accord with the energy barrier of the unimolecular dissociation pathways. The calculated barrier for the ring-opening isomerization of cyclohexane is 88.7 kcal/mol [11], as shown in Fig. 3.1. In methylcyclohexane and ethylcyclohexane pyrolysis, the most important decomposition pathway is the methyl and ethyl side chain loss. In this work, the calculated energy barrier for the methyl loss channel is 84 kcal/mol. For ethylcyclohexane, the energy barrier for dissociation by way of ethyl loss is ~2.5 kcal/mol lower than the methyl loss channel [12] of methylcyclohexane. In addition, the sensitivity analysis showed that the H-atom abstraction reactions had high sensitivity coefficient for the consumption of cyclohexane, methylcyclohexane, and ethylcyclohexane. From cyclohexane to methylcyclohexane, and to ethylcyclohexane, the total H-atom abstraction rate constants increased, which also promoted fuel consumption.

The profiles of the C<sub>6</sub>–C<sub>8</sub> alkenes in Fig. 6.2b show that the maximum mole fraction of 1-hexene is much higher than C<sub>7</sub>H<sub>14</sub> and C<sub>8</sub>H<sub>16</sub> alkenes. This distinguishing feature of cyclohexane pyrolysis could be explained by its unique initiation reactions. In cyclohexane pyrolysis, the dominant unimolecular initiation

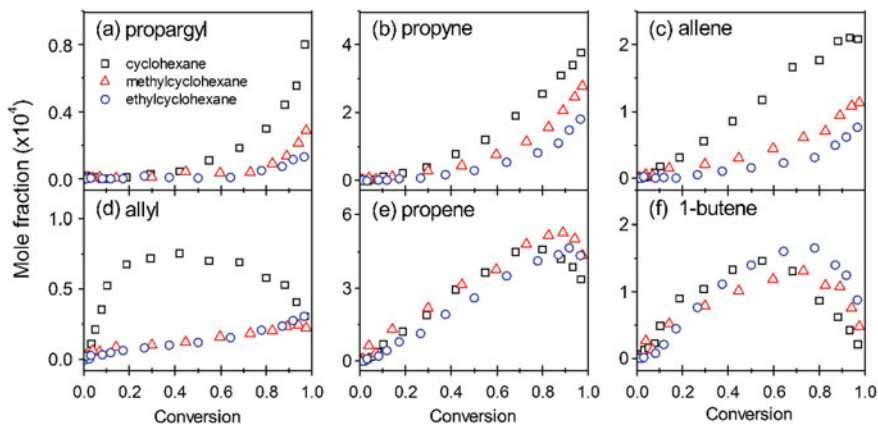


**Fig. 6.2** Mole fraction profiles of cyclohexane, methylcyclohexane and ethylcyclohexane **a** isomerization products **b** during 30 Torr pyrolysis. Data for  $C_8H_{16}$  measured by GC

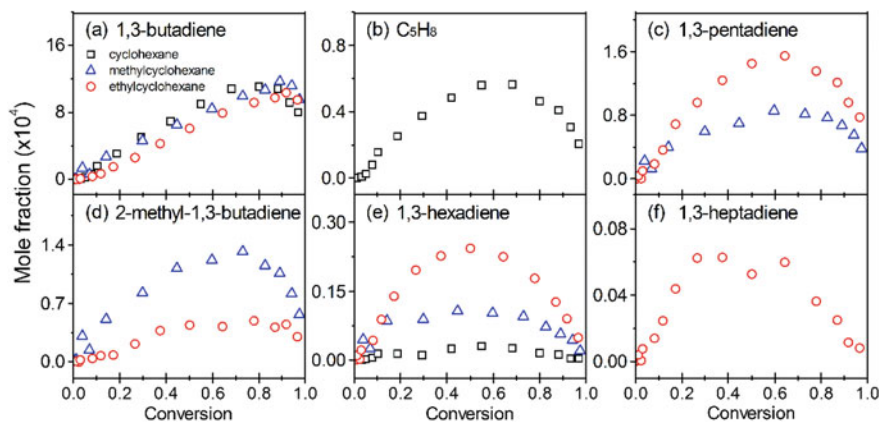
reaction is the ring-opening isomerization to 1-hexene [13]; while the dominant unimolecular reactions of methylcyclohexane and ethylcyclohexane are side chain fission that releases cyclohexyl and methyl/ethyl radicals. The isomerization channels to  $C_7H_{14}$  and  $C_8H_{16}$  alkenes are not important under the temperature range in the pyrolysis experiment, resulting in lesser formation of these isomerization products.

The profiles of C3 products and 1-butene are presented in Fig. 6.3. The initial mole fractions of the three fuels were the same (0.02), but their carbon numbers differed. In the comparison, mole fractions were normalized by the carbon number of each fuel. The most notable discrepancy was the mole fractions of the allyl radical, as shown in Fig. 6.3d. As noted, 1-hexene was the initial product from cyclohexane pyrolysis; it decomposed primarily into allyl and n-propyl radical. This explains the larger formation of allyl radical, especially at lower fuel conversion. Due to the large formation of allyl radical, higher mole fractions of allene, propyne, and propargyl radical were formed in cyclohexane pyrolysis than in methylcyclohexane and ethylcyclohexane pyrolysis. As shown in Fig. 6.3e, f, similar amounts of propene and 1-butene were formed in the pyrolysis of the three fuels. The recombination of allyl radical with H atom and methyl radical were the dominant sources of propene and 1-butene in cyclohexane pyrolysis. These two channels are also important for propene and 1-butene in methylcyclohexane and ethylcyclohexane pyrolysis; but there are other pathways related to the fuel structure. For example, the  $\beta$ -C-C scissions of 1-hepten-6-yl and 2-methyl-5-hexen-1-yl radicals in methylcyclohexane pyrolysis directly form propene; the  $\beta$ -C-C scissions of 1-octen-6-yl and 2-ethyl-5-hexen-1-yl radicals directly form 1-butene in ethylcyclohexane pyrolysis.

Figure 6.4 compares the mole fraction distribution of  $C_4$ - $C_7$  chain dienes. Among these intermediates, 1,3-butadiene (Fig. 6.4a) had the largest mole fraction. The mole fractions of  $C_5H_8$  (Fig. 6.4b, including both 1,3-pentadiene and 2-methyl-1,3-butadiene), as well as 1,3-hexadiene (Fig. 6.4e) during cyclohexane pyrolysis were much lower than those in methylcyclohexane and ethylcyclohexane



**Fig. 6.3** Mole fraction profiles of C3 intermediates and 1-butene in cyclohexane, methylcyclohexane and ethylcyclohexane pyrolysis at 30 Torr. Mole fraction normalized by carbon number of each fuel. X-coordinate is fuel conversion percentage



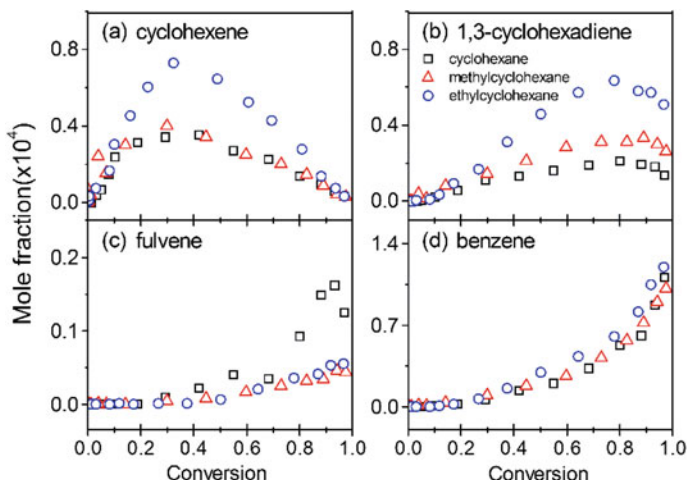
**Fig. 6.4** Mole fraction profiles of C4–C7 chain dienes in cyclohexane, methylcyclohexane and ethylcyclohexane pyrolysis at 30 Torr. Mole fraction normalized by carbon number of each fuel. X-coordinate is fuel conversion percentage

pyrolysis. Methylcyclohexane pyrolysis produced the largest amount of 2-methyl-1,3-butadiene, while ethylcyclohexane pyrolysis resulted in the largest amount of 1,3-pentadiene, 1,3-hexadiene and 1,3-heptadiene. In the kinetic model, 1,3-butadiene was easily formed from the ring-opening isomerization of cyclohexyl radical, methylcyclohexane radicals, and ethylcyclohexane radicals. Therefore, the formation of the C<sub>5</sub>–C<sub>7</sub> dienes are strongly related to the fuel structure.

For 1,3-pentadiene, there are two channels from methylcyclohexane pyrolysis, i.e., the  $\beta$ -C–C scission of 5-hepten-1-yl and 3-methyl-5-hexen-1-yl radicals, while

only one pathway exists from ethylcyclohexane pyrolysis—the  $\beta$ -C-C scission of 6-octen-1-yl radical. 2-Methyl-1,3-butadiene is formed from methylcyclohexane radical due to the existence of the methyl side chain. 1,3-Hexadiene is produced during cyclohexane pyrolysis from the  $\beta$ -C-H scission of 1-hexen-3-yl radical. However, this channel is not favored because the  $\beta$ -C-C scission of 1-hexen-3-yl radical to 1,3-butadiene and ethyl radical is much easier. The existence of the side chain provides direct pathways for 1,3-hexadiene from the  $\beta$ -C-C scission of 3-methyl-5-hexen-1-yl radical in methylcyclohexane pyrolysis, and 5-octen-1-yl and 4-ethyl-1-hexen-3-yl radicals in ethylcyclohexane pyrolysis. The expected increase in 1,3-hexadiene with increased side chain length is in agreement with the experimental observation, as shown in Fig. 6.4e. Moreover, the small amount of 1,3-heptadiene in ethylcyclohexane pyrolysis was formed from the  $\beta$ -C-C scission of 3-octen-5-yl radical.

In cyclohexane, methylcyclohexane, and ethylcyclohexane pyrolysis, cyclohexene, 1,3-cyclohexadiene, fulvene, and benzene were measured, as shown in Fig. 6.5. More cyclohexene and 1,3-cyclohexadiene was formed in ethylcyclohexane pyrolysis. Correspondingly, the mole fraction of benzene in ethylcyclohexane was slightly higher than in cyclohexane and methylcyclohexane pyrolysis. Additional fulvene was formed in cyclohexane pyrolysis because of the higher mole fraction of propargyl and allyl radicals in Fig. 6.3. In the pyrolysis of the three fuels, benzene was produced from multiple channels, including the H-elimination of cyclohexadienyl radical, the H-atom assisted isomerization of fulvene, and the recombination of small radicals. In cyclohexane pyrolysis, the H-atom-assisted isomerization of fulvene and the recombination of small radicals are important

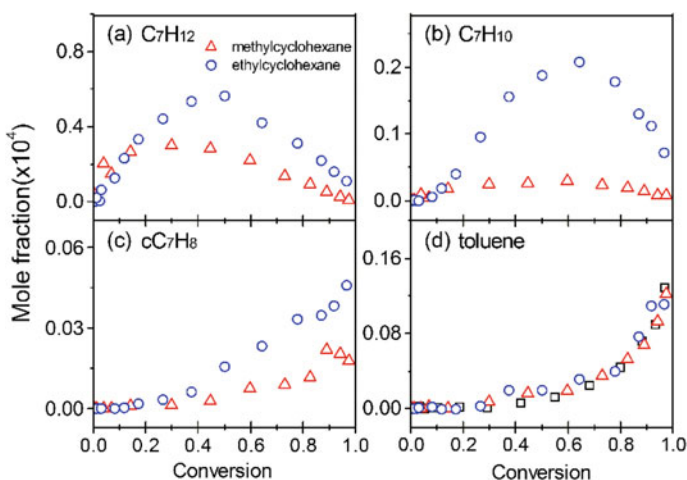


**Fig. 6.5** Mole fraction profiles of cyclohexene, 1,3-cyclohexadiene, fulvene, and benzene in cyclohexane, methylcyclohexane and ethylcyclohexane pyrolysis at 30 Torr. Mole fraction normalized by the carbon number of each fuel. X-coordinate is fuel conversion percentage. Mole fraction of cyclohexene in ethylcyclohexane pyrolysis taken from GC analysis



benzene formation channels. In methylcyclohexane and ethylcyclohexane pyrolysis, the H-elimination of cyclohexadienyl radical is more important. Although the contribution of these benzene precursors differs, the mole fraction of benzene formed in the pyrolysis of cyclohexane, methylcyclohexane, and ethylcyclohexane at 30 Torr is similar.

Some cyclic C7 intermediates like  $C_7H_{12}$ ,  $C_7H_{10}$ ,  $cC_7H_8$  and toluene were measured in methylcyclohexane and ethylcyclohexane pyrolysis, as shown in Fig. 6.6. The mole fraction of  $C_7H_{12}$  intermediate in ethylcyclohexane pyrolysis is a factor of two higher than that in methylcyclohexane pyrolysis. As discussed in Chaps. 4 and 5, the major component of  $C_7H_{12}$  in methylcyclohexane pyrolysis is methylcyclohexenes, while in ethylcyclohexane pyrolysis is methylenecyclohexane. The formation of methylenecyclohexane from the  $\beta$ -C-C scission of ethylcyclohexane radical is much easier than methylcyclohexenes formed from the  $\beta$ -C-H scission of methylcyclohexane radicals. Also, methylcyclohexene is largely consumed by the retro-Diels-Alder reaction under pyrolysis conditions. However, this pathway is not feasible for methylenecyclohexane, which is mainly consumed by H-atom abstraction reactions to cyclic  $C_7H_{11}$  radicals, which then decompose into cyclic  $C_7H_{10}$  intermediate (e.g., 3-methylene-cyclohexene as the main component) by  $\beta$ -C-H scission. The easy formation of methylenecyclohexane, and its frequent tendency to cyclic  $C_7H_{10}$  intermediates, explains the higher mole fraction of  $C_7H_{10}$  in ethylcyclohexane pyrolysis than in methylcyclohexane pyrolysis. The further step-wise dehydrogenation of 3-methylene-cyclohexene led to  $cC_7H_8$  (*o*-isotoluene and *p*-isotoluene), a factor of two higher than in methylcyclohexane pyrolysis.



**Fig. 6.6** Mole fraction profiles of C7 cyclic intermediates in methylcyclohexane and ethylcyclohexane pyrolysis at 30 Torr. Mole fraction normalized by the carbon number of each fuel. X-coordinate is fuel conversion percentage

The mole fraction of toluene in the pyrolysis of three cycloalkanes is shown in Fig. 6.6d. In cyclohexane pyrolysis, toluene results from the recombination of H atom with benzyl radical, which originates from the combination of propargyl radical ( $C_3H_3$ ). In methylcyclohexane pyrolysis, the step-wise dehydrogenation of methylcyclohexane is the main source of toluene. In ethylcyclohexane pyrolysis, an important pathway for toluene is the recombination of H atom with benzyl radical, from the step-wise dehydrogenation of ethylcyclohexane; in this process, methylenecyclohexane, 3-methylene-cyclohexene, and  $cC_7H_8$  (*o*-isotoluene and *p*-isotoluene) were formed. The different structure and length of the side chain of the three cycloalkanes resulted in different precursors for toluene. Like benzene, the production of toluene is close in the pyrolysis of cyclohexane, methylcyclohexane and ethylcyclohexane.

Cyclic intermediates such as  $C_8H_{14}$  and  $C_8H_{12}$ , and the isomers of ethylbenzene were measured in ethylcyclohexane pyrolysis, but they were not measured in cyclohexane and methylcyclohexane pyrolysis. The discussion in Chap. 5 explains that these cyclic intermediates are produced from the step-wise dehydrogenation of ethylcyclohexane and are potential precursors of ethylbenzene and styrene.

## 6.2 Low-Pressure Premixed Flame

In Chaps. 3, 4 and 5, the kinetic model for cyclohexane, methylcyclohexane, and ethylcyclohexane was examined by speciation in fuel-rich laminar premixed flames. The agreement between experiment and simulation was satisfactory. In this section, the reaction kinetics of the three cycloalkanes flame were analyzed by the simulation of the kinetic models. The conditions for the three flames are presented in Table 6.2. The pressure of the flame was 30 Torr, equivalence ratio was 1.75, C/O ratio was 0.583, the mole fraction of the dilution gas was 50%, and the temperature of the unburnt gas was 450 K. Simulation was performed using the PREMIX module of CHEMKIN-PRO software. The gas energy equation was solved in the calculations and the thermal diffusion (i.e., the Soret effect) was considered.

**Table 6.2** Conditions for cyclohexane, methylcyclohexane, and ethylcyclohexane premixed flame

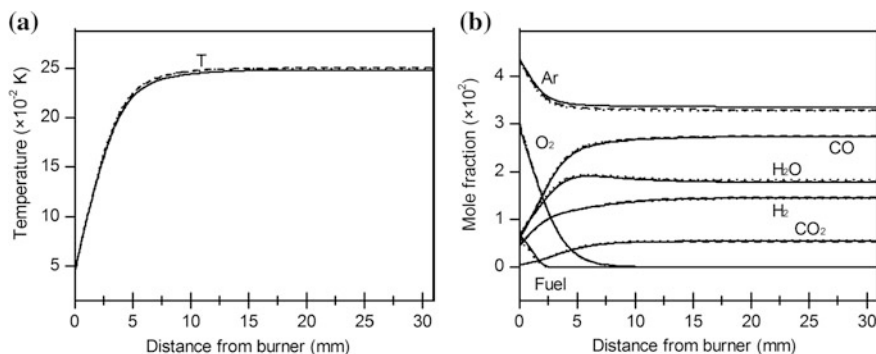
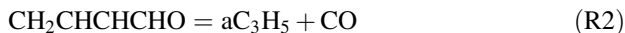
Fuel	$\phi$	C/O	P/ Torr	$X_{Fuel}$	$X_{O_2}$	$X_{Ar}$	V/cm $s^{-1}$	MFR/g $cm^{-2}$ $s^{-1}$
Cyclohexane	1.75	0.583	30	8.14	41.86	50.00	50.00	0.0322
Methylcyclohexane	1.75	0.583	30	7.14	42.86	50.00	50.00	0.0326
Ethylcyclohexane	1.75	0.583	30	6.36	43.64	50.00	50.00	0.0329

Note  $X_i$  is initial mole fraction of species *i*; V is velocity of unburnt gas at 300 K; MFR is mass flow rate

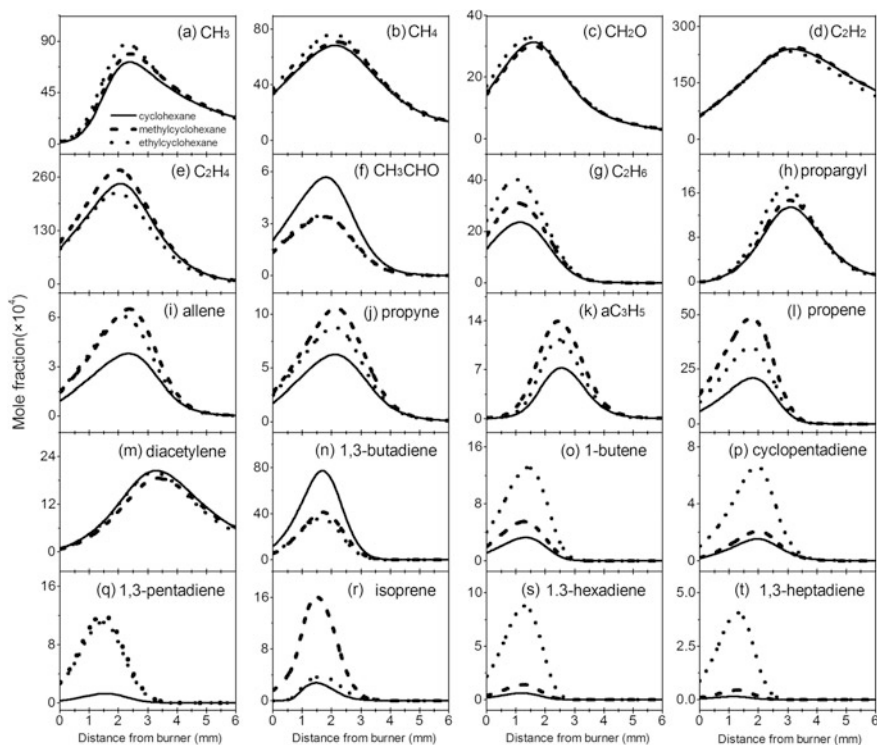
The flame temperature and mole fraction profiles of the major combustion intermediates are presented in Fig. 6.7. The calculated maximum flame temperature was 2483, 2509, and 2503 K for cyclohexane, methylcyclohexane, and ethylcyclohexane, respectively. The flame structure of the three cycloalkanes, including the consumption of the reactants (fuel and O<sub>2</sub>), the formation of major combustion products (H<sub>2</sub>O, CO, CO<sub>2</sub>, and H<sub>2</sub>), and the mole expansion effect of the flame (i.e., Ar profile) was very close.

Mole fractions of the important flame intermediates are presented in Figs. 6.8 and 6.9. The reaction zone of the three flames was the same, while the distribution of some flame intermediates differed. The C1–C2 intermediates with the largest discrepancy were acetaldehyde and ethane. More acetaldehyde was produced in cyclohexane flame than alkyl-cyclohexanes (Fig. 6.8f). Reaction pathway analysis showed that acetaldehyde formed from the reaction of 1,3-butadiene with OH radical. As shown in Fig. 6.8n, the mole fraction of 1,3-butadiene in cyclohexane flame was a factor of two higher than in methylcyclohexane and ethylcyclohexane flames. The higher production of 1,3-butadiene resulted in higher mole fraction of acetaldehyde. In the three flames, ethane resulted from the recombination of methyl radical; the trend of ethane mole fraction was the same as methyl radical, i.e., cyclohexane < methylcyclohexane < ethylcyclohexane.

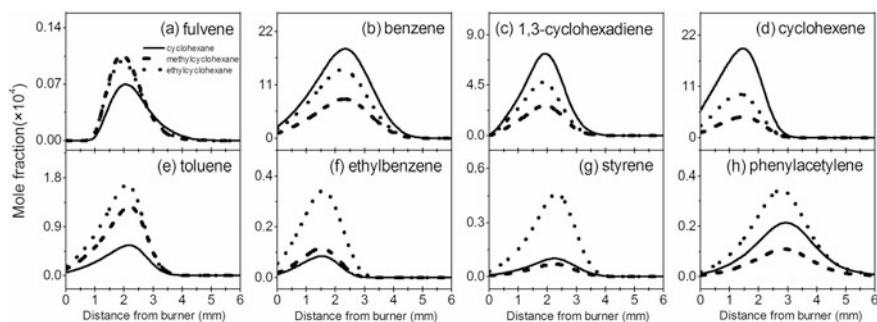
For the C3 intermediates in Fig. 6.8h–l, apart from propargy radical (C<sub>3</sub>H<sub>3</sub>), the mole fraction trend of allene, propyne, allyl radical, and propene was on the order of cyclohexane < ethylcyclohexane < methylcyclohexane. The common pathways for allyl radical (aC<sub>3</sub>H<sub>5</sub>) in the three flames are



**Fig. 6.7** Temperature profiles **a** mole fraction profiles of major combustion products **b** in cyclohexane (solid line), methylcyclohexane (dashed line), and ethylcyclohexane (dotted line) flame at 30 Torr and with equivalence ratio of 1.75



**Fig. 6.8** Mole fraction profiles of C1–C7 chain hydrocarbons in cyclohexane (solid line), methylcyclohexane (dashed line), and ethylcyclohexane (dotted line) flame at 30 Torr and with equivalence ratio of 1.75



**Fig. 6.9** Mole fraction profiles of C6–C7 cyclic intermediates in cyclohexane (solid line), methylcyclohexane (dashed line), and ethylcyclohexane (dotted line) flame at 30 Torr and with equivalence ratio of 1.75

However, the methylcyclohexane flame has one specific pathway for allyl radical, which results from the ring-opening isomerization of cyclohexylmethyl radical (Fig. 4.18b). This pathway is the dominant source for allyl radical. In methylcyclohexane flame, the ring-opening isomerization of 3-methyl-cyclohexyl radical led directly to propene (Fig. 4.18f). In addition, the reactions of 2-methyl-1,3-butadiene are another important source for propene in methylcyclohexane flame. The higher mole fraction of 2-methyl-1,3-butadiene (Fig. 6.8r) in methylcyclohexane flame further promotes propene formation. The propene in ethylcyclohexane flame is mainly formed from the reactions of 1-butene with H atom (R3). In ethylcyclohexane flame, the higher mole fraction of 1-butene (Fig. 6.8) than cyclohexane and methylcyclohexane flame also promotes propene formation.



The propene in cyclohexane flame derives mainly from the recombination of allyl radical with H atom, the  $\beta$ -C-H scission of  $\text{iC}_3\text{H}_7$ , and R3. These pathways do not produce propene as efficiently as the pathways in methylcyclohexane and ethylcyclohexane flame.

The mole fraction profiles of three C4 intermediates are presented in Fig. 6.8m–o. The three flames form similar amounts of diacetylene, cyclohexane flame forms more 1,3-butadiene, ethylcyclohexane flame forms more 1-butene. Multiple pathways led to 1,3-butadiene in the three flames; the dominant route to 1,3-butadiene in cyclohexane flame is ring-opening isomerization of cyclohexyl radical. 1-butene is formed from the recombination of allyl radical with methyl radical and the recombination of 1-buten-3-yl radical with H atom in cyclohexane and methylcyclohexane flame. However, the ring-opening isomerization of 3-ethyl-cyclohexyl radical directly forms 1-butene (Fig. 5.4e) in ethylcyclohexane flame. In addition, the ring-opening isomerization of 4-ethyl-cyclohexyl radical forms 2-butyl radical (Fig. 5.4c), whose  $\beta$ -C-H scission also forms 1-butene. These two pathways from the decomposition of ethylcyclohexane radicals cause the large formation of 1-butene in ethylcyclohexane flame.

The mole fraction profiles of three C5 intermediates are presented in Fig. 6.8p–r. Ethylcyclohexane flame formed higher mole fractions of cyclopentadiene, methylcyclohexane flame produced higher mole fraction of 2-methyl-1,3-butadiene (i.e., isoprene in Fig. 6.8r), while these two flames formed a similar amount of 1,3-pentadiene. Cyclopentadiene was produced from the H-loss of  $\text{IC}_5\text{H}_7$  radical. However, the source for  $\text{IC}_5\text{H}_7$  radical was different in the three flames. In cyclohexane flame,  $\text{IC}_5\text{H}_7$  resulted from the recombination of  $\text{iC}_4\text{H}_5$  radical with methyl radical and the H-atom abstraction of 1,3-pentadiene; the dominant source for  $\text{IC}_5\text{H}_7$  in methylcyclohexane flame was the H-atom abstraction of 1,3-pentadiene; the source for  $\text{IC}_5\text{H}_7$  in ethylcyclohexane flame was the  $\beta$ -C-C scission of 1,3-hexadiene and 1,3-heptadiene, and the H-atom abstraction of 1,3-pentadiene. The distribution of 1,3-pentadiene (Fig. 6.8q), 1,3-hexadiene (Fig. 6.8s), and 1,3-heptadiene (Fig. 6.8t) were in accord with the distribution of cyclopentadiene in the three flames. In methylcyclohexane and ethylcyclohexane flame, the

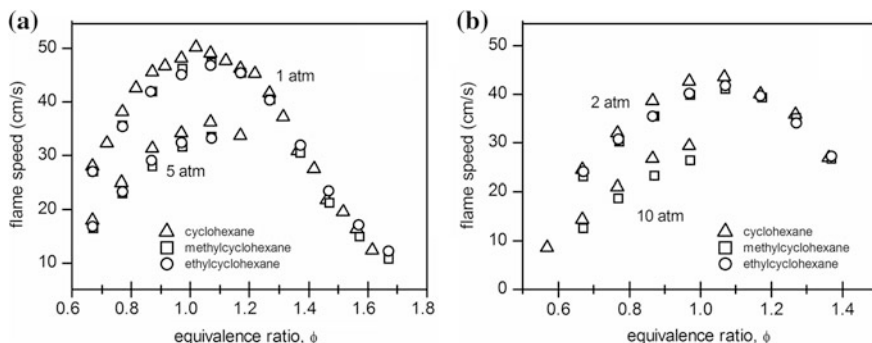
ring-opening of the methylcyclohexane radical (Fig. 4.18d) and ethylcyclohexane radical (Fig. 5.4a) was the main source for 1,3-pentadiene. For 2-methyl-1,3-butadiene in cyclohexane and ethylcyclohexane flame, the main source was the built-up reactions of smaller intermediates. However, this intermediate was produced directly from the decomposition of methylcyclohexane radicals (Fig. 4.18c, d). This was the main reason for the favorable production of 2-methyl-1,3-butadiene in methylcyclohexane flame.

Because of the existence of a six-membered ring, the combustion of cyclohexane and alkyl-cyclohexanes has a frequent tendency to form aromatics [14]. The mole fraction profiles of the C6–C8 cyclic intermediates in the three flames are presented in Fig. 6.9. The reaction pathways for fulvene in the three flames were similar, but the flame of two alkyl-cyclohexane formed a slightly higher mole fraction of fulvene (Fig. 6.9a). The comparison in Fig. 6.9b–d shows that the mole fractions of cyclohexene, 1,3-cyclohexadiene and benzene were in the order of cyclohexane > ethylcyclohexane > methylcyclohexane. However, the kinetic model of cyclohexane over-predicted the mole fraction of cyclohexene, 1,3-cyclohexadiene, and benzene in the simulation of cyclohexane flame by Li et al. [15]. Further experimental studies under the same conditions are needed to clarify the benzene formation tendency in the combustion of cyclohexane, methylcyclohexane, and ethylcyclohexane.

The methylcyclohexane and ethylcyclohexane flames produced higher mole fraction of toluene than the cyclohexane flame (Fig. 6.9e). In methylcyclohexane flame, toluene resulted from the step-wise dehydrogenation of methylcyclohexane. In ethylcyclohexane, toluene was mainly formed from the recombination of H atom with benzyl radical, from the step-wise dehydrogenation of methylenecyclohexane, by way of 3-methylene-cyclohexene and  $\text{cC}_7\text{H}_8$  (*o*-isotoluene and *p*-isotoluene). In cyclohexane flame, toluene was also formed largely from the recombination of H atom with benzyl radical. However, benzyl radical was produced by the reaction of phenyl radical with methyl radical; another pathway for benzyl radical was the step-wise dehydrogenation of 3-methyl-cyclohexene, from the recombination of 2-cyclohexen-1-yl radical with methyl radical. Production of ethylbenzene and styrene (Fig. 6.9f, g) is more favorable in the ethylcyclohexane flame, since the step-wise dehydrogenation of ethylcyclohexane could lead directly to these two aromatics.

### 6.3 Laminar Flame Speed

The laminar flame speeds of cyclohexane/air, methylcyclohexane/air, and ethylcyclohexane/air were measured by Wu et al. [16], as shown in Fig. 6.10. The unburnt gas temperature was 353 K and pressure was 1, 2, 5, and 10 atm. The flame speeds of methylcyclohexane and ethylcyclohexane were close under all the pressures, while both were slightly slower than the flame speed of cyclohexane. The maximum flame speed of cyclohexane at 1 atm was 3% faster than those of the



**Fig. 6.10** Laminar flame speed of cyclohexane/air, methylcyclohexane/air, and ethylcyclohexane/air with unburnt gas temperature of 353 K and pressure of 1, 2, 5, and 10 atm. Reprinted from Ref. [16], Copyright 2012, with permission from Elsevier

two alkyl-cyclohexanes. The discrepancy increased to 13% when the pressure was 10 atm. In Wu et al.'s work, the JetSurF 1.0 model [17] was adopted to simulate the flame speeds of the three fuels under different pressures. The agreement between experiment and simulation was good. The discrepancies for the flame speed between cyclohexane and alkylcyclohexanes are discussed with the help of model analysis. In this work, the developed kinetic model for cyclohexane, methylcyclohexane, and ethylcyclohexane also captured the flame speeds of the three fuels well. Analysis for the speciation of the flame intermediates and sensitivity analysis for the flame speeds was in accord with the work of Wu et al. In the following discussion on the discrepancy of the flame speed, the results from Wu et al. were adopted.

The laminar flame speeds of fuel/air mixture under the same experimental conditions are determined mainly by thermal and chemical effects. The three flames of cyclohexane/air, methylcyclohexane/air, and ethylcyclohexane/air have very close adiabatic flame temperature; therefore the thermal effect should not be the reason for the flame speed discrepancy between cyclohexane/air and alkyl-cycloalkane/air. In addition, the transport properties of the three cycloalkanes are similar to those of the C6–C8 normal alkanes; the flame speed of the n-hexane/air, n-heptane/air, and n-octane/air are very close [18].

The simulation showed that cyclohexane and alkylcyclohexane have different flame structure (e.g., flame temperature profile and heat release profile). The profiles for temperature and heat release of methylcyclohexane and ethylcyclohexane flame are very close; however, the two profiles in cyclohexane flame are different from those of the two alkyl-cyclohexane flames. The steeper temperature profile indicates stronger heat release of the cyclohexane flame. Moreover, this difference is more evident at higher pressures. For example, the maximum difference in the heat release rate between cyclohexane and alkyl-cyclohexanes flame at 1 atm is 3%, while this value is 8% at 10 atm flame. Considering the very close adiabatic flame temperature of the three cycloalkane flames, the difference for the heat release rate

reflects the different kinetic behavior of cyclohexane compared to the alkyl-cyclohexanes [16].

Sensitivity analysis proved that the reactions of C0–C4 intermediates significantly affect flame speed [16]. Comparison of flame distribution intermediates revealed that the profiles for H, OH, O, and CO in cyclohexane and methylcyclohexane flame were very close; the discrepancy becomes larger for the profiles of CH<sub>3</sub>, CH<sub>4</sub>, C<sub>2</sub>H<sub>2</sub>, and C<sub>2</sub>H<sub>4</sub>, however, they are still on the same order of magnitude. The apparent difference is in the profiles of propene and 1,3-butadiene; the maximum mole fraction of propene in cyclohexane flame is 40% of that in methylcyclohexane flame, while the maximum mole fraction of 1,3-butadiene in cyclohexane flame is twice that in methylcyclohexane flame.

The discrepancy between propene and 1,3-butadiene explains the flame speed difference of cyclohexane compared to alkyl-cyclohexane [16]. The reactivity of propene is lower than that of 1,3-butadiene. The H-atom abstraction of propene forms allyl radical, which then combines with H atom and forms propene. In contrast, the reactions of 1,3-butadiene with the H atom to produce ethylene and vinyl radical, which have high reactivity.

The sensitivity analysis and the distribution of the C3–C4 intermediates can also explain the pressure effect on heat release rates and flame speed [16]. Compared to the flame at 1 atm, the reactions of the C3 and C4 intermediates have even higher sensitivity at 10 atm. For example, the high pressure promotes chain terminating third-body reactions, such as  $aC_3H_5 + H + M = C_3H_6 + M$ .

To summarize, the symmetric structure of cyclohexane caused higher production of chain-branching intermediate 1,3-butadiene and lower production of chain-terminating intermediate propenes. The side-chains of methylcyclohexane and ethylcyclohexane made the distribution of the flame intermediates more balanced and led to similar reactivity [16].

## References

1. Cool, T. A., Nakajima, K., Mostefaoui, T. A., Qi, F., McIlroy, A., Westmoreland, P. R., et al. (2003). Selective detection of isomers with photoionization mass spectrometry for studies of hydrocarbon flame chemistry. *Journal of Chemical Physics*, 119(16), 8356–8365.
2. Cool, T. A., Wang, J., Nakajima, K., Taatjes, C. A., & McIlroy, A. (2005). Photoionization cross sections for reaction intermediates in hydrocarbon combustion. *International Journal of Mass Spectrometry*, 247(1–3), 18–27.
3. Wang, J., Yang, B., Cool, T. A., Hansen, N., & Kasper, T. (2008). Near-threshold absolute photoionization cross-sections of some reaction intermediates in combustion. *International Journal of Mass Spectrometry*, 269(3), 210–220.
4. Yang, B., Wang, J., Cool, T. A., Hansen, N., Skeen, S., & Osborn, D. L. (2012). Absolute photoionization cross-sections of some combustion intermediates. *International Journal of Mass Spectrometry*, 309, 118–128.
5. Zhou, Z., Xie, M., Wang, Z., & Qi, F. (2009). Determination of absolute photoionization cross-sections of aromatics and aromatic derivatives. *Rapid Communications in Mass Spectrometry*, 23(24), 3994–4002.



6. Zhou, Z., Zhang, L., Xie, M., Wang, Z., Chen, D., & Qi, F. (2010). Determination of absolute photoionization cross-sections of alkanes and cyclo-alkanes. *Rapid Communications in Mass Spectrometry*, 24(9), 1335–1342.
7. Hansen, N., Klippenstein, S. J., Miller, J. A., Wang, J., Cool, T. A., Law, M. E., et al. (2006). Identification of C<sub>5</sub>H<sub>x</sub> isomers in fuel-rich flames by photoionization mass spectrometry and electronic structure calculations. *The Journal of Physical Chemistry A*, 110(13), 4376–4388.
8. Soorkia, S., Trevitt, A. J., Selby, T. M., Osborn, D. L., Taatjes, C. A., Wilson, K. R., et al. (2010). Reaction of the C<sub>2</sub>H radical with 1-butyne (C<sub>4</sub>H<sub>6</sub>): Low-temperature kinetics and isomer-specific product detection. *The Journal of Physical Chemistry A*, 114(9), 3340–3354.
9. Zhang, F., Wang, Z., Wang, Z., Zhang, L., Li, Y., & Qi, F. (2013). Kinetics of decomposition and isomerization of methylcyclohexane: Starting point for kinetic modeling mono-alkylated cyclohexanes. *Energy & Fuels*, 27(3), 1679–1687.
10. Linstrom, P. J., & Mallard, W. G. (2005). *NIST chemistry webbook*. Gaithersburg, MD: National Institute of Standard and Technology, number 69. <http://webbook.nist.gov/>.
11. Kiefer, J. H., Gupte, K. S., Harding, L. B., & Klippenstein, S. J. (2009). Shock tube and theory investigation of cyclohexane and 1-hexene decomposition. *Journal of Physical Chemistry A*, 113(48), 13570–13583.
12. Luo, Y. R. (2007). *Comprehensive handbook of chemical bond energies*. Boca Raton, FL: CRC Press.
13. Wang, Z., Cheng, Z., Yuan, W., Cai, J., Zhang, L., Zhang, F., et al. (2012). An experimental and kinetic modeling study of cyclohexane pyrolysis at low pressure. *Combustion and Flame*, 159(7), 2243–2253.
14. Crossley, S. P., Alvarez, W. E., & Resasco, D. E. (2008). Novel micropyrolysis index (MPI) to estimate the sooting tendency of fuels. *Energy & Fuels*, 22(4), 2455–2464.
15. Li, W., Law, M. E., Westmoreland, P. R., Kasper, T., Hansen, N., & Kohse-Höinghaus, K. (2011). Multiple benzene-formation paths in a fuel-rich cyclohexane flame. *Combustion and Flame*, 158(11), 2077–2089.
16. Wu, F., Kelley, A. P., & Law, C. K. (2012). Laminar flame speeds of cyclohexane and mono-alkylated cyclohexanes at elevated pressures. *Combustion and Flame*, 159(4), 1417–1425.
17. Sirjean, B., Dames, E., Sheen, D. A., You, X.-Q., Sung, C., Holley, A. T., et al. (2009). A high-temperature chemical kinetic model of n-alkane oxidation. *JetSurF Version 1.0* (Sept 15).
18. Kelley, A. P., Smallbone, A. J., Zhu, D. L., & Law, C. K. (2011). Laminar flame speeds of C5 to C8 n-alkanes at elevated pressures: Experimental determination, fuel similarity, and stretch sensitivity. *Proceedings of the Combustion Institute*, 33(1), 963–970.

## Chapter 7

# Conclusions and Perspective

In this thesis, the combustion kinetics of cyclohexane, methylcyclohexane and ethylcyclohexane pyrolysis and oxidation were investigated by flow reactor pyrolysis and laminar premixed flame experiments, reaction pathway computations, and rate constant evaluations. The kinetic models for the high temperature pyrolysis and oxidation of cyclohexane, methylcyclohexane and ethylcyclohexane were developed from experimental observation, quantum chemistry computation, and literature review; model validation was carried out by speciation in the three cycloalkane pyrolysis and oxidation measured in this work and in JSR oxidation reported in the literature, as well as ignition delay times and laminar flame speed.

The main conclusions from experimental study are as follows:

- (1) The flow reactor pyrolysis of cyclohexane, methylcyclohexane, and ethylcyclohexane at 30, 150, and 760 Torr was investigated using synchrotron radiation photoionization molecular beam mass spectrometry (SR-PI-MBMS). Pyrolysis intermediates were identified by measuring the photoionization efficiency spectra, including radicals and various isomers. Their mole fractions, with temperature, were measured; these clarified the pyrolysis mechanism and validated the kinetic model. The combination of flow reactor pyrolysis with GC/GC-MS analysis was adopted to study the pyrolysis of ethylcyclohexane at 30, 150, and 760 Torr. GC enabled more efficient separation of the isomers and the detection of some low concentration intermediates. The SR-PI-MBMS and GC data for ethylcyclohexane pyrolysis were in good agreement and were complementary.
- (2) In the pyrolysis of cyclohexane, methylcyclohexane, and ethylcyclohexane, the species pool was similar. With the increased side chain, intermediates related to the fuel structure were detected. Large amounts of chain and branched dienes were measured, including 1,3-butadiene, 1,3-pentadiene, and 2-methyl-1,3-butadiene, and 1,3-heptadiene. The mole fraction of 1,3-butadiene in the pyrolysis of the three cycloalkanes was very high. Methylcyclohexane pyrolysis produced the highest mole fraction of 2-methyl-1,3-butadiene, while

ethylcyclohexane pyrolysis resulted in the highest mole fraction of 1,3-hexadiene, 2-ethyl-1,3-butadiene, and 1,3-heptadiene.

- (3) A series of C6–C8 cyclic alkenes, dienes, and trienes were measured. In the pyrolysis of three cycloalkanes, both cyclohexene and 1,3-cyclohexadiene were specifically measured. The C7 cyclic alkenes were measured in methylcyclohexane and ethylcyclohexane pyrolysis. The major component for C7 cyclic alkenes in methylcyclohexane pyrolysis is methycyclohexenes, while the main component in ethylcyclohexane pyrolysis is methylenecyclohexane. The isomers of toluene, i.e.,  $\text{C}_7\text{H}_8$  (*o*-isotoluene and *p*-isotoluene) were measured during methylcyclohexane and ethylcyclohexane pyrolysis. The C8 cyclic alkenes, dienes, and the isomers of ethylbenzene (e.g., 1-ethenyl-1,3-cyclohexadiene) were measured in the pyrolysis of ethylcyclohexane. Measurement of these cyclic compounds confirmed that the step-wise dehydrogenation/dealkylation of cyclohexane and alkyl-cyclohexanes are precursors of aromatics.
- (4) Low-pressure premixed flames of methylcyclohexane and ethylcyclohexane at 30 Torr, and with equivalence ratio of 1.75, were measured using the SR-PI-MBMS. The hydrocarbon species measured in the flame of cycloalkanes were similar to those formed during their pyrolysis. The flame temperature and speciation of the flame intermediates were measured; these are useful in the study of flame structure of methylcyclohexane and ethylcyclohexane, and in validating the kinetic model. The C6–C8 cyclic intermediates were also measured in the flames; they are important aromatic precursors for benzene, toluene, ethylbenzene, and styrene, etc. In addition, a large amount of 1,3-butadiene was produced in the two alkyl-cyclohexane flames.

The main conclusions from theoretical study are as follows:

- (1) The adiabatic ionization energy of cyclic C7 and C8 intermediates was calculated, which are helps to identify the structure of these species. Thermodynamic data of some cyclic intermediates  $\text{C}_7\text{H}_{13}$ ,  $\text{C}_7\text{H}_{12}$ ,  $\text{C}_7\text{H}_{11}$ ,  $\text{C}_7\text{H}_{10}$ ,  $\text{C}_7\text{H}_9$ , and  $\text{C}_7\text{H}_8$  were estimated from quantum chemistry calculations and isodesmic reactions.
- (2) The reaction pathways of methylcyclohexane decomposition, i.e., methyl-loss and ring-opening isomerization, were computed. The potential energy surface showed that ring-opening isomerization via the C–C bond scission adjacent to the side chain had the lowest energy barriers of all the isomerization channel. The methyl-loss channel is also competitive with isomerization pathways. High pressure limit rate constants indicated that the ring-opening isomerization via the C–C bond scission adjacent to the side chain had the highest rate constants of all the isomerization channels. The channel to 2-heptene was the dominant isomerization pathway for methylcyclohexane. The pressure dependence of the isomerization pathways was more apparent than the methyl-loss channel. Theoretical calculation of the initial unimolecular reactions of methylcyclohexane formed the basis for understanding the reaction kinetics of methylcyclohexane and ethylcyclohexane combustion.

- (3) The reaction pathways of H-atom abstraction of methylcyclohexane by H atom were computed, and the evaluated rate constants were in agreement with reports in the literature. Unimolecular decomposition pathways of the methylcyclohexane radicals were computed, as well as temperature- and pressure-dependent rate constants. The unimolecular decomposition pathways of ethylcyclohexane radicals were also computed; results showed that, in most cases, the energy barrier for the same reaction type of methylcyclohexane and ethylcyclohexane radical was close. Thus, the rate constants of methylcyclohexane radical unimolecular decomposition can be used to estimate the rate constants of ethylcyclohexane radicals.

The main conclusions from kinetic modeling follow:

- (1) A combustion model of cyclohexane, methylcyclohexane, and ethylcyclohexane was developed. The existence of the side chain complicated the reaction mechanism of the alkyl-cyclohexane. The sub-mechanism of methylcyclohexane was developed from the calculation of the unimolecular reactions of methylcyclohexane, the H-atom abstraction of methylcyclohexane by H atom, and the unimolecular decomposition of methylcyclohexane radicals. The sub-mechanism of ethylcyclohexane was developed by referring to the sub-mechanism of methylcyclohexane. Some novel reaction pathways were proposed and developed from experimental observations and quantum chemistry calculations, including the detailed initial decomposition pathways of methylcyclohexane and ethylcyclohexane, pathways from the step-wise dehydrogenation of methylcyclohexane and ethylcyclohexane to aromatics like benzene, toluene, ethylbenzene, and styrene, and the intramolecular radical addition on the double bond of the long-chain alkenyl radicals. The kinetic model was validated by the speciation in flow reactor pyrolysis, premixed flame, and JSR oxidation, as well as ignition delay times and laminar flame speeds. The kinetic model, particularly unimolecular decomposition and H-atom abstraction reactions of the cycloalkanes, and subsequent reactions of the cycloalkane radicals, were examined under a wide range of pressures (30–7600 Torr), temperatures (700–2100 K), and equivalence ratios (0.25– $\infty$ ).
- (2) Pyrolysis and flame kinetics of cyclohexane, methylcyclohexane and ethylcyclohexane were discussed with the aid of model simulation. Under the pyrolysis experiment in this work, the fuel was consumed by both unimolecular decomposition and H-atom abstraction reactions. The only unimolecular pathway for cyclohexane was its isomerization to 1-hexene, while the dominant unimolecular pathway for methylcyclohexane and ethylcyclohexane was the side chain loss that formed cyclohexyl radical. H-atom abstraction pathways were the dominant pathways for consumption of cyclohexane, methylcyclohexane and ethylcyclohexane under flame conditions. The H-atom abstraction by H atom was more important in fuel-rich flames, while under fuel-lean flames, the reactions with OH radical were more important. In JSR oxidation, H-atom abstraction by OH radical was the main route for consumption of the three fuels.

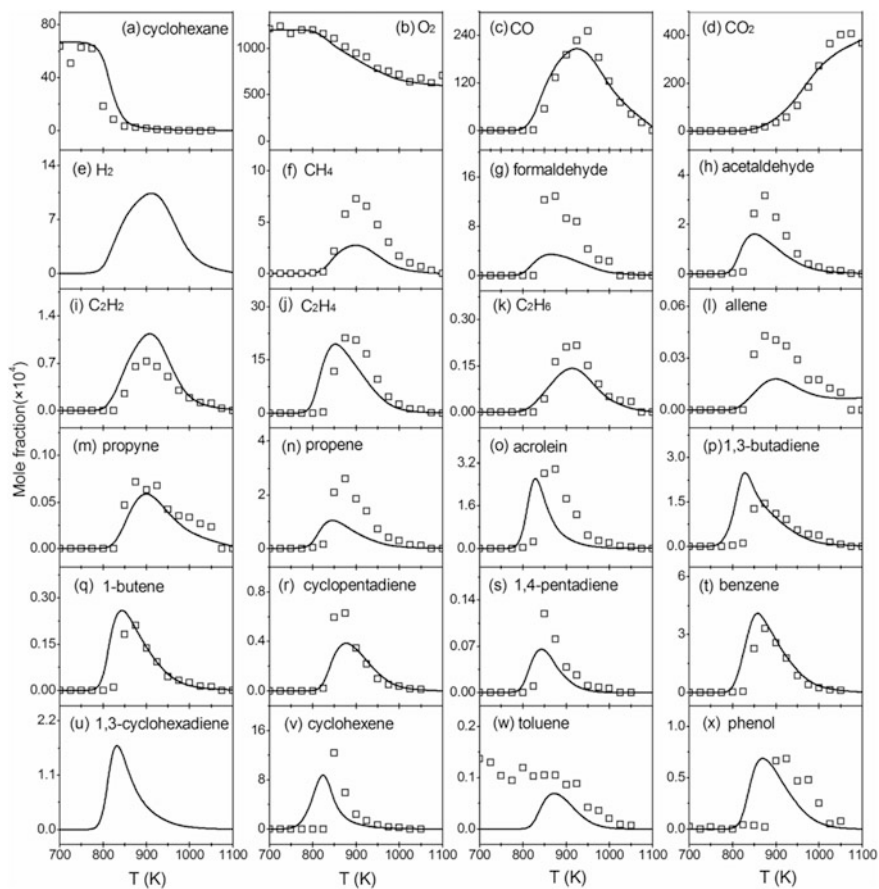
- (3) The reactivity of cyclohexane, methylcyclohexane and ethylcyclohexane was discussed, as well as the distribution of pyrolysis intermediates like alkenes from the initial isomerization, C3 intermediates, C4–C7 chain and branched dienes, C6–C8 cyclic alkene, diene, triene, and aromatics. The flame structure of the three cycloalkanes was discussed, with a focus on mole fraction discrepancy of the flame intermediates. The reaction kinetic causing the slightly higher flame speed of cyclohexane compared to methylcyclohexane and ethylcyclohexane was also discussed.

The perspective of this thesis includes:

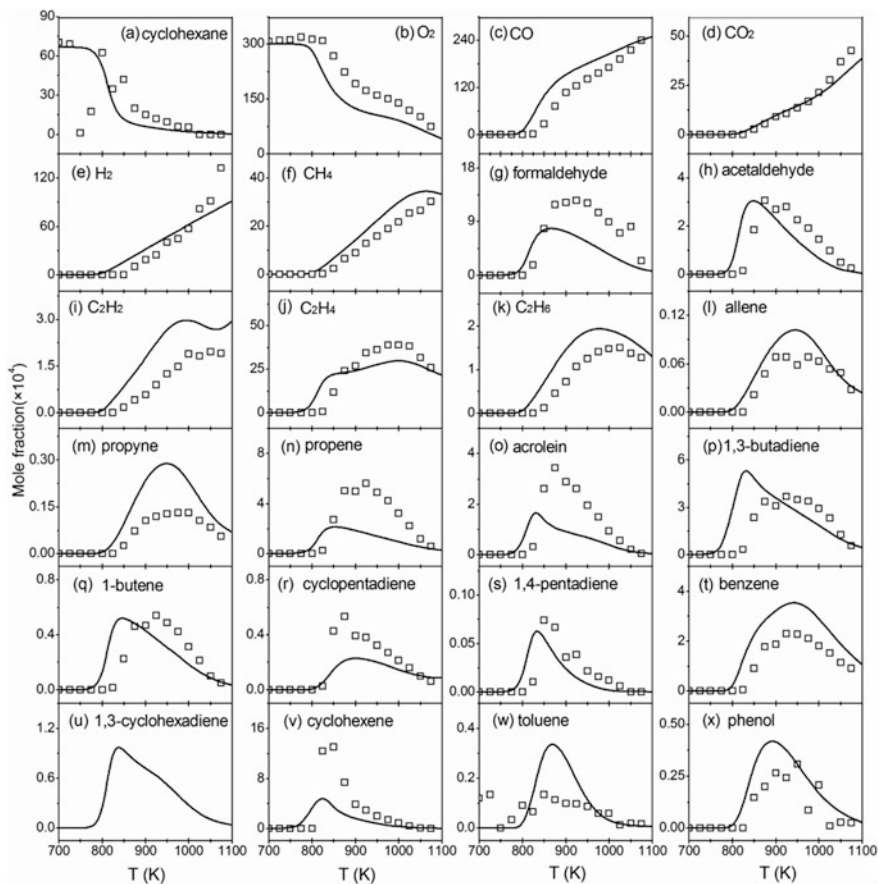
- (1) Study of the reaction kinetics of C6–C8 alkenes, C4–C7 chain and branched dienes, and cyclic C6–C8 alkenes and dienes. These species are important intermediates in cyclohexane, methylcyclohexane, and ethylcyclohexane combustion. Studies on these species is scarce and detailed experimental and theoretical investigation is needed, which will prove valuable for improving the combustion kinetic model of cycloalkanes.
- (2) Investigating the combustion kinetics of long chain alkyl-cyclohexanes such as n-propylcyclohexane and n-butylcyclohexane and multiple chain alkyl-cyclohexane.
- (3) Developing the low-temperature oxidation mechanism of cyclohexane and alkyl-cyclohexanes and extend kinetic models to lower temperatures and higher pressures.

## Appendix A

See Figs. [A.1](#), [A.2](#), [A.3](#) and [A.4](#).

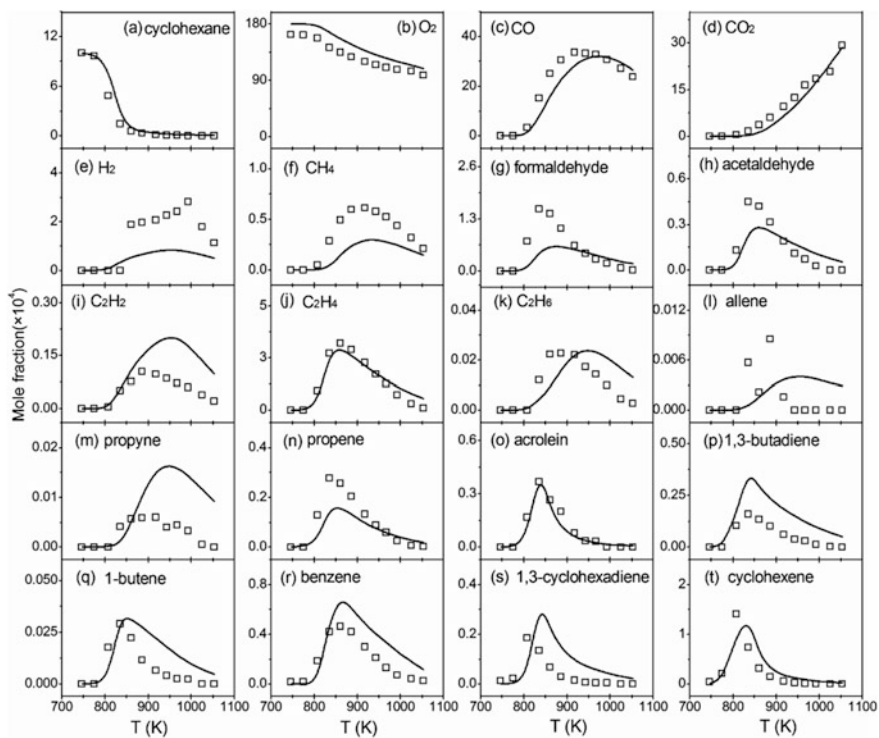


**Fig. A.1** Experimental (symbols) and simulated (lines) mole fraction profiles of reactants, major products, and C1–C7 intermediates during cyclohexane oxidation with equivalence ratio of 0.5 and pressure of 1.05 atm

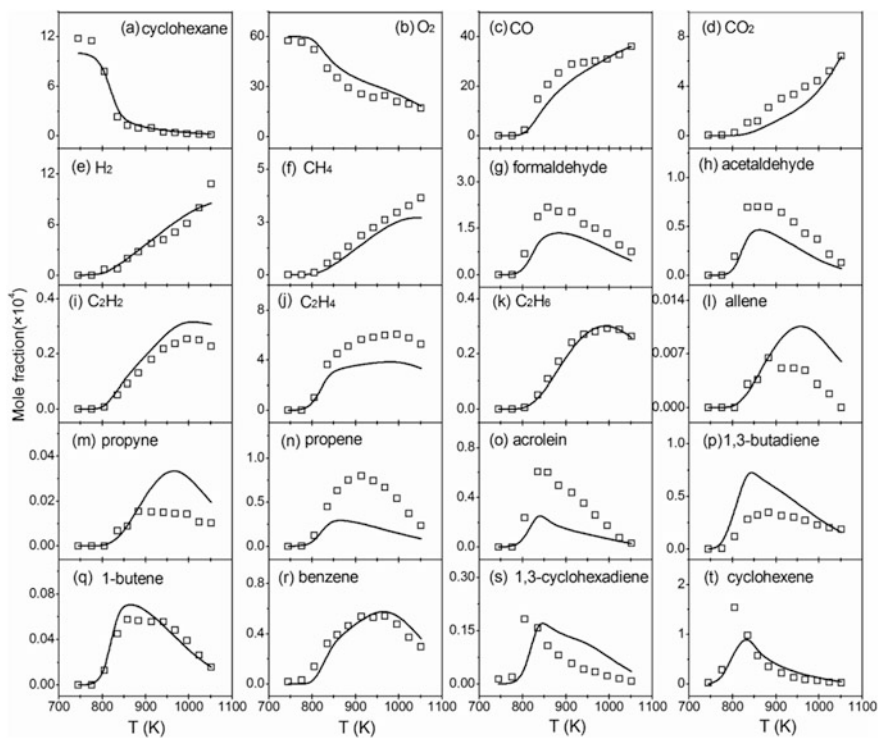


**Fig. A.2** Experimental (symbols) and simulated (lines) mole fraction profiles of reactants, major products, and C1–C7 intermediates during cyclohexane oxidation with equivalence ratio of 2.0 and pressure of 1.05 atm





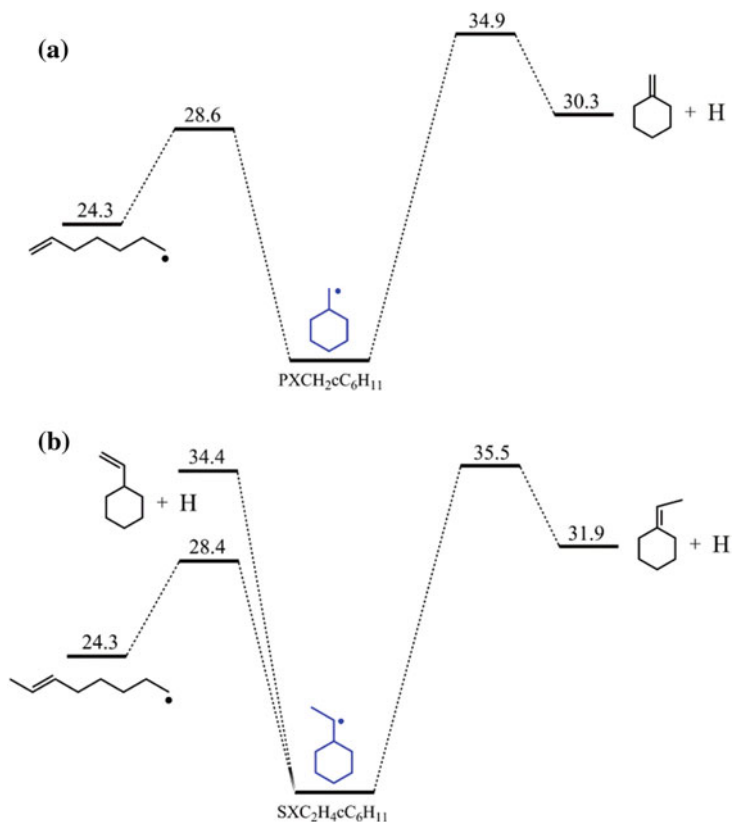
**Fig. A.3** Experimental (symbols) and simulated (lines) mole fraction profiles of reactants, major products, and C1–C6 intermediates during cyclohexane oxidation with equivalence ratio of 0.5 and pressure of 10 atm



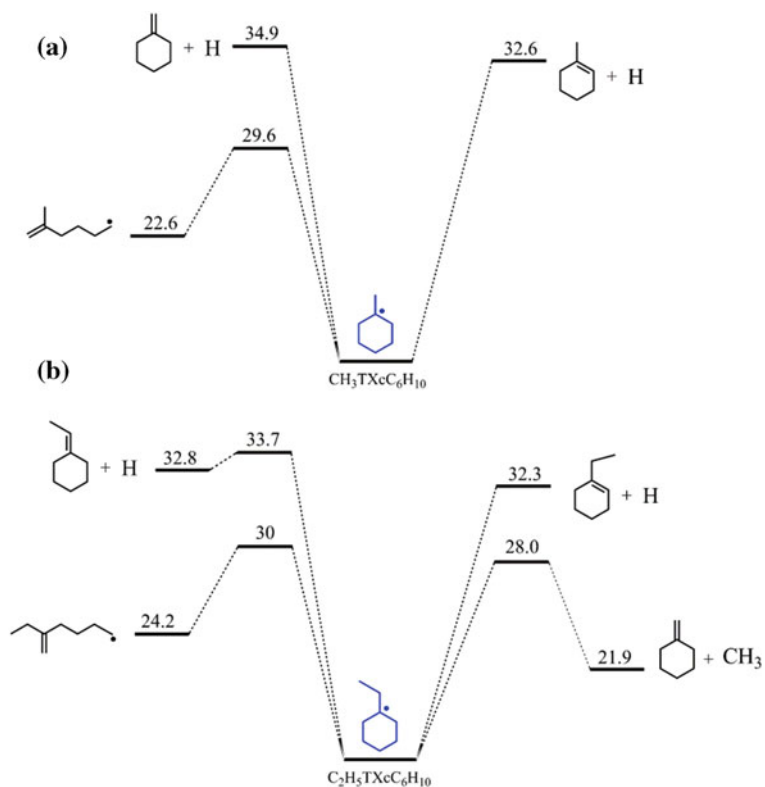
**Fig. A.4** Experimental (symbols) and simulated (lines) mole fraction profiles of reactants, major products, and C1–C6 intermediates during cyclohexane oxidation with equivalence ratio of 1.5 and pressure of 10 atm

## Appendix B

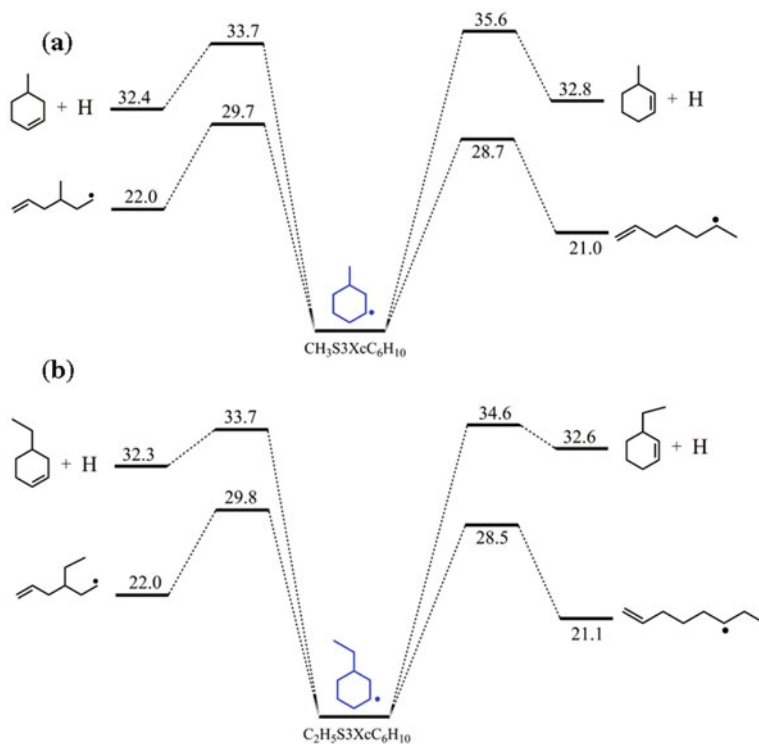
See Figs. B.1, B.2, B.3 and B.4.



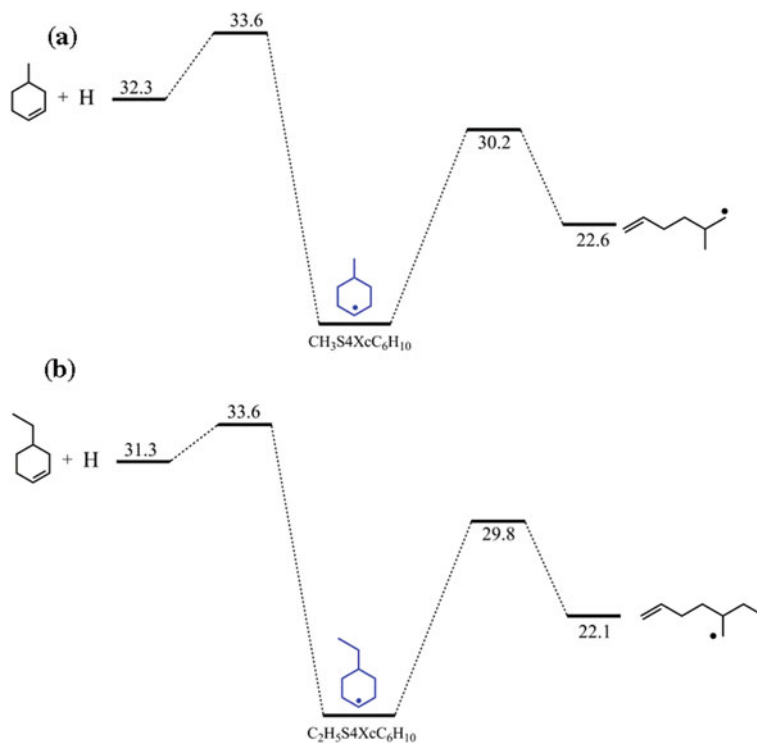
**Fig. B.1** Potential energy surfaces for the unimolecular reactions of cyclohexylmethyl radical (a) and 1-cyclohexyl-1-ethyl radical (b). Reprinted from Ref. [18] in Chap. 5, Copyright 2015, with permission from Elsevier



**Fig. B.2** Potential energy surfaces for the unimolecular reactions of 1-methyl-cyclohexyl radical (a) and 1-ethyl-cyclohexyl radical (b). Reprinted from Ref. [18] in Chap. 5, Copyright 2015, with permission from Elsevier



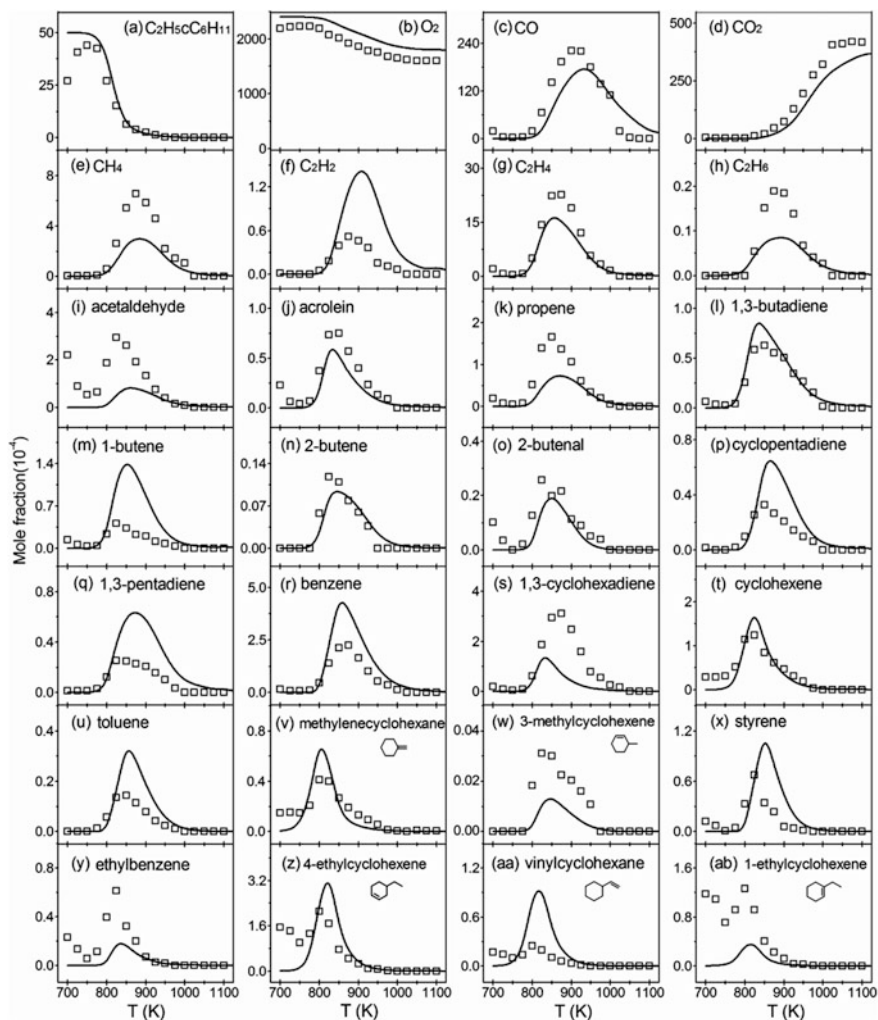
**Fig. B.3** Potential energy surfaces for the unimolecular reactions of 3-methyl-cyclohexyl radical (a) and 3-ethyl-cyclohexyl radical (b). Reprinted from Ref. [18] in Chap. 5, Copyright 2015, with permission from Elsevier



**Fig. B.4** Potential energy surfaces for the unimolecular reactions of 4-methyl-cyclohexyl radical (a) and 4-ethyl-cyclohexyl radical (b). Reprinted from Ref. [18] in Chap. 5, Copyright 2015, with permission from Elsevier

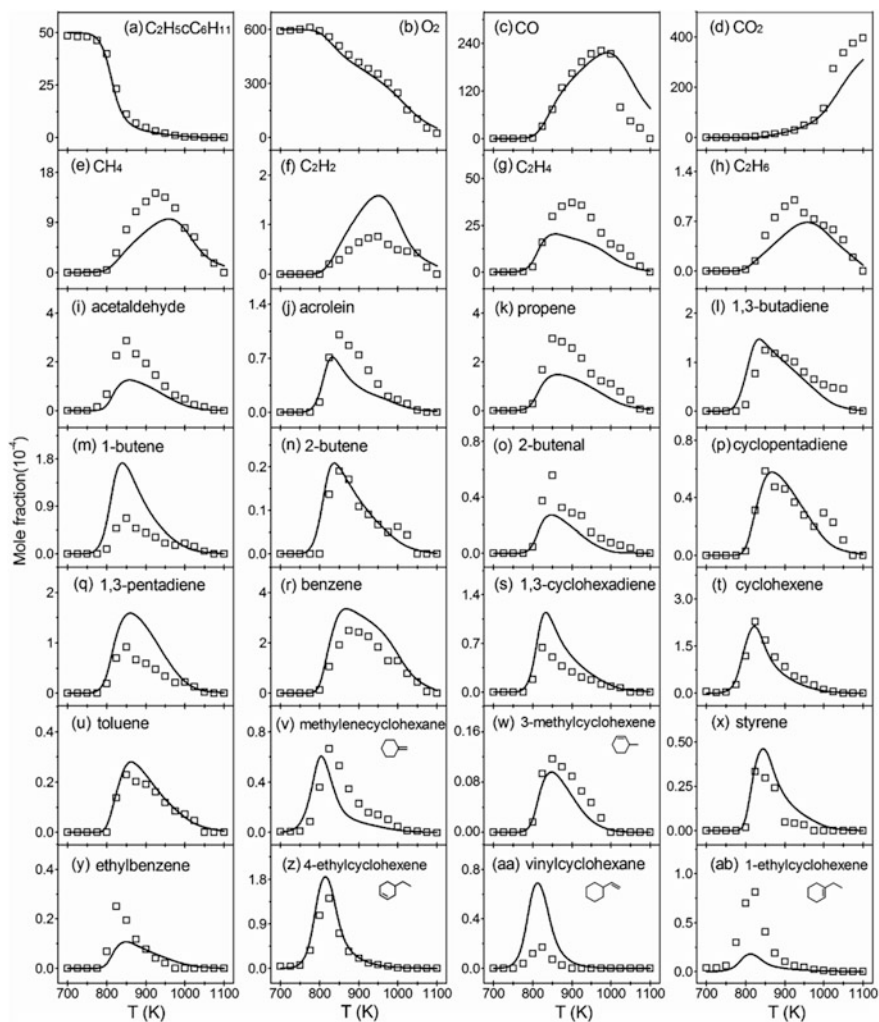
## Appendix C

See Figs. C.1 and C.2.



**Fig. C.1** Mol fraction profiles of reactants, major oxidation products, and C1–C8 intermediates in ethylcyclohexane oxidation at 800 Torr and equivalence of 0.25. Symbols from literature data of Husson et al. Lines from simulation. Reprinted from Ref. [18] in Chap. 5, Copyright 2015, with permission from Elsevier





**Fig. C.2** Mol fraction profiles of reactants, major oxidation products, and C1–C8 intermediates in ethylcyclohexane oxidation at 800 Torr and equivalence of 1.0. Symbols from literature data of Husson et al. Lines are from simulation. Reprinted from Ref. [18] in Chap. 5, Copyright 2015, with permission from Elsevier